Modelling and Control of Modular Multilevel Converter for High-speed Railway Traction Power Supply

Peiliang SUN

School of Electronic and Electrical Engineering
University of Leeds

Submitted in accordance with the requirements for the degree of
Doctor of Philosophy

March 2022

Declaration

I hereby declare that except where specific reference is made to the work of others, the contents of this dissertation are original and have not been submitted in whole or in part for consideration for any other degree or qualification in this, or any other university. This dissertation is my own work and contains nothing which is the outcome of work done in collaboration with others, except as specified in the text and Acknowledgements. This dissertation contains fewer than 65,000 words including appendices, bibliography, footnotes, tables and equations and has fewer than 150 figures.

Details of the publications which has been used in this thesis are as following:

In Chapter 2:

Peiliang Sun, Kang Li, Chen Xing. "A partial compensation scheme for MMC-based railway cophase power supply." Transportation Safety and Environment, Volume 2, Issue 4, December 2020, Pages 305–317.

As the lead author, the candidate contributed to all the technical modelling and simulation work as well as the draft writing. Prof. Kang Li, the supervisor who revised the structure of paper and did the proof-reading of the paper. Chen Xing helped in studying the model and checked the equation and assisted in composing the research idea.

In Chapter 4:

Peiliang Sun, Kang Li, Yongfei Li, Li Zhang. "DC voltage control for MMC-based railway power supply integrated with renewable generation." IET Renewable Power Generation. Volume 14, Issue 18, 21 December 2020, p. 3679 – 3689.

As the lead author, the candidate did the draft writing and most of the technical work in modelling and analysis. Kang Li, the supervisor who provided the topic of this work and proofread the paper. Yongfei Li helped in debugging the simulation model. Dr. Li Zhang provided suggestions on the development of the paper.

Peiliang SUN
March 2022

Acknowledgements

I would like to acknowledge the help and support from all the people I met as well as other natural resources that I consumed. It is a real privilege to be one of the Homo sapiens having the free will to live and think. I deeply believe this is exceptionally rare in the universe.

I cannot be at this stage without all the great support from my parents who devoted the best of their life for my education. The work presented in this thesis cannot be done without the opportunity offered by my supervisor Prof. Kang Li who presented this interesting topic to me.

Power electronics and control is a new topic for me at the start of my PhD study. I would like to give my gratitude to Dr. Li Zhang, Dr. Yongfei Li and Xuejiao Pan for their help in power electronics technologies.

I would also need to present my heartfelt thanks to the other group members: Dr. Shaojun Gan, Chen Xing, Xuan Liu, Mingjia Yin, Dr. Yanxia Wang, Dr. Yihuan Li and Dr. Xiang Li, who kindly offered lots of help in the past few years.

Finally, I would present my love to my dear wife Tianyu Yu and my beloved newborn daughter.

Abstract

Over 50 countries and regions worldwide have communicated their commitments to net-zero by the middle of this century. Transportation is responsible for 27% carbon emissions in the UK in 2019. Railway is recognised as one of the most energy efficient means for travel as well as for freight transport. However, only 38% of the current railway route is electrified in the UK. Diesel-based internal combustion engine trains will be phased out in the next decades. Long term plans are necessary for the success in meeting the 2050 goal. This includes not only electrifying the non-electrified railway network, but upgrading the existing infrastructure to increase power supply capacity.

The traditional feeder stations in traction power supply systems (TPSS) are based on different transformers to convert power from the three phase utility grid power to a single phase traction AC overhead line. Power quality issues such as voltage imbalance and current harmonics exist in the legacy system, and the neutral sections between each supply phase hinder the evolution of the traction power network to a fully connected smart network. Furthermore, this type of station does not provide convenient interfaces for renewable source integration.

The electronic converter based static frequency converter (SFC) has been introduced into the feeder station construction. This SFC solution can solve most of the power quality issues through its flexible operation scheme, and RES can be integrated into the SFC based feeder station by altering the converter topology. The modular multilevel converter (MMC) is viewed as a promising topology for high power conversion applications. However, the cost of this solution is high at the moment when using SFC to replace the station transformer.

In this thesis, a MMC is chosen as the primary topology and novel control strategies are developed to improve its performance. Firstly, the traditional cascaded linear control approach is summarised and modified to improve the DC power delivery performance. Then model based MMC modelling and its detailed internal dynamics are analysed for long horizon predictive controller design, which provides superior transient response speed over conventional approaches.

Regarding railway TPSS, a compensation method for voltage imbalance issue in the V/v transformer substation is investigated. A simulation platform for AT-based TPSS is then developed to support mobile traction load analysis under different supply control schemes.

To mitigate the power quality issue with reduced investment, a partial compensation strategy based MMC cophase scheme is investigated. The proposed design and control method reduces electronic converter capacity, which provides a hybrid approach for substation design with lower SFC investment.

To improve the SFC operational performance, a long horizon model predictive controller is designed for back to back MMC based feeder station, which has optimal performance under the most demanding load condition.

To integrate the renewable energy generation, wind generation power is coupled at the DC-link of the back to back MMC substation. A modified MMC control is designed for DC link voltage stability despite drastic generation/load change.

To improve substation reliability and energy efficiency, batteries are interfaced to each submodule in the MMC arms. This topology provides greater connection flexibility and operational reliability. The internal energy for charging and discharging is controlled by MPC under the hierarchical scheme. The ESS can be charged by utility grid or a train's regenerative power, and can be discharged for supporting traction load in grid fault condition.

To fully utilise the freedom of SFC substation control, a power sharing strategy is proposed in the two SFC stations scenario where two SFCs are collaboratively supplying an AT-network from both ends. A frequency droop method is designed to assign the optimal power to each SFC. The proposed method achieves balance in capacity enhancement and transmission loss reduction.

In summary, this thesis presents a comprehensive study on the modelling and control of MMC based SFC applications for future railway power suppl. The proposed work has the potential of reduction SFC overall cost by smaller capacity converter and smaller size capacitors. Renewable sources integration approaches may assist with transforming current TPSS to an eco-friendly and smarter system in the future.

Table of contents

List of figures xiii

List of tables xvii

Nomenclature xix

1 Introduction 1

1.1 Overview of railway electrification 1

1.1.1 AC electrified railway systems 1

1.1.2 Railway electrification in the UK 3

1.2 Power converter application in high-speed rail power supply 3

1.2.1 Converter topology 4

1.2.2 SFC applications in railway networks 4

1.3 Motivation and thesis structure 5

1.3.1 Motivation of the work 5

1.3.2 Thesis structure 6

2 Modular multilevel converter for cophase scheme 9

2.1 Overview of cophase technology for power conditioning 9

2.2 Design of partial compensation cophase power conditioning for V/v transformer 11

2.2.1 V/v transformer feeder station and the inherent power quality issues 11

2.2.2 Compensation strategy design for cophase power supply system 13

2.2.3 Modelling and control of the MMC-based power conditioner 18

2.3 Simulation and discussion 22

2.3.1 System control scheme and simulation setup 22

2.3.2 Cophase supply for static load 23

2.3.3 Cophase compensation for variable loads 26

2.4 Summary 28

3 Model predictive control for modular multilevel converters 29

3.1 Overview of MPC method for multilevel back to back converter control 29

3.1.1 MPC for AC/DC power electronic converters 29
3.1.2 MPC for MMC 32
3.1.3 MPC for B2B converters 34
3.2 Modelling of MMC substation for MPC design 35
3.2.1 MMC AC side equivalent circuit modelling 36
3.2.2 MMC DC side equivalent circuit modelling 38
3.2.3 MMC arm energy modelling 39
3.2.4 System model for predictive control 40
3.3 Model predictive controller design 41
3.3.1 Reference design 41
3.3.2 Controller constraints design 47
3.3.3 Cost function design 50
3.4 Simulation and discussion 50
3.4.1 MPC model setup for simulation 50
3.4.2 Control scheme for back to back converter 53
3.4.3 Grid side three phase MMC 54
3.4.4 Traction side single phase MMC 62
3.4.5 B2B MMC system 63
3.5 Summary 65

4 Modular multilevel converter with renewable energy generation integration 67
4.1 Overview of renewable energy generation integration in railway power supply 67
4.2 Modelling and control of DC link coupled wind power generation substations 69
4.2.1 System topology and operation 69
4.2.2 Wind power generator modelling and control 72
4.3 MMC based static frequency converter station 74
4.3.1 Modelling and design of the back to back converter 74
4.3.2 AC voltage control of MMC 79
4.3.3 DC link voltage control of MMC 81
4.3.4 Inner control of MMC 83
4.3.5 MMC modulation 84
4.4 Simulation results and discussion 84
4.4.1 Train load profile and wind power profile 85
4.4.2 Steady state performance analysis 85
4.4.3 Transient performance analysis 88
4.5 Summary 92

5 Modular multilevel converter with energy storage integration 93
5.1 Review of energy storage system integration in railway power supply . . . 93
5.1.1 Energy storage research and application in railway . . . 93
5.1.2 MMC integration with energy storage system . . . 94
5.2 Model predictive controller for ESS integrated MMC substation . . . 98
5.2.1 MMC-ESS topology . . . 98
5.2.2 Analysis of MMC arm energy dynamics . . . 99
5.2.3 MMC-ESS control scheme . . . 100
5.3 Simulation and discussion . . . 106
5.3.1 Simulation settings . . . 106
5.3.2 Simulation result . . . 107
5.4 Summary . . . 110

6 Control of parallel SFC substations for continuous traction AC power supply 113
6.1 Overview of SFC applications for continuous railway power supply . . . 113
6.2 Modelling of a single track railway power supply network . . . 115
6.2.1 Substation and transformer model . . . 116
6.2.2 Conductor line model . . . 116
6.2.3 Traction load model . . . 118
6.2.4 Simulation setup . . . 119
6.3 Adaptive droop controller for optimal power sharing of dual-end SFCs . . . 121
6.3.1 Power sharing strategy for single train . . . 122
6.3.2 Power sharing strategy for three trains . . . 123
6.3.3 Droop control design . . . 124
6.3.4 Droop controller parameter design . . . 125
6.4 Simulation results and discussion . . . 131
6.4.1 Simulation results . . . 131
6.4.2 Comparison of power supply schemes - single traction load . . . 131
6.4.3 Comparison of power supply schemes - three train scenario . . . 133
6.5 Summary . . . 135

7 Conclusion and future work 139
7.1 Summary of the research work . . . 139
7.2 Discussion and prospect . . . 141

References 143

Appendix A Modelling and control of modular multilevel converters 155
A.1 MMC modelling . . . 155
A.1.1 MMC basic topology . . . 156

A.1.2 Single phase MMC analysis 157
A.2 MMC control and operation 159
A.2.1 Current control 160
A.2.2 Internal energy control 160
A.2.3 Modulation 161

Appendix B Deadbeat controller implementation for MMC **165**

List of figures

1.1 Typical AC railway network configurations . . . 2
1.2 Traction drive system . . . 2
1.3 Thesis structure illustration . . . 7

2.1 Railway traction power supply structures and active power quality controller configurations 10
2.2 V/v transformer and V/x transformer feeder station . . . 11
2.3 Phasor diagrams[1] of V/v transformer with different load conditions . . . 12
2.4 V/v transformer with MMC-based cophase connection . . . 13
2.5 Full compensation phasor diagram . . . 14
2.6 Partial compensation phasor diagram . . . 15
2.7 Compensation percentage comparison: full compensation v.s. partial compensation . . 18
2.8 Compensation strategy for different load conditions . . . 18
2.9 Resistive loss comparison (normalised loss value) . . . 19
2.10 MMC topology and single phase equivalent circuit . . . 19
2.11 Reference current design scheme . . . 21
2.12 Capacitor voltage balance control and current control . . . 22
2.13 Cophase system and control scheme diagram . . . 23
2.14 Voltage unbalance factor under static load . . . 24
2.15 Grid voltage and current under static load . . . 24
2.16 Grid side power factor correction under static load . . . 25
2.17 MMC internal status: capacitor voltage and circulating current . . . 25
2.18 FFT analysis of grid current I_A before and after compensation (static rectifier load) . . 26
2.19 Compensation for varying current source load . . . 27
2.20 Voltage unbalance under load step change . . . 27

3.1 MMC three-phase AC side equivalent circuit model . . . 36
3.2 MMC single-phase AC side equivalent circuit model . . . 37
3.3 MMC three phase DC side equivalent circuit model . . . 38
3.4 MMC single phase dc side equivalent circuit model . . . 39
3.5 Linear approximation of voltage constraints . . . 49

3.6 Essential measurements of B2B MMC substation 53
3.7 Inner loop control scheme for B2B MMC substation: grid side (left), traction side (right) 53
3.8 Outer loop control scheme for traction side MMC 54
3.9 Outer loop control scheme for grid side MMC 54
3.10 Three phase MMC DC current tracking 55
3.11 Three phase MMC grid current tracking (10 MW step change at 1 s) 56
3.12 Three phase MMC averaged capacitor voltage value of each arm 56
3.13 Three phase MMC steady state tracking error 56
3.14 Comparison of horizon length influence on controller performance 58
3.15 Three phase grid current comparison 59
3.16 DC-link current comparison 60
3.17 Arm capacitor voltage comparison 60
3.18 Parameter variation influence on steady state current tracking error 61
3.19 Parameter variation influence on transient current tracking error 61
3.20 Traction network voltage (10 MW load change at 0.4 s) 62
3.21 Single phase MMC current tracking (10 MW load change at 0.4 s) 62
3.22 Singe phase MMC capacitor voltage (10 MW load change at 0.4 s) 63
3.23 B2B-MMC current performance (10 MW step change) 63
3.24 B2B-MMC DC-link measurement 64
3.25 Averaged submodule capacitor voltage in each arm of B2B-MMC system 64

4.1 Different connection schemes for integrating renewable energy source into railway supply system. (a) RES interfaced with high voltage distribution grid. (b) RES interfaced with medium voltage 25 kV overhead line. (c) RES interfaced with power grid compensator. (d) RES interfaced with railway power conditioner. (e) RES interfaced with cophase supply conditioner. (f) RES interfaced with static converter based station 69
4.2 Configuration of a wind power connection into static converter based railway substation 71
4.3 Power flow illustration for the hybrid railway supply system 71
4.4 Permanent magnet synchronous generator with neutral point clamped three level converter 72
4.5 Controller diagram for PMSG drive 74
4.6 Topology of the MMC back to back static converter 75
4.7 Simplified equivalent differential common mode model of single MMC phase 77
4.8 Range of modulation index and output voltage with average capacitor voltage $u_C^{\text{ave}} = aV_{\text{dc}}/N$ 78
4.9 Control diagram of the three phase grid AC voltage controller 80
4.10 Single phase MMC railway traction network supply 81
4.11 Control diagram of the single phase ac traction supply 81
4.12 DC voltage double frequency oscillation suppression 82
4.13 DC voltage stabilisation control 83

4.14 Circulating current control diagram . . . 83
4.15 Capacitor balance control diagram . . . 84
4.16 MMC control reference calculation and modulation . . . 84
4.17 Steady state power flow (*Case A*) . . . 86
4.18 Steady state DC-link voltage comparison 1 (*Case A*) . . . 87
4.19 Steady state DC-link voltage comparison 2 (*Case A*) . . . 87
4.20 Instantaneous power flow in *Case* B_1 simulation . . . 88
4.21 DC link voltage comparison (*Case* B_1) . . . 89
4.22 Instantaneous power flow in *Case* B_2 simulation . . . 90
4.23 DC link voltage comparison (*Case* B_2) . . . 90
4.24 DC link voltage (*Case* C_{1-4}) . . . 91
4.25 Voltage references for upper branch of phase A (*Case* B_1) . . . 91
4.26 Comparison of the composite modulation references of phase A upper branch $m_{\mathrm{au}}^{\mathrm{ref}}$ (*Case* B_1) . . . 91

5.1 System structure of the ESS integrated SFC station . . . 98
5.2 Topology of ESS integration into MMC substation . . . 99
5.3 Hierarchical approach for MMC-ESS substation operation control . . . 102
5.4 Measurement and control scheme . . . 102
5.5 MMC-ESS substation power supply mode decision flowchart . . . 104
5.6 Power profile for MMC-ESS simulation test . . . 107
5.7 Power and AC current result of the Type-I station . . . 108
5.8 DC current of the Type-I MMC-ESS station . . . 108
5.9 Arm energy (filtered) of the Type-I MMC-ESS station . . . 109
5.10 Power and AC current result of the Type-II station . . . 109
5.11 DC current of the Type-II MMC-ESS station . . . 110
5.12 Arm energy (filtered) of the Type-II MMC-ESS station . . . 111

6.1 Single-end power supply (left) and dual-end power supply (right) . . . 113
6.2 Conductor line model . . . 116
6.3 Variable impedance multi-conductor component simulation model . . . 117
6.4 Traction load force profile . . . 118
6.5 Single traction load profile . . . 119
6.6 Three trains’ load profile . . . 119
6.7 Highspeed train simulation model . . . 120
6.8 Illustration of the dual-end parallel feeding simulation model . . . 121
6.9 Frequency droop line for two substations . . . 122
6.10 Two SFC substation in dual-end feeding for single train load . . . 122
6.11 Optimal power ratio for single traction load . . . 123

6.12 Modified droop curve with power saturation protection 125
6.13 Droop control scheme for SS1 substation 125
6.14 Eigenvalue analysis result (real parts) 128
6.15 Eigenvalue analysis result of maximum imaginary parts magnitude 129
6.16 Different droop curve with saturation point setting 129
6.17 Comparison of different droop controller inertia settings. LPF T_f value: a) 1/10 s, b) 1/50 s, c) 1/200 s. 130
6.18 Comparison of different saturation set points $P_{\text{sat}}/P_{\max}$ setting: a) 50%, b) 75%, c) 90%. 130
6.19 Comparison of active power consumption (single traction load) 132
6.20 Comparison of capacity demand at SS1 substation (single traction load) 132
6.21 Comparison of network voltage frequency 133
6.22 Comparison of traction side voltage RMS value (single traction load) 133
6.23 Comparison of active power consumption (three traction load) 134
6.24 Power demand on SS1 substation 134
6.25 Network frequency (three trains) 135
6.26 Train side voltage RMS measurement (three trains) 136
6.27 Comparison of traction side voltage (three trains) 136

A.1 Single phase MMC circuit diagram 156
A.2 MMC submodule operating mode 157
A.3 MMC single phase model: (a) averaged model, (b) differential mode model, (c) common mode model 158
A.4 MMC internal dynamics control principle 159
A.5 Arm voltage control reference versus available voltage 162

List of tables

2.1 Power quality of V/v transformer station 12

2.2 Simulation system parameters 24

3.1 B2B MMC simulation parameter 55

3.2 The instantaneous power exchange in MMC arms 57

4.1 System parameters of wind power generation system 73

4.2 Parameters of SFC substation back to back converter 79

4.3 Simulation and control parameters setting 85

5.1 The instantaneous power exchange in MMC upper and lower arm 101

6.1 Substation output transformer parameter 120

6.2 Autotransformer parameter 120

6.3 Multiconductor model parameter 120

Nomenclature

Roman Symbols

$\boldsymbol{A}(\cdot)$	system state matrix
$\boldsymbol{B}(\cdot)$	system input matrix
C	capacitor
F	force
i, I	instantaneous current value, constant current value
J	cost function
L	inductor
m	modulation index
N	number of MMC submodules in one arm branch
N_h	prediction horizon length
R	resistor
T_s	simulation model sampling time
T_sc	controller sampling time
u, V	instantaneous voltage value, constant voltage value

Greek Symbols

ε	MMC arm branch energy
g	acceleration of gravity, switch gate signal
λ	cost function weighting factor
ω	AC component angular speed
φ	current phase angle

Superscripts

$*$	reference value
M	electric machine
$\vee$	phasor value
$\top$	matrix transpose

Subscripts

a,b,c,e,f	phase identifier
ave	averaged value
br	MMC branch
C	capacitor value
com	MMC common mode model component
d	quadrature axis value in Park transformation
DC,dc	DC-link value
dif	MMC differential mode model component
eq	equivalent value
g	grid side value
max	minimal value
min	maximum value
nom	nominal value
q	direct axis value in Park transformation
sub	MMC submodule value
tr	traction load side value
u,l	upper arm, lower arm

Acronyms / Abbreviations

1ph,3ph	Single Phase, Three Phase
AC	Alternating Current
AT	Auto Transformer — simple three-tap transformer used to create a negative feeder along a catenary system
B2B	Back to Back

BT	Booster Transformer — transformer arranged along the catenary to provide EMC immunisation
CCS	Continuous Control Set
CPS	Carrier Phase Shift
DAB	Dual Active Bridge
DC	Direct Current
EMU	Electric Multiple Unit
ESS	Energy Storage System
FCS	Finite Control Set
FOH	First-order Hold
LPF	Low Pass Filter
MIMO	Multi-input Multi-output
MMC	Modular Multilevel Converter
MPC	Model Predictive Control
NPC	Neutral Point Clamped
p.u.	Per Unit system
PI	Proportional Integral
PR	Proportional Resonant
PWM	Pulse Width Modulation
RES	Renewable Energy Source
RMS	Root Mean Square
RPC	Railway Power Conditioner
SFC	Static Frequency Converter
SOC	State Of Charge
SOH	State Of Health
SQP	Sequential Quadratic Programming
STATCOM	Static Synchronous Compensator
TPSS	Traction Power Supply System
WTG	Wind Turbine Generator
ZOH	Zero-order Hold

Chapter 1

Introduction

1.1 Overview of railway electrification

1.1.1 AC electrified railway systems

In the AC powered railway system, the high voltage power source provided by the utility grid is reduced to a suitable level and is fed to the railway conductors. The frequency standards in AC electric railway are $16\frac{2}{3}$ Hz (Central Europe), 25 Hz (North America), 50 Hz and 60 Hz. The low frequency solutions are designed in the early 20th century. Countries which developed electrification after technology advancement adopted the 50 Hz for single phase railway system. 25 kV was chosen to reduce the transmission losses with longer distance between stations.

AC feeder transformer (7.5 MW to 60 MW) is essential in the conventional substations. Generally the transformer connects between three phase AC grid (usually from 110 kV to 400 kV [1]) and single phase overhead line system.

Figure 1.1 shows two typical railway network configurations: the boost transformer with return conductor and autotransformer connection. A boost transformer collects the current from the rail and return it to the conductor. It is used to eliminate the stray current and the disturbance by forcing the current flowing to the 'return conductor' as shown in Figure 1.1a. The autotransformer is used to balance the voltage between the contact line and the earth and then distribute the return current between these two phases. It provides two phases with 180 degree phase shift with the midpoint connected to the ground.

Figure 1.2 shows the typical electric multiple unit (EMU) traction drive system. A back-to-back conversion system is used to drive multiple traction motors. In the braking period, the kinetic energy of the train are sent back to the contact line. Thanks to the single phase full bridge line converter technology, the new high speed train can operate at near unity power factor.

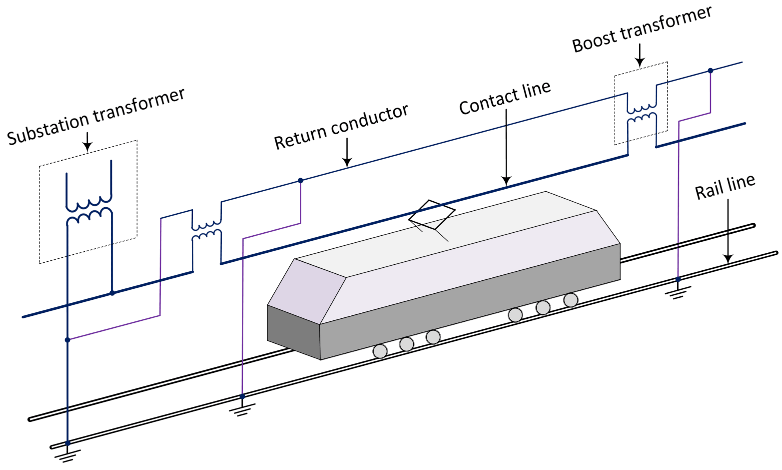

(a) Boost transformer with return conductor

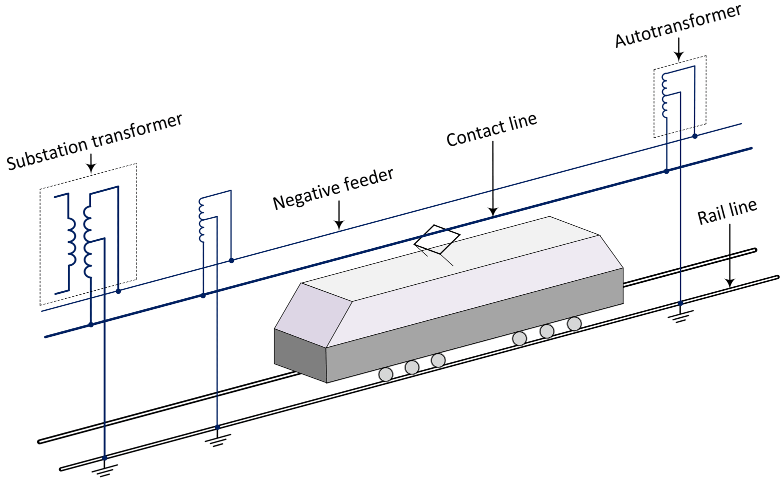

(b) Autotransformer supply

Fig. 1.1 Typical AC railway network configurations

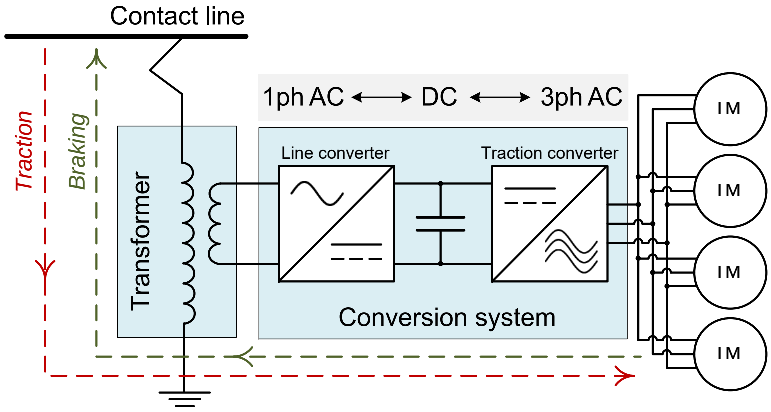

Fig. 1.2 Traction drive system

1.1.2 Railway electrification in the UK

Three types of arrangements are used in Britain's power supply: 25 kV AC overhead line equipment, 1.5 kV DC overhead line equipment and 650/750 V DC third rail system [2]. The overhead line standard is 25 kV 50 Hz AC chosen by British Rail in the mid 20th century [3, 4].

The UK government has targeted to remove all diesel trains by 2040 and to meet net-zero carbon emission target by 2050 [5]. This requires the upgrading of 1/3 of the current trains and infrastructure [6]. However, without an immediate rolling program for electrification over the next decades, it will be extremely challenging to meet these targets [7]. In 2021, an open letter was signed by a collective of railway and freight associations to call on the UK government to implement a program of railway electrification [8].

Electrified railway transportation is an effective way to reduce carbon emission for the UK transportation system. To meet the increasing demands on railway system, high performance trains are needed which create a need for network capacity enhancement [9]. The report published by Transport Committee in March 2021 also stated that 'electrification is the only immediately viable decarbonization option for most of the network' [10].

According to the data published in 2020, the total route length of the UK's railway system is 15,904 km and 6,049 km of the mainline railway route is now electrified which accounts for 38% of all routes [2]. To achieve full electrification by 2050, [11] stated that 13,000 single-track km needed to be electrified and this is about 450 single track kilometre (STK) per year from now on.

Although onboard energy storage technology such as chemical batteries and hydrogen are feasible solutions to abandon the use of petroleum, this type of solutions will consume too much space in the interior space or add extra weight to the vehicle. Further, the technology maturity has not yet reached the commercialisation level. Currently, the electrification using overhead line offers the highest energy efficiency solution among other methods [9].

1.2 Power converter application in high-speed rail power supply

So far, the power electronic technologies have become mature for high voltage and high power applications with the advancement of high power semiconductor switches. Full power electronic converter based railway traction feeder station has been researched and used [1]. These power electronic converter based substations are also named as "static frequency converter (SFC)" in the community and which are back to back conversion systems.

The power quality issues brought by transformers can be solved in the full converter based substation. Moreover, the SFC station enables effective feeding of regenerative power back to the grid or other on-board or line-side stationary storage devices. Because the SFC does not require the support of the high capacity high voltage utility grid [12], Network Rail estimates that 'SFC technology could reduce the cost of a new feeder station by 60%' [9]. Converter-based substations make the connection to a weaker utility grid possible, and no neutral zones are needed so that the traction can be supplied by multiple substations from both ends and the catenary can be lighter [13].

1.2.1 Converter topology

Conventional two level converter topology is usually not used for railway substation purposes due to its capacity limitation and bulky filter implementation. Diode clamped multilevel converter, cascaded H-bridge and modular multilevel converter are often founds in real applications.

Diode clamped multilevel converter One topology used in practice is the diode clamped multilevel converters and the three level topology has been widely used. Two 3ph 3-level bridges were employed on the grid side and four 1ph 3-level bridges cascaded for traction side supply [14]. [15] designed a five level DCMC back to back converter in a scaled down experiment for solid state transformer substation concept validation.

Cascaded H-bridges converter One solution is to use multiple full bridge converters in parallel connected to one DC-link and the AC side is coupled by multi-winding transformers. In Japan Shinkansen electronic frequency converter solution, this topology is used based on the cascaded H-bridge topology. [16] presented IEGT (4.5 kV 2.1 kA) based Electronic Frequency Converter (EFC) system to replace rotary frequency changer in Shinkansen railyard. Two units are paralleled at one station for total 60 MWVA capacity.

Modular multilevel converter The modular multilevel converter topology has been intensively researched in recent years and has shown its advantages in high voltage direct current (HVDC) transmission system and high power conversion applications [17–20]. A SFC product based on self-commutated modular multilevel converters with power level between 12 MVA to 120 MVA was reported in [21]. This topology is selected as the converter topology in this study.

1.2.2 SFC applications in railway networks

Currently, SFC based railway applications have been built in different countries worldwide with SFC supplied from some major international companies.

United States Early applications of SFCs can be referred to late 20 centuries. A SFC system was installed in Philadelphia operated by Southeastern Pennsylvania Transportation Authority [22]. Thyristor type SFC was used to convert 60 Hz to 25 Hz used back at that time.

Japan In Japan, SFC has been installed in Tsunashima, Nishisagami, and Numazu for energy saving and less maintenance [23].

Queensland rail network In Australia, the SFC application was investigated the SFC application in Queensland [1]. The whole life assessment is considered in new and upgrade projects. Wulkuraka is one of the new SFC feeder station of Queensland Railway with the capacity of 20 MVA reported in 2015 [24]. Results showed that the SFC technology can reduce operation and maintenance cost while increasing system efficiency and reliability [24].

The largest Australia's heavy haul railway operator, Aurizon, commissioned the world first 50 Hz to 50 Hz SFC installation [25]. These potential benefits by introducing SFCs such as harmonic filtering, load balancing, efficiency, connection cost reduction are analysed through comparison with RPC, HVDC and ESS technologies [25]. However, the SFC does not offer temporary overload capacity, leading to implicated protection issue.

Central Europe Switzerland and Germany has $16\frac{2}{3}$ Hz railway lines, so the rotating machine method has been used to convert frequency. SFC has been applied to replace rotary converters [26].

UK The first application of SFC in the UK is in the project of the 'East Coast Power Supply Upgrade'. The two SFCs installed at Hambleton and Marshall Meadows are both having 132 kV connections and are expected to reduce cost by 60% [27]. Recently, a SFC feeder station was commissioned at Doncaster (UK) which enabled connection with 33 kV grid.

1.3 Motivation and thesis structure

1.3.1 Motivation of the work

The motivation of this thesis is to investigate technical solutions to answer some questions about the future development of electrification power supply infrastructures.

The MMC topology has been favoured in HVDC power transmission and other high power DC/AC applications. This thesis selects this topology and plans to improve the conventional control scheme for the high speed railway applications.

SFC offers high quality and flexible power supply, but its main drawback[1] is higher cost [28]. It is beneficial to incorporate legacy transformer system with power electronic converter to avoid full size power converter station.

In the future, more renewable sources are likely to be introduced into the SFC supplied railway network and new operation modes are yet to be developed. The introduction of renewable sources imposes demand of connection interface. Furthermore, specialised control objectives have to be considered for traction network power supply.

---

[1] SFC is more expensive compared to transformers, but the system cost might be lower because of the flexibility in the grid connection.

The current SFC stations connected in the same network are operated in synchronised mode without active control. There are controllable freedoms in fully SFC supplied network system which needs further discussions.

To address the above-mentioned four aspects, related research objectives are designed in the thesis as listed below.

1. Investigate the modular multilevel converter modelling and control aspects for high power traction network power supply application. Conduct detailed analysis of MMC internal dynamics for modelling and control. Build the simulation model of an MMC based SFC railway substation and its control system for various applications. Improve control performance of the MMC based SFC station by using modifying conventional control structure and adopting new control methods.
2. Investigate a hybrid supply structure to reduce the required capacity of the power electronic converter so that the infrastructure cost can be kept down. The solution should guarantee the good power quality feature reside in full power converter based stations.
3. Analyse the integration of renewable energy into the feeder station for green generation and energy storage using the modular multilevel converter topology. Design the control schemes to satisfy the requirements found in traction AC power supply application.
4. Study on a more flexible power supply scheme for SFC supplied traction network. Explore the usage of additional flexibility which does not exist in the traditional supply system to improve energy efficiency and power supply capacity.

1.3.2 Thesis structure

Figure 1.3 summarises the topic of each chapter.

Chapter 1 introduces the basic AC electrified railway system standard, application of electronic converter based SFC as well as the research objectives.

Chapter 2 to Chapter 5 present the research result of the thesis, the fundamental modelling and control scheme of an MMC based converter are explained in Chapter A.

Chapter 2 proposes a partial compensation strategy based MMC cophase converter connection for power quality improvement with the potential benefit of removing the neutral section at the substation exit. The proposed solution reduces the SFC capacity.

Chapter 3 develops a long horizon MPC for back to back MMC based feeder station. The long horizon and arm energy modelling approach improves system performance. The MPC is compared with linear controller and deadbeat controller.

Chapter 4 investigates the renewable generation connected through DC-link. A modified MMC control is proposed to mitigate the influence of single phase traction load and intermittent renewable generation. DC-link voltage error is reduced with the proposed controller.

Chapter 5 modifies the MPC investigated in Chapter 4 to accommodate flexible ESS integration. With ESS integrated to submodules, the power at MMC input and output are decoupled. ESS integrated

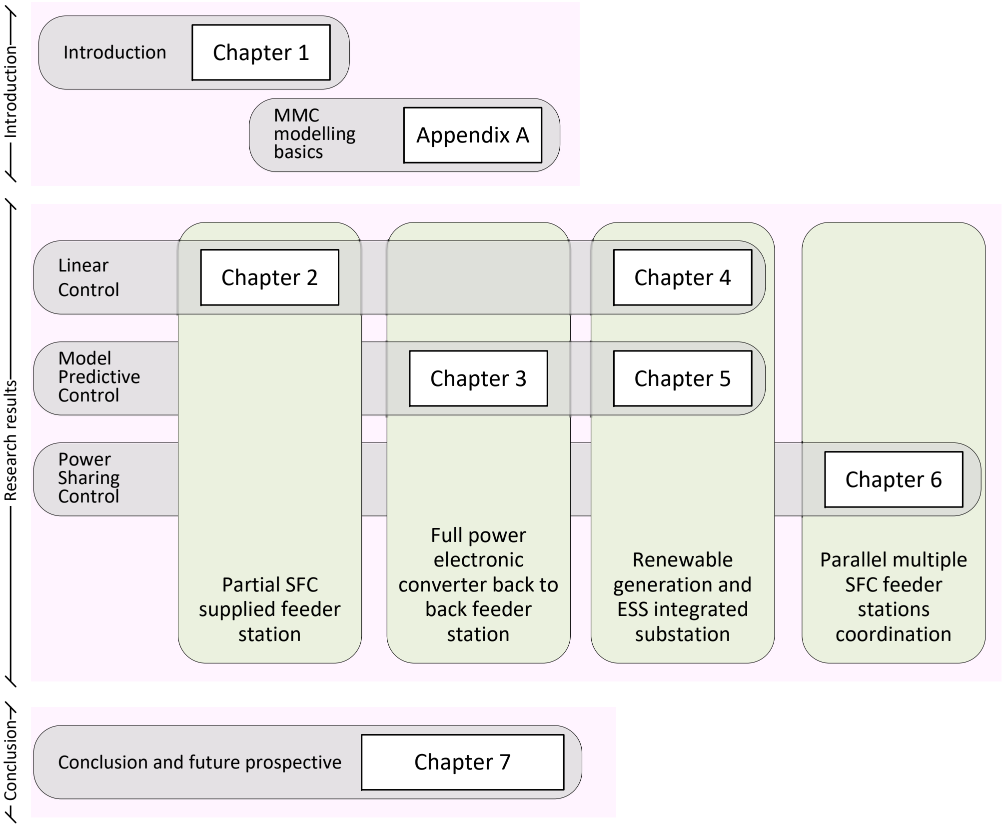

Fig. 1.3 Thesis structure illustration

MMC substation can support traction network when the grid capacity is compromised and can absorb regenerative power. The proposed control scheme realises fast dynamics in different operation modes.

Chapter 2 & 4 adopt the linear control approach while Chapter 3 & 5 use the model based predictive controller. Both of these approaches are simulated for grid connection traction network power supply and renewable source integration. By using these developed systems, a faster response of SFC operation is achievable.

Chapter 6 proposes an initial exploration of SFC parallel feeding scheme. This chapter focuses more on the network power supply—-the two SFC feeder station schemes with power sharing function. The optimal power sharing strategy is designed according to train position and power consumption. A simple droop controller is implemented for power sharing realisation. The result is simulated based on a single track AT connection network with up to three moving traction loads.

Chapter 7 concludes the research results and shortcomings in these chapters. Finally, expectations for future research are presented.

Chapter 2

Modular multilevel converter for cophase scheme

2.1 Overview of cophase technology for power conditioning

Three electrified railway traction power supply solutions are widely used, namely the 16 2/3 Hz 15 kV AC system, 50 Hz 25 kV AC system and 3 kV DC system. Among them, 25 kV 50 Hz AC traction power supply is most popular and in such a system, the feeder station converts three phase power supply (often at 110 kV) from the distribution network to single phase power supply (often at 25 kV) feeding to the railway overhead line (Fig. 2.1(a)). To step down the voltages, V/v (V/x) transformers with autotransformer connection are widely used in high speed railway systems [29]. These transformers generate two single phase voltage sources for two traction supply arms, which however inevitably introduces power unbalance and low power factor current into the grid, causing power quality issues. Furthermore, these transformers lack the ability to suppress harmonic currents produced by variable traction loads.

To address these issues from the power source perspective, improved transformers with a special connection typology have been developed and installed to reduce the negative sequence issue, such as the Scott transformer and Wood-bridge transformer, which can eliminate the negative sequence current provided that both sides are equally loaded [30]. However, non-balance transformers like I/i, V/v and YNd11 cannot eliminate negative sequence current even the loads at two sides are perfectly balanced, unless certain reactive current is added externally [31].

Another approach to improve the traction power quality is to use additional devices to compensate reactive power, negative sequence current and harmonics. Various types of compensators for railway applications are intensively researched [32–35]. These devices can be either installed at the grid side of the feeder stations or at the traction power supply side.

Since the last decade, many power electronics based compensators are used directly on the traction power network side for power quality conditioning. These converters in various forms include railway power regulator, active power quality compensator (APQC), railway power conditioner (RPC), power

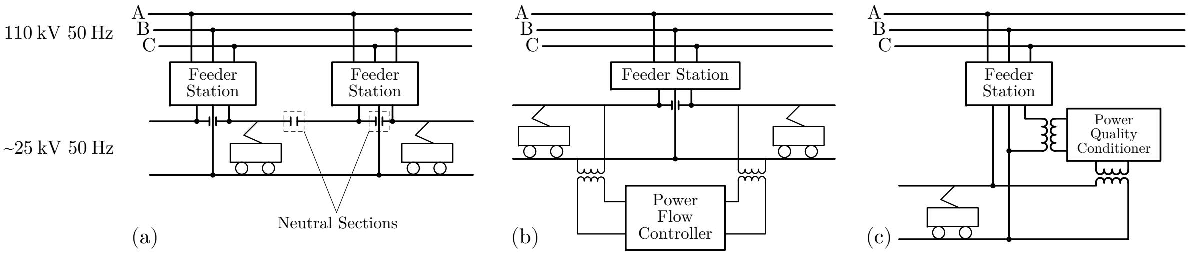

Fig. 2.1 Railway traction power supply structures and active power quality controller configurations

quality conditioner (PQC), power flow controller (PFC), etc. Their topology falls into two categories: power quality conditioning between two supply arms (Fig. 2.1(b)) or combining two arms into one as a cophase system (Fig. 2.1(c)). Both topology designs can balance the grid side current, but the cophase system has the advantage of reducing or even eliminating the neutral sections [36].

In the existing solutions, large LC impedance matching filters and transformers are needed for connection between converters and transformers. In [34], a special design is investigated to reduce the DC-link voltage via coupling impedance design that the reactive power is absorbed by the passive filter, however this is only applicable in certain current load conditions. Chen et al. use magnetic static var compensator (MSVC) to dynamically change impedance in response to the locomotive load variations [35]. Although the passive impedance can reduce the conditioner's voltage rating, the MSVC cannot follow rapid load change perfectly. Power electronics based compensators still have to provide some reactive power.

Cophase conditioners proposed in the literature are operated with a fixed compensation strategy or under the minimum active power capacity criteria. However, these approaches cannot fully minimise the loss when the traction load is lower than the nominal capacity of the conditioning system. Additionally, existing proposals use a bang-bang (hysteresis) controller for compensation current tracking control which may not be an acceptable option. Because the switching frequency is not directly constrained, and a high switching frequency is required to achieve good performance, the bang-bang control is hardly suitable for real applications nor for the multilevel converters.

This chapter investigates the V/v transformer-based cophase supply scheme, and employs a single-phase 25-level half-bridge modular multilevel converter (MMC) back-to-back topology to enable direct connection to the traction network without a transformer or additional passive filters. Compensation current reference is calculated in real-time to satisfy different load variations. The converter is controlled by proportional resonant (PR) controllers for current tracking, and carrier wave phase shifted pulse width modulation (CPS-PWM) is adopted to control the states of switches.

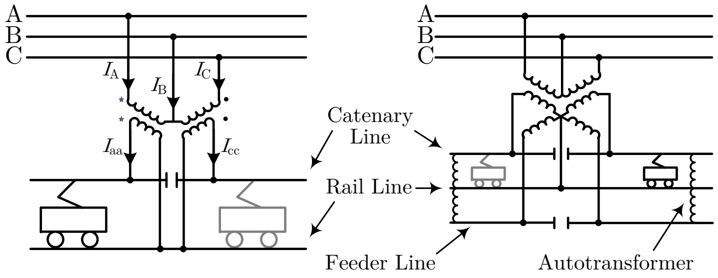

Fig. 2.2 V/v transformer and V/x transformer feeder station

2.2 Design of partial compensation cophase power conditioning for V/v transformer

2.2.1 V/v transformer feeder station and the inherent power quality issues

The wiring diagrams of V/v and V/x transformer are illustrated in Fig. 2.2. There are two single phase transformers connecting phase AB and phase CB and these types of transformers are widely used in current railway systems. V/x transformer is similar to V/v wiring type and can cancel the autotransformer (AT) within the feeder station. To make the following analysis easier to follow, $\check{I}_{\mathrm{bb}}$ (a virtual current at the transformer secondary side) is used. The relation of the currents at both sides of the transformer are expressed in Equ. (2.1).

$$\begin{cases} \check{I}_{\mathrm{aa}} = N\check{I}_{\mathrm{A}} \\ \check{I}_{\mathrm{cc}} = N\check{I}_{\mathrm{C}} \\ \check{I}_{\mathrm{bb}} = -(\check{I}_{\mathrm{aa}} + \check{I}_{\mathrm{cc}}) = N\check{I}_{\mathrm{B}} \end{cases} \tag{2.1}$$

To facilitate the analysis, $\check{I}_{\mathrm{aa}}, \check{I}_{\mathrm{bb}}, \check{I}_{\mathrm{cc}}$ are used to represent the three phase current condition at the grid side. The phasor diagram of V/v transformer with three different load conditions are illustrated in Fig. 2.3: (a) single-side load, (b) both sides have equal load, and (c) one side is half loaded than the other side. I_{TrL} and I_{TrR} are the traction load current RMS values on the left supply arm and on the right supply arm respectively. Due to different voltage phases of the two supply arm, a neutral section is necessary inside each feeder station. The existence of the neutral section blocks the energy sharing between two supply arms and introduces a no power zone where the train has to rely on inertia and on-board energy source without external supply.

Another issue is the inevitable negative sequence current, no matter how balanced the traction loads are in each supply arm. As shown in Fig. 2.3, the three phase current unbalance is most severe when only one side is loaded (Fig. 2.3(a): $I_{\mathrm{aa}} = I_{\mathrm{bb}} = I_{\mathrm{Tr}}$, $I_{\mathrm{cc}} = 0$) and is lightest when both sides are equally loaded (Fig. 2.3(c): $I_{\mathrm{aa}} = I_{\mathrm{cc}} = I_{\mathrm{Tr}}$, $I_{\mathrm{bb}} = \sqrt{3}I_{\mathrm{Tr}}$). The grid side negative sequence components are calculated by

---

[1] Vectors A, B and C represent the phase angles of the ideal three phase grid voltage phasors $\check{U}_{\mathrm{A}}, \check{U}_{\mathrm{B}}, \check{U}_{\mathrm{C}}$.

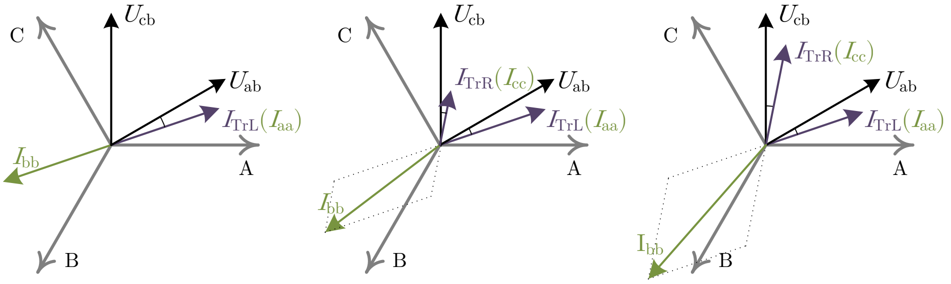

(a) $I_{\mathrm{TrL}}{=}I_{\mathrm{Tr}}\quad I_{\mathrm{TrR}}{=}0$ (b) $I_{\mathrm{TrL}}{=}I_{\mathrm{Tr}}\quad I_{\mathrm{TrR}}{=}0.5I_{\mathrm{Tr}}$ (c) $I_{\mathrm{TrL}}{=}I_{\mathrm{Tr}}\quad I_{\mathrm{TrR}}{=}I_{\mathrm{Tr}}$

Fig. 2.3 Phasor diagrams[1] of V/v transformer with different load conditions

Table 2.1 Power quality of V/v transformer station

Load condition		Fig. 2.3(a)	Fig. 2.3(b)	Fig. 2.3(c)
Current unbalance factor		100%	77.2%	63.4%
Power factor	pf_{A}	0.979	0.979	0.979
	pf_{B}	0.667	0.667	0.95
	pf_{C}	NA	0.874	0.667

[1] Assumption: traction load power factor $\mathrm{pf}_{\mathrm{Tr}} = 0.95$

transforming the three unbalance current phasors into three sets of symmetric phasors by Equ. (2.2).

$$\begin{bmatrix} \check{I}^{0} \\ \check{I}^{-} \\ \check{I}^{+} \end{bmatrix} = \frac{1}{N} \begin{bmatrix} 1 & 1 & 1 \\ 1 & \alpha^2 & \alpha \\ 1 & \alpha & \alpha^2 \end{bmatrix} \begin{bmatrix} \check{I}_{\mathrm{aa}} \\ \check{I}_{\mathrm{bb}} \\ \check{I}_{\mathrm{cc}} \end{bmatrix}, \quad \alpha \equiv \mathrm{e}^{+\mathrm{j}120^\circ} \tag{2.2}$$

The current unbalance factor is defined in Equ. (2.3):

$$\varepsilon_{\mathrm{I}} = \frac{\left|\check{I}^{-}\right|}{\left|\check{I}^{+}\right|} \times 100\%\,. \tag{2.3}$$

Negative sequence current will induce an unbalanced voltage in the grid and the definition of voltage unbalance ratio ε_{U} is similar to ε_{I} and can be estimated by Equ. (2.4):

$$\varepsilon_{\mathrm{U}} = \frac{\sqrt{3}\left|\check{I}^{-}\right| U_{\mathrm{L}}}{S_{\mathrm{k}}} \times 100\%\,, \tag{2.4}$$

where U_{L} is the RMS value of the grid line to line voltage and S_{k} is the grid short-circuit capacity.

Besides the negative sequence issue, the reactive power problem is also evident in that currents are not in phase with three phase grid voltage. Table 2.1 lists the current unbalance factor and power factors in different load conditions of the V/v transformer power supply.

The aforementioned issues all occur at the fundamental frequency (50 Hz), and there exists higher order harmonics mainly generated by converters in the train. These harmonics can be coupled into the

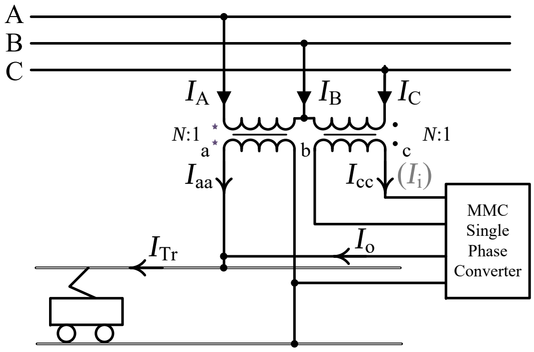

Fig. 2.4 V/v transformer with MMC-based cophase connection

power grid through transformers which cause extra losses and become a destabilising factor. In the next two sections, an MMC based cophase supply scheme is presented to solve those problems and the neutral zone inside the station can be cancelled.

2.2.2 Compensation strategy design for cophase power supply system

Topology and full compensation

A back-to-back converter is connected between phase ab and cb to form a cophase supply scheme in Fig. 2.4. The positive direction of current value is defined by the arrows' direction. I_{i}, I_{o} and I_{Tr} represent the current RMS values of the converter input current, converter output current and traction load current respectively. We assume the transformer is ideal so that Equ. (2.1) holds true.

Full compensation is defined as the negative sequence current is zero and the grid side power factors are kept to unity. Therefore, the three phase currents are all in-phase with the corresponding supply voltages and have the same magnitude. The phasor diagram is shown in Fig. 2.5. Current $\check{I}_{\mathrm{aa}}$, $\check{I}_{\mathrm{o}}$ and $\check{I}_{\mathrm{i}}$ are decomposed into orthogonal components that are in phase/perpendicular to the corresponding supply voltage phasor, and the magnitude of these orthogonal components are represented by $I_{\mathrm{aap}}, I_{\mathrm{aaq}}, I_{\mathrm{ip}}, I_{\mathrm{iq}}, I_{\mathrm{op}}, I_{\mathrm{oq}}$ respectively as shown in Fig. 2.5 and Fig. 2.6. Based on the energy conservation law, real power flow into and out of the converter should be equal (Equ. (2.5)) if losses are ignored.

$$\begin{aligned} I_{\mathrm{ip}} = I_{\mathrm{op}} \quad &\Rightarrow \quad I_{\mathrm{Tr}}\cos\phi_{\mathrm{Tr}} - I_{\mathrm{aap}} = I_{\mathrm{cc}}\cos\phi_{\mathrm{Tr}} \\ &\Rightarrow \quad I_{\mathrm{cc}} = \frac{I_{\mathrm{Tr}}\cos\phi_{\mathrm{Tr}}}{\cos(\pi/6)} - I_{\mathrm{aa}} \end{aligned} \tag{2.5}$$

The remaining phasors can be intuitively derived by geometric methods and the magnitude of each phasor is expressed in Equ. (2.6).

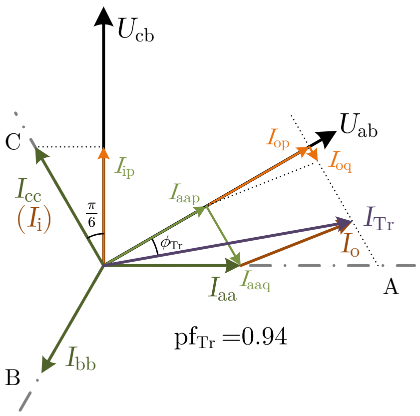

Fig. 2.5 Full compensation phasor diagram

$$\begin{cases} I_{aa} = I_{bb} = I_{cc} = I_{Tr} \cos \phi_{Tr} / \sqrt{3} \\ I_{op} = I_{Tr} \cos \phi_{Tr} / 2 \\ I_{oq} = I_{Tr} \left(\sin \phi_{Tr} - \cos \phi_{Tr} / 2\sqrt{3} \right) \end{cases} \tag{2.6}$$

These expressions show that to achieve full compensation operation, the converter has to provide half of the active power and a certain portion of the reactive power. The required capacity of the whole conditioner can be evaluated by the apparent power ratio (k_{size}) of the converter to the load as shown in Equ. (2.7). Assume the traction load power factor varies from 0.85 to 1, then the required capacity of the cophase conditioner should be 57.74% of the maximum traction load power for full compensation.

$$\begin{aligned} k_{size} = \frac{S_{Conditioner}}{S_{TractionLoad}} &= \frac{\max(I_o, I_i) \cdot U_{ab/(cb)}}{I_{Tr} \cdot U_{ab}} \\ &= \max \left(\sqrt{\frac{4 - 2\cos(2\phi_{Tr}) - \sqrt{3}\sin(2\phi_{Tr})}{6}} \right) \end{aligned} \tag{2.7}$$

In order to reduce the construction cost of the cophase power conditioner, k_{size} needs to be minimised. But there is no freedom to reduce k_{size}, because of the strict symmetric three phase current restriction in full compensation. However, the grid has the ability to withstand certain unbalanced current, so it is possible to relax the constraint to reduce system capacity.

Partial compensation strategy Design

Figure 2.6 shows the partial compensation strategy where each phase current is not necessarily in-phase with the supply voltage. φ_A , φ_B , φ_C are grid side current phase angles lagging to grid side voltage[2]. θ_{ab} and θ_{cb} are phase angles of the actual transformer's secondary side voltages which may not be 30° and 90° in the real system.

---

[2] In Fig. 2.6, $\check{I}_{aa}$ and $\check{I}_{cc}$ are actual leading to the voltages, therefore negative sign exists.

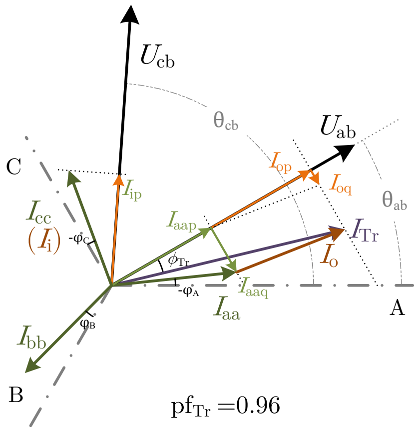

Fig. 2.6 Partial compensation phasor diagram

The first two equations in Equ. (2.5) still hold true and are expanded in Equ. (2.8):

$$\begin{aligned} I_{\mathrm{Tr}}\cos\left(\phi_{\mathrm{Tr}}\right) - I_{\mathrm{aa}}\cos\left(\theta_{\mathrm{ab}} + \varphi_{\mathrm{A}}\right) & \\ = I_{\mathrm{cc}}\cos\left(120^\circ - \theta_{\mathrm{cb}} - \varphi_{\mathrm{C}}\right) . & \end{aligned} \tag{2.8}$$

As shown in Fig. 2.4, three phase currents obey Kirchhoff's law which leads to Equ. (2.9):

$$\check{I}_{\mathrm{aa}} + \check{I}_{\mathrm{bb}} + \check{I}_{\mathrm{cc}} = 0 . \tag{2.9}$$

Partial compensation relies on the grid code[3] about the limit of permissible voltage unbalance and regulation for distribution network operators is often set at 2%. Phasor $\check{I}_{\mathrm{aa}}$, $\check{I}_{\mathrm{bb}}$ and $\check{I}_{\mathrm{cc}}$ contain six undetermined values (magnitude and phase angle of each phasor). We can decompose Equ. (2.9) into two constraints as shown in Equ. (2.10) and convert these equations into Equ. (2.11):

$$\begin{aligned} proj_{\alpha}(\check{I}_{\mathrm{aa}}) + proj_{\alpha}(\check{I}_{\mathrm{cc}}) &= -proj_{\alpha}(\check{I}_{\mathrm{bb}}) \\ proj_{\beta}(\check{I}_{\mathrm{aa}}) + proj_{\beta}(\check{I}_{\mathrm{cc}}) &= -proj_{\beta}(\check{I}_{\mathrm{bb}}) \end{aligned} , \tag{2.10}$$

where $proj_{\alpha}$ projects the phasor to α axis which is aligned with phase A, and $proj_{\beta}$ projects the phasor to β axis which is 90° behind A axis.

$$\begin{aligned} I_{\mathrm{aa}}\cos\left(\varphi_A\right) - I_{\mathrm{cc}}\sin\left(30^\circ - \varphi_C\right) &= I_{\mathrm{bb}}\cos\left(60^\circ - \varphi_B\right) \\ -I_{\mathrm{aa}}\sin\left(\varphi_A\right) + I_{\mathrm{cc}}\cos\left(30^\circ - \varphi_C\right) &= I_{\mathrm{bb}}\sin\left(60^\circ - \varphi_B\right) \end{aligned} . \tag{2.11}$$

In addition to voltage unbalance limit, power factor has to be corrected above 0.9, implying $\varphi_{\mathrm{A,(B,C)}} \in (-25.8^\circ, 25.8^\circ)$. So three constraints are imposed on the phase angles $\varphi_{\mathrm{A,(B,C)}}$, leading to six constraints in total with Equ. (2.8) and Equ. (2.11) to explicitly formulate the desired current phasors $\check{I}_{\mathrm{aa,(bb,cc)}}$. Finally, the RMS values of the transformer secondary side current are expressed in Equ. (2.12).

---

[3] According to National Grid report 'GC0088-Voltage Unbalance'

So far, each current phasor in the system can be derived using vector addition and subtraction operations illustrated in Fig. 2.6. We have thus shown that the desired compensation result can be achieved by setting a suitable set of three phase current phase angles.

$$
\begin{aligned}
I_{\mathrm{aa}} &= \frac{2I_{\mathrm{Tr}}\cos\left(\phi_{\mathrm{Tr}}\right)\cos\left(30^\circ-\varphi_{\mathrm{B}}+\varphi_{\mathrm{C}}\right)}{2\cos\left(\theta_{\mathrm{ab}}+\varphi_{\mathrm{A}}\right)\cos\left(30^\circ-\varphi_{\mathrm{B}}+\varphi_{\mathrm{C}}\right)+\sin\left(\theta_{\mathrm{cb}}-\varphi_{\mathrm{A}}+\varphi_{\mathrm{B}}+\varphi_{\mathrm{C}}\right)-\cos\left(30^\circ+\theta_{\mathrm{cb}}+\varphi_{\mathrm{A}}-\varphi_{\mathrm{B}}+\varphi_{\mathrm{C}}\right)}\\
I_{\mathrm{bb}} &= \frac{I_{\mathrm{Tr}}\cos\left(\phi_{\mathrm{Tr}}\right)\csc\left(30^\circ+\varphi_{\mathrm{B}}\right)\left(\cos\left(30^\circ-\varphi_{\mathrm{A}}-\varphi_{\mathrm{B}}+\varphi_{\mathrm{C}}\right)-\sin\left(\varphi_{\mathrm{A}}-\varphi_{\mathrm{B}}-\varphi_{\mathrm{C}}\right)\right)}{2\cos\left(\theta_{\mathrm{ab}}+\varphi_{\mathrm{A}}\right)\cos\left(30^\circ-\varphi_{\mathrm{B}}+\varphi_{\mathrm{C}}\right)+\sin\left(\theta_{\mathrm{cb}}-\varphi_{\mathrm{A}}+\varphi_{\mathrm{B}}+\varphi_{\mathrm{C}}\right)-\cos\left(30^\circ+\theta_{\mathrm{cb}}+\varphi_{\mathrm{A}}-\varphi_{\mathrm{B}}+\varphi_{\mathrm{C}}\right)}\\
I_{\mathrm{cc}} &= \frac{2I_{\mathrm{Tr}}\cos\left(\phi_{\mathrm{Tr}}\right)\cos\left(30^\circ-\varphi_{\mathrm{A}}+\varphi_{\mathrm{B}}\right)}{2\cos\left(\theta_{\mathrm{ab}}+\varphi_{\mathrm{A}}\right)\cos\left(30^\circ-\varphi_{\mathrm{B}}+\varphi_{\mathrm{C}}\right)+\sin\left(\theta_{\mathrm{cb}}-\varphi_{\mathrm{A}}+\varphi_{\mathrm{B}}+\varphi_{\mathrm{C}}\right)-\cos\left(30^\circ+\theta_{\mathrm{cb}}+\varphi_{\mathrm{A}}-\varphi_{\mathrm{B}}+\varphi_{\mathrm{C}}\right)}
\end{aligned}
\tag{2.12}
$$

The essence of partial compensation is to reduce the system costs, and two types of costs can be reduced: reducing construction cost by reducing the capacity of the cophase system, and reducing resistive losses to save the operational costs. These two objectives can be achieved using the partial compensation optimisation procedure in Algorithm 1, and in our case study we consider a traction power supply system with the following defined parameters: current phase angle limit $\varphi_{\mathrm{limit}} = 25^\circ$, grid short-circuit capacity $S_{\mathrm{k}} = 500\,\mathrm{MVA}$, traction load power factor $\mathrm{pf}_{\mathrm{Tr}} \in [0.85, 1]$, minimum traction load active power $P_{\mathrm{min}} = 1\,\mathrm{MVA}$, maximum traction load active power $P_{\mathrm{max}} = 30\,\mathrm{MVA}$ and voltage unbalance limit $\varepsilon_{\mathrm{U_{limit}}} = 1.9\%$.

As illustrated in Algorithm 1, the first step is to minimise the current capacity under the maximum load condition with different load power factors. The optimal result of the first step is then fed to the second step to search for the optimal angles for the three phase currents to minimise the resistive energy losses. To obtain the optimal solutions, this chapter adopts an exhaustive search approach, where the search space for the power factor and the power capacity are segmented into small meshes with the mesh scale of 1.25×10^{-2} for the power factor and 1 MW for the power. The accuracy for the resultant phase angle of the three phase currents $[\varphi_{\mathrm{A}}, \varphi_{\mathrm{B}}, \varphi_{\mathrm{C}}]$ is set to 0.1°.

Through exhaustive search, Algorithm 1 optimises the converter size, resulting in $I_{\mathrm{max}} = 471.33\,\mathrm{A}$ with the maximum capacity 12.96 MVA and $k_{\mathrm{size}} = 0.367$. The maximum capacity is required when the load has the highest active power and the lowest power factor. In this case study, when the partial compensation scheme is applied, k_{size} is reduced by 27.9% (5 MVA) compared with the full compensation scheme. Figure 2.7 shows the compensation ratios of apparent power and active power using full and partial compensation strategies.

The phase angles under different traction load conditions are illustrated in the three contour plots (Fig. 2.8). The target phase angles of three phase current vary according to different traction load characteristics and there is no single optimal combination that suits all conditions. In several cophase conditioner studies [36, 37], researchers only minimise the converter active power capacity under different loads, and this approach is equivalent to minimising the current magnitude of the conditioner. Here in our studies, we assume total operational losses is mainly resistive losses ($P_{\mathrm{loss}} \propto I^2$). Figure 2.9 illustrates the minimal resistive losses using our proposed optimisation scheme when the total currents

Algorithm 1 Partial compensation optimisation procedure

```
Initialisation:
  Current phase angle limit $\varphi_{\mathrm{limit}}$;
  Maximum voltage unbalance factor $\varepsilon_{\mathrm{U_{limit}}}$;
  Grid short-circuit capacity $S_{\mathrm{k}}$;
  Active power boundary of traction load $P_{\mathrm{min}}, P_{\mathrm{max}}$;
  Power factor boundary of traction load $\mathrm{pf}_{\mathrm{min}}, \mathrm{pf}_{\mathrm{max}}$
Optimisation output:
  Maximum RMS value of the conditioner $I_{\mathrm{max}}$;
  Optimised phase angles $[\varphi_{\mathrm{A}}, \varphi_{\mathrm{B}}, \varphi_{\mathrm{C}}]$ for given traction active power $P_{\mathrm{Tr}}$ and power factor $\mathrm{pf}_{\mathrm{Tr}}$.

  Step 1:
  function CAPACITY REDUCTION($P_{\mathrm{max}}, \mathrm{pf}_{\mathrm{min}}, \mathrm{pf}_{\mathrm{max}}$)
      $I_{\mathrm{max}} \leftarrow \infty$
      for $\mathrm{pf} = \mathrm{pf}_{\mathrm{min}}$ to $\mathrm{pf}_{\mathrm{max}}$ do
          $\underset{\varphi_{\mathrm{A}}, \varphi_{\mathrm{B}}, \varphi_{\mathrm{C}}}{\mathrm{minimise}} \quad \tilde{I}_{\mathrm{max}} = \max(I_{\mathrm{i}}, I_{\mathrm{o}})$
          subject to $\max(|\varphi_{\mathrm{A}}|, |\varphi_{\mathrm{B}}|, |\varphi_{\mathrm{C}}|) \leq \varphi_{\mathrm{limit}}$,
                     $I_{\mathrm{Tr}} = P_{\mathrm{max}}/U_{\mathrm{ab}}/\mathrm{pf}$,
                     $\varepsilon_{\mathrm{U}} < \varepsilon_{\mathrm{U_{limit}}}$.
          if $\tilde{I}_{\mathrm{max}} < I_{\mathrm{max}}$ then
              $\tilde{I}_{\mathrm{max}} \leftarrow I_{\mathrm{max}}$
          end if
      end for
      return $I_{\mathrm{max}}$
  end function

  Step 2:
  function STRATEGY SEARCH($P_{\mathrm{min}}, P_{\mathrm{max}}, \mathrm{pf}_{\mathrm{min}}, \mathrm{pf}_{\mathrm{max}}, I_{\mathrm{max}}$)
      for $P_{\mathrm{Tr}} = P_{\mathrm{min}}$ to $P_{\mathrm{max}}$ do
          for $\mathrm{pf} = \mathrm{pf}_{\mathrm{min}}$ to $\mathrm{pf}_{\mathrm{max}}$ do
              $\underset{\varphi_{\mathrm{A}}, \varphi_{\mathrm{B}}, \varphi_{\mathrm{C}}}{\mathrm{minimise}} \quad I_{\mathrm{i}}^2 + I_{\mathrm{o}}^2$
              subject to $\max(|\varphi_{\mathrm{A}}|, |\varphi_{\mathrm{B}}|, |\varphi_{\mathrm{C}}|) \leq \varphi_{\mathrm{limit}}$,
                         $I_{\mathrm{Tr}} = P_{\mathrm{Tr}}/U_{\mathrm{ab}}/\mathrm{pf}$,
                         $\varepsilon_{\mathrm{U}} < \varepsilon_{\mathrm{U_{limit}}}$,
                         $\max(I_{\mathrm{i}}, I_{\mathrm{o}}) \leq I_{\mathrm{max}}$.
              Save strategy vector $[P_{\mathrm{Tr}}, \phi_{\mathrm{Tr}}, \varphi_{\mathrm{A}}, \varphi_{\mathrm{B}}, \varphi_{\mathrm{C}}]$
          end for
      end for
      return strategy matrix $[\boldsymbol{P}_{\mathrm{Tr}}, \boldsymbol{\phi}_{\mathrm{Tr}}, \boldsymbol{\varphi}_{\mathrm{A}}, \boldsymbol{\varphi}_{\mathrm{B}}, \boldsymbol{\varphi}_{\mathrm{C}}]$
  end function
```

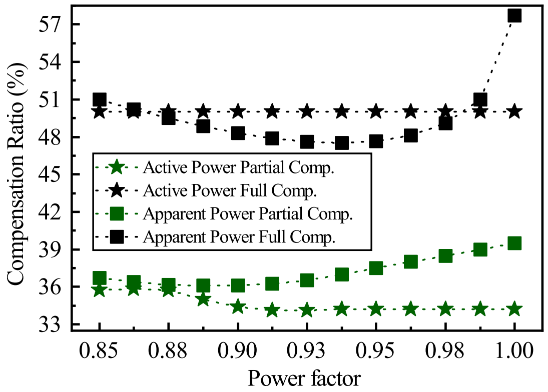

Fig. 2.7 Compensation percentage comparison: full compensation v.s. partial compensation

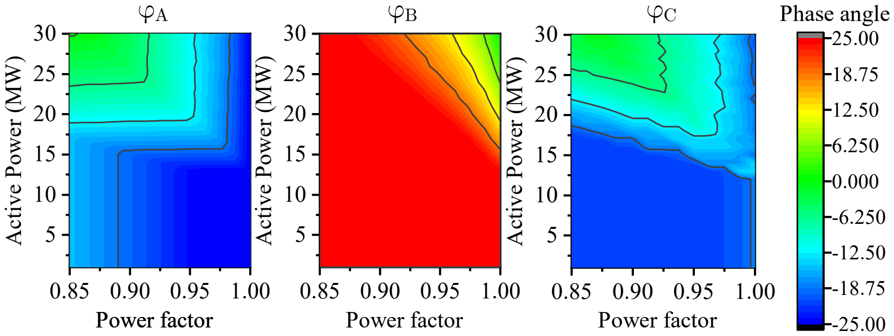

Fig. 2.8 Compensation strategy for different load conditions

$I_o^2 + I_i^2$ of both sides of the converter are minimised. In Fig. 2.9, z-axis values are normalised and the orange bars are the additional losses if the magnitude of output current is minimised (compared to our approach 'blue bars'). Figure 2.9 shows that the resistive losses are reduced significantly (18.7%) at unity power factor load which is a typical characteristic for high-speed train traction drive systems.

Using the phase angles of three phase current as the control objectives, the cophase controller can dynamically compensate the unbalanced current arising from the traction load such that the negative sequence component and the grid side power factor are corrected to the desired limits with the least resistive loss.

2.2.3 Modelling and control of the MMC-based power conditioner

In this section, a four phase MMC back-to-back converter is used to implement the proposed cophase supply scheme. The converter topology is shown in Fig. 2.10(a) where phase a and phase b operate as a rectifier, and phase e and phase f operate as an inverter.

Single phase model and modulation

Each branch of the MMC phases is composed of many half-bridge modules ($\mathrm{SM}_1 \ldots \mathrm{SM}_N$) with floating capacitors connected in series with an arm inductor (L_{br}). Two identical branches form one phase

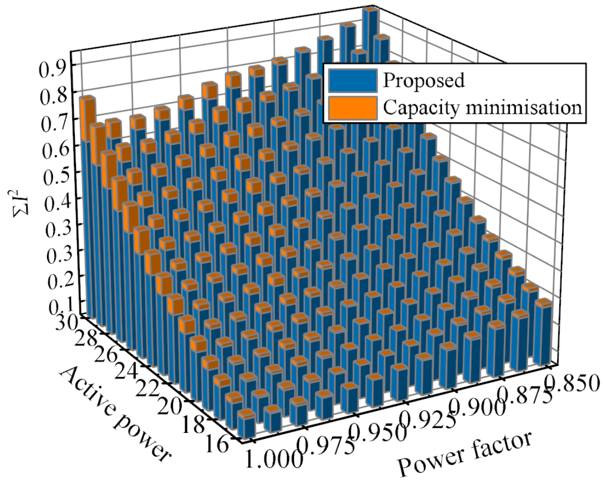

Fig. 2.9 Resistive loss comparison (normalised loss value)

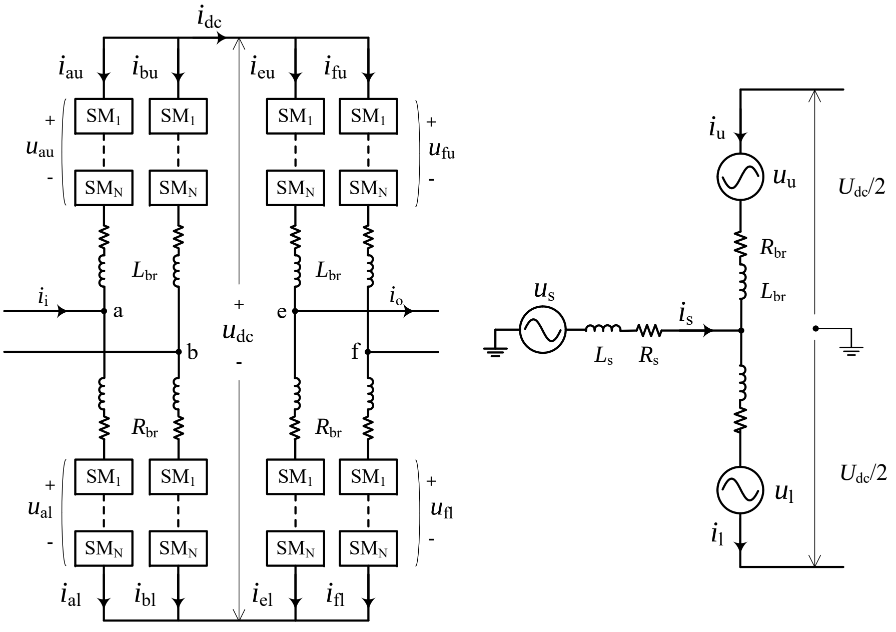

(a) (b)

Fig. 2.10 MMC topology and single phase equivalent circuit which can be simplified by an average model. In Fig. 2.10(b), modules in upper and lower branches are represented by controlled voltage sources u_u and u_l while u_s is the external voltage source. Assume the capacitor voltage is regulated to support stabilising U_dc, according to the Kirchhoff's law, the circuit equations of upper and lower branches are:

$$u_\mathrm{s} - L_\mathrm{s}\frac{\mathrm{d}i_\mathrm{s}}{\mathrm{d}t} - R_\mathrm{s}i_\mathrm{s} + R_\mathrm{br}i_\mathrm{u} + L_\mathrm{br}\frac{\mathrm{d}i_\mathrm{u}}{\mathrm{d}t} + u_\mathrm{u} = \frac{U_\mathrm{dc}}{2}, \tag{2.13}$$

$$u_\mathrm{s} - L_\mathrm{s}\frac{\mathrm{d}i_\mathrm{s}}{\mathrm{d}t} - R_\mathrm{s}i_\mathrm{s} - R_\mathrm{br}i_\mathrm{l} - L_\mathrm{br}\frac{\mathrm{d}i_\mathrm{l}}{\mathrm{d}t} - u_\mathrm{l} = -\frac{U_\mathrm{dc}}{2}, \tag{2.14}$$

then add and subtract (2.13) and (2.14) yielding (2.15) and (2.16).

$$\begin{aligned} u_\mathrm{s} = {} & R_\mathrm{s}i_\mathrm{s} + L_\mathrm{s}\frac{\mathrm{d}i_\mathrm{s}}{\mathrm{d}t} \\ & + R_\mathrm{br}\underbrace{\frac{i_\mathrm{l} - i_\mathrm{u}}{2}}_{i_\mathrm{dif}} + L_\mathrm{br}\frac{\mathrm{d}}{\mathrm{d}t}\underbrace{\frac{i_\mathrm{l} - i_\mathrm{u}}{2}}_{i_\mathrm{dif}} + \underbrace{\frac{u_\mathrm{l} - u_\mathrm{u}}{2}}_{u_\mathrm{dif}} \end{aligned} \tag{2.15}$$

$$\frac{U_\mathrm{dc}}{2} = R_\mathrm{br}\underbrace{\frac{i_\mathrm{u} + i_\mathrm{l}}{2}}_{i_\mathrm{com}} + L_\mathrm{br}\frac{\mathrm{d}}{\mathrm{d}t}\underbrace{\frac{i_\mathrm{u} + i_\mathrm{l}}{2}}_{i_\mathrm{com}} + \underbrace{\frac{u_\mathrm{u} + u_\mathrm{l}}{2}}_{u_\mathrm{com}} \tag{2.16}$$

Expressed in Equ. (2.15) and (2.16), the terminal voltage can be controlled by the differential-mode voltage between the upper and lower branches $u_\mathrm{dif} = (u_\mathrm{l} - u_\mathrm{u})/2$, and the DC-link voltage is maintained by the common-mode voltage $u_\mathrm{com} = (u_\mathrm{l} + u_\mathrm{u})/2$. Similarly, differential-mode current $i_\mathrm{dif} = (i_\mathrm{l} - i_\mathrm{u})/2$ determines the output terminal current i_s, ($i_\mathrm{s} + i_\mathrm{u} = i_\mathrm{l}$) and common-mode current $i_\mathrm{com} = (i_\mathrm{l} + i_\mathrm{u})/2$ represents the energy transfer between branches. Therefore, the terminal voltage and current are determined by the differential-mode values of two branches in each phase while the internal states are controlled by the common-mode values.

The carrier wave phase-shifted ($2\pi/N$) PWM method has been used for MMC modulation. Although the nearest level modulation (NLM) enjoys lower switching losses, the proposed 25-level converter does not have enough modules for direct NLM. All branches share the same phase shifted carrier waves. These carrier waves are compared with the voltage reference to generate switching pulses to drive each half-bridge.

Current control and capacitor balancing

The rectifier side of the MMC draws current with the designed phase angle while stabilising the average DC-link voltage. While the other two phases (phases e,f) inject current into the load for direct compensation. We assume that real-time phasor measurement of voltage and current at transformer secondary terminals are available with one unit sample time delay. The desired compensation current can be derived by the subtraction of current reference $i_\mathrm{aa}^\mathrm{ref}$ (derived by Equ. (2.12)) and real measurement i_Tr. Figure 2.11 illustrates the procedure of reference current calculation for $i_\mathrm{i}^\mathrm{ref}$ and $i_\mathrm{o}^\mathrm{ref}$.

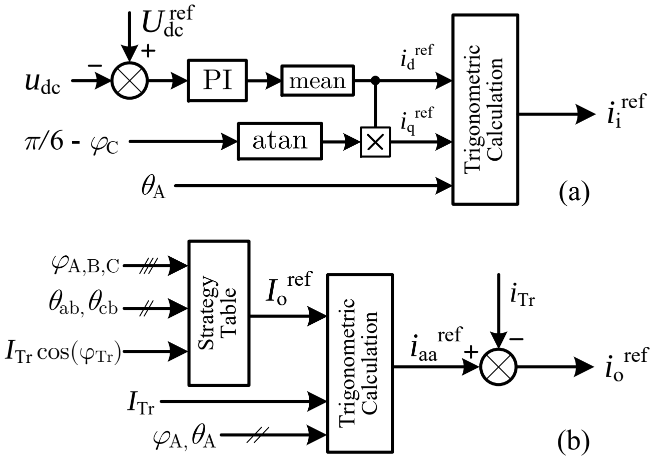

Fig. 2.11 Reference current design scheme

In most recent literature [38, 37], bang-bang control has been used for current tracking, but good tracking performance requires very narrow hysteresis width which results in unpredictable and high switching frequency. However, in reality, high power switches cannot accept very high switching frequency.

Alternatively we can either transform the single phase current into rotating dq frame with respect to the transformer terminal voltage and adopt two PI (proportional-integral) controllers, or directly use PR (proportional-resonant) controllers to track sinusoidal reference components. Based on internal model principle, a PR controller is the combination of a proportional gain, a fundamental resonant term and harmonic compensator terms [39].

$$C_{PR}(s) = K_p + K_{r1}\frac{s}{s^2+\omega_1^2} + \sum_{h=3,5,\ldots} K_{rh}\frac{s}{s^2+(\omega_1 h)^2} \tag{2.17}$$

The principal frequency components in the reference signal can be controlled by specifically designed resonant terms and the residual component is controlled by the proportional term. In this case, the fundamental component and the third order harmonic have the largest portions, a PR controller is designed as given in Equ. (2.18):

$$\begin{aligned} C_{PR}(z) &= K_P \\ &+ K_{r1}\frac{1}{\omega_1^2 T_{sc}}\frac{(1-\cos(\omega_1 T_{sc}))z^2+\cos(\omega_1 T_{sc})-1}{z^2-2\cos(\omega_1 T_{sc})z+1}, \\ &+ K_{r3}\frac{1}{\omega_3^2 T_{sc}}\frac{(1-\cos(\omega_3 T_{sc}))z^2+\cos(\omega_3 T_{sc})-1}{z^2-2\cos(\omega_3 T_{sc})z+1} \end{aligned} \tag{2.18}$$

where the ‘first zero hold’ method is adopted for discretisation, $\omega_1 = 100\pi$, $\omega_3 = 300\pi$ and T_{sc} is the controller sampling time.

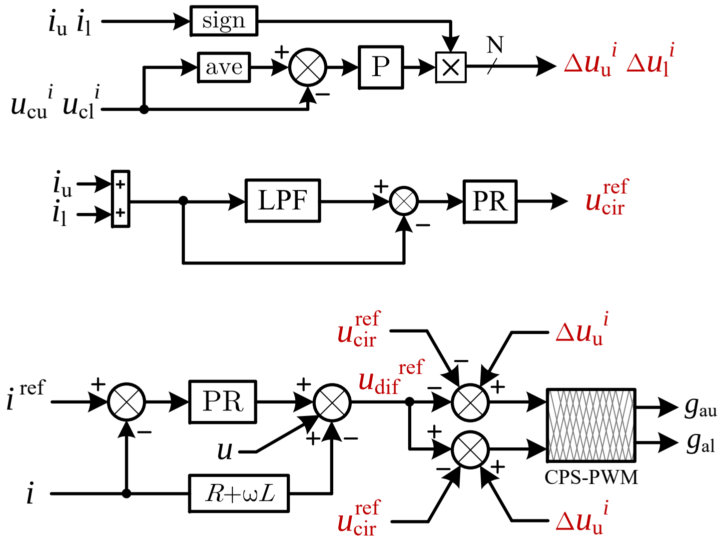

Fig. 2.12 Capacitor voltage balance control and current control

The capacitor voltage in each submodule cannot be guaranteed if we solely modulate the MMC for current tracking. A simple voltage balance scheme based on the proportional control is introduced by adding a small portion signal into the original voltage reference. Capacitors with a lower voltage than average will turn on for a longer time during charging period while capacitors with higher voltage than average will turn on for longer time in the discharging period. The charging and discharging status is decided by the direction of the branch current.

Control diagrams of the current control and the voltage balancing are illustrated in Fig. 2.12, and each sub-module has an individual control signal added to the voltage reference for each branch. The composite references are compared with phase shifted carrier waves to generate PWM signals for switches in phase a. The control schemes for the other phases are similar, but the differential-mode voltage reference has to be reversed in phases b, f.

2.3 Simulation and discussion

2.3.1 System control scheme and simulation setup

A 25-level single phase back-to-back MMC is simulated for cophase conditioning; the system and simulation parameters[4] are listed in Table 2.2. A control diagram of the whole system is presented in Fig. 2.13. Real-time phasor measurements of voltage/current at transformer/converter ports are assumed to be fully available. The compensation parameters are derived by linear interpolation of the strategy matrix based on instantaneous active and reactive traction power and the parameters are updated at

---

[4] The grid impedance is selected according to conventional AC power grid. 500 MVA short-circuit capacity is chosen for a more stringent scenario. In the real application, the traction load should be connected to a stronger power grid which requires smaller amount of the compensation current.

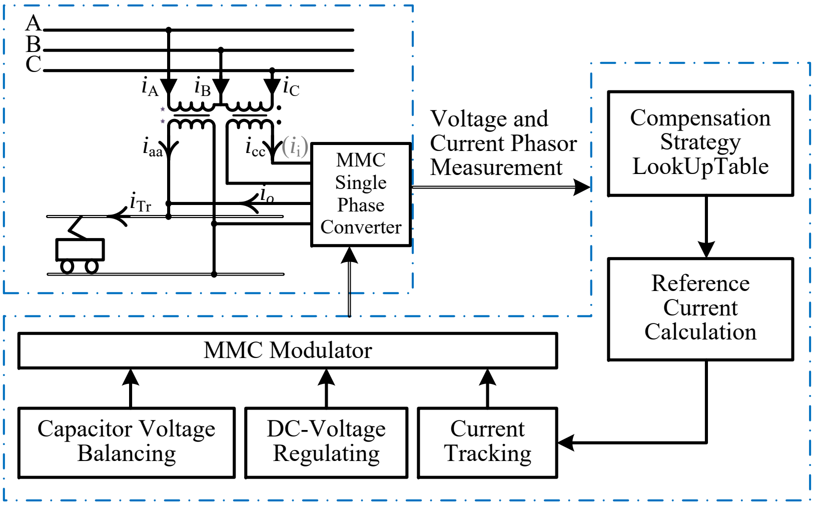

Fig. 2.13 Cophase system and control scheme diagram

100 Hz frequency. Then a series of MMC control actions are implemented accordingly. Two sets of simulations are designed to test the performance of the proposed cophase operation scheme for 20 MW static load and dynamic load varying from 0 MW to 30 MW.

2.3.2 Cophase supply for static load

We first discuss the performance of static load compensation where a controlled current source is used to simulate a 20 MW (pf=0.95) static load. The load power and grid voltage unbalance are illustrated in Fig. 2.14; the power conditioner starts to compensate at 0.4 s. It is shown that the voltage unbalance ratio drops from 4.5% to 2% in 60 ms and finally settles to 1.95%. Three phase grid voltages and currents are presented in Fig. 2.15. It is noticeable that the voltage amplitudes (green lines) have larger differences before the compensation is implemented, but they are restored to approximately equal amplitude at 0.45 s. The grid side current I_C is almost zero before compensation (see Fig. 2.3(a)) and the three phase currents remain unbalanced to some degree in the partial compensation strategy. As shown in Fig. 2.16 which plots the power factor at the grid side, it is clear that the three phase power factors are corrected above 0.9 with the proposed compensation.

Modern electrified railway rolling stock is powered by ‘AC-DC’ or ‘AC-DC-AC’ conversion systems through traction drives where the converters inject harmonic currents into the power supply system [40]. To investigate harmonic issues, rectifiers are modelled as several 3-level single phase NPC (neutral-point clamped) converters with fixed load at DC side. These converters are connected to the railway power supply system through a step-down transformer. Single phase rectifiers will naturally generate harmonic components which are used to represent the harmonics issue.

In the proposed control strategy, third order harmonics (150 Hz) can be directly suppressed using the current reference signal design procedure. The MMC conditioner cancels most of the 3rd order harmonics and suppresses a few high order harmonics as well. As illustrated in Fig. 2.18(a), the grid

Table 2.2 Simulation system parameters

Parameter	Symbol	Value
Supply system parameter		
grid voltage	V_{ph2ph}	110 kV
short-circuit capacity	S_{k}	500 MVA
X/R ratio		7
transformer ratio	N	110 kV/27.5 kV
MMC parameter		
DC-link voltage	V_{dc}	48 kV
submodule number	n_{sub}	24
submodule voltage	V_{sub}	2 kV
submodule capacitor	C_{sub}	2 mF
branch inductor	L_{br}	30 mH
switching frequency	f_{sw}	500 Hz
Simulation parameter		
solver type		ode23t
simulation step	T_{s}	5 μs
control sampling time	T_{sc}	100 μs

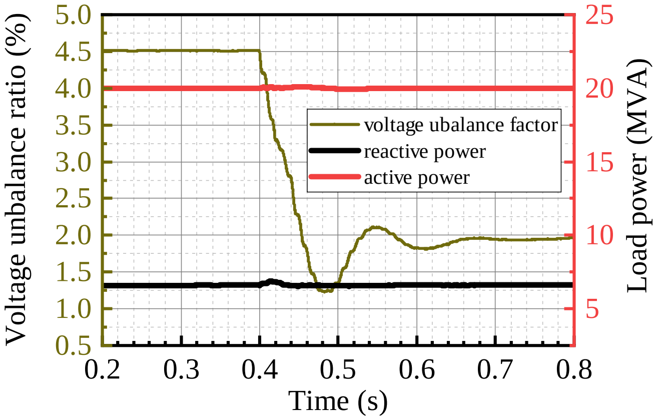

Fig. 2.14 Voltage unbalance factor under static load

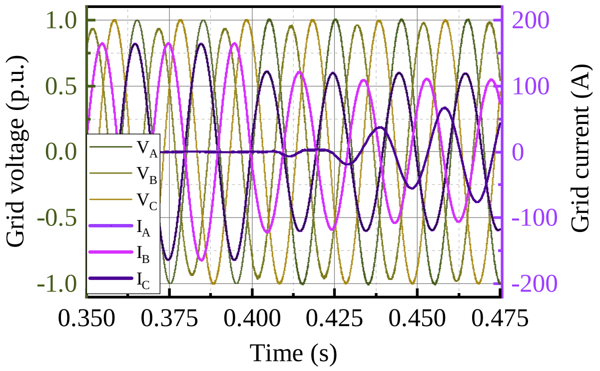

Fig. 2.15 Grid voltage and current under static load

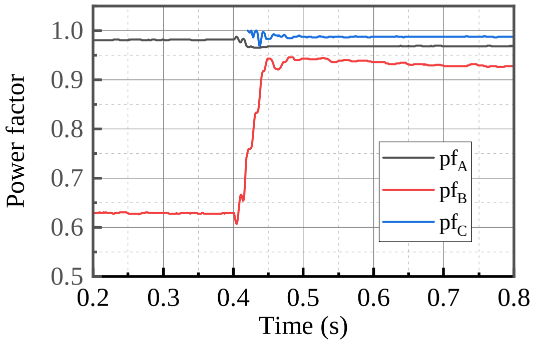

Fig. 2.16 Grid side power factor correction under static load

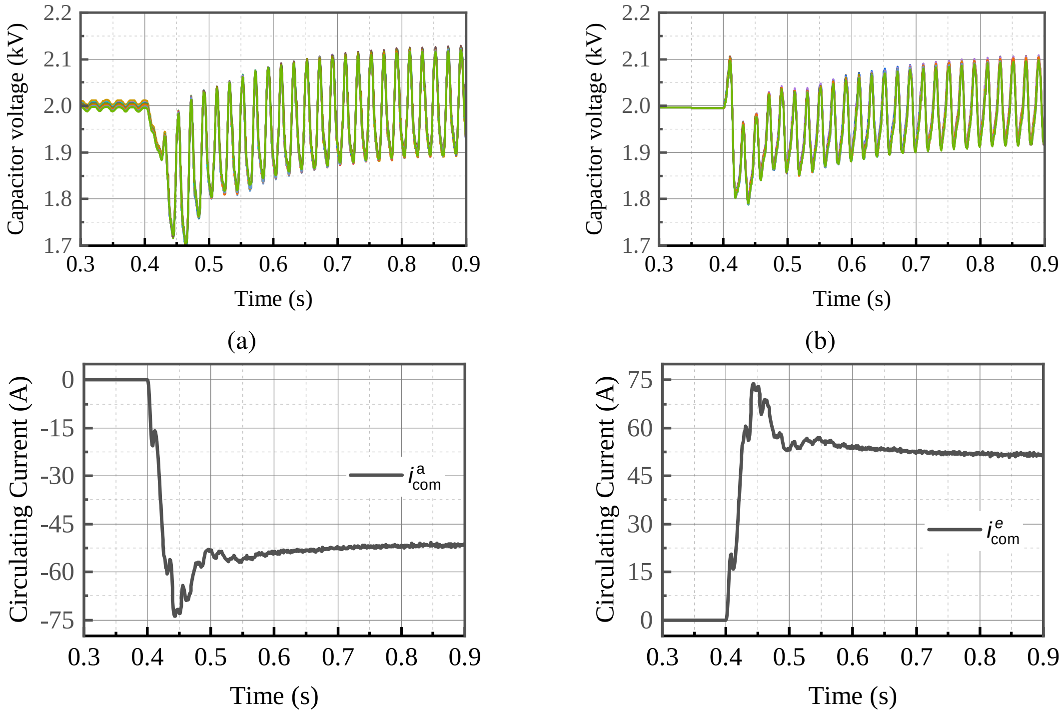

(a) (b)

(c) (d)

Fig. 2.17 MMC internal status: capacitor voltage and circulating current

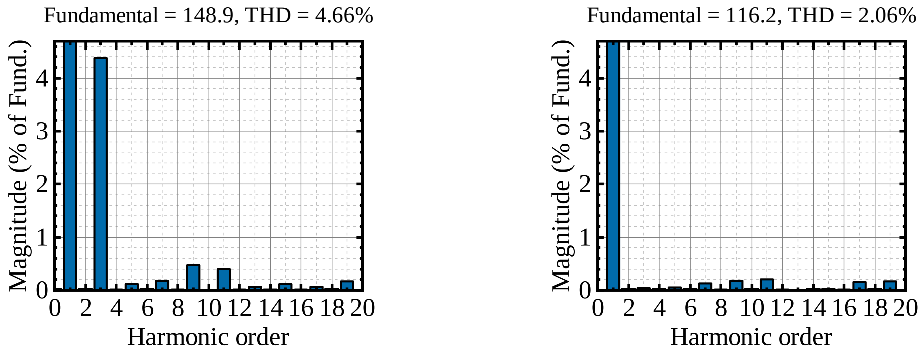

(a) I_A one cycle at 0.2 s

(b) I_A one cycle at 0.8 s

Fig. 2.18 FFT analysis of grid current I_A before and after compensation (static rectifier load)

current I_A contains 4.38% of 3rd order harmonics and some small 9th and 11th order harmonics before compensation. After the compensation starts, the 3rd order harmonic becomes negligible, and the remaining odd harmonics are all suppressed below 2.06%. The MMC internal states including submodule capacitor voltages and circulating currents (i_com) in phase a and phase e are shown in Fig. 2.17. Due to the topology symmetry, phase b and phase f exhibit the same behaviour. The capacitor voltages in each submodule are balanced and the circulating currents have little oscillating components at steady state.

2.3.3 Cophase compensation for variable loads

In practice, the load can vary drastically rather than being constant. For simplicity, the load is simulated by a controlled current source which delivers different active and reactive power at different time instant. Figure 2.19(a) illustrates the designed dynamic load profile: the active power increases from 0 MW to 30 MW during 0.1 s to 6 s, and decreases afterwards. The red line shows the designed profile of varying power factor.

The green line in Fig. 2.19(b) shows the voltage unbalance ratio. Although the load keeps changing, the voltage unbalance factor can be fully controlled below 2%. When the traction active power is below 15 MW, the proposed cophase system controls power factor while simultaneously meeting the voltage unbalance requirement. When the traction active power is above 15 MW, the voltage unbalance ratio is restricted to 1.9% deliberately. But the actual ε_U settles at 1.9942% in the test due to some modelling error and delays.

Traction loads can change rapidly in cases where multiple trains start or accelerate simultaneously. Figure 2.20 shows the grid voltage unbalance curve under a step load change where a 30 MW (pf=0.85) load is connected into the system at 0.2 s. This has lead to an overshoot of 3.09% and a total duration of 67 ms of violating the grid code limit (2%). Because of the delay in load detection and compensation response, there is a oscillation during the first 50 ms after the step change. Finally, voltage unbalance ratio is controlled within 2% after three grid cycles.

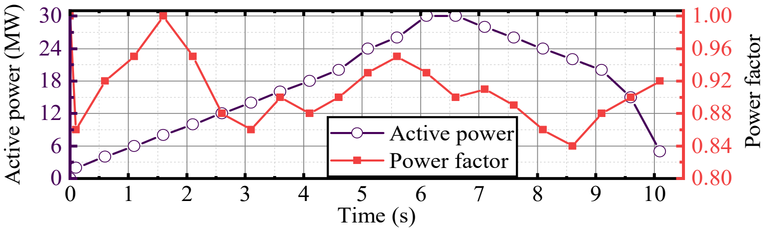

(a) Varying load profile

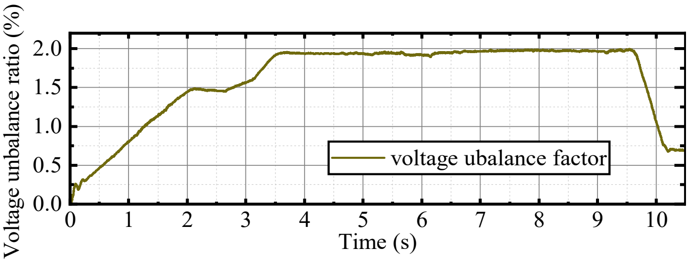

(b) Voltage unbalance ratio

Fig. 2.19 Compensation for varying current source load

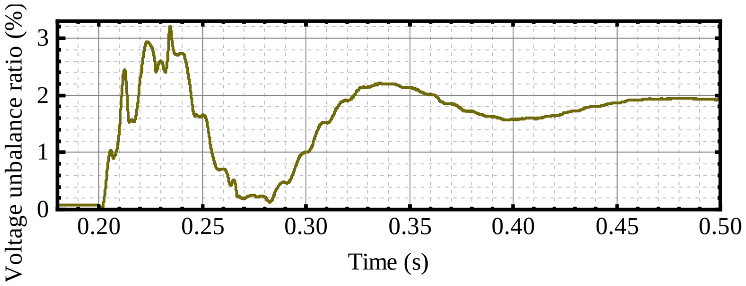

Fig. 2.20 Voltage unbalance under load step change

2.4 Summary

This chapter proposes a cophase supply conditioner using a 25-level modular multilevel single phase back-to-back converter for power flow control. The conditioner is directly connected to the ports of V/v transformer for compensation of reactive power, unbalanced current and for low order harmonics suppression. Phasor diagrams of the cophase system are analysed to derive the reference current for partial compensation which can be achieved by choosing suitable phase angles of the three phase grid-side currents.

With the aim of minimising the converter capacity and operation losses, a two step strategy is designed. A case study shows that around 27.9% (5 MW) of capacity can be reduced by the partial compensation scheme for 30 MW traction load. And the conditioner operates with the least resistive losses under dynamic traction load. While variable impedance unit like MSVC can be used to further reduce converters capacity, yet this compensation strategy design is still applicable to the whole conditioning system design.

The optimised grid side current phase angles are chosen as the control strategy for real time reference current calculation and PR controllers are adopted for current tracking rather than bang bang control used in the previous works. The current signals have very little harmonics content with 500 Hz switching frequency modulated by CPS-PWM.

Simulation results confirm that, the proposed cophase conditioner can regulate voltage unbalance within 40 ms even in the worst scenario (load step change from zero to maximum). When the load varies continuously without large step changes, the negative sequence component can be perfectly controlled. Third order and other low order harmonics induced by traction line converters can be effectively suppressed by MMC conditioner with the proposed control scheme.

These conclusions are only valid when the analytical model parameter perfectly matches the real infrastructure. The linear model analysis result is designed based on infinite grid capacity and ideal transformer model. However, in real applications, there exists non-negligible leakage inductance in the transformer and the grid capacity is finite. These can be tackled by upgrading the control strategy in this cophase compensation system to accommodate more realistic conditions. For example, to eliminate the error by increasing the compensation ratio if steady state error occurs. In the simulation result, it can be seen that small error exists in steady state which is caused by grid finite capacity, the designed compensation strategy is set to 1.9% in linear analysis to get the 2% result in the simulation.

Chapter 3

Model predictive control for modular multilevel converters

3.1 Overview of MPC method for multilevel back to back converter control

A modular multilevel converter is a multi-variable control system with several constraints which is analysed in chapter A. If the traditional single input and single output controller is deployed for MMC, a complex cascaded control scheme is required. The model predictive control (MPC) is developed to deal with multi-input and multi-output (MIMO) cases with constraints. MPC adopts the receding horizon concept which can be traced back to 50 year ago [41, 42]. After decades of development, MPC has become an advanced control technology that has made substantially used in a range of industrial sectors [43].

In MPC control, the standard state space model formulation is often used to implement the receding horizon optimisation. The basics concept and the applications of MPC in power electronics converters are briefly reviewed in this section.

3.1.1 MPC for AC/DC power electronic converters

The increasing processor computing power enables the successful MPC applications in the field of power electronics control. The applications of MPC to power electronics converter and drive systems started to emerge since 2000 [44]. In these applications, the MPC are mostly formulated in the discrete time domain with a small sampling interval T_s. Usually the discrete time state space model is used to describe the nonlinear dynamics of the conversion system via (3.1)

$$x(k+1) = f(x(k), u(k)), \quad k \in \{0, 1, 2, \ldots\}, \tag{3.1}$$

where $x(k)$ is the state value at time k, and $u(k)$ is the control input.

Constraints to the state variables and control inputs can be configured such as:

$$\begin{matrix} x \in \mathbb{X} \subseteq \mathbb{R}^n \\ u \in \mathbb{U} \subseteq \mathbb{R}^m \end{matrix}, \quad k \in \{0,1,2,\dots\}, \tag{3.2}$$

where $\mathbb{X},\mathbb{U}$ are polytopes; n,m are the dimension of the state $x(k)$ and input $u(k)$ at each sampling step. The constraints are mostly current and voltage limits which are set to avoid over current and over modulation issue. Then at each time instant k, an optimisation problem with finite length horizon is formulated as:

$$J\left(x(k),u^*(k)\right) = \sum_{l=k}^{k+N-1} L\left(x(l),u(l)\right) + F\left(x(k+N)\right), \tag{3.3}$$

where $L(\cdot,\cdot)$ and $F(\cdot)$ are weighting functions to evaluate the system dynamics such as current/flux tracking, voltage regulation, switching efforts, etc. for the entire horizon length [45]. Although, the optimised control variable $u^*(k)$ contains all control inputs for horizon h (a vector of $h \times m$ elements), only the first m elements is adopted. Then at the next sampling time, the same procedure repeats, so that a typical MPC is performed in this open loop optimisation with feedback update framework.

Several typical MPC approaches in power electronics converter control are briefly introduced in the following paragraphs.

Generally speaking, we can classify different controllers into two categories: the continuous control set (CCS) and the finite control set (FCS). In a CCS-MPC formulation, continuous control input is used, so a modulator is required to convert the real number signals into binary control commands for electronic switches. Unlike CCS-MPC, in FCS-MPC method, the discrete nature of the converter switches are directly modelled and the modulator is avoided in this case, and the optimal control input can be directly fed into each switch drive.

CCS-MPC

In the CCS-MPC formulation, the optimisation problem is to solve the optimal duty cycle or voltage reference for the PWM modulator. This approach approximates each converter leg to an averaged model. Given a converter has n_{leg} of legs, the dimension of u is $h \times n_{\text{leg}}$. So a long horizon MPC has less computational burden compared to FCS-MPC. In addition, because the conventional modulator is used, the harmonics content can be designed and fixed switching frequency can be guaranteed [46]. However, because the CCS-MPC is modelled based on averaged behaviour of each converter, model linearisation is required for different operation points.

FCS-MPC

In the FCS-MPC formulation, the optimisation problem is to select the optimal combination of all possible switching states for the converter. This approach has the potential to surpass the SVM and carrier wave PMW via its optimisation procedure [47]. However, FCS-MPC suffers from high computational burden. If each converter leg has a number of switching states n_s with n_leg legs, the possible switching states for horizon length h is $n_\mathrm{s}^{(n_\mathrm{leg} \times h)}$. The complexity increases exponentially which cannot be bounded by a polynomial like CCS-MPC.

Due to this exponentially increased number of states, most applications only use one prediction horizon MPC to reduce the computational burden. However, long horizon could bring better performance. Geyer et al. demonstrated in [48] that long horizon MPC approach is less sensitive to noise and contains less current distortion in steady state without negative impact on transient states settling time. To alleviate the high computational complexity, sphere decoding [49] is effective in reducing computational burden by 4 orders of magnitude [48, 47].

The solution for the multi-step long horizon problem can be also accelerated by neural networks which can be trained to imitate FCS-MPC algorithm. Novak [50] developed a surrogate model via ANN for fast optimisation so that the computational burden can stop increasing with the extension of prediction horizon. The merit of this approach is that the size of ANN is not correlated with the complexity of the original FCS-MPC and the same performance are approximately maintained with less online calculation effort [51].

Some special MPC formulation strategies can also achieve extended horizon with less complexity such as ‘Moving Blocking’, ‘Extrapolation’ and ‘Event based method’ [52]. The moving block strategy combines short and long sampling interval to achieve longer prediction horizon with less calculation [53]. The extrapolation strategy [54] used few time steps for switching optimisation along with extrapolated trajectories from the final control slope to achieve longer horizon prediction. The event based method [55] used an offline optimised pulse pattern as starting point and then modifies the pre-calculated switching to compensate the tracking error in real time.

Modulated MPC

Another issue related to the FCS-MPC is the variable switching frequency. One of the solution is to modify the original FCS-MPC to Modulated MPC [56]. In this variant, the modulation scheme is included in the cost function design where the switching state and the switching on time duration are considered. This method has been applied to several power converter topologies to guarantee a fixed frequency [57–59]. The Modulated MPC can be viewed as an online optimised space vector modulation approach. This approach improves the computation speed, fixes the current frequency and reduces the high ripple in control variables [60].

Explicit MPC

Another solution to reduce computational burden is to use offline optimisation results. Bemporad et al. [61] presented an algorithm to explicitly determine the feedback control law of a quadratic linear time invariant system, so that the online computation of the finite horizon problem reduces to evaluation of an explicitly defined piece-wise linear function. This initial explicit MPC approach is not applicable to multilevel converters due to its high dimensional problem. Jeong at al. [62] presented a region-less explicit MPC to reduce the memory requirements with the cost of online computation [63]. Jeong demonstrated the algorithm on Cyclone V FPGA for MMC control with 96% reduction in memory requirement compared to other region based method [62].

3.1.2 MPC for MMC

MPC for MMC control has gradually gained attention in the last decade [64, 65]. This approach brings faster response performance and compensates delay which is difficult to achieve using the PID scheme. Moreover, [66] pointed out that the MPC is suitable for small inductance and small capacitance value in the MMC system. Although the nonlinear MPC modelling for MMC control achieves better steady state result but has drawback of high computational demand due to the nonlinear optimisation problem [66]. So only linear MPC are discussed in this chapter.

MPC modelling for MMC

FCS-MPC In the MMC control problem, the original FCS-MPC which explicitly evaluates all combination of switching states is practical only for small number of submodules per arm [67]. It is not suitable for MMC with large number of voltage levels [68]. So researchers modified this idea to use the number of total inserted submodules in each arm as the control input to reduce the computational cost while maintain the discrete voltage level characteristic of MMC. Even we only consider the number of voltage level as control input, there is still $(N+1)^6$ possible combinations in the three phase MMC inverter. This 'voltage level based MPC' can be simplified if the total number of inserted submodules can be constrained within $N \pm 1$ or $N \pm 2$ [68]. Also, some algorithms are developed to reduce the complexity, e.g. Gao proposed a box constrained QP solver to greatly reduce the switching combinations needs to be evaluated [69].

Deadbeat controller Some researchers use the deadbeat control [70] idea which can be viewed as a simplified version of model predictive control whose horizon equals to one with no constraints. Due to its exceptional simplicity, the optimal voltage control command can be calculated directly in one-step expression which makes it one of the fastest predictive controller [71]. A typical application of this control method for MPC is shown in [72], where the deadbeat controller is formulated to obtain the two optimal modulation references for each arm with very low computational burden. Another advantage of this method is that weighting factor tuning is avoided, but on the other hand it does not support constraints nor the multi-objective control purposes.

Mei et al. [73] improved the original deadbeat controller by combining two deadbeat controllers with different sampling interval length and compared multiple step performance by extrapolation over multiple steps. The author concluded that this multi-step MPC improves the current tracking and stability margin.

Modulated MPC Similarly, the modulated MPC concept is also investigated in the MMC domain. Most of the modulation MPC methods for MMC control are designed based on deadbeat controller plus a special optimised modulation scheme.

Yin et al. [74] proposed a grouping method based modulation method for voltage level selection after the employing the deadbeat controller. The improved modulation method can enhance the current control performance with large number of submodules.

Gong et al. [75] used this modulated MPC to overcome the drawbacks brought by FCS-MPC. The original SVM modulation is not suitable for MMC modulation, Ramirez et al. designed a special SVM for MMC by searching the nearest voltage vectors among numerous available candidates. In [75] a submodule unified PWM method is used for modulated MPC implementation.

CCS-MPC Some researchers focus on realising long horizon MPC rather than one-step prediction for MMC control. In this case, the CCS-MPC approach is often selected for this purpose. For example, [64] modelled the dynamic behaviour of a three phase MMC and designed a CCS-MPC with controlled states for load current, DC-link current and sum of the inserted capacitors in each arm. The MPC model is usually linearized for control implementation around an operational point with Euler exact discretization method.

The open-loop verification in [64] showed that the linearized model tends to be inaccurate when the prediction length is more than 5 ms. To improve the error caused by linearization, [66] Fuchs and Biela added the time varying reference for internal arm voltage prediction and compared it with accurate nonlinear model. Although the nonlinear model has better steady state performance but the nonlinear MPC cannot be solved in real-time.

Poblete et al.[76] further reduced the high computational complexity by taking advantage of the phase shifted PWM carrier wave pattern. A predictive controller is built to obtain independent reference signal for each carrier in a sequential manner for PS-PWM modulation [76], therefore each optimisation problem has longer time to get solved.

Cost function design

The cost function used in MPC for MMC has multiple usually comprises several terms. These terms are designed for current tracking, energy tracking and other control purposes. The current related cost can be AC current tracking, DC current tracking, arm current tracking and current change penalty. Current reference design for either balanced grid or unbalanced grid is the same to other control scheme (e.g. PI, hysteresis), and the ideal circulating current reference can be acquired [75] based on the output current value. The energy related cost can be formulated in voltage or energy expression. Other cost terms can be soft constraint cost, control effort cost, etc. Although the MPC can easily deal with MIMO problems, there is still trade off when selecting weighting factors in the cost function design [77] under different operation conditions.

Energy balancing control

Among the many studies, some researchers still use external control loop for energy balance control [71, 69, 67, 72, 74, 76], where the essential circulating current required to maintain the capacitor voltages is calculated in separate controllers [78]. Some proposed control schemes resort to energy balance to modulation stage [75]. If the balancing control can be integrated inside the MPC, the separate controllers are eliminated. Some typical approaches for achieving energy balance within cost functions are briefly introduced as follows.

A rough approach is to control the overall MMC energy. Darivianakis et al. [64] devised the reference AC current and DC voltage for current tracking and sum of capacitor voltage tracking. However, this approach does not achieve the minimum circulating current. If the fixed DC voltage reference is used for energy balance, the capacitors in each arm do not have steady performance but an irregular bounded performance.

There are different energy dynamics patterns in common mode and differential mode. Zhang et al. [68] used the sum and difference of upper/lower arm energy in the cost function design. The reference of energy difference is set to zero while the sum of the energy is set to nominal fixed value according to the DC-link voltage. The circulating current penalty terms must have a relatively greater weighting factor for good steady state performance.

To achieve better energy balancing result, it is desirable to model this dynamics with higher accuracy. Fuchs et al. [79] proposed a novel method to model the nonlinear dynamics of the internal energy through grid voltage information. This approach further reduces the prediction error and achieve the arm energy balance by special designed dynamic reference.

To avoid complex energy modelling approach, Gao et al. [77] presented an alternative way to regulate arm energy by taking instantaneous power term into the cost function. In such a way, the system can stably operate at a wide frequency range.

3.1.3 MPC for B2B converters

Most of the aforementioned MPC algorithms designed for the power electronic converter are for current tracking of one single converter. In the back to back system, two converters are interfaced through a DC link, therefore special attention is needed to stablise the DC voltage.

Four most commonly used B2B control architectures are briefly introduced. Most of the projects are based on two or three level converters, but these approaches are applicable to MMC B2B system as well.

Conventional PI approach The traditional approach is using outer voltage controller design where a DC link voltage controller is cascaded with the inner MPC controller [68]. This conventional approach usually requires a large DC-link capacitor as an energy buffer to slow down the rate of change of the DC voltage. So that the outer loop voltage controller has a smaller bandwidth than the inner controller. This control method is used in Chapter 5.

Centralised control The best approach is to model the whole B2B system in detail irrespective of the problem complexity. This approach is called centralised/unified control. Cabero et al. [80] proposed a unified modelling approach for the complete converter system. The energy for charging and discharging the DC-link capacitor are modelled so that the detailed dynamic in both converters and DC-link is predictable. The proposed unified method has negligible transient changes of DC voltage under step changes and a reduced size capacitor becomes acceptable.

Quasi-centralised approach However, the centralised control get the complexity multiplied which is not easy to implement in two level converters let alone the multilevel converters. Zhang [81] proposed the quasi-centralised control strategy for B2B system. The quasi-centralised MPC uses a dynamic DC voltage reference (3.4) to estimate the required power to be exchanged at the DC-link [82]. Then the current references for both sides are obtained accordingly. Note that because the voltage reference is always gradually approaching the nominal value, the voltage overshoot issue which is common in PI controller is not observed in this QC-MPC controller.

$$V_{\mathrm{dc}}^{\mathrm{ref}} = V_{\mathrm{dc}}(k) + \frac{1}{N_{\mathrm{s}}}\left(V_{\mathrm{dc},\infty} - V_{\mathrm{dc}}(k)\right) , \tag{3.4}$$

where N_{s} is the number of control steps to reach the nominal DC voltage value $V_{\mathrm{dc},\infty}$. Though the QC-MPC reduces the overshoot and undershoot, [83] mentioned that it is more sensitive to system parameter deviation. The PI controller is more robust by comparison. [84] modified this QC-MPC by adjusting the switching point variable, so the implementation time of control inputs are optimised. This approach gains an extra degree of freedom which can be used to minimise the negative effect of low DC-link capacitance design.

Sequential predictive control Grimm and Zhang proposed another solution to improve the efficiency issue of centralised control [85, 86]. The optimal solution is solved in sequential procedure that the system is split into two linear models and one nonlinear model. Firstly two converters are modelled as linear system and solved for two sets of the best solutions. Then the combination of these solutions are examined in the nonlinear model (for the dynamic of DC-link) by exhaustive search. In this way, long horizon MPC can be achieved within acceptable computation time [85].

3.2 Modelling of MMC substation for MPC design

One of the main purposes to use MPC approach for MMC control is to simplify the complex cascaded linear controller loops. The traditional MMC control scheme has nested control loops so that multiple control objectives can be achieved. However, even the MPC is adopted, there is still a trade off in the cost function design. To alleviate this issue, the modelling approach introduced in [79] is adopted and modified for the B2B traction power supply system.

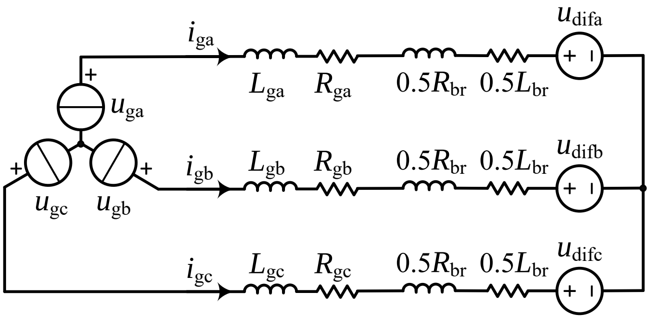

Fig. 3.1 MMC three-phase AC side equivalent circuit model

In this approach the optimal energy reference is precisely designed so that there is no contradiction between energy balance and current tracking in the steady state.

MMC has intrinsic MIMO characteristics. In MMC, the stored energy in each arm is influenced by DC side and AC side and the DC-link introduces coupling effect between phases. The model predictive control used in this chapter is designed to utilise the MIMO feature where not only the internal currents are modelled but the capacitor energy in each arm is also considered to achieve a better transient performance in the back to back MMC substation system.

Additionally, the MPC is formulated as a constrained linear quadratic optimisation problem, the maximum available voltage, current limits and energy limits are taken into account. So the over current and over modulation phenomenon observed in PI controllers can be reduced from the controller perspective.

A CCS-MPC is adopted for MMC control to guarantee a good steady state performance, so a traditional modulation module is indispensable. Furthermore, long horizon ($N_{\mathrm{h}} \geq 2$) is used to effectively control the submodule energy especially in traction load change condition.

3.2.1 MMC AC side equivalent circuit modelling

Three phase AC connection for grid connection

Assume the power grid interface is a star connection three phase system, which has phase to ground voltage values u_{ga}, u_{gb}, u_{gc}. The MMC is analysed using the averaged differential mode equation (A.6). Equation (3.5) describes the circuit model illustrated in Figure 3.1.

$$\begin{aligned}
u_{\mathrm{ga}} &= +u_{\mathrm{dif,a}} + \left(0.5R_{\mathrm{br}} + R_{\mathrm{ga}}\right) i_{\mathrm{ga}} + \left(0.5L_{\mathrm{br}} + L_{\mathrm{ga}}\right) \frac{\mathrm{d}}{\mathrm{d}t} i_{\mathrm{ga}} \\
u_{\mathrm{gb}} &= +u_{\mathrm{dif,b}} + \left(0.5R_{\mathrm{br}} + R_{\mathrm{gb}}\right) i_{\mathrm{gb}} + \left(0.5L_{\mathrm{br}} + L_{\mathrm{gc}}\right) \frac{\mathrm{d}}{\mathrm{d}t} i_{\mathrm{gb}} \\
u_{\mathrm{gc}} &= +u_{\mathrm{dif,c}} + \left(0.5R_{\mathrm{br}} + R_{\mathrm{gc}}\right) i_{\mathrm{gc}} + \left(0.5L_{\mathrm{br}} + L_{\mathrm{gc}}\right) \frac{\mathrm{d}}{\mathrm{d}t} i_{\mathrm{gc}}
\end{aligned} \tag{3.5}$$

Then a state space model (3.6) can be derived using three phase grid current $[i_{\mathrm{ga}} \quad i_{\mathrm{gb}} \quad i_{\mathrm{gc}}]^{\top}$ as state variables.

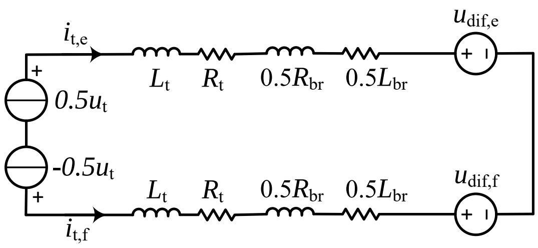

Fig. 3.2 MMC single-phase AC side equivalent circuit model

$$\begin{aligned}\frac{\mathrm{d}}{\mathrm{d}t}\begin{bmatrix} i_{\mathrm{ga}} \\ i_{\mathrm{gb}} \\ i_{\mathrm{gc}} \end{bmatrix} = &\begin{bmatrix} -\frac{0.5R_{\mathrm{br}}+R_{\mathrm{ga}}}{0.5L_{\mathrm{br}}+L_{\mathrm{ga}}} & 0 & 0 \\ 0 & -\frac{0.5R_{\mathrm{br}}+R_{\mathrm{gb}}}{0.5L_{\mathrm{br}}+L_{\mathrm{gb}}} & 0 \\ 0 & 0 & -\frac{0.5R_{\mathrm{br}}+R_{\mathrm{gc}}}{0.5L_{\mathrm{br}}+L_{\mathrm{gc}}} \end{bmatrix}\begin{bmatrix} i_{\mathrm{ga}} \\ i_{\mathrm{gb}} \\ i_{\mathrm{gc}} \end{bmatrix} \\ &+\begin{bmatrix} \frac{1}{0.5L_{\mathrm{br}}+L_{\mathrm{ga}}} & 0 & 0 \\ 0 & \frac{1}{0.5L_{\mathrm{br}}+L_{\mathrm{gb}}} & 0 \\ 0 & 0 & \frac{1}{0.5L_{\mathrm{br}}+L_{\mathrm{gc}}} \end{bmatrix}\begin{bmatrix} u_{\mathrm{ga}}-u_{\mathrm{dif,a}} \\ u_{\mathrm{gb}}-u_{\mathrm{dif,b}} \\ u_{\mathrm{gc}}-u_{\mathrm{dif,c}} \end{bmatrix},\end{aligned} \tag{3.6}$$

where the difference between differential voltage and grid voltage $(u_{\mathrm{dif,a}}-u_{\mathrm{ga}})$, $(u_{\mathrm{dif,b}}-u_{\mathrm{gb}})$, $(u_{\mathrm{dif,c}}-u_{\mathrm{gc}})$ are treated as control variables.

In a balanced grid connection without fault, we can assume the grid connection impedance is the same across each phases, i.e. $R_{\mathrm{g}}=R_{\mathrm{ga}}=R_{\mathrm{gb}}=R_{\mathrm{gc}}$ and $L_{\mathrm{g}}=L_{\mathrm{ga}}=L_{\mathrm{gb}}=L_{\mathrm{gc}}$, then the three phase AC side current SS model can be simplified as (3.7):

$$\begin{gathered}\frac{\mathrm{d}}{\mathrm{d}t}\begin{bmatrix} i_{\mathrm{ga}} \\ i_{\mathrm{gb}} \\ i_{\mathrm{gc}} \end{bmatrix} = \boldsymbol{A}_{\mathrm{g}}\begin{bmatrix} i_{\mathrm{ga}} \\ i_{\mathrm{gb}} \\ i_{\mathrm{gc}} \end{bmatrix} + \boldsymbol{B}_{\mathrm{g}}\begin{bmatrix} u_{\mathrm{dif,a}}-u_{\mathrm{ga}} \\ u_{\mathrm{dif,b}}-u_{\mathrm{gb}} \\ u_{\mathrm{dif,c}}-u_{\mathrm{gc}} \end{bmatrix} \\ \boldsymbol{A}_{\mathrm{g}} = \frac{0.5R_{\mathrm{br}}+R_{\mathrm{g}}}{0.5L_{\mathrm{br}}+L_{\mathrm{g}}}\begin{bmatrix} -1 & 0 & 0 \\ 0 & -1 & 0 \\ 0 & 0 & -1 \end{bmatrix}, \boldsymbol{B}_{\mathrm{g}} = \frac{1}{0.5L_{\mathrm{br}}+L_{\mathrm{g}}}\begin{bmatrix} -1 & 0 & 0 \\ 0 & -1 & 0 \\ 0 & 0 & -1 \end{bmatrix}\end{gathered} \tag{3.7}$$

Single phase AC conversion for traction network power supply

To model the single-phase side equivalent circuits, the traction network voltage is split into two opposite signed voltage sources, the network connection impedance (passive filter and transformer) is simplified as R_{t}, L_{t}. Similar to the previous three phase side modelling approach, the circuit equation (3.8) can be derived from the equivalent model shown in Figure 3.2. The single phase side AC current state space model is given in (3.9).

$$\begin{aligned} 0.5u_{\mathrm{t}} &= +u_{\mathrm{dif,e}}+(0.5R_{\mathrm{br}}+R_{\mathrm{t}})\,i_{\mathrm{t,e}}+(0.5L_{\mathrm{br}}+L_{\mathrm{t}})\frac{\mathrm{d}}{\mathrm{d}t}i_{\mathrm{t,e}} \\ -0.5u_{\mathrm{t}} &= +u_{\mathrm{dif,f}}+(0.5R_{\mathrm{br}}+R_{\mathrm{t}})\,i_{\mathrm{t,f}}+(0.5L_{\mathrm{br}}+L_{\mathrm{t}})\frac{\mathrm{d}}{\mathrm{d}t}i_{\mathrm{t,f}} \end{aligned}. \tag{3.8}$$

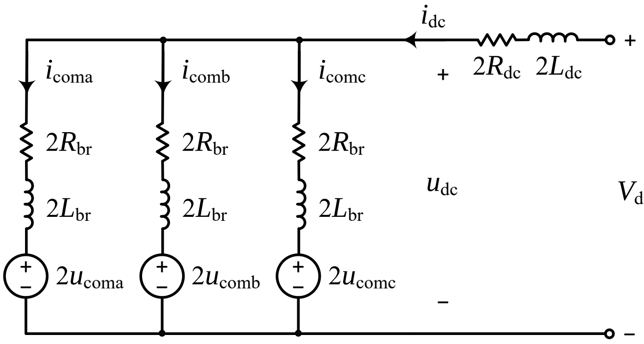

Fig. 3.3 MMC three phase DC side equivalent circuit model

$$\begin{gathered}\frac{\mathrm{d}}{\mathrm{d}t}\begin{bmatrix} i_{\mathrm{t,e}} \\ i_{\mathrm{t,f}} \end{bmatrix} = \boldsymbol{A}_{\mathrm{t}} \begin{bmatrix} i_{\mathrm{t,e}} \\ i_{\mathrm{t,f}} \end{bmatrix} + \boldsymbol{B}_{\mathrm{t}} \begin{bmatrix} u_{\mathrm{dif,e}} - 0.5u_{\mathrm{t}} \\ u_{\mathrm{dif,f}} + 0.5u_{\mathrm{t}} \end{bmatrix}, \\ \boldsymbol{A}_{\mathrm{t}} = \frac{0.5R_{\mathrm{br}} + R_{\mathrm{t}}}{0.5L_{\mathrm{br}} + L_{\mathrm{t}}} \begin{bmatrix} -1 & 0 \\ 0 & -1 \end{bmatrix}, \ \boldsymbol{B}_{\mathrm{t}} = \frac{1}{0.5L_{\mathrm{br}} + L_{\mathrm{t}}} \begin{bmatrix} -1 & 0 \\ 0 & -1 \end{bmatrix}. \end{gathered} \tag{3.9}$$

3.2.2 MMC DC side equivalent circuit modelling

MMC1 DC side model

The equivalent DC side circuit model is shown in Figure 3.3 which is derived via MMC averaged common mode analysis. u_{dc} is the measured DC voltage at MMC phase leg and V_{dc} is the DC-link nominal voltage. R_{dc} and L_{dc} are the DC-link impedance. We can write out the circuit equation of the DC voltage of MMC1 from arm current perspective as (3.10).

$$\begin{aligned} u_{\mathrm{dc}} &= 2u_{\mathrm{com,a}} + 2R_{\mathrm{br}} i_{\mathrm{com,a}} + 2L_{\mathrm{br}} \frac{\mathrm{d}}{\mathrm{d}t} i_{\mathrm{com,a}} \\ u_{\mathrm{dc}} &= 2u_{\mathrm{com,b}} + 2R_{\mathrm{br}} i_{\mathrm{com,b}} + 2L_{\mathrm{br}} \frac{\mathrm{d}}{\mathrm{d}t} i_{\mathrm{com,b}} \\ u_{\mathrm{dc}} &= 2u_{\mathrm{com,c}} + 2R_{\mathrm{br}} i_{\mathrm{com,c}} + 2L_{\mathrm{br}} \frac{\mathrm{d}}{\mathrm{d}t} i_{\mathrm{com,c}} \end{aligned} . \tag{3.10}$$

And from the view of DC-link, circuit equation can be written as (3.11):

$$\begin{aligned} u_{\mathrm{dc}} &= V_{\mathrm{dc}} - 2R_{\mathrm{dc}} i_{\mathrm{dc}} - 2L_{\mathrm{dc}} \frac{\mathrm{d}}{\mathrm{d}t} i_{\mathrm{dc}} \\ i_{\mathrm{dc}} &= i_{\mathrm{com,a}} + i_{\mathrm{com,b}} + i_{\mathrm{com,c}} \end{aligned} . \tag{3.11}$$

Combining equation (3.10) and (3.11), we can derive the SS model for the three phase MMC1 DC side current dynamics as (3.12). The voltage differences between the common mode voltages and half of the DC-link voltage are defined as the control inputs to this subsystem. It is clear to see that because of the DC-link impedance, the current dynamics and control effect in each phase are coupled.

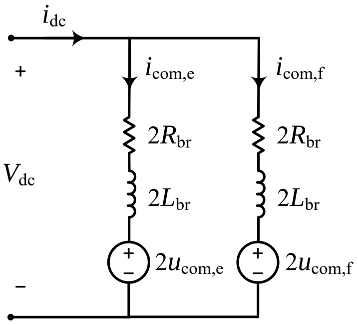

Fig. 3.4 MMC single phase dc side equivalent circuit model

$$\frac{\mathrm{d}}{\mathrm{d}t}\begin{bmatrix} i_{\mathrm{com,a}} \\ i_{\mathrm{com,b}} \\ i_{\mathrm{com,c}} \end{bmatrix} = \boldsymbol{A}_{\mathrm{com1}}\begin{bmatrix} i_{\mathrm{com,a}} \\ i_{\mathrm{com,b}} \\ i_{\mathrm{com,c}} \end{bmatrix} + \boldsymbol{B}_{\mathrm{com1}}\begin{bmatrix} u_{\mathrm{com,a}}-0.5V_{\mathrm{dc}} \\ u_{\mathrm{com,b}}-0.5V_{\mathrm{dc}} \\ u_{\mathrm{com,c}}-0.5V_{\mathrm{dc}} \end{bmatrix} \tag{3.12}$$

$$\boldsymbol{A}_{\mathrm{com1}} = \frac{-1}{L_{\mathrm{br}}\left(L_{\mathrm{br}}+3L_{\mathrm{dc}}\right)}\begin{bmatrix} L_{\mathrm{br}}R_{\mathrm{br}}+L_{\mathrm{br}}R_{\mathrm{dc}}+2L_{\mathrm{dc}}R_{\mathrm{br}} & L_{\mathrm{br}}R_{\mathrm{dc}}-L_{\mathrm{dc}}R_{\mathrm{br}} & L_{\mathrm{br}}R_{\mathrm{dc}}-L_{\mathrm{dc}}R_{\mathrm{br}} \\ L_{\mathrm{br}}R_{\mathrm{dc}}-L_{\mathrm{dc}}R_{\mathrm{br}} & L_{\mathrm{br}}R_{\mathrm{br}}+L_{\mathrm{br}}R_{\mathrm{dc}}+2L_{\mathrm{dc}}R_{\mathrm{br}} & L_{\mathrm{br}}R_{\mathrm{dc}}-L_{\mathrm{dc}}R_{\mathrm{br}} \\ L_{\mathrm{br}}R_{\mathrm{dc}}-L_{\mathrm{dc}}R_{\mathrm{br}} & L_{\mathrm{br}}R_{\mathrm{dc}}-L_{\mathrm{dc}}R_{\mathrm{br}} & L_{\mathrm{br}}R_{\mathrm{br}}+L_{\mathrm{br}}R_{\mathrm{dc}}+2L_{\mathrm{dc}}R_{\mathrm{br}} \end{bmatrix}.$$

$$\boldsymbol{B}_{\mathrm{com1}} = \frac{-1}{L_{\mathrm{br}}\left(L_{\mathrm{br}}+3L_{\mathrm{dc}}\right)}\begin{bmatrix} L_{\mathrm{br}}+2L_{\mathrm{dc}} & -L_{\mathrm{dc}} & -L_{\mathrm{dc}} \\ -L_{\mathrm{dc}} & L_{\mathrm{br}}+2L_{\mathrm{dc}} & -L_{\mathrm{dc}} \\ -L_{\mathrm{dc}} & -L_{\mathrm{dc}} & L_{\mathrm{br}}+2L_{\mathrm{dc}} \end{bmatrix}.$$

MMC2 DC side model

Similarly, the single phase DC side current model can be derived in the same way shown in (3.13):

$$\frac{\mathrm{d}}{\mathrm{d}t}\begin{bmatrix} i_{\mathrm{com,e}} \\ i_{\mathrm{com,f}} \end{bmatrix} = \boldsymbol{A}_{\mathrm{com2}}\begin{bmatrix} i_{\mathrm{com,e}} \\ i_{\mathrm{com,f}} \end{bmatrix} + \boldsymbol{B}_{\mathrm{com2}}\begin{bmatrix} u_{\mathrm{com,e}}-0.5V_{\mathrm{dc}} \\ u_{\mathrm{com,f}}-0.5V_{\mathrm{dc}} \end{bmatrix}. \tag{3.13}$$

$$\boldsymbol{A}_{\mathrm{com2}} = \frac{R_{\mathrm{br}}}{L_{\mathrm{br}}}\begin{bmatrix} -1 & 0 \\ 0 & 1 \end{bmatrix}, \ \boldsymbol{B}_{\mathrm{com2}} = \frac{1}{L_{\mathrm{br}}}\begin{bmatrix} -1 & 0 \\ 0 & -1 \end{bmatrix}.$$

Here, the DC-link impedance can be omitted if we concentrate the impedance to the MMC1 model.

3.2.3 MMC arm energy modelling

During the MMC operation, energy stored in each arm continuously flows between the AC and DC sides. The instantaneous power of each arm energy exchange is calculated as $p_{x\mathrm{u}} = i_{x\mathrm{u}}u_{x\mathrm{u}}$, and $p_{x\mathrm{l}} = i_{x\mathrm{l}}u_{x\mathrm{l}}$ where x represents each phase a, b, c, e, f and $p_{x,\mathrm{u}}$ and $p_{x\mathrm{l}}$ represent the instantaneous power in MMC upper arm and lower arm respectively.

Rewrite the arm current in differential and common mode components. The first order differential equation of arm energy ε can be expressed as (3.14):

$$\left.\begin{aligned}\frac{\mathrm{d}}{\mathrm{d}t}\varepsilon_{x\mathrm{u}} = p_{x\mathrm{u}} = i_{x\mathrm{u}}u_{x\mathrm{u}} = (i_{\mathrm{com},x} - i_{\mathrm{dif},x}) \times (u_{\mathrm{com},x} - u_{\mathrm{dif},x}) \\ \frac{\mathrm{d}}{\mathrm{d}t}\varepsilon_{x\mathrm{l}} = p_{x\mathrm{l}} = i_{x\mathrm{l}}u_{x\mathrm{l}} = (i_{\mathrm{com},x} + i_{\mathrm{dif},x}) \times (u_{\mathrm{com},x} + u_{\mathrm{dif},x})\end{aligned}\right., \quad x = \mathrm{a,b,c,e,f}. \tag{3.14}$$

Clearly, in (3.14) the energy terms $\varepsilon_{x\mathrm{u}}$, $\varepsilon_{x\mathrm{l}}$ will be updated by the product of state variables and control variables in the previous models (3.21), (3.22) which results in a nonlinear model. Ideally, in the steady state, the common mode voltage and differential voltage can be exactly expressed (see 3.3.1), therefore, we can approximate the energy dynamics by replacing the voltage control inputs with designed voltage reference. In this way, the state space model of arm energy in two MMC converters are simplified as (3.15) and (3.16).

$$\frac{\mathrm{d}}{\mathrm{d}t}\begin{bmatrix}\varepsilon_{\mathrm{au}} & \varepsilon_{\mathrm{bu}} & \varepsilon_{\mathrm{cu}} & \varepsilon_{\mathrm{al}} & \varepsilon_{\mathrm{bl}} & \varepsilon_{\mathrm{cl}} \end{bmatrix}^{\top} = \boldsymbol{A}_{\varepsilon 1}\begin{bmatrix}i_{\mathrm{ga}} & i_{\mathrm{gb}} & i_{\mathrm{gc}} & i_{\mathrm{coma}} & i_{\mathrm{comb}} & i_{\mathrm{comc}}\end{bmatrix}^{\top}. \tag{3.15}$$

$$\boldsymbol{A}_{\varepsilon 1} = \begin{bmatrix} -\frac{u^*_{\mathrm{com,a}}-u^*_{\mathrm{dif,a}}}{2} & 0 & 0 & u^*_{\mathrm{com,a}}-u^*_{\mathrm{dif,a}} & 0 & 0 \\ 0 & -\frac{u^*_{\mathrm{com,b}}-u^*_{\mathrm{dif,b}}}{2} & 0 & 0 & u^*_{\mathrm{com,b}}-u^*_{\mathrm{dif,ba}} & 0 \\ 0 & 0 & -\frac{u^*_{\mathrm{com,c}}-u^*_{\mathrm{dif,c}}}{2} & 0 & 0 & u^*_{\mathrm{com,c}}-u^*_{\mathrm{dif,c}} \\ \frac{u^*_{\mathrm{com,a}}+u^*_{\mathrm{dif,a}}}{2} & 0 & 0 & u^*_{\mathrm{com,a}}+u^*_{\mathrm{dif,a}} & 0 & 0 \\ 0 & \frac{u^*_{\mathrm{com,b}}+u^*_{\mathrm{dif,b}}}{2} & 0 & 0 & u^*_{\mathrm{com,b}}+u^*_{\mathrm{dif,ba}} & 0 \\ 0 & 0 & \frac{u^*_{\mathrm{com,c}}+u^*_{\mathrm{dif,c}}}{2} & 0 & 0 & u^*_{\mathrm{com,c}}+u^*_{\mathrm{dif,c}} \end{bmatrix}.$$

$$\frac{\mathrm{d}}{\mathrm{d}t}\begin{bmatrix}\varepsilon_{\mathrm{eu}} & \varepsilon_{\mathrm{fu}} & \varepsilon_{\mathrm{el}} & \varepsilon_{\mathrm{fl}}\end{bmatrix}^{\top} = \boldsymbol{A}_{\varepsilon 2}\begin{bmatrix}i_{\mathrm{t,e}} & i_{\mathrm{t,f}} & i_{\mathrm{com,e}} & i_{\mathrm{com,f}}\end{bmatrix}^{\top}. \tag{3.16}$$

$$\boldsymbol{A}_{\varepsilon 2} = \begin{bmatrix} -\frac{u^*_{\mathrm{com,e}}-u^*_{\mathrm{dif,e}}}{2} & 0 & u^*_{\mathrm{com,e}}-u^*_{\mathrm{dif,e}} & 0 \\ 0 & -\frac{u^*_{\mathrm{com,f}}-u^*_{\mathrm{dif,f}}}{2} & 0 & u^*_{\mathrm{com,f}}-u^*_{\mathrm{dif,f}} \\ \frac{u^*_{\mathrm{com,e}}+u^*_{\mathrm{dif,e}}}{2} & 0 & u^*_{\mathrm{com,e}}+u^*_{\mathrm{dif,e}} & 0 \\ 0 & \frac{u^*_{\mathrm{com,f}}+u^*_{\mathrm{dif,f}}}{2} & 0 & u^*_{\mathrm{com,f}}+u^*_{\mathrm{dif,f}} \end{bmatrix}.$$

3.2.4 System model for predictive control

In summary, the MMC arm current and arm energy are selected as system state variables. The differential mode voltage and common mode voltage generated in each phase are the manipulated variables. $\boldsymbol{x}_1$, $\boldsymbol{x}_2$ and $\boldsymbol{u}_1$, $\boldsymbol{u}_2$ are the state variable and control input of MMC1 and MMC2 respectively.

$$\boldsymbol{x}_1 = \begin{bmatrix}i_{\mathrm{ga}}, & i_{\mathrm{gb}}, & i_{\mathrm{gc}}, & i_{\mathrm{com,a}}, & i_{\mathrm{com,b}}, & i_{\mathrm{com,c}}, & \varepsilon_{\mathrm{au}}, & \varepsilon_{\mathrm{bu}}, & \varepsilon_{\mathrm{cu}}, & \varepsilon_{\mathrm{al}}, & \varepsilon_{\mathrm{bl}}, & \varepsilon_{\mathrm{cl}}\end{bmatrix}^{\top}. \tag{3.17}$$

$$\boldsymbol{x}_2 = \begin{bmatrix}i_{\mathrm{te}}, & i_{\mathrm{tf}}, & i_{\mathrm{com,e}}, & i_{\mathrm{com,f}}, & \varepsilon_{\mathrm{eu}}, & \varepsilon_{\mathrm{fu}}, & \varepsilon_{\mathrm{el}}, & \varepsilon_{\mathrm{fl}}\end{bmatrix}^{\top}. \tag{3.18}$$

$$\boldsymbol{u}_1 = \left[u_{\text{dif,a}} - u_{\text{ga}},\ u_{\text{dif,a}} - u_{\text{gb}},\ u_{\text{dif,c}} - u_{\text{gc}},\ u_{\text{com,a}} - \tfrac{V_{\text{dc}}}{2},\ u_{\text{com,b}} - \tfrac{V_{\text{dc}}}{2},\ u_{\text{com,c}} - \tfrac{V_{\text{dc}}}{2}\right]^{\top}. \tag{3.19}$$

$$\boldsymbol{u}_2 = \left[u_{\text{dif,e}} - \tfrac{u_{\text{t}}}{2},\ u_{\text{dif,f}} + \tfrac{u_{\text{t}}}{2},\ u_{\text{com,e}} - \tfrac{V_{\text{dc}}}{2},\ u_{\text{com,f}} - \tfrac{V_{\text{dc}}}{2}\right]^{\top}. \tag{3.20}$$

Two state space models for three phase and single phase converters are shown in (3.21) and (3.22) repectively. The dimension of each element is shown in the subscripts.

$$\begin{aligned}
&\frac{\mathrm{d}}{\mathrm{d}t}\boldsymbol{x}_{1\,(12\times1)} = \boldsymbol{A}_{1(12\times12)}\boldsymbol{x}_{1\,(12\times1)} + \boldsymbol{B}_{1(12\times6)}\boldsymbol{u}_{1\,(6\times1)},\\
&\boldsymbol{A}_{1(12\times12)} = \begin{bmatrix} \begin{matrix} \boldsymbol{A}_{g\,(3\times3)} & \boldsymbol{0}_{(3\times3)} \\ \boldsymbol{0}_{(3\times3)} & \boldsymbol{A}_{\text{com1}\,(3\times3)} \end{matrix} & \boldsymbol{0}_{(6\times6)} \\ \boldsymbol{A}_{\varepsilon1\,(6\times6)}\left(u^{*}_{\text{com1}}, u^{*}_{\text{dif1}}\right) & \boldsymbol{0}_{(6\times6)} \end{bmatrix},\ \boldsymbol{B}_{1(12\times6)} = \begin{bmatrix} \begin{matrix} \boldsymbol{B}_{g(3\times3)} & \boldsymbol{0}_{(3\times3)} \\ \boldsymbol{0}_{(3\times3)} & \boldsymbol{B}_{\text{com1}(3\times3)} \end{matrix} \\ \boldsymbol{0}_{(6\times6)} \end{bmatrix}.
\end{aligned} \tag{3.21}$$

$$\begin{aligned}
&\frac{\mathrm{d}}{\mathrm{d}t}\boldsymbol{x}_{2(8\times1)} = \boldsymbol{A}_{2(8\times8)}\boldsymbol{x}_{2(8\times1)} + \boldsymbol{B}_{2(8\times4)}\boldsymbol{u}_{2(4\times1)},\\
&\boldsymbol{A}_{2(8\times8)} = \begin{bmatrix} \begin{matrix} \boldsymbol{A}_{\text{t}(2\times2)} & \boldsymbol{0}_{(2\times2)} \\ \boldsymbol{0}_{(2\times1)} & \boldsymbol{A}_{\text{com2}\,(2\times2)} \end{matrix} & \boldsymbol{0}_{(4\times4)} \\ \boldsymbol{A}_{\varepsilon2\,(4\times4)}\left(u^{*}_{\text{com2}}, u^{*}_{\text{dif2}}\right) & \boldsymbol{0}_{(4\times4)} \end{bmatrix},\ \boldsymbol{B}_{2(8\times4)} = \begin{bmatrix} \begin{matrix} \boldsymbol{B}_{\text{t}(2\times2)} & \boldsymbol{0}_{(2\times2)} \\ \boldsymbol{0}_{(2\times2)} & \boldsymbol{B}_{\text{com2}(2\times2)} \end{matrix} \\ \boldsymbol{0}_{(4\times4)} \end{bmatrix}.
\end{aligned} \tag{3.22}$$

3.3 Model predictive controller design

Given the SS model, three essential parts of the MPC design: reference, constraint and cost function are designed in this section for MMC converter.

3.3.1 Reference design

The references are designed from the steady state operation perspective.

Current reference

AC current reference design Firstly, assume the three phase grid voltage vector $[u_{\text{ga}}, u_{\text{gb}}, u_{\text{gc}}]^{\top}$ has expression as (3.23) and the traction side voltage u_{t} is controlled as (3.24), where V_{g} is the RMS value of phase to ground voltage and V_{t} is the RMS value of catenary to ground voltage.

$$\begin{bmatrix} u_{\text{ga}} \\ u_{\text{gb}} \\ u_{\text{gc}} \end{bmatrix} = \frac{\sqrt{2}}{\sqrt{3}}V_{\text{g}} \begin{bmatrix} \cos\left(\omega_{\text{g}}t\right) \\ \cos\left(\omega_{\text{g}}t\frac{-2\pi}{3}\right) \\ \cos\left(\omega_{\text{g}}t - \frac{4\pi}{3}\right) \end{bmatrix}. \tag{3.23}$$

$$u_{\text{t}} = \sqrt{2}V_{\text{t}}\cos\left(\omega_{\text{t}}t\right). \tag{3.24}$$

Define the grid side phase current reference RMS value as I_{g}^{*}, the instantaneous reference of three phase current is shown in (3.25). The apparent power reference from the grid is $S_1^{*}=\sqrt{3}I_{\mathrm{g}}^{*}V_{\mathrm{g}}$.

$$\boldsymbol{i}_{\mathrm{g}}^{*}=\begin{bmatrix} i_{\mathrm{ga}}^{*} \\ i_{\mathrm{gb}}^{*} \\ i_{\mathrm{gc}}^{*} \end{bmatrix}=\begin{bmatrix} \sqrt{2}I_{\mathrm{g}}^{*}\cos\left(\omega_{\mathrm{g}}t-\varphi_1\right) \\ \sqrt{2}I_{\mathrm{g}}^{*}\cos\left(\omega_{\mathrm{g}}t-\varphi_1-\frac{2\pi}{3}\right) \\ \sqrt{2}I_{\mathrm{g}}^{*}\cos\left(\omega_{\mathrm{g}}t-\varphi_1-\frac{4\pi}{3}\right) \end{bmatrix}. \tag{3.25}$$

Similarly, the instantaneous traction side current reference is given in (3.26); the apparent power reference to the traction network is $S_2^{*}=I_{\mathrm{t}}^{*}V_{\mathrm{t}}$.

$$\boldsymbol{i}_{t}^{*}=\begin{bmatrix} i_{\mathrm{t,e}}^{*} \\ i_{\mathrm{t,f}}^{*} \end{bmatrix}=\begin{bmatrix} \sqrt{2}I_{\mathrm{t}}^{*}\cos\left(\omega_{\mathrm{g}}t-\varphi\right) \\ -\sqrt{2}I_{\mathrm{t}}^{*}\cos\left(\omega_{\mathrm{g}}t-\varphi\right) \end{bmatrix}. \tag{3.26}$$

DC current reference design Secondly, on the DC side, the ideal steady state current shall be a constant DC value which does not contain any oscillating AC components. Additionally, the DC-link current shall distribute equally to each MMC phase. Therefore, the DC current reference is designed as (3.27)

$$\boldsymbol{i}_{\mathrm{com1}}^{*}=\begin{bmatrix} i_{\mathrm{com,a}}^{*} & i_{\mathrm{com,b}}^{*} & i_{\mathrm{com,c}}^{*} \end{bmatrix}^{\top}=\frac{1}{3}I_{\mathrm{dc1}}^{*}\begin{bmatrix} 1 \\ 1 \\ 1 \end{bmatrix}, \quad \boldsymbol{i}_{\mathrm{com2}}^{*}=\begin{bmatrix} i_{\mathrm{com,e}}^{*} & i_{\mathrm{com,f}}^{*} \end{bmatrix}^{\top}=\frac{1}{2}I_{\mathrm{dc2}}^{*}\begin{bmatrix} 1 \\ 1 \end{bmatrix}, \tag{3.27}$$

where I_{dc1}^{*} and I_{dc2}^{*} are the DC-link current references for MMC1 and MMC2 respectively.

The relationship between AC and DC current reference As shown above, current references are defined by I_{g}^{*}, I_{t}^{*}, I_{dc1}^{*}, I_{dc2}^{*}, φ_1 and φ_2. If the energy losses are ignored, the instantaneous power exchanged at AC side is equal to the DC side in the steady state. Under this assumption, the power and current relationship between AC and DC side is shown in (3.28):

$$0=P_{\mathrm{dc}}+P_{\mathrm{ac}}\Rightarrow\begin{cases} I_{\mathrm{dc}}=-\dfrac{\sqrt{3}I_{\mathrm{g}}V_{\mathrm{g}}\cos\varphi_1}{V_{\mathrm{dc}}} \\ I_{\mathrm{g}}=-\dfrac{V_{\mathrm{dc}}I_{\mathrm{dc}}}{\sqrt{3}V_{\mathrm{g}}\cos\varphi_1} \end{cases}. \tag{3.28}$$

However, energy losses do exist, if we use the resistor R_{br}, R_{g} and R_{dc} to represent the averaged losses at each arm, grid connection and DC-link. The energy losses in phase ‘a’ at MMC branch, grid side and DC-link can be expressed as (3.29), (3.30) and (3.31) respectively.

$$P_{\mathrm{loss,mmc,a}}=i_{\mathrm{au}}^{2}R_{\mathrm{br}}+i_{\mathrm{al}}^{2}R_{\mathrm{br}}=\frac{2}{9}\left(I_{\mathrm{dc}}^{*}\right)^{2}R_{\mathrm{br}}+\frac{1}{2}\left(I_{\mathrm{g}}^{*}\right)^{2}R_{\mathrm{br}}+\frac{\cos\left(2\omega_{\mathrm{g}}t-2\varphi_1\right)}{2}\left(I_{\mathrm{g}}^{*}\right)^{2}R_{\mathrm{br}}. \tag{3.29}$$

$$P_{\text{loss,grid,a}} = \left(\sqrt{2}I_{\text{g}}^{*}\cos\left(\omega_{\text{g}}t-\varphi_1\right)\right)^2 R_{\text{g}} = \left(I_{\text{g}}^{*}\right)^2 R_{\text{g}} + \left(I_{\text{g}}^{*}\right)^2 R_{\text{g}}\cos\left(2\omega_{\text{g}}t-2\varphi_1\right). \tag{3.30}$$

$$P_{\text{loss,dc,a}} = \frac{2}{3}\left(I_{\text{dc}}^{*}\right)^2 R_{\text{dc}}. \tag{3.31}$$

Take the energy losses into consideration, we can update the simplified power equation (3.28) to (3.32). And an accurate current reference for grid side MMC can be calculated using (3.33).

$$0 = P_{\text{dc1}}^{*} + P_{\text{ac}}^{*} - \sum_{x=\text{a,b,c}}\left(P_{\text{loss,dc},x} + P_{\text{loss,mmc},x} + P_{\text{loss,grid},x}\right). \tag{3.32}$$

$$I_{\text{g}}^{*}\left(V_{\text{g}},\varphi_1,P_{\text{dc1}}\right) = \frac{\sqrt{3}V_{\text{g}}\cos\varphi_1 - \sqrt{3V_{\text{g}}^2\cos^2\varphi_1 + 4\left(\frac{3}{2}R_{\text{br}}+3R_{\text{g}}\right)\left(P_{\text{dc1}} - \frac{2}{3}\frac{P_{\text{dc1}}^2 R_{\text{br}}}{V_{\text{dc}}^2} - 2\frac{P_{\text{dc1}}^2 R_{\text{dc}}}{V_{\text{dc}}^2}\right)}}{3R_{\text{br}}+6R_{\text{g}}}. \tag{3.33}$$

Note that in B2B converter control, the DC-link side energy determines the grid side power, so we use DC-link power reference to generate grid side current reference. Similarly, the accurate energy relationship on the traction side is (3.34) and the accurate DC-link current reference for traction side MMC is derived in (3.35). Obviously, on the traction side, the DC-link power is mainly dominated by the power required by traction load power.

$$0 = P_{\text{dc2}}^{*} + P_{\text{t}}^{*} - \sum_{x=\text{e,f}}\left(P_{\text{loss,mmc},x} + P_{\text{loss,traction},x}\right). \tag{3.34}$$

$$I_{\text{dc2}}^{*}\left(V_{\text{dc}},P_{\text{t}}^{*}\right) = \frac{V_{\text{dc}} - \sqrt{V_{\text{dc}}^2 + 4P_{\text{t}}^{*}R_{\text{br}} - 4\left(\frac{P_{\text{t}}^{*}}{V_{\text{t}}}\right)^2 R_{\text{br}}^{*} - 8\left(\frac{P_{\text{t}}^{*}}{V_{\text{t}}}\right)^2 R_{\text{br}}R_{\text{t}}}}{2R_{\text{br}}}. \tag{3.35}$$

In general, the grid power factor is controlled to be unity and the grid voltage magnitude can be regarded as constant, so the grid side MMC current reference I_{g}^{*} for MMC1 is a function of DC-link power requirement and the DC current reference for traction side MMC depends on the DC-link voltage and traction active power consumption.

Voltage reference design

Given the above designed current references, the voltage references for both MMCs are calculated by the circuit equations.

$$\begin{aligned}
\begin{bmatrix} u_{\text{dif,a}}^{*}-u_{\text{ga}} \\ u_{\text{dif,b}}^{*}-u_{\text{gb}} \\ u_{\text{dif,c}}^{*}-u_{\text{gc}} \end{bmatrix} &= -\sqrt{2}I_{\text{g}}^{*}\left|Z_1\right| \begin{bmatrix} \cos\left(\omega_{\text{g}}t-\varphi_1-\arg\left(Z_1\right)\right) \\ \cos\left(\omega_{\text{g}}t-\varphi_1-\frac{2\pi}{3}-\arg\left(Z_1\right)\right) \\ \cos\left(\omega_{\text{g}}t-\varphi_1-\frac{4\pi}{3}-\arg\left(Z_1\right)\right) \end{bmatrix}, \\
\begin{bmatrix} u_{\text{com,a}}^{*}-0.5V_{\text{dc}} \\ u_{\text{com,b}}^{*}-0.5V_{\text{dc}} \\ u_{\text{com,c}}^{*}-0.5V_{\text{dc}} \end{bmatrix} &= I_{\text{dc}}^{*}\left(\frac{1}{3}R_{\text{br}}+R_{\text{dc}}\right)\begin{bmatrix} 1 \\ 1 \\ 1 \end{bmatrix},
\end{aligned} \tag{3.36}$$

where the impedance Z_1 is (3.37).

$$|Z_1| = \sqrt{\left(0.5R_{\mathrm{br}}+R_{\mathrm{g}}\right)^2+\left(\omega_{\mathrm{g}}\left(0.5L_{\mathrm{br}}+L_{\mathrm{g}}\right)\right)^2},\ \arg\left(Z_1\right) = \arctan\left(\frac{\omega_{\mathrm{g}}\left(0.5L_{\mathrm{br}}+L_{\mathrm{g}}\right)}{0.5R_{\mathrm{br}}+R_{\mathrm{g}}}\right). \tag{3.37}$$

$$\begin{aligned}\begin{bmatrix} u^*_{\mathrm{dif,e}}-0.5u_{\mathrm{t}} \\ u^*_{\mathrm{dif,f}}+0.5u_{\mathrm{t}} \end{bmatrix} &= -\sqrt{2}I^*_{\mathrm{t}}\left|Z_2\right| \begin{bmatrix} \cos\left(\omega_{\mathrm{t}}t-\varphi_2-\arg\left(Z_2\right)\right) \\ \cos\left(\omega_{\mathrm{t}}t-\varphi_2-\arg\left(Z_2\right)-\pi\right) \end{bmatrix}, \\ \begin{bmatrix} u^*_{\mathrm{com,e}}-0.5V_{\mathrm{dc}} \\ u^*_{\mathrm{com,f}}-0.5V_{\mathrm{dc}} \end{bmatrix} &= -\frac{1}{2}R_{\mathrm{br}}I^*_{\mathrm{dc}}\begin{bmatrix} 1 \\ 1 \end{bmatrix},\end{aligned} \tag{3.38}$$

where the impedance Z_2 is (3.39).

$$|Z_2| = \sqrt{\left(0.5R_{\mathrm{br}}+R_{\mathrm{t}}\right)^2+\left(\omega_{\mathrm{t}}\left(0.5L_{\mathrm{br}}+L_{\mathrm{t}}\right)\right)^2}, \arg\left(Z_2\right) = \arctan\left(\frac{\omega_{\mathrm{t}}\left(0.5L_{\mathrm{br}}+L_{\mathrm{t}}\right)}{0.5R_{\mathrm{br}}+R_{\mathrm{t}}}\right). \tag{3.39}$$

$$\begin{aligned}\boldsymbol{u}_1^* &= \begin{bmatrix} u^*_{\mathrm{dif,a}}-u_{\mathrm{ga}} & u^*_{\mathrm{dif,b}}-u_{\mathrm{gb}} & u^*_{\mathrm{dif,c}}-u_{\mathrm{gc}} & u^*_{\mathrm{com,a}}-0.5V_{\mathrm{dc}} & u^*_{\mathrm{com,b}}-0.5V_{\mathrm{dc}} & u^*_{\mathrm{com,c}}-0.5V_{\mathrm{dc}} \end{bmatrix}^\top \\ \boldsymbol{u}_2^* &= \begin{bmatrix} u^*_{\mathrm{dif,e}}-0.5u_{\mathrm{t}} & u^*_{\mathrm{dif,f}}+0.5u_{\mathrm{t}} & u^*_{\mathrm{com,e}}-0.5V_{\mathrm{dc}} & u^*_{\mathrm{com,f}}-0.5V_{\mathrm{dc}} \end{bmatrix}^\top\end{aligned}$$

Note that the voltage references $\boldsymbol{u}_1^*$, $\boldsymbol{u}_2^*$ are almost identical to the steady state result when state tracking errors are nearly eliminated. In this MPC approach, the main function of these voltage value function is to predict the capacitor energy variation as discussed in Section 3.2.3.

Arm energy reference design

One of the objectives of MMC internal state control is to minimise the circulating current so that the internal losses are minimised. Based on this assumption, we can estimate the ideal arm energy variation in the steady state where the AC currents are perfectly 50 Hz sinusoidal and DC currents are perfectly constant DC values. The phase ‘a’ of the grid side MMC converter is used as an example of arm energy variation analysis in this part. In MMC1 phase ‘a’, the arm voltage and arm current are expressed in (3.40) and (3.41):

$$\begin{aligned} u_{\mathrm{au}} &= u_{\mathrm{com,a}} - u_{\mathrm{dif,a}} \\ &= \frac{1}{2}V_{\mathrm{dc}} - I^*_{\mathrm{dc}}\left(\frac{1}{3}R_{\mathrm{br}}+R_{\mathrm{dc}}\right) - \frac{\sqrt{2}}{\sqrt{3}}V_g\cos\left(\omega_g t\right) + \sqrt{2}I^*_{\mathrm{g}}\left|Z_1\right|\cos\left(\omega_g t-\varphi_1-\arg\left(Z_1\right)\right) \\ u_{\mathrm{al}} &= u_{\mathrm{com,a}} + u_{\mathrm{dif,a}} \\ &= \frac{1}{2}V_{\mathrm{dc}} - I^*_{\mathrm{dc}}\left(\frac{1}{3}R_{\mathrm{br}}+R_{\mathrm{dc}}\right) + \frac{\sqrt{2}}{\sqrt{3}}V_g\cos\left(\omega_g t\right) - \sqrt{2}I^*_{\mathrm{g}}\left|Z_1\right|\cos\left(\omega_g t-\varphi_1-\arg\left(Z_1\right)\right) \end{aligned}. \tag{3.40}$$

$$\begin{array}{l} i_{\mathrm{au}} = i_{\mathrm{com,a}} - i_{\mathrm{dif,a}} = \frac{1}{3} I_{\mathrm{dc}}^{*} - \frac{\sqrt{2}}{2} I_{\mathrm{g}}^{*} \cos\left(\omega_{\mathrm{g}} t - \varphi_1\right) \\ i_{\mathrm{al}} = i_{\mathrm{com,a}} + i_{\mathrm{dif,a}} = \frac{1}{3} I_{\mathrm{dc}}^{*} + \frac{\sqrt{2}}{2} I_{\mathrm{g}}^{*} \cos\left(\omega_{\mathrm{g}} t - \varphi_1\right) \end{array} . \tag{3.41}$$

Then the instantaneous power in upper and lower arm of phase ‘a’ can be calculated as $p_{\mathrm{au}} = u_{\mathrm{au}} i_{\mathrm{au}}$ and $p_{\mathrm{al}} = u_{\mathrm{al}} i_{\mathrm{al}}$. The energy exchange expressions at upper and lower arm energy are shown as follows in (3.42) and (3.43).

$$\begin{array}{l} p_{\mathrm{au}} = \frac{1}{6} V_{\mathrm{dc}} I_{\mathrm{dc}}^{*} - \left(\frac{1}{9} R_{\mathrm{br}} + \frac{1}{3} R_{\mathrm{dc}}\right) \left(I_{\mathrm{dc}}^{*}\right)^2 \\ \quad + \frac{1}{\sqrt{3}} V_g \cos\left(\omega_{\mathrm{g}} t\right) I_{\mathrm{g}}^{*} \cos\left(\omega_{\mathrm{g}} t - \varphi_1\right) - \left(I_{\mathrm{g}}^{*}\right)^2 \cos\left(\omega_{\mathrm{g}} t - \varphi\right) |Z| \cos\left(\omega_{\mathrm{g}} t - \varphi - \arg\left(Z_1\right)\right) \\ \quad - \frac{\sqrt{6}}{9} V_g \cos\left(\omega_g t\right) I_{\mathrm{dc}}^{*} + \frac{\sqrt{2}}{3} I_{\mathrm{g}}^{*} \cos\left(\omega_{\mathrm{g}} t - \varphi_1 + \arg\left(Z_1\right)\right) I_{\mathrm{dc}}^{*} \left|Z_1\right| - \frac{\sqrt{2}}{4} V_{\mathrm{dc}} I_{\mathrm{g}}^{*} \cos\left(\omega_{\mathrm{g}} t - \varphi_1\right) + \frac{\sqrt{2}}{2} \left(\frac{R_{\mathrm{br}}}{3} + R_{\mathrm{dc}}\right) I_{\mathrm{dc}}^{*} I_{\mathrm{g}}^{*} \cos\left(\omega_{\mathrm{g}} t - \varphi\right) \end{array} , \tag{3.42}$$

$$\begin{array}{l} p_{\mathrm{al}} = \frac{1}{6} V_{\mathrm{dc}} I_{\mathrm{dc}}^{*} - \left(\frac{1}{9} R_{\mathrm{br}} + \frac{1}{3} R_{\mathrm{dc}}\right) \left(I_{\mathrm{dc}}^{*}\right)^2 \\ \quad + \frac{1}{\sqrt{3}} V_g \cos\left(\omega_g t\right) I_{\mathrm{g}}^{*} \cos\left(\omega_{\mathrm{g}} t - \varphi_1\right) - \left(I_{\mathrm{g}}^{*}\right)^2 \cos\left(\omega_{\mathrm{g}} t - \varphi_1\right) \left|Z_1\right| \cos\left(\omega_{\mathrm{g}} t - \varphi - \arg\left(Z_1\right)\right) \\ \quad + \frac{\sqrt{6}}{9} V_g \cos\left(\omega_g t\right) I_{\mathrm{dc}}^{*} - \frac{\sqrt{2}}{3} I_{\mathrm{g}}^{*} \cos\left(\omega_{\mathrm{g}} t - \varphi + \arg\left(Z_1\right)\right) I_{\mathrm{dc}}^{*} \left|Z_1\right| + \frac{\sqrt{2}}{4} V_{\mathrm{dc}} I_{\mathrm{g}}^{*} \cos\left(\omega_{\mathrm{g}} t - \varphi_1\right) - \frac{\sqrt{2}}{2} \left(\frac{R_{\mathrm{br}}}{3} + R_{\mathrm{dc}}\right) I_{\mathrm{dc}}^{*} I_{\mathrm{g}}^{*} \cos\left(\omega_{\mathrm{g}} t - \varphi_1\right) \end{array} , \tag{3.43}$$

where the first row in both equations represents the energy exchanged at DC side; the second row represents the result of AC current and AC voltage coupling while the third row is the coupling effect between AC and DC components.

Through trigonometric transformation, the instantaneous power exchange in upper and lower arm of MMC1 phase ‘a’ is transformed into different frequency components shown in (3.44) and (3.45).

$$\begin{array}{l} p_{\mathrm{au}} = \underbrace{\frac{1}{6} V_{\mathrm{dc}} I_{\mathrm{dc1}}^{*} - \left(\frac{1}{9} R_{\mathrm{br}} + \frac{1}{3} R_{\mathrm{dc}}\right) \left(I_{\mathrm{dc1}}^{*}\right)^2 + \frac{\sqrt{3}}{6} V_g I_{\mathrm{g}}^{*} \cos\varphi_1 - \frac{1}{2} \left(I_{\mathrm{g}}^{*}\right)^2 \left|Z_1\right| \cos\left(\arg\left(Z_1\right)\right)}_{\text{0 order component}} \\ \underbrace{- \frac{\sqrt{6}}{9} V_g I_{\mathrm{dc1}}^{*} \cos\left(\omega_g t\right) + \frac{\sqrt{2}}{3} I_{\mathrm{g}}^{*} I_{\mathrm{dc1}}^{*} \left|Z_1\right| \cos\left(\omega_{\mathrm{g}} t - \varphi_1 - \arg\left(Z_1\right)\right) - \frac{\sqrt{2}}{4} V_{\mathrm{dc}} I_{\mathrm{g}}^{*} \cos\left(\omega_{\mathrm{g}} t - \varphi_1\right) + \frac{\sqrt{2}}{2} \left(\frac{1}{3} R_{\mathrm{br}} + R_{\mathrm{dc}}\right) I_{\mathrm{dc1}}^{*} I_{\mathrm{g}}^{*} \cos\left(\omega_{\mathrm{g}} t - \varphi_1\right)}_{\text{1st order 50 Hz component}} \\ \underbrace{+ \frac{\sqrt{3}}{6} V_g I_{\mathrm{g}}^{*} \cos\left(2\omega_{\mathrm{g}} t - \varphi_1\right) - \frac{1}{2} \left(I_{\mathrm{g}}^{*}\right)^2 \left|Z_1\right| \left(\cos\left(2\omega_{\mathrm{g}} t - 2\varphi_1 - \arg\left(Z_1\right)\right)\right)}_{\text{2nd order 100Hz component}} \end{array} \tag{3.44}$$

$$
\begin{aligned}
p_{\mathrm{al}} = {} & \frac{1}{6}V_{\mathrm{dc}}I_{\mathrm{dc1}}^{*} - \left(\frac{1}{9}R_{\mathrm{br}} + \frac{1}{3}R_{\mathrm{dc}}\right)\left(I_{\mathrm{dc1}}^{*}\right)^{2} + \frac{\sqrt{3}}{6}V_{g}I_{\mathrm{g}}^{*}\cos\varphi_{1} - \frac{1}{2}\left(I_{\mathrm{g}}^{*}\right)^{2}\left|Z_{1}\right|\cos\left(\arg\left(Z_{1}\right)\right) \\
& + \frac{\sqrt{6}}{9}V_{g}I_{\mathrm{dc1}}^{*}\cos\left(\omega_{g}t\right) - \frac{\sqrt{2}}{3}I_{\mathrm{g}}^{*}I_{\mathrm{dc1}}^{*}\left|Z_{1}\right|\cos\left(\omega_{\mathrm{g}}t - \varphi_{1} - \arg\left(Z_{1}\right)\right) + \frac{\sqrt{2}}{4}V_{\mathrm{dc}}I_{\mathrm{g}}^{*}\cos\left(\omega_{\mathrm{g}}t - \varphi_{1}\right) - \frac{\sqrt{2}}{2}\left(\frac{1}{3}R_{\mathrm{br}} + R_{\mathrm{dc}}\right)I_{\mathrm{dc1}}^{*}I_{\mathrm{g}}^{*}\cos\left(\omega_{\mathrm{g}}t - \varphi_{1}\right) \\
& + \frac{\sqrt{3}}{6}V_{g}I_{\mathrm{g}}^{*}\cos\left(2\omega_{\mathrm{g}}t - \varphi_{1}\right) - \frac{1}{2}\left(I_{\mathrm{g}}^{*}\right)^{2}\left|Z_{1}\right|\left(\cos\left(2\omega_{\mathrm{g}}t - 2\varphi_{1} - \arg\left(Z_{1}\right)\right)\right)
\end{aligned}
\tag{3.45}
$$

The above equations reveal that even in the ideal steady state, first order and second order oscillation exists in each arm. The zero order component should be zero in steady state when the power balancing equation (3.32) is satisfied. Integrate the arm instantaneous power, the optimal arm energy variation reference Δe_{au} and Δe_{al} can be obtained and is shown in (3.47) and (3.47) respectively.

$$
\begin{aligned}
\Delta e_{\mathrm{au}}\left(t, I_{\mathrm{dc1}}^{*}, I_{\mathrm{g}}^{*}, \varphi_{1}\right) = {} & \int p_{\mathrm{au}}\,\mathrm{d}t \\
= {} & -\frac{\sqrt{6}}{9\omega_{g}}V_{g}I_{\mathrm{dc1}}^{*}\sin\left(\omega_{g}t\right) + \frac{\sqrt{2}}{3\omega_{g}}I_{\mathrm{g}}^{*}I_{\mathrm{dc1}}^{*}\left|Z_{1}\right|\sin\left(\omega_{\mathrm{g}}t - \varphi_{1} - \arg\left(Z_{1}\right)\right) \\
& - \frac{\sqrt{2}}{4\omega_{\mathrm{g}}}V_{\mathrm{dc}}I_{\mathrm{g}}^{*}\sin\left(\omega_{\mathrm{g}}t - \varphi_{1}\right) + \frac{\sqrt{2}}{2\omega_{\mathrm{g}}}\left(\frac{1}{3}R_{\mathrm{br}} + R_{\mathrm{dc}}\right)I_{\mathrm{dc}}^{*}I_{\mathrm{g}}^{*}\sin\left(\omega_{\mathrm{g}}t - \varphi_{1}\right) \\
& + \frac{\sqrt{3}}{12\omega_{\mathrm{g}}}V_{g}I_{\mathrm{g}}^{*}\sin\left(2\omega_{\mathrm{g}}t - \varphi_{1}\right) - \frac{1}{4\omega_{\mathrm{g}}}\left(I_{\mathrm{g}}^{*}\right)^{2}\left|Z_{1}\right|\sin\left(2\omega_{\mathrm{g}}t - 2\varphi_{1} - \arg\left(Z_{1}\right)\right)
\end{aligned}
\quad . \tag{3.46}
$$

$$
\begin{aligned}
\Delta e_{\mathrm{al}}\left(t, I_{\mathrm{dc1}}^{*}, I_{\mathrm{g}}^{*}, \varphi_{1}\right) = {} & \int p_{\mathrm{al}}\,\mathrm{d}t \\
= {} & +\frac{\sqrt{6}}{9\omega_{g}}V_{g}I_{\mathrm{dc1}}^{*}\sin\left(\omega_{g}t\right) - \frac{\sqrt{2}}{3\omega_{g}}I_{\mathrm{g}}^{*}I_{\mathrm{dc1}}^{*}\left|Z_{1}\right|\sin\left(\omega_{\mathrm{g}}t - \varphi_{1} - \arg\left(Z_{1}\right)\right) \\
& + \frac{\sqrt{2}}{4\omega_{\mathrm{g}}}V_{\mathrm{dc}}I_{\mathrm{g}}^{*}\sin\left(\omega_{\mathrm{g}}t - \varphi_{1}\right) - \frac{\sqrt{2}}{2\omega_{\mathrm{g}}}\left(\frac{1}{3}R_{\mathrm{br}} + R_{\mathrm{dc}}\right)I_{\mathrm{dc}}^{*}I_{\mathrm{g}}^{*}\sin\left(\omega_{\mathrm{g}}t - \varphi_{1}\right) \\
& + \frac{\sqrt{3}}{12\omega_{\mathrm{g}}}V_{g}I_{\mathrm{g}}^{*}\sin\left(2\omega_{\mathrm{g}}t - \varphi_{1}\right) - \frac{1}{4\omega_{\mathrm{g}}}\left(I_{\mathrm{g}}^{*}\right)^{2}\left|Z_{1}\right|\sin\left(2\omega_{\mathrm{g}}t - 2\varphi_{1} - \arg\left(Z_{1}\right)\right)
\end{aligned}
\quad . \tag{3.47}
$$

If all impedance are ignored, then $I_{\mathrm{dc1}}^{*} = -\frac{S_{1}\cos\varphi}{V_{\mathrm{dc}}}$, $I_{\mathrm{g}}^{*} = \frac{S_{1}}{\sqrt{3}V_{\mathrm{g}}}$, and the above equations can be simplified into an approximated form which is a function of time, apparent power, and power angle as shown in (3.48).

$$
\begin{aligned}
\Delta e_{\mathrm{au}}\left(t, S_{1}, \varphi_{1}\right) &\approx \frac{\sqrt{6}}{9\omega_{g}}\frac{V_{g}}{V_{\mathrm{dc}}}S_{1}\cos\varphi\sin\left(\omega_{g}t\right) - \frac{\sqrt{6}}{12\omega_{\mathrm{g}}}\frac{V_{\mathrm{dc}}}{V_{\mathrm{g}}}S_{1}\sin\left(\omega_{\mathrm{g}}t - \varphi_{1}\right) + \frac{1}{12\omega_{\mathrm{g}}}S_{1}\sin\left(2\omega_{\mathrm{g}}t - \varphi_{1}\right) \\
\Delta e_{\mathrm{al}}\left(t, S_{1}, \varphi_{1}\right) &\approx -\frac{\sqrt{6}}{9\omega_{g}}\frac{V_{g}}{V_{\mathrm{dc}}}S_{1}\cos\varphi_{1}\sin\left(\omega_{g}t\right) + \frac{\sqrt{6}}{12\omega_{\mathrm{g}}}\frac{V_{\mathrm{dc}}}{V_{\mathrm{g}}}S_{1}\sin\left(\omega_{\mathrm{g}}t - \varphi_{1}\right) + \frac{1}{12\omega_{\mathrm{g}}}S_{1}\sin\left(2\omega_{\mathrm{g}}t - \varphi_{1}\right)
\end{aligned}
\quad . \tag{3.48}
$$

Similarly, the accurate form of optimal energy variation reference for single-phase (phase ‘e’) is given in (3.49) & (3.50):

$$\begin{aligned}\Delta e_{\mathrm{eu}}\left(t, I_{\mathrm{dc}_2}^{*}, I_{\mathrm{t}}^{*}, \varphi_2\right) = & -\frac{\sqrt{2}}{2\omega_{\mathrm{t}}} V_{\mathrm{t}} I_{\mathrm{dc2}}^{*} \sin\left(\omega_{\mathrm{t}} t\right) + \frac{\sqrt{2}}{2\omega_{\mathrm{t}}} I_{\mathrm{t}}^{*} I_{\mathrm{dc2}}^{*} \left|Z_2\right| \sin\left(\omega_{\mathrm{t}} t - \varphi_2 - \arg\left(Z_2\right)\right) \\ & -\frac{\sqrt{2}}{4\omega_{\mathrm{t}}} V_{\mathrm{dc}} I_{\mathrm{t}}^{*} \sin\left(\omega_{\mathrm{t}} t - \varphi_2\right) + \frac{\sqrt{2}}{4\omega_{\mathrm{t}}} R_{\mathrm{br}} I_{\mathrm{dc2}}^{*} I_{\mathrm{t}}^{*} \sin\left(\omega_{\mathrm{t}} t - \varphi_2\right) \\ & + \frac{1}{4\omega_{\mathrm{t}}} V_{\mathrm{t}} I_{\mathrm{t}}^{*} \sin\left(2\omega_{\mathrm{t}} t - \varphi_2\right) - \frac{1}{4\omega_{\mathrm{t}}} \left(I_{\mathrm{t}}^{*}\right)^2 \left|Z_2\right| \sin\left(2\omega_{\mathrm{t}} t - 2\varphi_2 - \arg\left(Z_2\right)\right)\end{aligned} . \tag{3.49}$$

$$\begin{aligned}\Delta e_{\mathrm{el}}\left(t, I_{\mathrm{dc}_2}^{*}, I_{\mathrm{t}}^{*}, \varphi_2\right) = & +\frac{\sqrt{2}}{2\omega_{\mathrm{t}}} V_{\mathrm{t}} I_{\mathrm{dc2}}^{*} \sin\left(\omega_{\mathrm{t}} t\right) - \frac{\sqrt{2}}{2\omega_{\mathrm{t}}} I_{\mathrm{t}}^{*} I_{\mathrm{dc2}}^{*} \left|Z_2\right| \sin\left(\omega_{\mathrm{t}} t - \varphi_2 - \arg\left(Z_2\right)\right) \\ & +\frac{\sqrt{2}}{4\omega_{\mathrm{t}}} V_{\mathrm{dc}} I_{\mathrm{t}}^{*} \sin\left(\omega_{\mathrm{t}} t - \varphi_2\right) - \frac{\sqrt{2}}{4\omega_{\mathrm{t}}} R_{\mathrm{br}} I_{\mathrm{dc}}^{*} I_{\mathrm{t}}^{*} \sin\left(\omega_{\mathrm{t}} t - \varphi_2\right) \\ & + \frac{1}{4\omega_{\mathrm{t}}} V_{\mathrm{t}} I_{\mathrm{t}}^{*} \sin\left(2\omega_{\mathrm{t}} t - \varphi_2\right) - \frac{1}{4\omega_{\mathrm{t}}} \left(I_{\mathrm{t}}^{*}\right)^2 \left|Z_2\right| \sin\left(2\omega_{\mathrm{t}} t - 2\varphi_2 - \arg\left(Z_2\right)\right)\end{aligned} . \tag{3.50}$$

We use the accurate form of arm energy variation equation to design the energy reference $\mathrm{e}_{\mathrm{au}}^{*}$, and $\mathrm{e}_{\mathrm{al}}^{*}$ by adding the average nominal value e_{nom}. Equations for phase ‘b’ and phase ‘c’ have the exact same form as phase ‘a’ but they have $2\pi/3$ and $4\pi/3$ time lag respectively. On the other hand, the formula for phase ‘f’ has the additional time delay of π respect to phase ‘e’.

$$\begin{aligned}\mathrm{e}_{\mathrm{au}}^{*} &= e_{\mathrm{nom}} + \Delta e_{\mathrm{au}}\left(t, I_{\mathrm{dc1}}^{*}, I_{\mathrm{g}}^{*}, \varphi_1\right) \\ \mathrm{e}_{\mathrm{al}}^{*} &= e_{\mathrm{nom}} + \Delta e_{\mathrm{al}}\left(t, I_{\mathrm{dc1}}^{*}, I_{\mathrm{g}}^{*}, \varphi_1\right)\end{aligned} . \tag{3.51}$$

Finally, the arm reference value vector for MMC1 and MMC2 can be designed accordingly:

$$\begin{aligned}\boldsymbol{\varepsilon}_1^{*} &= \left[\mathrm{e}_{\mathrm{au}}^{*} \quad \mathrm{e}_{\mathrm{bu}}^{*} \quad \mathrm{e}_{\mathrm{cu}}^{*} \quad \mathrm{e}_{\mathrm{al}}^{*} \quad \mathrm{e}_{\mathrm{bl}}^{*} \quad \mathrm{e}_{\mathrm{cl}}^{*}\right]^{\top} \\ \boldsymbol{\varepsilon}_2^{*} &= \left[\mathrm{e}_{\mathrm{eu}}^{*} \quad \mathrm{e}_{\mathrm{fu}}^{*} \quad \mathrm{e}_{\mathrm{el}}^{*} \quad \mathrm{e}_{\mathrm{fl}}^{*}\right]^{\top}\end{aligned} . \tag{3.52}$$

3.3.2 Controller constraints design

Current constraints

Currents should be limited according to the maximum current limit in MMC or network specifications:

$$-\begin{bmatrix} i_{\mathrm{grid}}^{\max} \\ i_{\mathrm{grid}}^{\max} \\ i_{\mathrm{grid}}^{\max} \end{bmatrix} \leq \begin{bmatrix} i_{\mathrm{ga}} \\ i_{\mathrm{gb}} \\ i_{\mathrm{gc}} \end{bmatrix} \leq \begin{bmatrix} i_{\mathrm{grid}}^{\max} \\ i_{\mathrm{grid}}^{\max} \\ i_{\mathrm{grid}}^{\max} \end{bmatrix} \quad \& \quad -\begin{bmatrix} i_{\mathrm{MMC}}^{\max} \\ i_{\mathrm{MMC}}^{\max} \\ i_{\mathrm{MMC}}^{\max} \end{bmatrix} \leq \begin{bmatrix} i_{\mathrm{com,a}} \\ i_{\mathrm{com,b}} \\ i_{\mathrm{com,c}} \end{bmatrix} \leq \begin{bmatrix} i_{\mathrm{MMC}}^{\max} \\ i_{\mathrm{MMC}}^{\max} \\ i_{\mathrm{MMC}}^{\max} \end{bmatrix} . \tag{3.53}$$

$$-\begin{bmatrix} i_{\mathrm{t}}^{\max} \\ i_{\mathrm{t}}^{\max} \end{bmatrix} \leq \begin{bmatrix} i_{\mathrm{t,e}} \\ i_{\mathrm{t,f}} \end{bmatrix} \leq \begin{bmatrix} i_{\mathrm{t}}^{\max} \\ i_{\mathrm{t}}^{\max} \end{bmatrix} \quad \& \quad -\begin{bmatrix} i_{\mathrm{MMC}}^{\max} \\ i_{\mathrm{MMC}}^{\max} \end{bmatrix} \leq \begin{bmatrix} i_{\mathrm{com,e}} \\ i_{\mathrm{com,f}} \end{bmatrix} \leq \begin{bmatrix} i_{\mathrm{MMC}}^{\max} \\ i_{\mathrm{MMC}}^{\max} \end{bmatrix} . \tag{3.54}$$

Arm energy constraints

Given the maximum and minimum limits of MMC submodule capacitor voltage, the constraints for the arm energy state variables can be set as (3.55):

$$\boldsymbol{\varepsilon}_{\mathrm{br}}^{\min} \le \boldsymbol{\varepsilon}_{\mathrm{br}} \le \boldsymbol{\varepsilon}_{\mathrm{br}}^{\max}, \quad \boldsymbol{\varepsilon}_{\mathrm{br}} = \left[\varepsilon_{\mathrm{au}} \quad \varepsilon_{\mathrm{bu}} \quad \varepsilon_{\mathrm{cu}} \quad \varepsilon_{\mathrm{al}} \quad \varepsilon_{\mathrm{bl}} \quad \varepsilon_{\mathrm{cl}}\right]^{\top} \text{ or } \left[\varepsilon_{\mathrm{eu}} \quad \varepsilon_{\mathrm{fu}} \quad \varepsilon_{\mathrm{el}} \quad \varepsilon_{\mathrm{fl}}\right]^{\top}, \tag{3.55}$$

where $\boldsymbol{\varepsilon}_{\mathrm{br}}^{\min} = \frac{1}{2} N C_{\mathrm{sub}} \left(v_{\mathrm{sub}}^{\min}\right)^2 \times \mathbf{1}$, $\boldsymbol{\varepsilon}_{\mathrm{br}}^{\max} = \frac{1}{2} N C_{\mathrm{sub}} \left(v_{\mathrm{sub}}^{\max}\right)^2 \times \mathbf{1}$.

Voltage constraints

The applicable arm voltage is limited by the sum of capacitor energy. Assume the voltage of submodule capacitors in each arm are evenly balanced, then arm energy in each phase can be calculated by (3.56). So the maximum arm voltage $v_{xy}^{\max}$ must satisfy the arm voltage constraint inequalities shown in (3.58).

$$\begin{array}{l} \varepsilon_{x\mathrm{u}} = \dfrac{1}{2} \dfrac{C_{\mathrm{sub}}}{N} \left(v_{x\mathrm{u}}^{\Sigma}\right)^2, \quad v_{x\mathrm{u}}^{\Sigma} = \displaystyle\sum_{k=1}^{N} v_{x\mathrm{u},k} \\ \varepsilon_{x\mathrm{l}} = \dfrac{1}{2} \dfrac{C_{\mathrm{sub}}}{N} \left(v_{x\mathrm{l}}^{\Sigma}\right)^2, \quad v_{x\mathrm{l}}^{\Sigma} = \displaystyle\sum_{k=1}^{N} v_{x\mathrm{l},k} \end{array}, \quad x = \mathrm{a,b,c,e,f}. \tag{3.56}$$

$$v_{xy}^{\max} = \sqrt{\frac{2N\varepsilon_{xy}}{C_{\mathrm{sub}}}}, \quad x = \mathrm{a,b,c,e,f.}, \ y = \mathrm{u,l}. \tag{3.57}$$

$$0 \le \begin{bmatrix} u_{\mathrm{au}} \\ u_{\mathrm{bu}} \\ u_{\mathrm{cu}} \end{bmatrix} \le \begin{bmatrix} \sqrt{\frac{2N\varepsilon_{\mathrm{au}}}{C_{\mathrm{sub}}}} \\ \sqrt{\frac{2N\varepsilon_{\mathrm{bu}}}{C_{\mathrm{sub}}}} \\ \sqrt{\frac{2N\varepsilon_{\mathrm{cu}}}{C_{\mathrm{sub}}}} \end{bmatrix}, \quad 0 \le \begin{bmatrix} u_{\mathrm{al}} \\ u_{\mathrm{bl}} \\ u_{\mathrm{cl}} \end{bmatrix} \le \begin{bmatrix} \sqrt{\frac{2N\varepsilon_{\mathrm{al}}}{C_{\mathrm{sub}}}} \\ \sqrt{\frac{2N\varepsilon_{\mathrm{bl}}}{C_{\mathrm{sub}}}} \\ \sqrt{\frac{2N\varepsilon_{\mathrm{cl}}}{C_{\mathrm{sub}}}} \end{bmatrix}. \tag{3.58}$$

Because $u_{\mathrm{dif},x} = \frac{(-u_{x\mathrm{u}} + u_{x\mathrm{l}})}{2}$, $u_{\mathrm{com},x} = \frac{(u_{x\mathrm{u}} + u_{x\mathrm{l}})}{2}$, the inequalities for the control inputs $\boldsymbol{u}_1$ is derived as (3.59).

$$\sqrt{\frac{N}{2C_{\mathrm{sub}}}} \begin{bmatrix} -\boldsymbol{I}_{(3\times3)} & \mathbf{0}_{(3\times3)} \\ \mathbf{0}_{(3\times3)} & \mathbf{0}_{(3\times3)} \end{bmatrix} \begin{bmatrix} \sqrt{\varepsilon_{\mathrm{au}}} \\ \sqrt{\varepsilon_{\mathrm{bu}}} \\ \sqrt{\varepsilon_{\mathrm{cu}}} \\ \sqrt{\varepsilon_{\mathrm{al}}} \\ \sqrt{\varepsilon_{\mathrm{bl}}} \\ \sqrt{\varepsilon_{\mathrm{cl}}} \end{bmatrix} - \begin{bmatrix} u_{\mathrm{ga}} \\ u_{\mathrm{gb}} \\ u_{\mathrm{gc}} \\ 0.5V_{\mathrm{dc}} \\ 0.5V_{\mathrm{dc}} \\ 0.5V_{\mathrm{dc}} \end{bmatrix} \le \boldsymbol{u}_1 \le \sqrt{\frac{N}{2C_{\mathrm{sub}}}} \begin{bmatrix} \mathbf{0}_{(3\times3)} & \boldsymbol{I}_{(3\times3)} \\ \boldsymbol{I}_{(3\times3)} & \boldsymbol{I}_{(3\times3)} \end{bmatrix} \begin{bmatrix} \sqrt{\varepsilon_{\mathrm{au}}} \\ \sqrt{\varepsilon_{\mathrm{bu}}} \\ \sqrt{\varepsilon_{\mathrm{cu}}} \\ \sqrt{\varepsilon_{\mathrm{al}}} \\ \sqrt{\varepsilon_{\mathrm{bl}}} \\ \sqrt{\varepsilon_{\mathrm{cl}}} \end{bmatrix} - \begin{bmatrix} u_{\mathrm{ga}} \\ u_{\mathrm{gb}} \\ u_{\mathrm{gc}} \\ 0.5V_{\mathrm{dc}} \\ 0.5V_{\mathrm{dc}} \\ 0.5V_{\mathrm{dc}} \end{bmatrix}, \tag{3.59}$$

where $\boldsymbol{u}_1 = \left[u_{\mathrm{dif,a}} - u_{\mathrm{ga}} \quad u_{\mathrm{dif,b}} - u_{\mathrm{gb}} \quad u_{\mathrm{dif,c}} - u_{\mathrm{gc}} \quad u_{\mathrm{com,a}} - 0.5V_{\mathrm{dc}} \quad u_{\mathrm{com,b}} - 0.5V_{\mathrm{dc}} \quad u_{\mathrm{com,c}} - 0.5V_{\mathrm{dc}}\right]^{\top}$. Clearly the square root operation of arm energy is nonlinear which is not compatible with the linear controller approach. As illustrated in Figure 3.5, the feasible region is under the power function $\sqrt{\frac{2N\varepsilon_{xy}}{C_{\mathrm{sub}}}}$ and the nonlinear boundary is approximated by two line function f_1,f_2. By choosing the correct interpo-

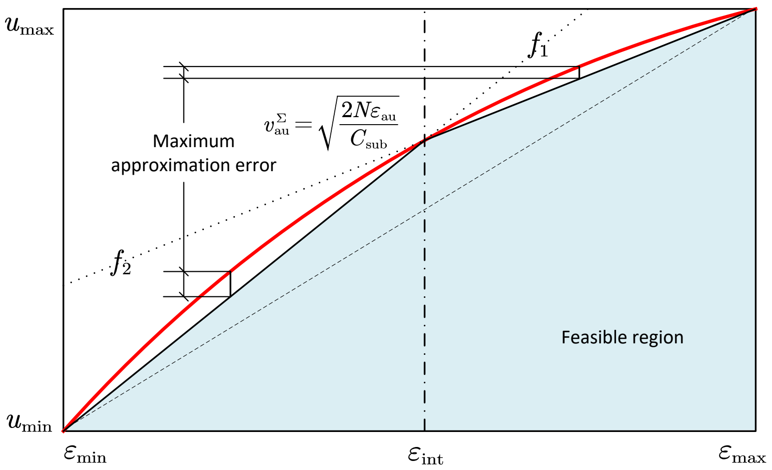

Fig. 3.5 Linear approximation of voltage constraints

lation point $\varepsilon_{\mathrm{int}}$, the approximation error can be less than 1%. So each nonlinear constraint inequality is converted to two linear inequalities in (3.60).

$$\begin{aligned} f_1(\boldsymbol{\varepsilon}) &= \left(\sqrt{\varepsilon_{\min}} - \left(\frac{\sqrt{\varepsilon_{\min}} - \sqrt{\varepsilon_{\mathrm{int}}}}{\varepsilon_{\min} - \varepsilon_{\mathrm{int}}}\right)\varepsilon_{\min}\right) + \left(\frac{\sqrt{\varepsilon_{\min}} - \sqrt{\varepsilon_{\mathrm{int}}}}{\varepsilon_{\min} - \varepsilon_{\mathrm{int}}}\right)\boldsymbol{\varepsilon}, \\ f_2(\boldsymbol{\varepsilon}) &= \left(\sqrt{\varepsilon_{\mathrm{int}}} - \left(\frac{\sqrt{\varepsilon_{\max}} - \sqrt{\varepsilon_{\mathrm{int}}}}{\varepsilon_{\max} - \varepsilon_{\mathrm{int}}}\right)\varepsilon_{\mathrm{int}}\right) + \left(\frac{\sqrt{\varepsilon_{\max}} - \sqrt{\varepsilon_{\mathrm{int}}}}{\varepsilon_{\max} - \varepsilon_{\mathrm{int}}}\right)\boldsymbol{\varepsilon} \end{aligned}, \tag{3.60}$$

where $\varepsilon_{\min}$ is the minimal arm energy; $\varepsilon_{\max}$ is the maximal arm energy; $\varepsilon_{\mathrm{int}}$ is the interpolation point between the max and min energy values. And $\boldsymbol{\varepsilon}$ is the arm energy vector. The control action constraints for MMC1 and MMC2 are approximated by these linear functions f_1 and f_2 as shown below.

$$\sqrt{\frac{N}{2C_{\mathrm{sub}}}}\begin{bmatrix} -\boldsymbol{I}_{3\times3} & \boldsymbol{0}_{3\times3} \\ \boldsymbol{0}_{3\times3} & \boldsymbol{0}_{3\times3} \end{bmatrix} f_{1,2}\left(\begin{bmatrix} \varepsilon_{\mathrm{au}} \\ \varepsilon_{\mathrm{bu}} \\ \varepsilon_{\mathrm{cu}} \\ \varepsilon_{\mathrm{al}} \\ \varepsilon_{\mathrm{bl}} \\ \varepsilon_{\mathrm{cl}} \end{bmatrix}\right) + \begin{bmatrix} u_{\mathrm{ga}} \\ u_{\mathrm{gb}} \\ u_{\mathrm{gc}} \\ 0.5V_{\mathrm{dc}} \\ 0.5V_{\mathrm{dc}} \\ 0.5V_{\mathrm{dc}} \end{bmatrix} \leq \boldsymbol{u}_1 \leq \sqrt{\frac{N}{2C_{\mathrm{sub}}}}\begin{bmatrix} \boldsymbol{0}_{3\times3} & \boldsymbol{I}_{3\times3} \\ \boldsymbol{I}_{3\times3} & \boldsymbol{I}_{3\times3} \end{bmatrix} f_{1,2}\left(\begin{bmatrix} \varepsilon_{\mathrm{au}} \\ \varepsilon_{\mathrm{bu}} \\ \varepsilon_{\mathrm{cu}} \\ \varepsilon_{\mathrm{al}} \\ \varepsilon_{\mathrm{bl}} \\ \varepsilon_{\mathrm{cl}} \end{bmatrix}\right) - \begin{bmatrix} u_{\mathrm{ga}} \\ u_{\mathrm{gb}} \\ u_{\mathrm{gc}} \\ 0.5V_{\mathrm{dc}} \\ 0.5V_{\mathrm{dc}} \\ 0.5V_{\mathrm{dc}} \end{bmatrix} \tag{3.61}$$

$$\sqrt{\frac{N}{2C_{\mathrm{sub}}}}\begin{bmatrix} -\boldsymbol{I}_{2\times2} & \boldsymbol{0}_{2\times2} \\ \boldsymbol{0}_{2\times2} & \boldsymbol{0}_{2\times2} \end{bmatrix} f_{1,2}\left(\begin{bmatrix} \varepsilon_{\mathrm{eu}} \\ \varepsilon_{\mathrm{fu}} \\ \varepsilon_{\mathrm{el}} \\ \varepsilon_{\mathrm{fl}} \end{bmatrix}\right) + \begin{bmatrix} u_{\mathrm{t,e}} \\ u_{\mathrm{t,f}} \\ 0.5V_{\mathrm{dc}} \\ 0.5V_{\mathrm{dc}} \end{bmatrix} \leq \boldsymbol{u}_2 \leq \sqrt{\frac{N}{2C_{\mathrm{sub}}}}\begin{bmatrix} \boldsymbol{0}_{2\times2} & \boldsymbol{I}_{2\times2} \\ \boldsymbol{I}_{2\times2} & \boldsymbol{I}_{2\times2} \end{bmatrix} f_{1,2}\left(\begin{bmatrix} \varepsilon_{\mathrm{eu}} \\ \varepsilon_{\mathrm{fu}} \\ \varepsilon_{\mathrm{el}} \\ \varepsilon_{\mathrm{fl}} \end{bmatrix}\right) - \begin{bmatrix} u_{\mathrm{t,e}} \\ u_{\mathrm{t,f}} \\ 0.5V_{\mathrm{dc}} \\ 0.5V_{\mathrm{dc}} \end{bmatrix} \tag{3.62}$$

3.3.3 Cost function design

A typical cost function for MPC with horizon length N_{h} is used and is formulated in (3.63):

$$\min_{\boldsymbol{U}_k} \sum_{l=0}^{N_{\mathrm{h}}-1} \left(\boldsymbol{x}_{k+l+1} - \boldsymbol{x}^*_{k+l}\right)^T \boldsymbol{Q} \left(\boldsymbol{x}_{k+l+1} - \boldsymbol{x}^*_{k+l}\right) + \left(\boldsymbol{u}_{k+l} - \boldsymbol{u}^*_{k+l}\right)^T \boldsymbol{R} \left(\boldsymbol{u}_{k+l} - \boldsymbol{u}^*_{k+l}\right). \tag{3.63}$$

where matrix $\boldsymbol{Q}$ and $\boldsymbol{R}$ define weighting factors for state and control variables respectively.

$$\boldsymbol{Q} = \begin{bmatrix} \boldsymbol{\lambda}_{ig} & \boldsymbol{0}_{3\times3} & \boldsymbol{0}_{3\times6} \\ \boldsymbol{0}_{3\times3} & \boldsymbol{\lambda}_{i\mathrm{dc}1} & \boldsymbol{0}_{3\times6} \\ \boldsymbol{0}_{6\times3} & \boldsymbol{0}_{6\times3} & \boldsymbol{\lambda}_{\varepsilon1} \end{bmatrix}, \quad \boldsymbol{\lambda}_{ig} = \lambda_{ig}\boldsymbol{I}_{3\times3}, \boldsymbol{\lambda}_{i\mathrm{dc}1} = \lambda_{i\mathrm{dc}1}\boldsymbol{I}_{3\times3}, \boldsymbol{\lambda}_{\varepsilon1} = \lambda_{\varepsilon1}\boldsymbol{I}_{6\times6} \tag{3.64}$$

$$\boldsymbol{R} = \begin{bmatrix} \boldsymbol{\lambda}_{u\mathrm{dif}1} & \boldsymbol{0}_{3\times3} \\ \boldsymbol{0}_{3\times3} & \boldsymbol{\lambda}_{u\mathrm{com}1} \end{bmatrix}, \quad \boldsymbol{\lambda}_{u\mathrm{dif}1} = \lambda_{\mathrm{udif}1}\boldsymbol{I}_{3\times3}, \boldsymbol{\lambda}_{u\mathrm{com}1} = \lambda_{u\mathrm{com}1}\boldsymbol{I}_{3\times3} \tag{3.65}$$

Obviously $\boldsymbol{Q}$ is a 12 by 12 diagonal matrix for MMC1 and is 8 by 8 for MMC2. $\boldsymbol{R}$ is 8 by 8 diagonal matrix for MMC1 and 4 by 4 for MMC2.

3.4 Simulation and discussion

3.4.1 MPC model setup for simulation

Discretization and approximation

Given a continuous system (3.66), a discrete time state space model (3.67) can be created by zero hold approximation.

$$\frac{\mathrm{d}}{\mathrm{d}t}\boldsymbol{x}(t) = \boldsymbol{A}_{\mathrm{C}}\boldsymbol{x}(t) + \boldsymbol{B}_{\mathrm{C}}\boldsymbol{u}(t). \tag{3.66}$$

$$\boldsymbol{x}(k+1) = \boldsymbol{A}_{\mathrm{d}}\boldsymbol{x}(k) + \boldsymbol{B}_{\mathrm{d}}\boldsymbol{u}(k). \tag{3.67}$$

The matrices in the discrete model can be calculated by $\boldsymbol{A}_{\mathrm{d}} = e^{\boldsymbol{A}_{\mathrm{C}}T_{\mathrm{sc}}}$, $\boldsymbol{A}_{\mathrm{C}}\boldsymbol{B}_{\mathrm{d}} = -\left(\boldsymbol{I} - \boldsymbol{A}_{\mathrm{d}}\right)\boldsymbol{B}_{\mathrm{C}}$ where T_{sc} is the sampling time. The forward Euler approximation is often sufficiently accurate for short sampling intervals of up to several tens of microseconds in combination with short prediction horizons. In this way, the discrete time system matrices are approximated by (3.68).

$$\boldsymbol{A}_{\mathrm{d}} = \boldsymbol{I} + \boldsymbol{A}_{\mathrm{C}}T_{\mathrm{sc}}, \quad \boldsymbol{A}_{\mathrm{C}}\boldsymbol{B}_{\mathrm{d}} = \boldsymbol{B}_{\mathrm{C}}T_{\mathrm{sc}}. \tag{3.68}$$

Note that the MMC system model is time varying, the system matrix of arm energy $\boldsymbol{A}_{\varepsilon1}\left(u^*_{\mathrm{com}}, u^*_{\mathrm{dif}}\right)$ and $\boldsymbol{A}_{\varepsilon2}\left(u^*_{\mathrm{com}}, u^*_{\mathrm{dif}}\right)$ change with control inputs which contain the sinusoidal voltage and variable DC voltage signals. So, the model needs to be updated at each sample time according to the measurements and estimated control values. At the time t the grid voltage is sampled, and the control action is implemented at $t+T_{\mathrm{sc}}$. To increase the model accuracy for grid voltage approximation in ZOH method, an averaged value u'_{ga} is the used in the controller during sample period.

$$u'_{\mathrm{ga}} = \frac{\sqrt{2}}{\sqrt{3}}\frac{V_g}{T_{sc}}\int_0^{T_{\mathrm{sc}}} \cos\left(\omega_{\mathrm{g}}t + \omega_{\mathrm{g}}\tau\right)\,\mathrm{d}\tau = \frac{\sqrt{2}}{\sqrt{3}}V_g\frac{\sin\left(\omega_{\mathrm{g}}t + \omega_{\mathrm{g}}T_{\mathrm{sc}}\right) - \sin\left(\omega_{\mathrm{g}}t\right)}{\omega_{\mathrm{g}}T_{sc}}, \tag{3.69}$$

where T_{sc} is the controller sampling time. Similarly, other sinusoidal waves can be approximated in the same way.

MPC transformation for QP solver

To solve the MPC problem, the model, constraints and cost functions are transformed into the linear quadratic programming standard form given in (3.70):

$$\begin{aligned} \underset{\boldsymbol{x}}{\text{minimise}} \quad & J = \frac{1}{2}\boldsymbol{x}^T\boldsymbol{H}\boldsymbol{x} + \boldsymbol{f}^T\boldsymbol{x} \\ \text{subject to} \quad & \boldsymbol{A}\boldsymbol{x} \le \boldsymbol{b} \\ & \boldsymbol{A}_{\mathrm{eq}} = \boldsymbol{b}_{\mathrm{eq}} \end{aligned} \tag{3.70}$$

Setting a control horizon N_{h}, the state vector for the long horizon MPC problem is $\boldsymbol{X}_k$ and control sequence of $\boldsymbol{U}_k$ is shown below.

$$\boldsymbol{X}_k = [\boldsymbol{x}_{k+1} \quad \boldsymbol{x}_{k+2} \quad \boldsymbol{x}_{k+3} \quad \cdots \quad \boldsymbol{x}_{k+N_{\mathrm{h}}-1} \quad \boldsymbol{x}_{k+N_{\mathrm{h}}}]^{\top} \tag{3.71}$$

$$\boldsymbol{U}_k = [\boldsymbol{u}_k \quad \boldsymbol{u}_{k+1} \quad \boldsymbol{u}_{k+2} \quad \cdots \quad \boldsymbol{u}_{k+N_{\mathrm{h}}-2} \quad \boldsymbol{u}_{k+N_{\mathrm{h}}-1}]^{\top} \tag{3.72}$$

As mentioned above, this system has time-varying dynamics, the system matrix for arm energy changes according to external terminal voltage and control references. Denote the system matrix at time step $k+l$ is $\boldsymbol{A}_l$, so the predicted system states at each time step from $k+1$ to $k+N_{\mathrm{h}}$ can be updated by (3.73).

$$\begin{aligned} \boldsymbol{x}_{k+1} &= \boldsymbol{A}_1\boldsymbol{x}_k + \boldsymbol{B}\boldsymbol{u}_k \\ \boldsymbol{x}_{k+2} &= \boldsymbol{A}_2\boldsymbol{A}_1\boldsymbol{x}_k + \boldsymbol{A}_2\boldsymbol{B}\boldsymbol{u}_k + \boldsymbol{B}\boldsymbol{u}_{k+1} \\ \boldsymbol{x}_{k+3} &= \boldsymbol{A}_3\boldsymbol{A}_2\boldsymbol{A}_1\boldsymbol{x}_k + \boldsymbol{A}_3\boldsymbol{A}_2\boldsymbol{B}\boldsymbol{u}_k + \boldsymbol{A}_3\boldsymbol{B}\boldsymbol{u}_{k+1} + \boldsymbol{B}\boldsymbol{u}_{k+2} \\ &\cdots \end{aligned} \tag{3.73}$$

Therefore, a new state space model (3.74) can be obtained:

$$\boldsymbol{X}_k = \boldsymbol{A}_{tx}\boldsymbol{x}_k + \boldsymbol{B}_{tx}\boldsymbol{U}_k \tag{3.74}$$

where state transition matrices $\boldsymbol{A}_{tx}$ and $\boldsymbol{B}_{tx}$ can be calculated in advance using the information of pre-calculated grid voltage, and control references in (3.75). The cost function defined in (3.63) is rewritten into canonical form for QP solver in (3.76).

$$\boldsymbol{A}_{tx}=\begin{bmatrix}\boldsymbol{A}_1\\ \boldsymbol{A}_2\boldsymbol{A}_1\\ \boldsymbol{A}_3\boldsymbol{A}_2\boldsymbol{A}_1\\ \vdots\\ \boldsymbol{A}_{N-1}\times\cdots\times\boldsymbol{A}_1\\ \boldsymbol{A}_N\times\cdots\times\boldsymbol{A}_1\end{bmatrix},\boldsymbol{B}_{tx}=\begin{bmatrix}\boldsymbol{B} & \boldsymbol{0} & \boldsymbol{0} & \cdots & \boldsymbol{0} & \boldsymbol{0}\\ \boldsymbol{A}_2\boldsymbol{B} & \boldsymbol{B} & \boldsymbol{0} & \cdots & \boldsymbol{0} & \boldsymbol{0}\\ \boldsymbol{A}_3\boldsymbol{A}_2\boldsymbol{B} & \boldsymbol{A}_3\boldsymbol{B} & \boldsymbol{B} & \cdots & \boldsymbol{0} & \boldsymbol{0}\\ \vdots & \vdots & \vdots & \ddots & \vdots & \vdots\\ \boldsymbol{A}_{N-1}\times\cdots\times\boldsymbol{A}_2\boldsymbol{B} & \boldsymbol{A}_{N-1}\times\cdots\times\boldsymbol{A}_3\boldsymbol{B} & \boldsymbol{A}_{N-1}\times\cdots\times\boldsymbol{A}_4\boldsymbol{B} & \cdots & \boldsymbol{B} & \boldsymbol{0}\\ \boldsymbol{A}_N\times\cdots\times\boldsymbol{A}_2\boldsymbol{B} & \boldsymbol{A}_N\times\cdots\times\boldsymbol{A}_3\boldsymbol{B} & \boldsymbol{A}_N\times\cdots\times\boldsymbol{A}_4 & \cdots & \boldsymbol{A}_N\boldsymbol{B} & \boldsymbol{B}\end{bmatrix} \tag{3.75}$$

$$\begin{aligned}&\min_{\boldsymbol{U}_k}\left(\boldsymbol{X}_k-\boldsymbol{X}_k^*\right)^\top\boldsymbol{Q}\left(\boldsymbol{X}_k-\boldsymbol{X}_k^*\right)+\left(\boldsymbol{U}_k-\boldsymbol{U}_k^*\right)^\top\boldsymbol{R}\left(\boldsymbol{U}_k-\boldsymbol{U}_k^*\right)\\ \Rightarrow&\min_{\boldsymbol{U}_k}\left(\boldsymbol{B}_{tx}\boldsymbol{U}_k+\left(\boldsymbol{A}_{tx}\boldsymbol{x}_k-\boldsymbol{X}_k^*\right)\right)^\top\boldsymbol{Q}\left(\boldsymbol{B}_{tx}\boldsymbol{U}_k+\left(\boldsymbol{A}_{tx}\boldsymbol{x}_k-\boldsymbol{X}_k^*\right)\right)+\left(\boldsymbol{U}_k-\boldsymbol{U}_k^*\right)^T\boldsymbol{R}\left(\boldsymbol{U}_k-\boldsymbol{U}_k^*\right)\\ \Rightarrow&\min_{\boldsymbol{U}_k}\frac{1}{2}\boldsymbol{U}_k{}^\top\boldsymbol{H}\boldsymbol{U}_k+\boldsymbol{f}^\top\boldsymbol{U},\quad \boldsymbol{H}=\boldsymbol{B}_{tx}^\top\boldsymbol{Q}\boldsymbol{B}_{tx}+\boldsymbol{R},\ \boldsymbol{f}^\top=\left(\boldsymbol{A}_{tx}\boldsymbol{x}_k-\boldsymbol{X}_k^*\right)^\top\boldsymbol{Q}\boldsymbol{B}_{tx}-\left(\boldsymbol{U}_k^*\right)^\top\boldsymbol{R}\end{aligned} \tag{3.76}$$

The state constraints are also converted into (3.77).

$$\begin{bmatrix}\boldsymbol{B}_{\text{tx}}\\ -\boldsymbol{B}_{\text{tx}}\end{bmatrix}\boldsymbol{U}_k\leq\begin{bmatrix}\left(\boldsymbol{X}_{\max}-\boldsymbol{A}_{tx}\boldsymbol{x}_k\right)\\ -\left(\boldsymbol{X}_{\min}-\boldsymbol{A}_{tx}\boldsymbol{x}_k\right)\end{bmatrix}, \tag{3.77}$$

where the vector $\boldsymbol{X}_{\max}$ and $\boldsymbol{X}_{\min}$ are composed by repeating constraint vectors as shown in (3.78).

$$\boldsymbol{X}_{\max}=\begin{bmatrix}\boldsymbol{x}_{k+1,\max}\\ \boldsymbol{x}_{k+2,\max}\\ \vdots\\ \boldsymbol{x}_{k+N_\text{h},\max}\end{bmatrix},\boldsymbol{X}_{\min}=\begin{bmatrix}\boldsymbol{x}_{k+1,\min}\\ \boldsymbol{x}_{k+2,\min}\\ \vdots\\ \boldsymbol{x}_{k+N_\text{h},\min}\end{bmatrix};\quad \boldsymbol{x}_{k+l,\max}=\begin{bmatrix}\boldsymbol{i}_{\text{grid}}^{\max}\\ \boldsymbol{i}_{\text{MMC}}^{\max}\\ \boldsymbol{\varepsilon}_{\text{br}}^{\max}\end{bmatrix},\boldsymbol{x}_{k+l,\min}=\begin{bmatrix}-\boldsymbol{i}_{\text{grid}}^{\max}\\ -\boldsymbol{i}_{\text{MMC}}^{\max}\\ \boldsymbol{\varepsilon}_{\text{br}}^{\min}\end{bmatrix},l=1,2\cdots N_h. \tag{3.78}$$

The inequality of long horizon voltage control input constraints (3.59) compatible for QP solver are (3.79) to (3.81) where two linear functions are used to approximate the nonlinear voltage constraints via arm capacitors' energy.

$$\begin{aligned}&-\left(\boldsymbol{I}+k_{f_{1,2}}\sqrt{\frac{N}{2C_\text{sub}}}\underbrace{\begin{bmatrix}\boldsymbol{E}_1 & & \\ & \ddots & \\ & & \boldsymbol{E}_1\end{bmatrix}}_{N_\text{h}}\underbrace{\begin{bmatrix}\boldsymbol{E}_2 & & \\ & \ddots & \\ & & \boldsymbol{E}_2\end{bmatrix}}_{N_\text{h}}\boldsymbol{B}_{tx}\right)\boldsymbol{U}_k\leq\sqrt{\frac{N}{2C_\text{sub}}}\underbrace{\begin{bmatrix}\boldsymbol{E}_1 & & \\ & \ddots & \\ & & \boldsymbol{E}_1\end{bmatrix}}_{N_\text{h}}\left(k_{f_{1,2}}\underbrace{\begin{bmatrix}\boldsymbol{E}_2 & & \\ & \ddots & \\ & & \boldsymbol{E}_2\end{bmatrix}}_{N_\text{h}}\boldsymbol{A}_{tx}\boldsymbol{X}_k+b_{f_{1,2}}\right)+\begin{bmatrix}\boldsymbol{u}_{\text{ext},k+1}\\ \boldsymbol{u}_{\text{ext},k+2}\\ \vdots\\ \boldsymbol{u}_{\text{ext},k+N_\text{h}}\end{bmatrix}\\ &\left(\boldsymbol{I}-k_{f_{1,2}}\sqrt{\frac{N}{2C_\text{sub}}}\underbrace{\begin{bmatrix}\boldsymbol{E}_3 & & \\ & \ddots & \\ & & \boldsymbol{E}_3\end{bmatrix}}_{N_\text{h}}\underbrace{\begin{bmatrix}\boldsymbol{E}_2 & & \\ & \ddots & \\ & & \boldsymbol{E}_2\end{bmatrix}}_{N_\text{h}}\boldsymbol{B}_{tx}\right)\boldsymbol{U}_k\leq\sqrt{\frac{N}{2C_\text{sub}}}\underbrace{\begin{bmatrix}\boldsymbol{E}_3 & & \\ & \ddots & \\ & & \boldsymbol{E}_3\end{bmatrix}}_{N_\text{h}}\left(k_{f_{1,2}}\underbrace{\begin{bmatrix}\boldsymbol{E}_2 & & \\ & \ddots & \\ & & \boldsymbol{E}_2\end{bmatrix}}_{N_\text{h}}\boldsymbol{A}_{tx}\boldsymbol{X}_k+b_{f_{1,2}}\right)-\begin{bmatrix}\boldsymbol{u}_{\text{ext},k+1}\\ \boldsymbol{u}_{\text{ext},k+2}\\ \vdots\\ \boldsymbol{u}_{\text{ext},k+N_\text{h}}\end{bmatrix}\end{aligned} \tag{3.79}$$

$$\boldsymbol{u}_{\text{ext},k+l}=\begin{bmatrix}u_\text{ga}(k+l) & u_\text{gb}(k+l) & u_\text{gc}(k+l) & 0.5V_\text{dc} & 0.5V_\text{dc} & 0.5V_\text{dc}\end{bmatrix}^\top,\boldsymbol{E}_1=\begin{bmatrix}\boldsymbol{I}_{3\times3} & \boldsymbol{0}_{3\times3}\\ \boldsymbol{0}_{3\times3} & \boldsymbol{0}_{3\times3}\end{bmatrix},\boldsymbol{E}_2=\begin{bmatrix}\boldsymbol{0}_{6\times6} & \boldsymbol{I}_{6\times6}\end{bmatrix},\boldsymbol{E}_3=\begin{bmatrix}\boldsymbol{0}_{3\times3} & \boldsymbol{I}_{3\times3}\\ \boldsymbol{I}_{3\times3} & \boldsymbol{I}_{3\times3}\end{bmatrix} \tag{3.80}$$

$$k_{f1}=\sqrt{\varepsilon_\text{min}}-\frac{\sqrt{\varepsilon_\text{min}}-\sqrt{\varepsilon_\text{int}}}{\varepsilon_\text{min}-\varepsilon_\text{int}}\varepsilon_\text{min},\ b_{f1}=\frac{\sqrt{\varepsilon_\text{min}}-\sqrt{\varepsilon_\text{int}}}{\varepsilon_\text{min}-\varepsilon_\text{int}};\quad k_{f2}=\sqrt{\varepsilon_\text{int}}-\frac{\sqrt{\varepsilon_\text{max}}-\sqrt{\varepsilon_\text{int}}}{\varepsilon_\text{max}-\varepsilon_\text{int}}\varepsilon_\text{int},\ b_{f2}=\frac{\sqrt{\varepsilon_\text{max}}-\sqrt{\varepsilon_\text{int}}}{\varepsilon_\text{max}-\varepsilon_\text{int}} \tag{3.81}$$

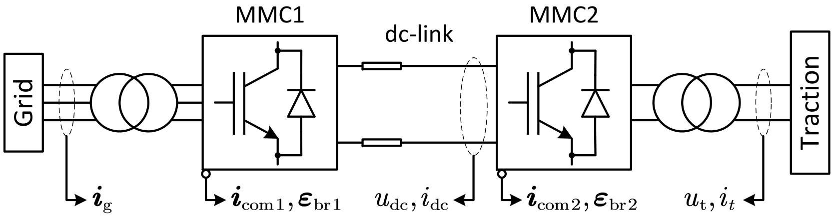

Fig. 3.6 Essential measurements of B2B MMC substation

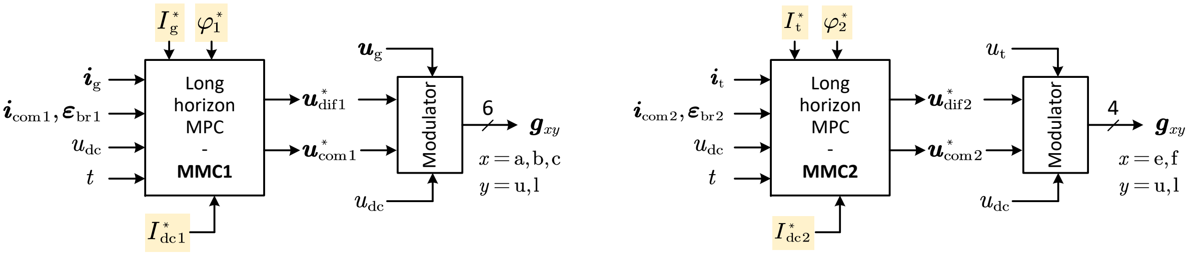

Fig. 3.7 Inner loop control scheme for B2B MMC substation: grid side (left), traction side (right)

Modelling using MATLAB Simulink

To solve the quadratic problem formulated above, the active-set QP solver is implemented in the Simulink environment where at each sample time T_{sc}, system model, cost function and constraints are formulated based on measurements, designed reference and horizon length N_{h}. Then only the first set of the optimised control sequences is implemented on MMC, and the active inequality information is passed to the next iteration to realise a warm start to speed up the computation process.

3.4.2 Control scheme for back to back converter

The MPC controller designed in the above section controls MMC internal state to track any given reference with the minimal error. This means that the outer control loop which is responsible for current reference design is still necessary. The system diagram and measurements is illustrated in Figure 3.6. Two MPC controllers take in the designed reference values and essential measurements as input and solve the optimal arm voltage control reference. Then a modulator converts the arm voltage command into switching patterns for each submodule. This MPC internal control scheme is shown in Figure 3.7.

The required highlighted reference values are calculated by outer loop controllers and the schemes of them are explained in Figure 3.8 and Figure 3.9. The traction side MMC2 supplies the railway network with a fixed magnitude 50 Hz voltage. Current references I_{t}^{*}, φ_{2}^{*} are generated by PI controllers based on the voltage magnitude and phase measurements. The reference $I_{\mathrm{dc}2}^{*}$ represents the required active power from DC-link and it is calculated to support traction network (by (3.35)) and to compensate internal energy error.

At the grid side MMC, DC-link voltage is stabilised by PI controller which converts voltage error into additional DC current reference $\delta_{i\mathrm{dc}}$. Combining the DC current requirement $I_{\mathrm{dc}2}^{*}$ at the traction

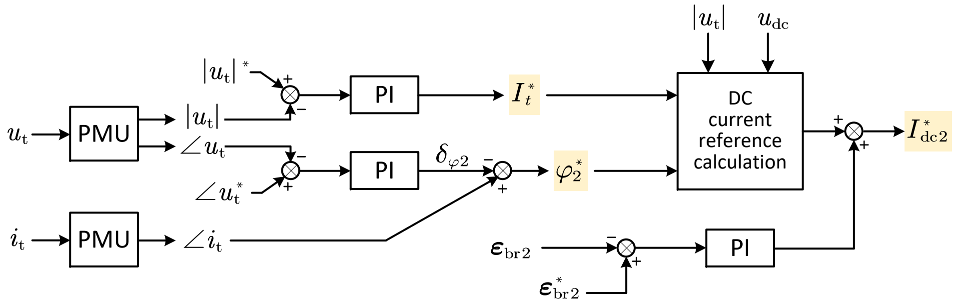

Fig. 3.8 Outer loop control scheme for traction side MMC

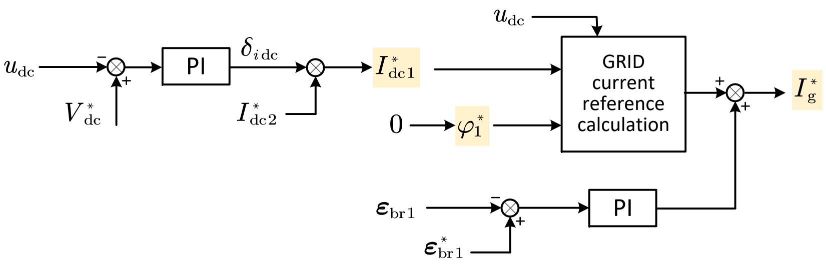

Fig. 3.9 Outer loop control scheme for grid side MMC

side, the DC current reference for MMC1 is designed as $I_{\text{dc1}}^* = -I_{\text{dc2}}^* - \delta_{i\text{dc}}$. This DC current reference is transformed into AC side reference by (3.33). This required DC side energy as well as the energy to compensate internal energy error is provided through grid connection. Note that, by convention, the grid current should be in-phase with the voltage. Therefore, the grid current reference signal I_{g}^*, φ_1^* are obtained.

3.4.3 Grid side three phase MMC

Firstly, the grid side three phase MMC is tested in current tracking performance. To test the proposed MPC, the system is set to invert a steady 10 MW from DC-link to the grid and then follows a step change to -10 MW in reverse at 1 s. Figure 3.10 shows the DC-link current tracking and common mode current tracking in each phase. The DC side current can follow a step change with almost no delay but suffers some oscillation after step change. The overshoot reaches 9 A (9.76%) in the DC link and the oscillation becomes less than 1% of the reference value after 3 cycles (0.06 s).

Figure 3.11 plots the grid current response to the -10 MW to 10 MW power change at the grid side[1] at 1 s. The result shows that all three phase currents can be reversed within less than $\frac{1}{4}$ cycle's time which proofs a fast grid current response. After the power change, the averaged arm capacitor voltages (Figure 3.12) has maximum 11% deviation from the nominal value and converges to less than 5% deviation after 0.1 s. Though the capacitor voltage performance is slower than the current tracking,

---

[1] Due to the definition of current direction, the sign of power flowing from grid side to DC-link side is opposite.

Table 3.1 B2B MMC simulation parameter

Grid			
Grid voltage (ph-ph)	66 kV (50 Hz)	Rated phase current	250 A
Inductance	1 mH	Resistance	1 Ω
MMC			
DC link voltage	120 kV	Rated power	20 MW
Submodule capacitance	1 mF	Number of submodule per arm	50
Arm resistance	1	Arm inductance	18.5 mH
DC link resistance	20 Ω	DC link inductance	1.4 μH
Traction network			
Network voltage	25 kV	Rated current	400 A
Resistance	1 Ω	Inductance	1 mH
Controller parameters			
Controller sampling time	200 μs	Model sampling time	5 μs
MPC weighting factor $[\lambda_{iac}, \lambda_{idc}, \lambda_{\varepsilon}, \lambda_{udif}, \lambda_{ucom}]$		[7.5, 1.5, 1, 0.001, 0.01]	

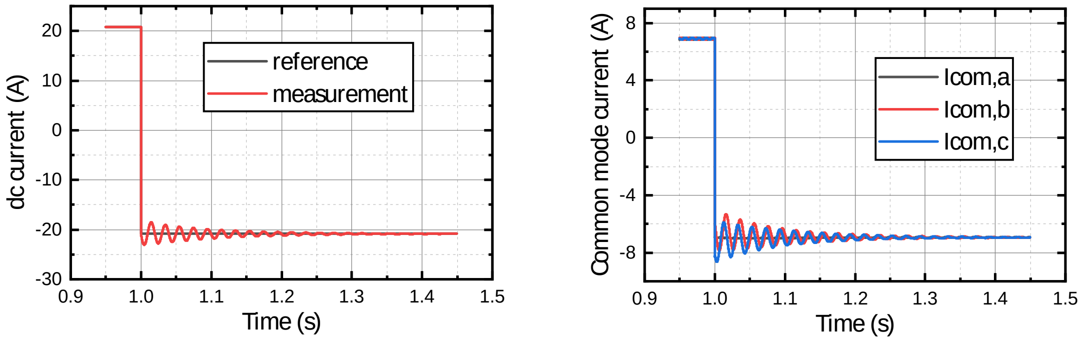

(a) DC-link current

(b) Common mode current

Fig. 3.10 Three phase MMC DC current tracking

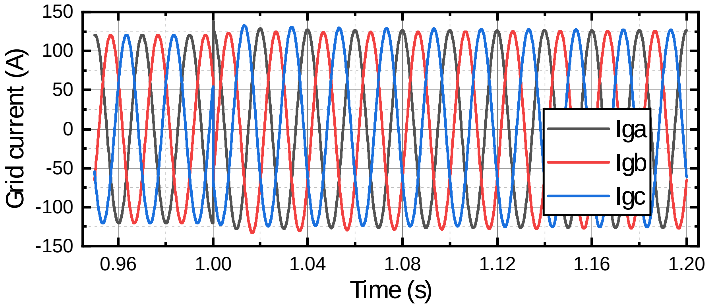

Fig. 3.11 Three phase MMC grid current tracking (10 MW step change at 1 s)

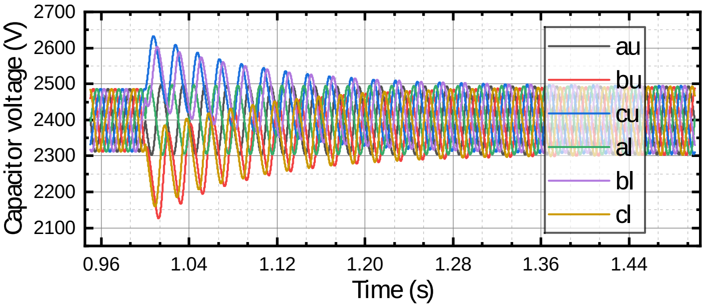

Fig. 3.12 Three phase MMC averaged capacitor voltage value of each arm

the voltage deviation is symmetric to the nominal value showing that the total energy stored in the whole MMC system is well maintained.

The controlled system state variables have achieved good steady state reference tracking performance. The grid currents follow the symmetric sinusoidal references; common mode currents are almost ideal DC component and arm energy values are varying in the optimal pattern. Four figures in 3.13 present the steady state performance (data logged 1 s after the step change) and all these state variables have less than 0.5% error[2].

---

[2] AC currents are normalised by the reference magnitude and; Common mode currents are normalised by DC current reference value and the energy values are normalised by the nominal arm energy value.

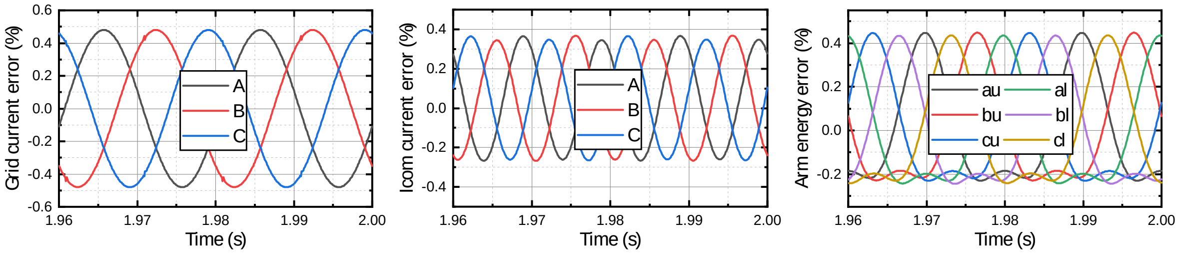

(a) I_g tracking error (b) i_{com} tracking error (c) ε_C tracking error

Fig. 3.13 Three phase MMC steady state tracking error

Table 3.2 The instantaneous power exchange in MMC arms

Horizon length	Maximum number of iterations	Averaged number of iterations in 1/4 cycle	Number of inequality constraints	Number of optimisation variables
2	3	1.16	96	12
3	5	1.28	144	18
4	7	1.4	192	24
5	8	1.44	240	30
6	10	1.52	288	36
7	10	1.48	336	42
8	10	1.44	384	48
9	10	1.4	432	54
10	10	1.4	480	60
11	10	1.4	528	66
12	10	1.4	576	72
13	10	1.4	624	78
14	10	1.4	672	84
15	10	1.4	720	90

Discussion on MPC horizon length

The above MPC test results use 10 sampling time steps as the MPC prediction horizon length. A long horizon length might bring faster convergence speed but also much heavier computational cost.

The number of optimisation variables (manipulated variable) is $6N_\mathrm{h}$ and the number of inequalities is $48N_\mathrm{h}$. The computational cost in each iteration increases in a polynomial way. However, the increasing number of constraints in long horizon MPC also increases the difficulty in searching for the feasible solution. Table 3.2 lists out the simulation result of the computational cost within 5 ms after the step load change. When horizon length is short ($N_\mathrm{h} = 2, 3$) even at the greatest step load change, only 3 to 5 iterations are required to get a feasible optimal result. And the averaged number of iteration is less than 1.3. But when horizon length is greater than 5, it takes 10 iterations to calculate the feasible optimal result. Note that for long horizon settings, not only the number of iteration cycles is greater than short ones, but the problem size also get multiplied.

Nevertheless, increasing MPC horizon length appropriately is beneficial to response speed. Figure 3.14a shows the grid current THD analysis result where one cycle is sampled after the step change and the greatest THD among three phase currents is chosen. MPC with longer horizon length can achieve low THD grid current with less time. Note that this pattern only holds true when $N_\mathrm{h} \leq 12$, because if horizon become too long, the modelling error becomes more significant and actually degrades the performance. Figure 3.14b compares the required time to reach less than 0.5% tracking error in each MPC with different horizon length . Obviously, the longer horizon length has faster response, but the effect gradually wears off even the computational cost keeps increasing.

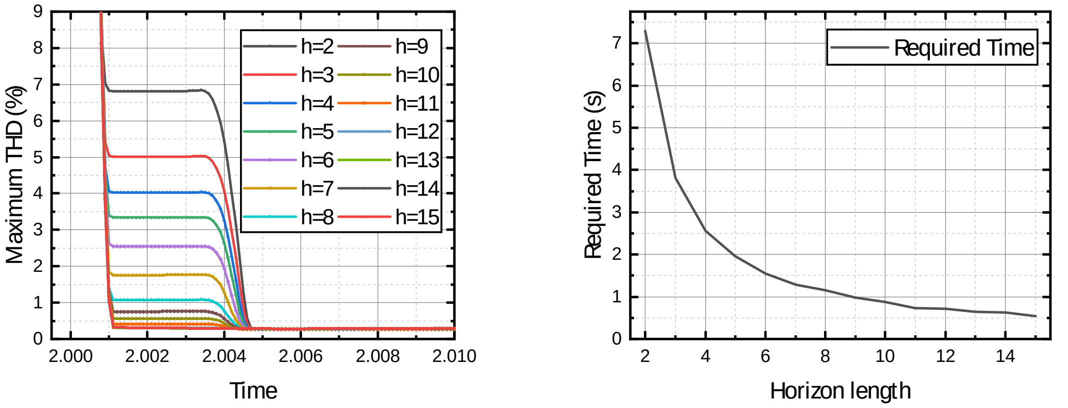

(a) Grid current THD (one cycle sampling)

(b) Required time to reach <0.5% tracking error

Fig. 3.14 Comparison of horizon length influence on controller performance

Performance comparison with other control approaches

The MPC control scheme is compared with traditional cascaded linear controller (PI) approach (see Appendix A) and deadbeat controller (see Appendix B)[3]. The power change from $-20\,\text{MW}$ to $20\,\text{MW}$ at 2s. Grid current, DC-link current and the capacitor voltage performance are required in the following three figures. In the following three performance comparison figures (Figure 3.15, 3.16, 3.17). In each set of figure, different subfigures' representation is explained as follows:

- Subfigure (a) shows the result of MPC approach with 2-step horizon length.
- Subfigure (b) shows the result of MPC approach with 12-step horizon length.
- Subfigure (c) shows the result of conventional cascaded linear controller approach (PI, PR controllers are used in the control scheme explained in Figure A.4).
- Subfigure (d) shows the result of a set of deadbeat controller.

Figure 3.15 compares the grid current tracking performance. It takes PI control approach $3/4$ cycle time to achieve good symmetric sinusoidal current waveform after the step change. The MPC with horizon 2 and deadbeat controller shows similar faster response that after $1/4$ cycle, the current is welled controlled and the result of deadbeat is observed with a bit less distortion. MPC having long horizon ($N_\text{h} = 12$) exhibits the finest result that not only the current can immediately be reversed one step after the reference change but a well smooth sinusoidal wave is preserved even within the first quarter cycle (5 ms).

As discussed in Section A.2 multi-objectives are controlled by DC side current including energy balance between phases, energy balance between arms and circulating current suppression. Therefore, unlike the grid current tracking[4], the DC current reference is a combination of multiple control references generated based on energy/voltage errors.

---

[3] Because controllers other than MPC cannot handle coupling effect at DC-link impedance, R_dc and L_dc are ignored in the comparison

[4] Grid side current references are simply three phase current which only have 50 Hz component.

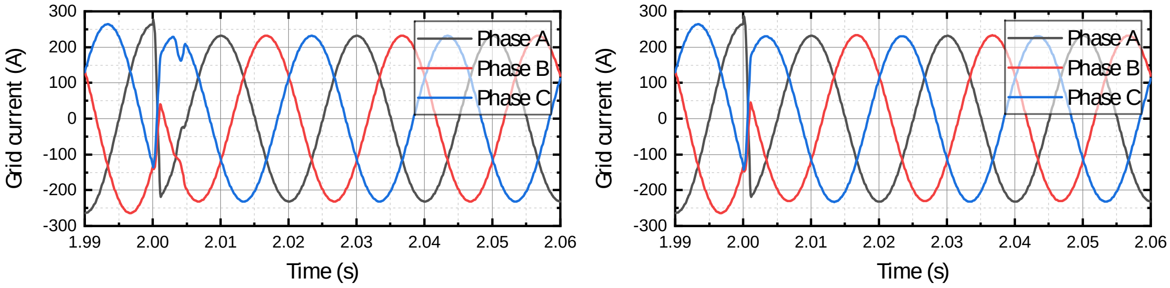

(a) MPC $N_\mathrm{h} = 2$ (b) MPC $N_\mathrm{h} = 12$

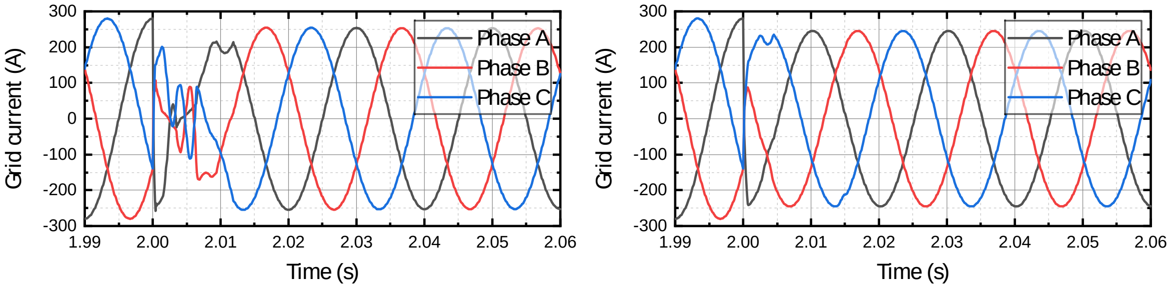

(c) Cascaded linear controller (d) Deadbeat controller

Fig. 3.15 Three phase grid current comparison

Figure 3.16 compares the DC-link current tracking performance and Figure 3.17 compares the capacitor voltage control performance. Both the linear and deadbeat controller get big overshoot and long settling time. This is because the DC side current reference is designed to achieve fast capacitor voltage control. Even the DC-link current is sacrificed for a better capacitor voltage regulation, the maximum voltage deviation is greater than MPC results, because the capacitor energy are set as constraints in the MPC approach. Additionally, in MPC results the energy stored in the capacitors are well maintained as the voltage deviations in different arms are symmetric to the nominal value.

Both in long and short horizon length MPC simulations, the overshoots and responses in DC-link current tracking are better than the other two methods. We can reduce the gain or set saturation in the energy controller to alleviate the overshoot in the linear and deadbeat controllers however this will also slow the capacitor voltage regulation. Because the DC current control and arm energy control are coupled in these controllers and the exact energy dynamic is not accurately modelled. It is difficult to achieve a balanced result in conventional approach.

Sensitivity analysis on MMC branch parameter variation

The result shown above is based on accurate modelling of the MMC system. In the ideal case, the model predictive controller has the correct parameter as the actual hardware. However, parameter mismatch can happen in the practical applications. Figure 3.18 shows current tracking error when the MMC branch inductance and resistance vary from 0.5 to 3 times of the nominal value. Thanks to the feedback principle of the predictive control, even large parameter mismatch exists, the controlled system is still

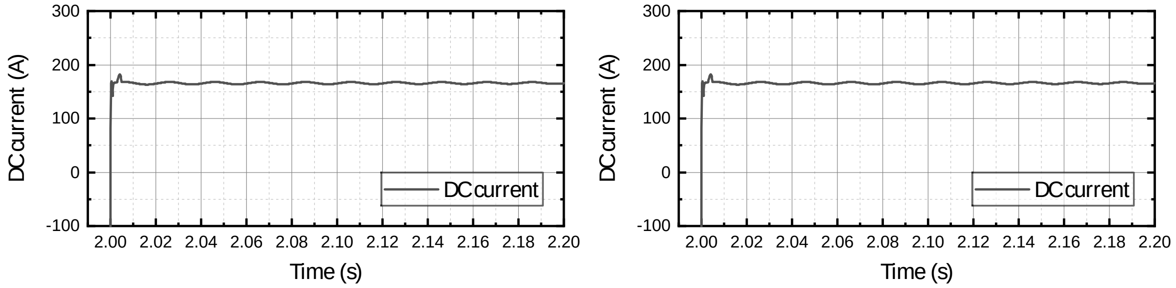

(a) MPC $N_h = 2$ (b) MPC $N_h = 10$

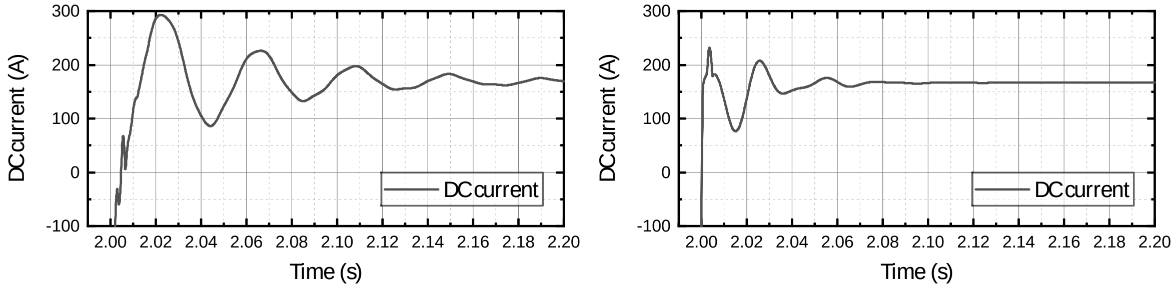

(c) Cascaded linear controller (d) Deadbeat controller

Fig. 3.16 DC-link current comparison

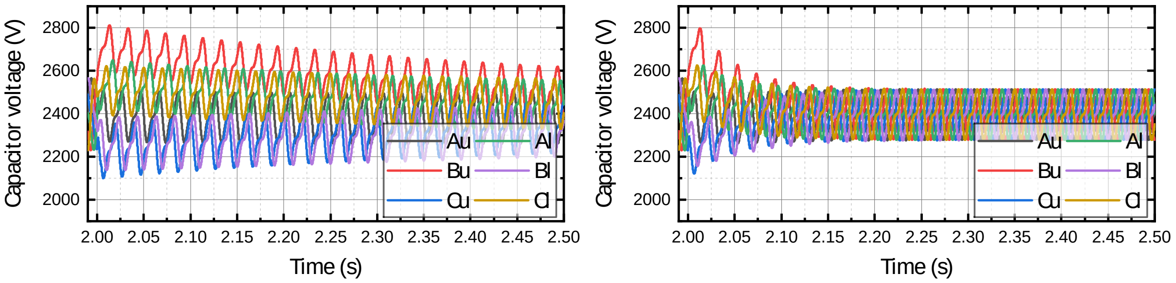

(a) MPC $N_h = 2$ (b) MPC $N_h = 10$

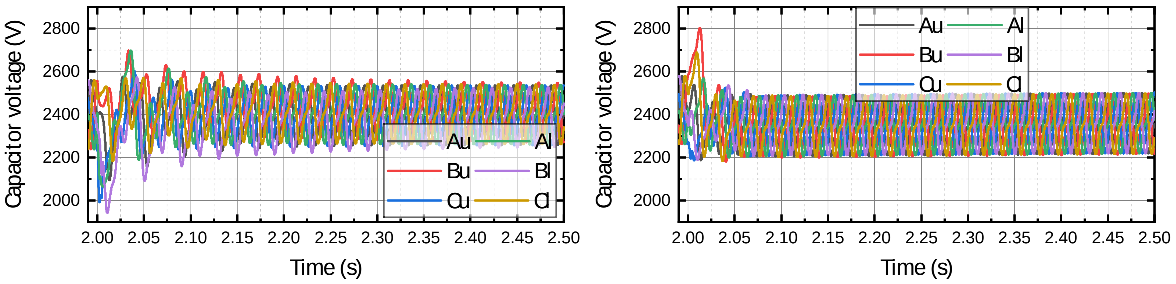

(c) Cascaded linear controller (d) Deadbeat controller

Fig. 3.17 Arm capacitor voltage comparison

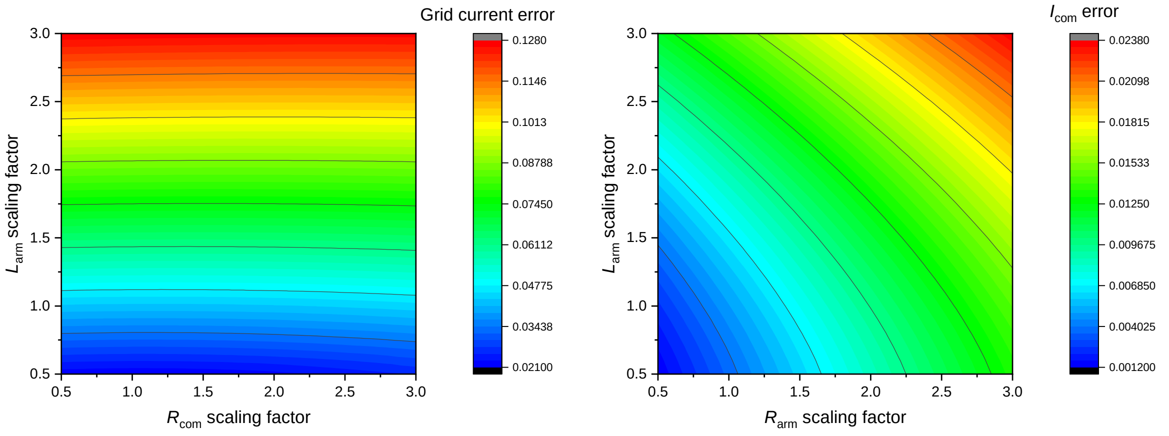

(a) Grid current AC tracking maximum error (b) Common mode DC current tracking maximum error

Fig. 3.18 Parameter variation influence on steady state current tracking error

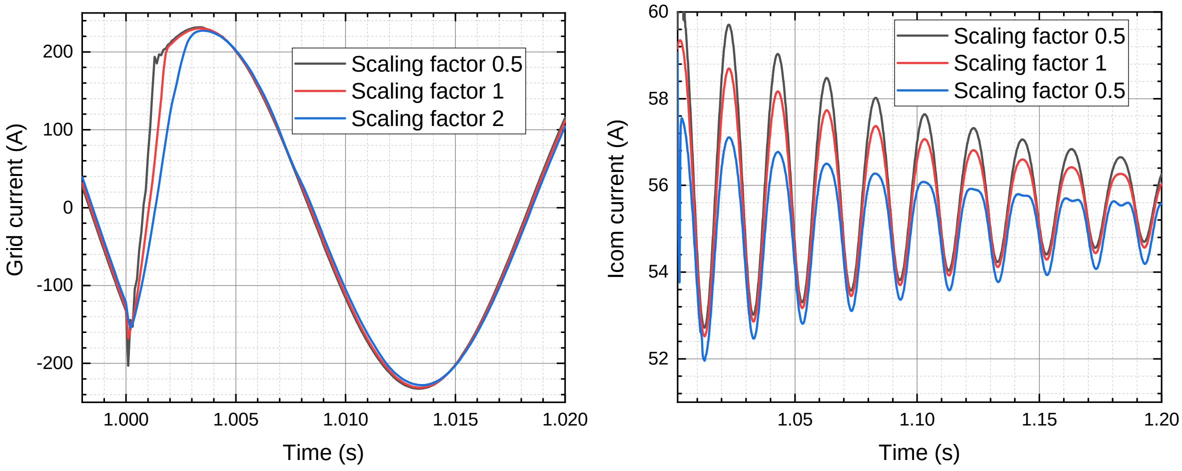

(a) Grid current tracking error (phase C) (b) Common mode dc current tracking error (phase C)

Fig. 3.19 Parameter variation influence on transient current tracking error

stable. It can be seen that the parameter mismatch in the inductance value affects both grid side AC current tracking and DC side current tracking while the resistance value variation shows little influence on the AC side current. In general, the greater branch line impedance varies, the greater the error exists in the steady state. However, when the actual impedance becomes less than the nominal value, the steady state error is actually reduced. Because this type of parameter mismatch results in a higher gain in the feedback control loop which contribute to a smaller tracking error.

Figure 3.19 shows the comparison in the transient power reversal condition where the impedance of each MMC branch has been scaled to 50% and 200%. When the actual impedance is larger than the value used in the controller, the system responses slower in the power reversal change. In the 50% scaling factor case, although the system gain is larger which contributes to less steady state errors, the overshoot becomes greater in the transient result.

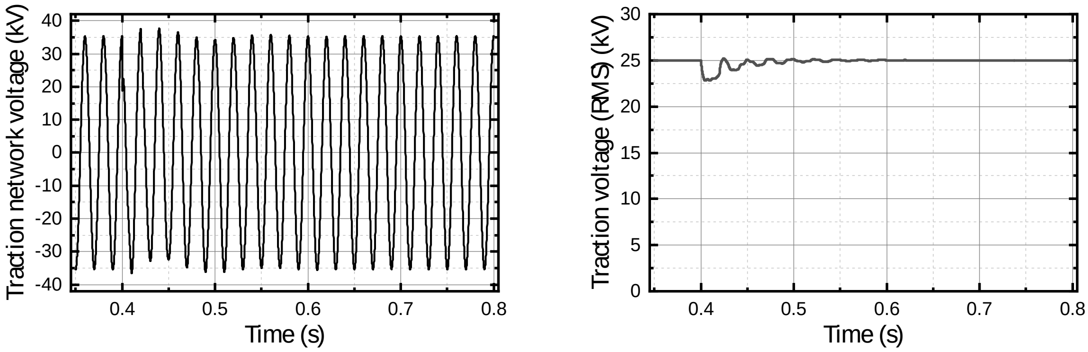

(a) Instantaneous measurement (b) RMS value

Fig. 3.20 Traction network voltage (10 MW load change at 0.4 s)

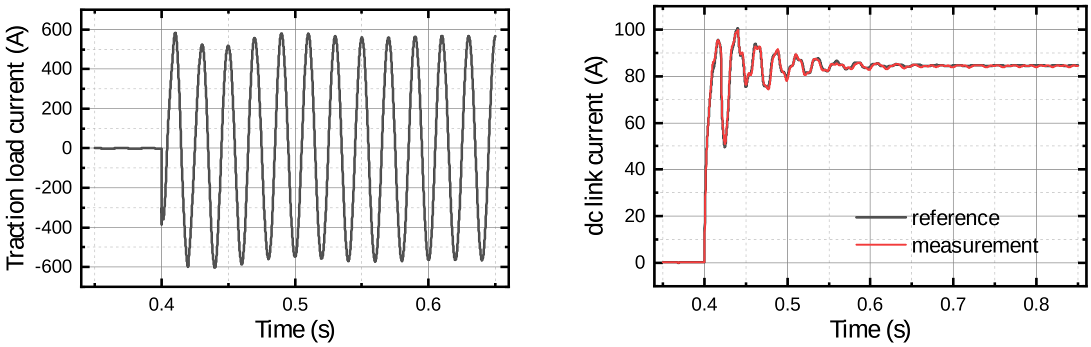

(a) Instantaneous traction network current (b) DC-link current

Fig. 3.21 Single phase MMC current tracking (10 MW load change at 0.4 s)

3.4.4 Traction side single phase MMC

For the traction side MMC2 test, a step of resistive load of 10 MW is connected at the single phase MMC side at 0.4 s. The single phase MMC is controlled to keep the network voltage at 25 kV. It can be seen from Figure 3.20 that after the step load change, the RMS value of traction voltage drops to 91.2% of the nominal value and restores to less than 5% deviation after 20 ms. The steady state error is negligible.

Figure 3.21 shows the current measured at the traction network and DC-link. There is almost no delay in current tracking after the load is connected. The DC-link current has 17.2% overshoot and takes 10 ms to settle to less than 5% error. After another 20 ms, the DC-link has less than 2% error. Note that this transient performance is mainly dominated by the outer loop controller rather than the MPC itself. In the steady state, there exists a small oscillated AC component in the DC-link current — a peak to peak value of the AC component is 0.51% of the DC reference value.

The averaged arm energy has 10% deviation from the nominal value when the step change starts (which is about 4.9% deviation in voltage perspective as shown in Figure 3.22). After two cycles' time (0.04 s) the energy error can be reduced to less than 5% (2.5% deviation in voltage).

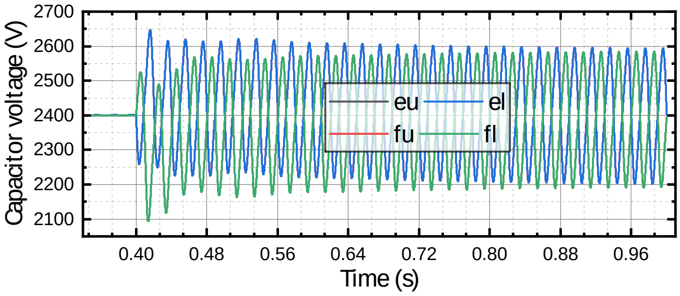

Fig. 3.22 Singe phase MMC capacitor voltage (10 MW load change at 0.4 s)

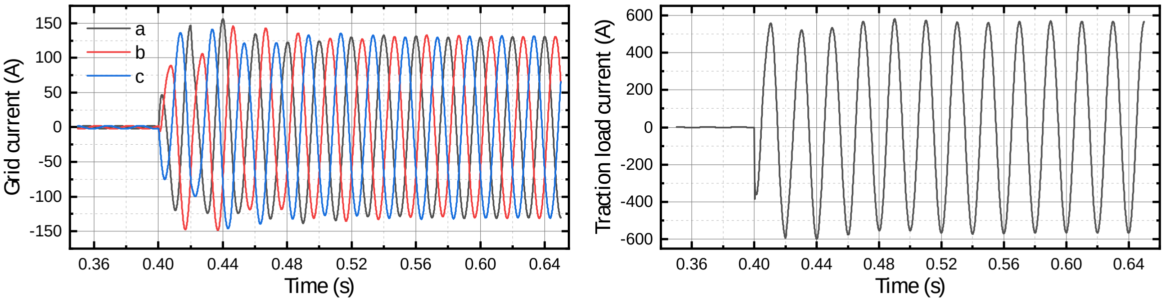

(a) Three phase grid current

(b) Traction network current

Fig. 3.23 B2B-MMC current performance (10 MW step change)

3.4.5 B2B MMC system

Combining the control scheme in Figure 3.9 and Figure 3.8, the two converters are connected as a back to back converter. The three phase MMC1 is controlled to support the DC-link and single phase MMC2 operates as an inverter to support the network as previously discussed. Note that in the proposed control scheme, the DC current reference generated for MMC2 will be fed to MMC1 controller side as feedforward term to improve the transient response.

The MPC controlled back to back conversion system enjoys superb DC link voltage stability even with 10 MW step load at the traction side (at 0.4 s). There is only 0.5% dip in DC-link voltage and 0.33% overshoot. After 0.5 s, only a tiny amount of AC component exists in DC voltage (peak to peak value is 0.0708% of the DC voltage reference).

However, in the B2B system because the current reference is updated from PI controllers, some oscillations exist in the DC-link current after load change. In Figure 3.24b, we can observe that the MPC successfully tracks the DC current reference well. But due to the outer controller, even after 0.1 s there exists small oscillations of about 5% of the DC reference value. The AC component in the steady state DC current is about 0.64% of the reference (peak to peak value).

The arm energy balancing results are almost identical to previous one side converter tests. In the grid MMC1, the maximum energy difference is 5% (in voltage) and can be reduced to less than 5% within three cycles. After 0.2s, the energy error is less than 3%. The arm energy performance of MMC2 is the same as previous results. Although both MMC1 and MMC2 deliver 10 MW power, due to the

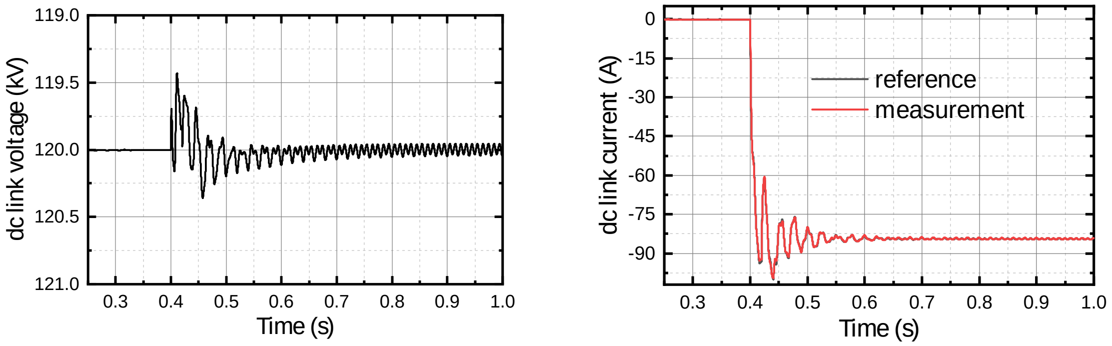

(a) DC-link voltage

(b) DC-link current

Fig. 3.24 B2B-MMC DC-link measurement

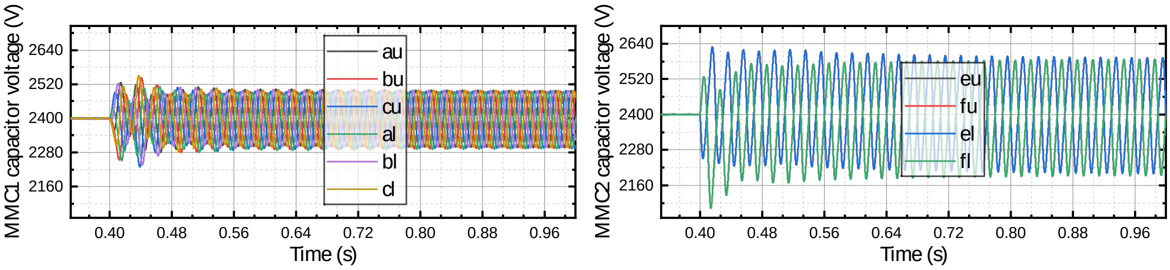

(a) Capacitor voltage of MMC1

(b) Capacitor voltage of MMC2

Fig. 3.25 Averaged submodule capacitor voltage in each arm of B2B-MMC system power flow direction and terminal voltage value, MMC2 exhibits greater voltage variation range than MMC1. It is possible to adopt different design parameters in both sides such as considering the number of submodules, submodule capacitance and terminal voltage level for reliability and cost optimisation.

3.5 Summary

Most of MPC schemes designed for MMC only implement one-step prediction horizon. In this chapter, a long horizon MPC which takes the internal arm energy into consideration is developed for B2B MMC railway feeder stations.

Having the receding horizon feature, the proposed MPC for B2B MMC substation has faster transient response, shorter settling time than cascaded PI controller and deadbeat approach. It is also shown that a slight increase of prediction horizon reduces convergence time after step reference change. Thanks to the external modulator, this approach also has good steady state performance. The parameter variation result shows that this control approach can maintain good results even the branch impedance has large variations.

In this modelling approach, the energy state is directly controlled and predicted within the MPC. An external balancing control loop is no longer required. This provides the possibility to accurately use most of the capacitor energy with less chance of over modulation.

As for future work, different back to back control methods can be further applied to this modelling approach.

Chapter 4

Modular multilevel converter with renewable energy generation integration

4.1 Overview of renewable energy generation integration in railway power supply

The landscape change of the energy sector for embracing significant renewable penetration has made the electrified railway an environmentally more friendly means of transportation than on-road vehicles and air transport. The AC power supply scheme is the most consolidated technology which enjoys popularity in current high-speed railway applications, and the 25 kV single phase ac power supply scheme is widely adopted in the traction power supply system (TPSS) in many countries such as Japan, China, UK and France etc. However, most of the existing 25 kV AC supply feeder stations are realised by conventional transformers which lead to several power quality issues such as voltage unbalance, low power factor and harmonics issues. Various compensation schemes and balanced transformers have been researched and implemented in railway systems to improve the power quality [13].

The successful application of power electronic converter not only improves the power quality but also facilitates a more flexible power supply system for the future electrical railway system (ERS). In the past decades, some pioneering work has been carried out to verify the feasibility of integrating renewable energy source (RES) and energy storage system (ESS) into ERS. The European Union initiated the MERLIN project [87] to achieve a more sustainable and optimised energy usage in European electric mainline railway system in 2012. Japanese researchers demonstrated the potential of using photovoltaic (PV) panels on platform roofs and railway premises to introduce the solar power into the ERS in 2013 [88]. Zero emission operation has been achieved in a local ‘Hiraizumi Station’ with solar energy generation and lithium-ion batteries [89].

To improve the energy efficiency, the East Japan Railway Company also studied the economic benefit of the dc railway regenerative energy utilisation by energy storage system [90]. In [91], PV generation with hybrid ESS is connected to the cophase traction power system for coordinating regenerative braking energy and local renewable energy, and energy management strategy is optimised to achieve the lowest daily cost. Şengör et al. also presented a mixed-integer programming model to minimise the daily operational cost of a similar system [92] where the model considers the dynamics of train load, pricing scheme, stochastic nature of state of energy (SOE) and uncertain PV generation. Zhu et al. [93] used passivity-based stability criterion to assess the stability of a PV plant tied into a medium voltage dc railway electrification system, and proposed a virtual impedance control scheme.

Railway power supply integrated with RESs and hybrid ESSs relies heavily on the ICT technologies to operate reliably, effectively and efficiently. Therefore, researchers have considered the next generation of ERS to be a smart railway system, where information and communication technologies are used to improve the overall controllability. Eduardo et al. discussed key features in a smart railway system, including 'smart train operation', 'smart operation of railway power supply', and 'smart interaction with other power systems' [87].

Aguado et al. proposed a methodology for optimal operation planning of railway energy systems considering the uncertainties associated to RES through scenario tree approach [94]. Hovak et al. presented a hierarchical coordination scheme for substation energy flow control and the individual traction control, and used a stationary energy storage system to minimise energy consumption [95]. Through interactions with other power systems, the ERS is transformed from a passive energy consumer into a proactive system which has the capability to respond to various grid demands. Sun et al. evaluated the impact of battery based railway transportation on power grid operation [96], and demonstrated that the mobile battery storage can relieve the transmission congestion while reduce the operation costs.

Most of the research works mainly focus on RES and ESS installation capacity and power flow optimisation. The accurate system dynamics in medium voltage ac railway supply system with RES integration has not been fully investigated. Renewable energy such as wind and solar energy are intermittent and cannot be accurately predicted. Similarly, the traction load has similar characteristics due to rail condition, carrying weight, weather and other factors. Unlike the conventional transformer based station, the power electronic converter based station needs to be controlled in real time to transfer the energy among the grid, RES and the train. The intermittent renewable energy generation and rapid changing train load will impose more stringent requirements on the converter performance.

The instantaneous power consumed by the single phase traction load introduces double frequency oscillation into the supply system [97]. The existence of sudden load change, intermittent renewable generation and oscillating single phase power challenge the stable operation of the hybrid railway power supply system.

In this chapter, a full power modular multilevel converter solution is proposed for railway traction power supply integrated with RES. The aforementioned problems of single phase oscillation and high power change are addressed by utilising floating capacitor in the MMC.

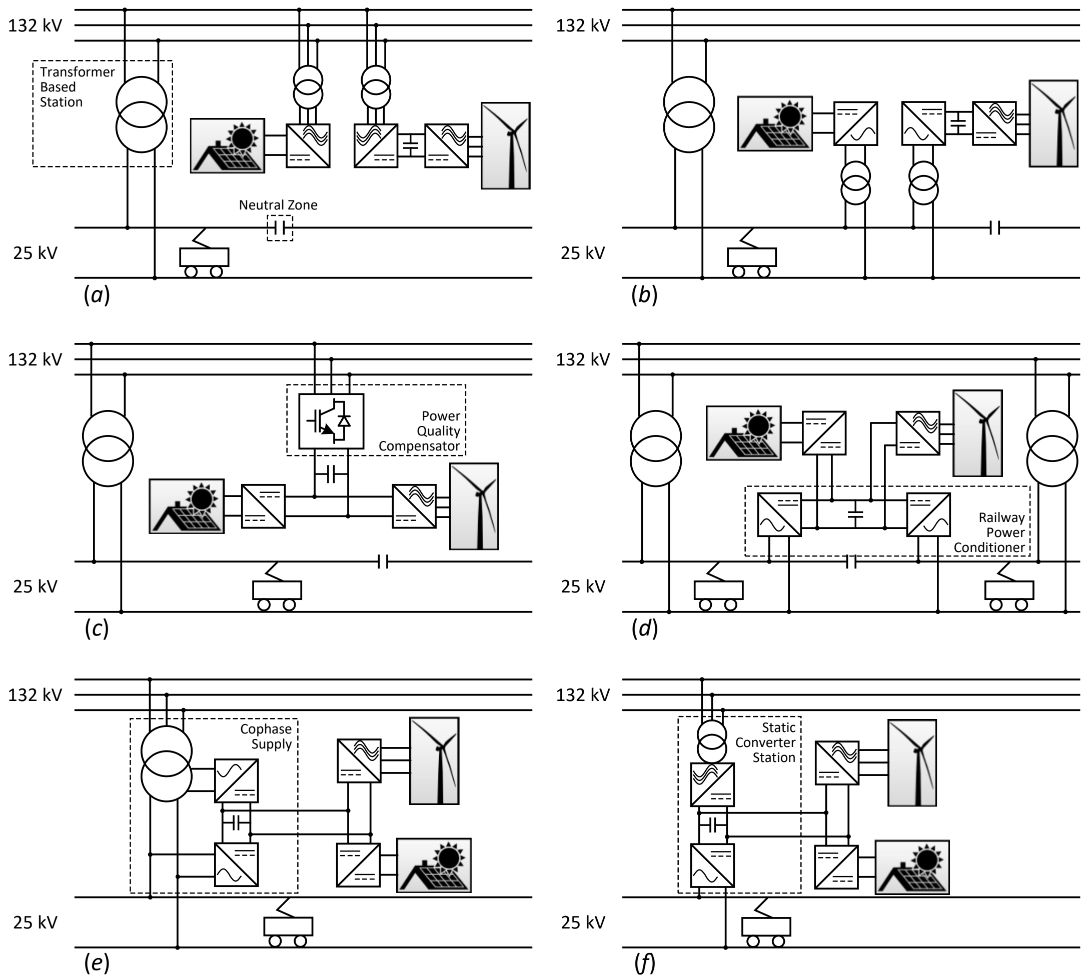

Fig. 4.1 Different connection schemes for integrating renewable energy source into railway supply system. (a) RES interfaced with high voltage distribution grid. (b) RES interfaced with medium voltage 25 kV overhead line. (c) RES interfaced with power grid compensator. (d) RES interfaced with railway power conditioner. (e) RES interfaced with cophase supply conditioner. (f) RES interfaced with static converter based station

4.2 Modelling and control of DC link coupled wind power generation substations

4.2.1 System topology and operation

Overview of different RES connection strategies

Six different configurations with RES integrated into railway traction supply system are illustrated in Fig. 4.1. Configurations presented in Figures 4.1a and 4.1b do not need any modification in the original stations, RES is directly connected to the power grid or traction overheadline. These two configurations are typical in conventional smart grid and their design and control are studied in [98].

Figures 4.1c and 4.1d represent the scenarios where the RES is connected to the grid side power quality compensator or railway power conditioner so that the dc/ac converter required in Fig. 4.1a,4.1b are cancelled. Both compensator and conditioner are responsible for addressing the power quality issues due to traction load. The power generated by RES will be used to balance grid current or compensate power flow between two supply arms. RES rating is limited by the conditioner capacity which is usually a portion of the feeder station. [99] analysed a multi-port railway power conditioner of Fig. 4.1d.

Configurations in Figures 4.1e,4.1f integrate the renewable generation into the station. Cophase connection with RES complicates the system design but provides more flexible control for traction supply because the number of neutral zone can be reduced or eliminated. Liu et al. investigated the energy management for this connection scheme [91].

Topologies presented in Fig. 4.1a–4.1e can be used regardless of the feeder station configuration. Due to the distinctive benefits of SFC based substation [100], configurations illustrated in Fig. 4.1f are investigated in this chapter, where RES are connected to the medium DC voltage link of the back to back converter. Railway feeder stations usually have power rating from 10 MW to 80 MW, so this topology has the capacity to accept more renewable generations than configurations illustrated in Fig. 4.1c–4.1e.

The proposed static converter station integrated with wind power generation

Figure 4.2 presents the equivalent diagram of a proposed supply system. MMC back to back converter is used to convert three phase voltage power into a single phase. As illustrated in Fig. 4.3, the MMC on the grid side is denoted as $\mathrm{MMC_G}$ and MMC connected to the traction overhead line is denoted as $\mathrm{MMC_L}$. The wind turbine generator (WTG) system brings power P_{W} into the DC-link, and the power flow of $\mathrm{MMC_G}$ denoted as P_{G} can be controlled in bi-direction depending on the DC-link voltage. P_{L} denotes traction side power and is delivered by $\mathrm{MMC_L}$.

The range of power flowing into or out of the grid (P_{G}) is determined by wind power, train load and regenerative efficiency. Generally regeneration power will be less than 80% of the maximum traction power, so we can define the power rating of $\mathrm{MMC_G}$ as:

$$\begin{aligned} &\max(P_{\mathrm{G}}^{+}) \geq P_{\mathrm{L}}^{\max} \\ &\min(P_{\mathrm{G}}^{-}) \leq -(0.8P_{\mathrm{L}}^{\max} + P_{\mathrm{W}}^{\max}) \end{aligned}, \tag{4.1}$$

where P_{G}^{+} denotes power flowing from the grid to DC-link via $\mathrm{MMC_G}$, P_{G}^{-} denotes power from DC-link back to the grid via $\mathrm{MMC_G}$, $P_{\mathrm{L}}^{\max}$ and $P_{\mathrm{W}}^{\max}$ denote the maximum wind power generation and traction load power respectively. However, if extra ESS is included in this system, then more wind power can be accepted without increase $\mathrm{MMC_G}$'s power rating. Different power flow patterns and the symbol definition are illustrated in Fig. 4.3. Based on the energy conservation law, the following equation (ignoring the energy inside inductors) can be derived:

$$\int_{t_1}^{t_2} (P_{\mathrm{W}} + P_{\mathrm{G}} - P_{\mathrm{L}})\,\mathrm{d}t = \sum \frac{C_{\mathrm{sub}}\left[{u_{\mathrm{C}}^{i}}^{2}(t_2) - {u_{\mathrm{C}}^{i}}^{2}(t_1)\right]}{2}, \tag{4.2}$$

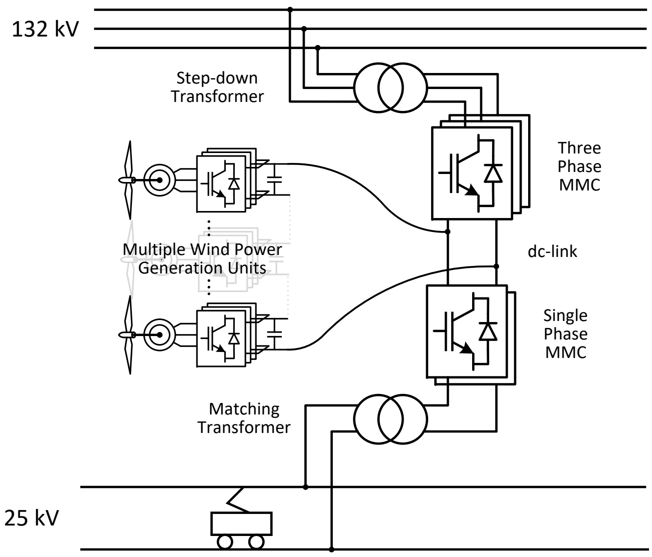

Fig. 4.2 Configuration of a wind power connection into static converter based railway substation

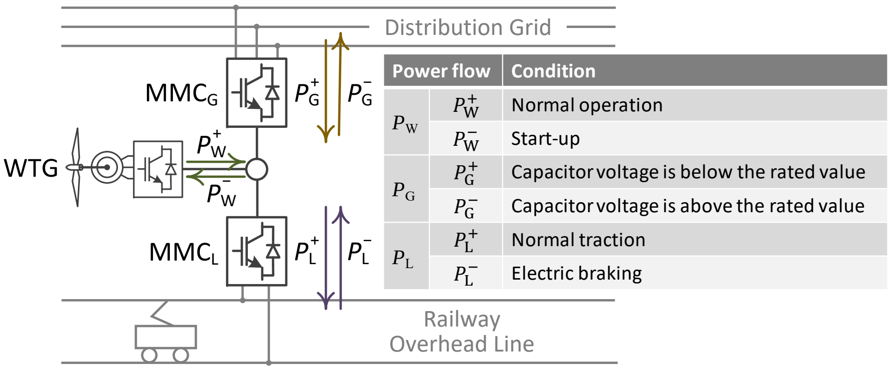

Power flow		Condition
P_W	P_W^+	Normal operation
	P_W^-	Start-up
P_G	P_G^+	Capacitor voltage is below the rated value
	P_G^-	Capacitor voltage is above the rated value
P_L	P_L^+	Normal traction
	P_L^-	Electric braking

Fig. 4.3 Power flow illustration for the hybrid railway supply system

where C_{sub} represents each capacitor's capacitance in the system and $u_C^i(t)$ is the corresponding voltage at time t. The fast and stable operation of wind power delivery and traction power supply depends on a stable DC-link voltage. If the DC-link voltage has large deviations or large magnitude oscillations, the system performance will be compromised and the device connected to the dc-bus may behave unexpectedly [101].

As mentioned in Section 4.1, P_L and P_W by nature have adverse effects on DC voltage stabilisation. Thus, MMC$_G$ must robustly control DC-link voltage by changing P_G and internal submodule states. Ideally, all capacitor voltages vary around their nominal values, but it is hard to achieve during transient states. For example, if P_L changes from 0 to maximum in short time in acceleration mode (or reversely in braking mode), the capacitor voltage will inevitably vary. It takes time to restore u_C^{ave} back to nominal its value and during that time DC-link voltage will be affected. Section 4.3 addresses this problem in details.

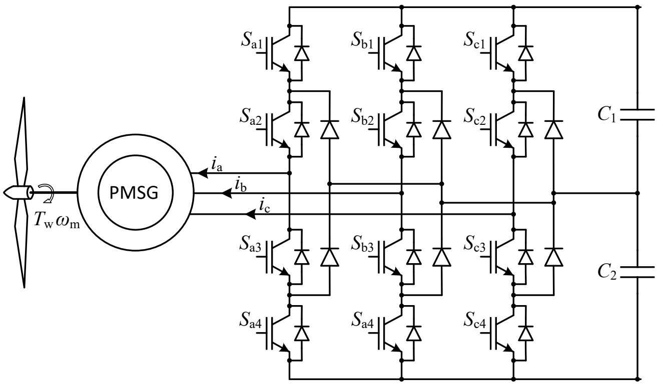

Fig. 4.4 Permanent magnet synchronous generator with neutral point clamped three level converter

It is preferable to build wind energy conversion system (WECS) near the location of SFC station to reduce transmission losses. We assume the WECS are a set of WTGs and transmit the power through HVDC line into SFC station. There are numerous research on different topology and control schemes for connecting wind farm and DB transmission [102]. The detailed wind farm control is beyond the scope of this chapter, and therefore only one equivalent generator unit is considered for simplicity.

4.2.2 Wind power generator modelling and control

The wind generation system is simplified into a single machine unit. In this section, a single 10 MW permanent magnet synchronous generator (PMSG) with three phase three level neutral point clamped (NPC) converter is used to represent the WTG system Fig. 4.4. The medium voltage DC side of NPC connects directly to the DC-link inside the SFC station

Wind power synchronous generator modelling

Figure 4.4 illustrates the circuit diagram of a typical wind energy conversion unit using a NPC converter. Table 4.1 lists the parameters of the equivalent WECS. Ignoring the effects of slotting, saturation, and end effect, etc., the simplified PMSG dynamic equations in dq-frame can be written as (4.3):

$$\begin{cases} v_d^{\mathrm{M}} = R_{\mathrm{s}}^{\mathrm{M}} i_d^{\mathrm{M}} - \omega_{\mathrm{e}}^{\mathrm{M}} L_q^{\mathrm{M}} i_q^{\mathrm{M}} + L_d^{\mathrm{M}} \dfrac{\mathrm{d}i_d^{\mathrm{M}}}{\mathrm{d}t} \\ v_q^{\mathrm{M}} = R_{\mathrm{s}}^{\mathrm{M}} i_q^{\mathrm{M}} + \omega_{\mathrm{e}}^{\mathrm{M}} L_d^{\mathrm{M}} i_d^{\mathrm{M}} + L_q^{\mathrm{M}} \dfrac{\mathrm{d}i_q^{\mathrm{M}}}{\mathrm{d}t} + \omega_{\mathrm{e}}^{\mathrm{M}} \psi_{\mathrm{m}} \end{cases}, \tag{4.3}$$

where $v_d^{\mathrm{M}}, v_q^{\mathrm{M}}$ are the machine terminal voltages in dq frame; $\omega_{\mathrm{e}}^{\mathrm{M}}$ is the electrical angular speed. Here it is assumed that the generator is a surface mount magnet generator, viz. $L_d^{\mathrm{M}} = L_q^{\mathrm{M}} = L_{\mathrm{m}}^{\mathrm{M}}$. The machine parameters[1] are shown in Table. 4.1.

---

[1] The parameters of the wind generator and its converter are set to represent a small wind which is able to deliver 10 MW generation power. Thus, these parameters does not represent any specific single wind generator system.

Table 4.1 System parameters of wind power generation system

PMSG machine		
Rated line voltage	V_l^{M}	26.4 kV
Rated stator frequency	$f_{\mathrm{s}}^{\mathrm{M}}$	20 Hz
Number of pole pairs	p	8
Rated rotor flux linkage	ψ_{m}	21.5 Wb
Stator winding resistance	$R_{\mathrm{s}}^{\mathrm{M}}$	1.6 Ω
Synchronous inductance	$L_{\mathrm{m}}^{\mathrm{M}}$	65.6 mH
NPC converter		
Rated DC voltage	V_{dc}	48 kV
NPC capacitors	$C_{1,2}^{\mathrm{M}}$	500 μF
Switching frequency	f_{npc}	2000 Hz

[1] Parameters do not necessarily represent a real system

The wind turbine model is also reduced to a controlled torque source. In this simplified system, the generator is controlled in constant speed operation with fast response to external torque input. We simulate different wind power generation by changing the value of applied torque on PMSG's shaft.

Generator controller design

To achieve fast response, a modified deadbeat control is adopted as machine controller. Deadbeat control is a model based control method which is equivalent to a simplified implementation of the horizon one model predictive controller. Discretize (4.3) using forward Euler method with controller sample time T_{sc}, the prediction of dq axis currents can be explicitly predicted:

$$\begin{aligned}\begin{bmatrix} i_d^{\mathrm{M}}(k+1) \\ i_q^{\mathrm{M}}(k+1) \end{bmatrix} &= \begin{bmatrix} 1-T_{\mathrm{sc}}\frac{R_{\mathrm{s}}^{\mathrm{M}}}{L_{\mathrm{m}}^{\mathrm{M}}} & T_{\mathrm{sc}}\omega_{\mathrm{e}}^{\mathrm{M}}(k) \\ -T_{\mathrm{sc}}\omega_{\mathrm{e}}^{\mathrm{M}}(k) & 1-T_{\mathrm{sc}}\frac{R_{\mathrm{s}}^{\mathrm{M}}}{L_{\mathrm{m}}^{\mathrm{M}}} \end{bmatrix} \begin{bmatrix} i_d^{\mathrm{M}}(k) \\ i_q^{\mathrm{M}}(k) \end{bmatrix} \\ &+ \begin{bmatrix} T_{\mathrm{sc}}\frac{1}{L_{\mathrm{m}}^{\mathrm{M}}} & 0 \\ 0 & T_{\mathrm{sc}}\frac{1}{L_{\mathrm{m}}^{\mathrm{M}}} \end{bmatrix} \begin{bmatrix} v_d^{\mathrm{M}}(k) \\ v_q^{\mathrm{M}}(k) \end{bmatrix} + \begin{bmatrix} 0 \\ -T_{\mathrm{sc}}\frac{\omega_{\mathrm{e}}^{\mathrm{M}}(k)\psi_{\mathrm{m}}}{L_{\mathrm{m}}^{\mathrm{M}}} \end{bmatrix}. \end{aligned} \tag{4.4}$$

As described in Fig. 4.5, reference current i_q^{Mref} is updated by PI controller and i_d^{Mref} is set to zero for maximum torque per ampere control. Therefore, we can calculate the required terminal voltage to generate the exact reference current in the next time step using (4.5).

$$\begin{aligned}\begin{bmatrix} v_d^{\mathrm{Mref}} \\ v_q^{\mathrm{Mref}} \end{bmatrix} &= \begin{bmatrix} R_{\mathrm{s}}^{\mathrm{M}}-\frac{1}{T_{\mathrm{sc}}}L_{\mathrm{m}}^{\mathrm{M}} & -L_{\mathrm{m}}^{\mathrm{M}}\omega_{\mathrm{e}}^{\mathrm{M}}(k) \\ L_{\mathrm{m}}^{\mathrm{M}}\omega_{\mathrm{e}}^{\mathrm{M}}(k) & R_{\mathrm{s}}^{\mathrm{M}}-\frac{1}{T_{\mathrm{sc}}}L_{\mathrm{m}}^{\mathrm{M}} \end{bmatrix} \begin{bmatrix} i_d^{\mathrm{M}}(k) \\ i_q^{\mathrm{M}}(k) \end{bmatrix} \\ &+ \begin{bmatrix} \frac{1}{T_{\mathrm{sc}}}L_{\mathrm{m}}^{\mathrm{M}} & 0 \\ 0 & \frac{1}{T_{\mathrm{sc}}}L_{\mathrm{m}}^{\mathrm{M}} \end{bmatrix} \begin{bmatrix} i_d^{\mathrm{Mref}} \\ i_q^{\mathrm{Mref}} \end{bmatrix} + \begin{bmatrix} 0 \\ \psi_{\mathrm{m}}\omega_{\mathrm{e}}^{\mathrm{M}}(k) \end{bmatrix} \end{aligned} \tag{4.5}$$

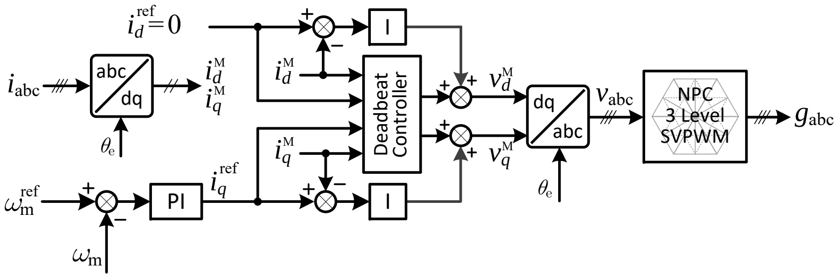

Fig. 4.5 Controller diagram for PMSG drive

Equation (4.5) expresses the control equations inside the deadbeat controller which calculate terminal voltage command to control $i_d^{\text{M}}, i_q^{\text{M}}$ to track the reference signal without error. However, the sampling time T_{sc} cannot be infinitesimal, so modelling error deteriorates its current control performance. For this reason, parallel integral controllers are added (Fig. 4.5) to improve the control robustness [103]. The composite voltage command signals are then transformed back to abc frame and the space vector pulse width modulation method (SVPWM) is used to decide switching states in the NPC controller.

4.3 MMC based static frequency converter station

4.3.1 Modelling and design of the back to back converter

Single phase model and control principle of MMC

Figure 4.6 shows the circuit topology of MMC-based static back to back converter. The back to back converter has three phases (a,b,c) working as a grid connection converter and two phases (e,f) connecting with railway traction overhead line.

Different phases have similar structure and each of them is composed of two sets of series connected half-bridge modules with branch inductor L_{br}. The DC-link voltage is measured as u_{dc}, and a virtual reference point is used to derive circuit equations. $u_{\text{ga}}, u_{\text{gb}}, u_{\text{gc}}$ are three phase voltages with star connection, and thus $i_{\text{ga}} + i_{\text{gb}} + i_{\text{gc}} = 0$. For simplicity, we consider discussing the single phase MMC model in the following explanation.

Symbols $u_{j\text{u}}$ and $u_{j\text{l}}$ represent the voltage of all inserted modules in upper and lower branches in phase j respectively. By Kirchhoff's law the current and voltage in phase a follow (4.6) to (4.8).

$$u_{\text{g}j} = -R_{\text{br}} i_{j\text{u}} - L_{\text{br}} \frac{\mathrm{d}i_{j\text{u}}}{\mathrm{d}t} - u_{j\text{u}} + 0.5u_{\text{dc}} \tag{4.6}$$

$$u_{\text{g}j} = +R_{\text{br}} i_{j\text{l}} + L_{\text{br}} \frac{\mathrm{d}i_{j\text{l}}}{\mathrm{d}t} + u_{j\text{l}} - 0.5u_{\text{dc}} \tag{4.7}$$

$$i_{\text{g}j} = -i_{j\text{u}} + i_{j\text{l}} \tag{4.8}$$

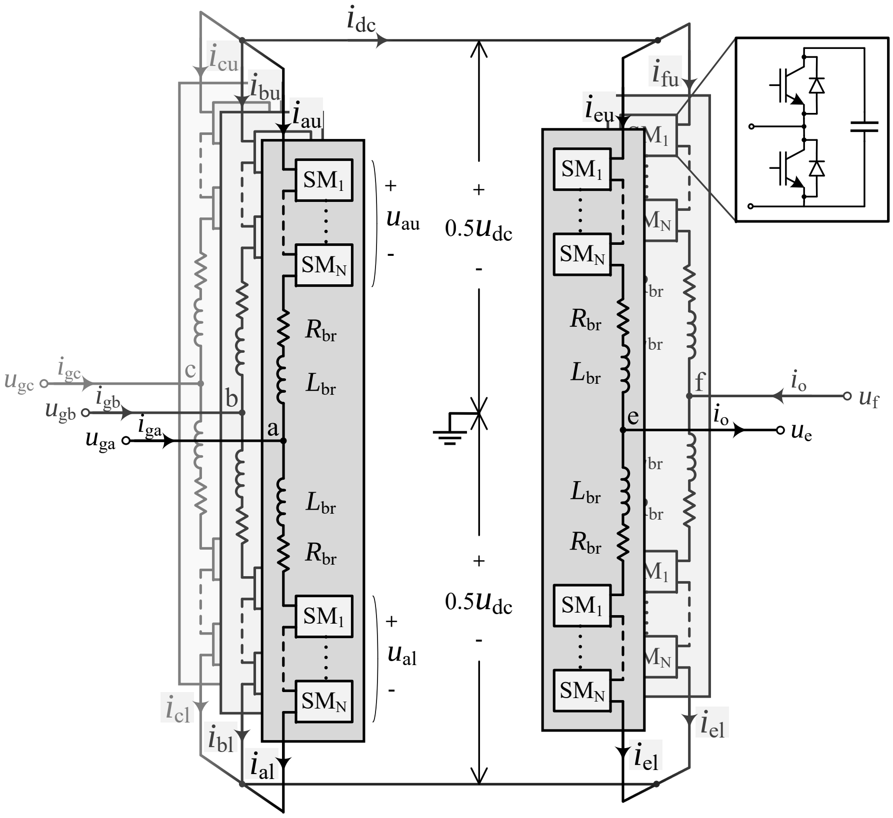

Fig. 4.6 Topology of the MMC back to back static converter

Then add and subtract (4.6) and (4.7) the following expressions of terminal voltage $u_{\mathrm{g}j}$ and DC-link voltage u_{dc} are obtained.

$$u_{\mathrm{dc}} = u_{j\mathrm{u}} + u_{j\mathrm{l}} + 2R_{\mathrm{br}}\frac{i_{j\mathrm{u}} + i_{j\mathrm{l}}}{2} + 2L_{\mathrm{br}}\frac{\mathrm{d}}{\mathrm{d}t}\frac{i_{j\mathrm{u}} + i_{j\mathrm{l}}}{2} \tag{4.9}$$

$$u_{\mathrm{g}j} = \frac{-u_{j\mathrm{u}} + u_{j\mathrm{l}}}{2} + R_{\mathrm{br}}\frac{-i_{j\mathrm{u}} + i_{j\mathrm{l}}}{2} + L_{\mathrm{br}}\frac{\mathrm{d}}{\mathrm{d}t}\frac{-i_{j\mathrm{u}} + i_{j\mathrm{l}}}{2} \tag{4.10}$$

We control MMC dynamics by switching on and off of each submodule to decide voltage of $u_{j\mathrm{u}}$ and $u_{j\mathrm{l}}$. If the number of submodules $N \to \infty$ or the switching frequency is sufficiently high, we can use modulation indices $m_{j\mathrm{u}}, m_{j\mathrm{l}}$ to represent the branch voltages:

$$u_{j\mathrm{u}} = m_{j\mathrm{u}} N u_{\mathrm{C}}^{\mathrm{ave}}, \quad u_{j\mathrm{l}} = m_{j\mathrm{l}} N u_{\mathrm{C}}^{\mathrm{ave}}, \tag{4.11}$$

where $u_{\mathrm{C}}^{\mathrm{ave}}$ is the average capacitor voltage.

Equation (4.8)–(4.10) imply that the AC terminal side value is decided by the difference value of upper and lower branch, and the DC side is determined by common values of two branches. Therefore, it is easier to view MMC topology in differential and common mode model, and the differential/common mode values are defined in (4.12):

$$x_{j\mathrm{com}} = (x_{j\mathrm{u}} + x_{j\mathrm{l}})/2, \quad x_{j\mathrm{dif}} = (-x_{j\mathrm{u}} + x_{j\mathrm{l}})/2, \tag{4.12}$$

where x represents modulation index, branch voltage or branch current, and the subscripts com, dif represent the common mode value and differential mode value respectively. For example, $i_{j\mathrm{dif}}$ represents the differential mode current of phase j which is defined by upper and lower branch currents $i_{j\mathrm{u}}$ and $i_{j\mathrm{l}}$.

Then the terminal voltage and current of one MMC phase can be rewritten using differential and common mode values:

$$u_{\mathrm{dc}} = m_{j\mathrm{com}} 2N u_{\mathrm{C}}^{\mathrm{ave}} + i_{j\mathrm{com}} 2R_{\mathrm{br}} + \frac{\mathrm{d}}{\mathrm{d}t}\left(i_{j\mathrm{com}} 2L_{\mathrm{br}}\right), \tag{4.13}$$

$$u_{\mathrm{g}j} = m_{j\mathrm{dif}} N u_{\mathrm{C}}^{\mathrm{ave}} + i_{j\mathrm{dif}} R_{\mathrm{br}} + \frac{\mathrm{d}}{\mathrm{d}t}\left(i_{\mathrm{adif}} L_{\mathrm{br}}\right), \tag{4.14}$$

$$i_{\mathrm{g}j} = 2 i_{j\mathrm{dif}}. \tag{4.15}$$

The MMC single phase equivalent model in (4.13) and (4.14) are illustrated in Fig. 4.7. In brief, $u_{\mathrm{g}j}$ is controlled by $m_{j\mathrm{dif}}$ and u_{dc} is controlled by $m_{j\mathrm{com}}$. In normal steady state operation, average capacitor voltage in each branch equals to $1/N$ of the nominal DC-link voltage V_{dc}. Consequently, in most of the applications, N modules are inserted in series to maintain DC-link voltage at each instance by default, which gives $m_{j\mathrm{com}} = 0.5$. Usually $i_{j\mathrm{com}}$ has to be controlled to suppress excessive AC components, then a small sinusoidal signal will be added to $m_{j\mathrm{com}}$ to achieve this objective.

Because the differential mode shows that the MMC can be controlled in the same way as conventional two level converters, most of the previous works only stabilise DC voltage by controlling average capacitor voltages and use $m_{j\mathrm{com}} = 0.5$ to indirectly maintain the DC voltage. However, if the load

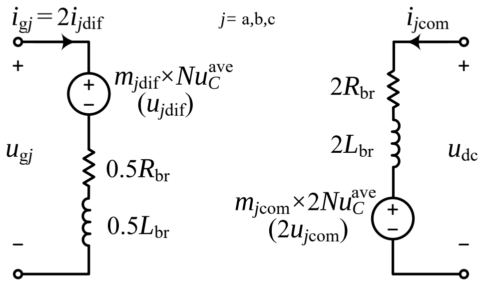

Fig. 4.7 Simplified equivalent differential common mode model of single MMC phase

change drastically, namely i_{dc} change greatly in very short period of time, average capacitor voltage will no longer be the nominal value ($u_{\mathrm{C}}^{\mathrm{ave}} \neq V_{\mathrm{dc}}/N$). Modulation signal of $m_{j\mathrm{com}} = 0.5$ can not guarantee stable DC-link voltage and u_{dc} changes with average capacitor voltage synchronously.

The conventional approach does not fully take advantage of the special characteristics of MMC. In fact the total number of inserted submodules can be modified to compensate transient voltage drop. For this reason, it is necessary to deliberately control $m_{j\mathrm{com}}$ such that DC-link voltage has less deviation from the nominal value in transient state.

Parameter design of MMC back to back converter

Assume right after a sudden load change, the average capacitor voltage becomes:

$$u_{\mathrm{C}}^{\mathrm{ave}} = a\frac{V_{\mathrm{dc}}}{N}\,, \tag{4.16}$$

where a is the average capacitor voltage factor, and we assume $a \in [0.5, 1.5]$. By (4.13), ignoring the voltage across the inductor, m_{com} has to be set to $0.5/a$ in order to stabilise the DC voltage perfectly.

Note that $m_{j\mathrm{u}}, m_{j\mathrm{al}} \in [0,1]$, and therefore $m_{a\mathrm{dif}}$ can vary from -0.5 to 0.5 if and only if $m_{j\mathrm{com}} = 0.5$. Also in this case, the no load voltage output range is $u_{\mathrm{g}j} \in [-0.5V_{\mathrm{dc}}, +0.5V_{\mathrm{dc}}]$. But under the condition when the average capacitor voltage has large deviation from the nominal, differential modulation range and terminal voltage are compromised if we adjust $m_{j\mathrm{com}} = 0.5/a$ to maintain DC-link voltage. Then the achievable ranges of modulation index and output voltage with this approach can be expressed as follows and plotted in Fig. 4.8.

$$\begin{aligned}
m_{j\mathrm{com}} &= 0.5/a \\
|m_{j\mathrm{dif}}|_{\max} &= \begin{cases} 1-0.5/a\,, & a<1 \\ 1/(2a)\,, & a\geq 1 \end{cases} \qquad (j=\mathrm{a,b,c}) \\
|u_{\mathrm{g}j}|_{\max} &= \begin{cases} (a-0.5)V_{\mathrm{dc}}\,, & a<1 \\ 0.5V_{\mathrm{dc}}\,, & a\geq 1 \end{cases}
\end{aligned} \tag{4.17}$$

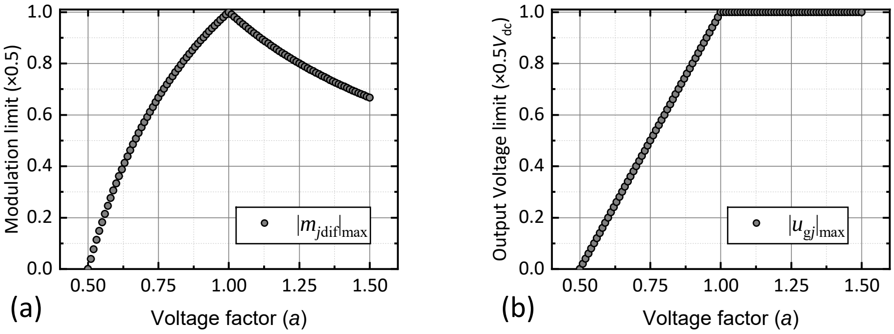

Fig. 4.8 Range of modulation index and output voltage with average capacitor voltage $u_{\mathrm{C}}^{\mathrm{ave}} = aV_{\mathrm{dc}}/N$

The ac terminal voltage output capability will not be affected when $a > 1$ but decrease linearly when $a < 1$. Apparently, system parameters have to be carefully designed to guarantee stable operation.

Converter MMC$_{\mathrm{g}}$ has to deliver power in bidirection. In no load condition, when current is small enough, the differential modulation index (denoted by $m_{j\mathrm{dif}_1}$) is:

$$m_{j\mathrm{dif}_1} = \sqrt{2}\frac{V_{\mathrm{gn}}}{V_{\mathrm{dc}}}, \quad j = \mathrm{a,b,c} \tag{4.18}$$

where V_{gn} is the phase to ground root mean square (RMS) voltage of the grid side transformer. In the rectifying mode, the differential modulation index for maximum load (denoted by $m_{j\mathrm{dif}_2}$) is calculated by the following equations:

$$m_{j\mathrm{dif}_2} = \frac{\sqrt{2}}{aV_{\mathrm{dc}}}\sqrt{V_{\mathrm{gn}}^2 + \left(\frac{PL_{\mathrm{eq}}\pi f_{\mathrm{g}}}{V_{\mathrm{gn}}}\right)^2}, \; P = \frac{\max\left(P_{\mathrm{G}}^{+}\right)}{3}, \tag{4.19}$$

where f_{g} is the grid frequency, L_{eq} is the equivalent inductance which is equal to the sum of $\frac{1}{2}L_{\mathrm{br}}$ and the transformer leakage inductance. Similarly, in the energy feedback mode, the $m_{j\mathrm{dif}_3}$ for maximum load is shown in (4.20):

$$m_{j\mathrm{dif}_3} = \frac{\sqrt{2}}{aV_{\mathrm{dc}}}\sqrt{V_{\mathrm{gn}}^2 + \left(\frac{PL_{\mathrm{eq}}\pi f_{\mathrm{g}}}{V_{\mathrm{gn}}}\right)^2}, \; P = \frac{\left|\min\left(P_{\mathrm{G}}^{-}\right)\right|}{3}. \tag{4.20}$$

It is easy to see that $m_{j\mathrm{dif}_1} < m_{j\mathrm{dif}_2} < m_{j\mathrm{dif}_3}$, $(j = \mathrm{a,b,c})$. In normal steady state operation, the upper limit for differential modulation is 0.5 and in case of voltage deviation, the upper limit constraint is expressed in (4.17). L_{eq} and V_{gn} have to be designed without violating these constraints.

According to [104], the series resonance angle frequency ω_{res} should be smaller than 1.55ω to avoid circulating current resonance. In this chapter, consider the largest series resonance angular frequency of one phase:

$$\omega_{\mathrm{res}} = \frac{1}{2}\sqrt{\frac{N/a}{2L_{\mathrm{br}}C_{\mathrm{sub}}}}, \quad a < 1; \tag{4.21}$$

Table 4.2 Parameters of SFC substation back to back converter

MMC		
Transformer voltage (ph-ph)	V_g	21.5 kV
Rated power	P_n	26 MW
Rated DC voltage	V_{dc}	48 kV
Numbers of submodule per branch	N	24
Submodule capacitance	C_{sub}	2 mF
Branch resistance	R_{br}	0.5 Ω
Branch inductor	L_{br}	18.5 mH
Switching frequency	f_{mmc}	500 Hz

obviously ω_{res} has larger value when capacitor voltage is below nominal value due to a greater number of capacitors being switched on. We can design the appropriate MMC branch inductance to satisfy these criteria.

In addition to satisfying power delivery and suppressing circulating current oscillation, the MMC branch inductor also has to suppress fault current rise rate during DC-link fault. To limit the magnitude of short-circuit current, the inductance value is set to 0.1 p.u. according to [105]. Consequently, the inductance in each MMC phase and transformer terminal voltage can be designed.

Assume the system changes its power supply linearly and reaches steady state after one cycle time (20 ms). Then the total energy stored in all submodules' capacitor (E_C^Σ) should satisfy (4.22):

$$E_C^\Sigma = \frac{3}{N} C_{sub} V_{dc}^2 \geq \frac{1}{2} \frac{P_G^{max}}{f_g \times |1-a^2|} \,. \tag{4.22}$$

Equation (4.23) estimates steady state voltage ripple of the submodule capacitor in each phase. Suppose the capacitor voltage can deviate 20% of the nominal value in the worst transient load change, viz. $0.8 \leq a \leq 1.2$. The capacitance of each submodule C_{sub} can be designed using constraints in (4.22) and (4.23):

$$\left| \frac{\Delta u_C}{V_{dc}/N} \right|_{max} \approx \frac{N P_j^*}{4\pi f_g C_{sub} V_{dc}^2} \frac{(1-m_{jdif}^2)^{\frac{3}{2}}}{m_{jdif}} \leq |1-a|_{max} \,, \tag{4.23}$$

where P_j^* is the power rating in phase j. Table 4.2 presents the MMC parameters.

4.3.2 AC voltage control of MMC

This section presents the control scheme to realise the AC connection to three phase power grid and single phase railway catenary. The back to back MMC generates synchronised voltage with the distribution grid and a 50 Hz sinusoidal voltage for railway power supply.

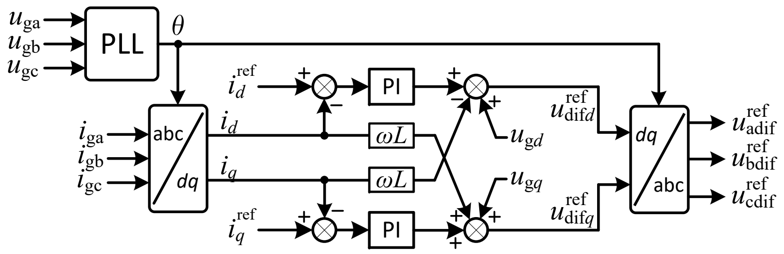

Fig. 4.9 Control diagram of the three phase grid AC voltage controller

Grid side converter

The equations of three phase AC side MMC dynamics are derived in (4.14) and can be rewritten as:

$$\begin{cases} u_{\mathrm{adif}} = u_{\mathrm{ga}} - \dfrac{R_{\mathrm{br}}}{2} i_{\mathrm{ga}} - \dfrac{L_{\mathrm{br}}}{2} \dfrac{\mathrm{d}}{\mathrm{d}t} i_{\mathrm{ga}} \\ u_{\mathrm{bdif}} = u_{\mathrm{gb}} - \dfrac{R_{\mathrm{br}}}{2} i_{\mathrm{gb}} - \dfrac{L_{\mathrm{br}}}{2} \dfrac{\mathrm{d}}{\mathrm{d}t} i_{\mathrm{gb}} \\ u_{\mathrm{cdif}} = u_{\mathrm{gc}} - \dfrac{R_{\mathrm{br}}}{2} i_{\mathrm{gc}} - \dfrac{L_{\mathrm{br}}}{2} \dfrac{\mathrm{d}}{\mathrm{d}t} i_{\mathrm{gc}} \end{cases} . \tag{4.24}$$

Use park transformation to map (4.24) into dq frame:

$$\begin{cases} u_{\mathrm{dif}d} = u_{gd} - \dfrac{R_{\mathrm{br}}}{2} i_d - \dfrac{L_{\mathrm{br}}}{2} \dfrac{\mathrm{d}}{\mathrm{d}t} i_d + \omega \dfrac{L_{\mathrm{br}}}{2} i_q \\ u_{\mathrm{dif}q} = u_{gq} - \dfrac{R_{\mathrm{br}}}{2} i_q - \dfrac{L_{\mathrm{br}}}{2} \dfrac{\mathrm{d}}{\mathrm{d}t} i_q - \omega \dfrac{L_{\mathrm{br}}}{2} i_d \end{cases} , \tag{4.25}$$

where ω is the angular velocity of the grid. Equation (4.25) has similar form with two level converter system. The classic control method is used for outer loop control shown in Fig. 4.9. Three phase AC current are transformed into DC values i_d, i_q and then PI controllers with feedforward terms compose the reference values for $u_{\mathrm{dif}}^{\mathrm{ref}}$ via inverse park transformation.

Traction side converter

Traction side catenary ac supply requires single phase voltage. The MMC traction side output voltage u_{o} is a sinusoidal voltage, and we can derive the circuit equation from the model shown in Fig. 4.10:

$$u_{\mathrm{o}} = -\left(R_{\mathrm{br}} i_{\mathrm{o}} + L_{\mathrm{br}} \frac{\mathrm{d}}{\mathrm{d}t} i_{\mathrm{o}} \right) + \left(u_{\mathrm{edif}} - u_{\mathrm{fdif}} \right) . \tag{4.26}$$

To maximise the difference between u_{edif} and u_{fdif}, they should be opposite to each other for maximum

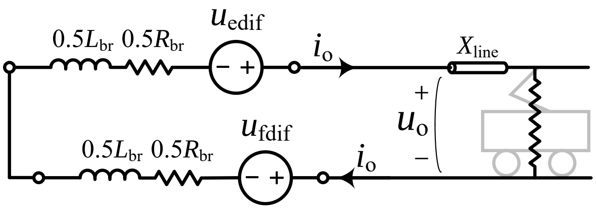

Fig. 4.10 Single phase MMC railway traction network supply

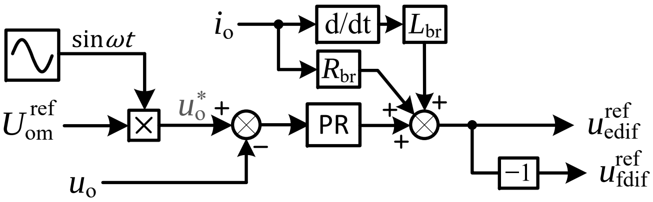

Fig. 4.11 Control diagram of the single phase ac traction supply

utilisation. Then the desired terminal voltage can be calculated as (4.27):

$$\begin{aligned} u_{\text{edif}} = -u_{\text{fdif}} &= \frac{1}{2}\left(u_{\text{o}} + R_{\text{br}} i_{\text{o}} + L_{\text{br}} \frac{\mathrm{d}}{\mathrm{d}t} i_{\text{o}}\right) \\ &= \left(k_{\text{p}}^{u_{\text{o}}} + \frac{k_{\text{r}}^{u_{\text{o}}} s}{s^2 + \omega^2}\right)(u_{\text{o}}^* - u_{\text{o}}) + \frac{1}{2}\left(R_{\text{br}} i_{\text{o}} + L_{\text{br}} \frac{\mathrm{d}i_{\text{o}}}{\mathrm{d}t}\right) \end{aligned} . \tag{4.27}$$

The control diagram of single phase voltage supply is illustrated in Fig. 4.11. Because the AC voltage is directly controlled without being transformed into a rotating coordinate system, a proportional resonant (PR) controller is used to follow the sinusoidal reference.

4.3.3 DC link voltage control of MMC

In ideal situations, the DC-link voltage is maintained to have as less deviations as possible. However, load disturbance can cause voltage sag or swell in short time and the single phase traction load introduces doubled frequency component in the DC voltage. Special control based on MMC is introduced in this section.

Single phase power flow oscillation suppression

Denote MMC output voltage on railway overhead line as u_o, and load current as i_o as shown in Fig. 4.10. The instantaneous power consumed by the traction load is $P_L(t)$:

$$\begin{aligned} P_{\text{L}}(t) &= U_{\text{om}} \sin \omega t \times I_{\text{om}} \sin(\omega t - \varphi) \\ &= \frac{U_{\text{om}} I_{\text{om}}}{2} [\cos \varphi - \cos(2\omega t - \varphi)] . \end{aligned} \tag{4.28}$$

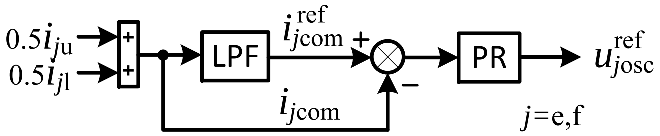

Fig. 4.12 DC voltage double frequency oscillation suppression

In Equ.(4.28), $U_{\mathrm{om}}, I_{\mathrm{om}}$ are the magnitude of MMC output voltage and output current respectively and φ is the traction load angle. Clearly, the traction load power has a double frequency component which has the comparable magnitude with its DC component. In traditional two level or multilevel NPC converters, where a shared capacitor exists, the DC-link voltage will inevitably have a 100 Hz oscillating component. For example in the on-board line converter of high speed train, DC voltage rectified from single phase converter contains the 100 Hz component and affects the traction line side current [106].

In contrast, the MMC has floating capacitors and does not exchange energy from a shared capacitor. It is therefore possible to eliminate double frequency component on the DC-link voltage. Referring to Fig. 4.6 and Fig. 4.7, we can have $i_{\mathrm{dc}} = 2i_{\mathrm{ecom}} = 2i_{\mathrm{fcom}}$ in steady state. Therefore, rejecting ac component in i_{dc} is equal to controlling $i_{\mathrm{ecom}}, i_{\mathrm{fcom}}$ to become dc values. Figure 4.12 shows the control diagram of this approach.

Here, calculation of the reference value common mode current $i_{j\mathrm{com}}^{\mathrm{ref}}$ is based on real time current measurement through a mean filter and thus 100 Hz signal is filtered out in calculating $i_{j\mathrm{com}}^{\mathrm{ref}}$. Then 100 Hz component in $i_{j\mathrm{com}}$ can be extracted and PR controller generates a 100 Hz control signal $u_{j\mathrm{osc}}^{\mathrm{ref}}$ as suppresses the oscillation current formulated in (4.29).

$$u_{j\mathrm{osc}}^{\mathrm{ref}} = \left(k_{\mathrm{p}}^{u_{\mathrm{osc}}} + \frac{k_{\mathrm{r}}^{u_{\mathrm{osc}}} s}{s^2 + \omega_{\mathrm{r}}^2}\right)\left(i_{j\mathrm{com}}^{\mathrm{ref}} - i_{j\mathrm{com}}\right), \tag{4.29}$$

where ω_{r} is the resonant frequency. With this approach, phases e, f of MMC at traction side will not introduce the oscillating power effect into the DC-link at steady state. The PR controller gains are tuned by optimising the $i_{j\mathrm{com}}$ tracking performance in response to the 10 MW traction load step change, where the accumulated absolute tracking error is minimised. The minimisation problem is solved by sequential quadratic programming method.

DC voltage stabilisation

In this back to back system, the submodule capacitor voltage is maintained and stabilised by grid side converter MMC$_{\mathrm{G}}$. The capacitor voltage deviation determines the reference value of i_{gd}^{ref} by a PI controller:

$$i_{gd}^{\mathrm{ref}} = \left(k_{\mathrm{p}}^{u_{\mathrm{C}}} + \frac{k_{\mathrm{i}}^{u_{\mathrm{C}}}}{s}\right)\left(\frac{V_{\mathrm{dc}}}{N} - u_{\mathrm{C}}^{\mathrm{ave}}\right). \tag{4.30}$$

Whenever there is a sudden load change, the capacitor voltage will deviate from the nominal value, because the PI controller in (4.30) cannot have infinity gain and the actual system needs time to respond. According to (4.17), we can alter m_{com} by $\Delta u_{\mathrm{dc}}^{\mathrm{ref}}$ to control the number of the inserted submodules to

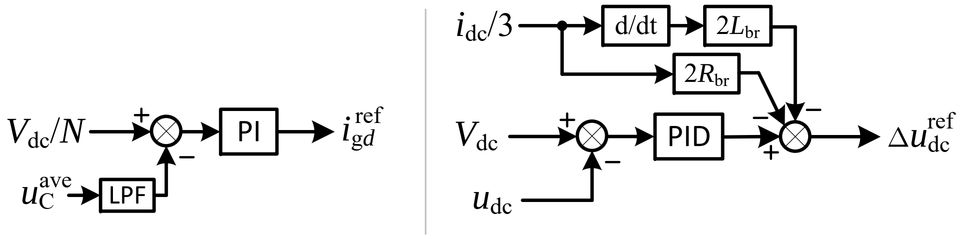

Fig. 4.13 DC voltage stabilisation control

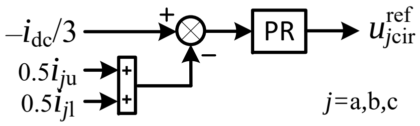

Fig. 4.14 Circulating current control diagram

reduce the DC voltage deviation, as shown in (4.31):

$$
\begin{aligned}
\Delta u_{dc}^{ref} = & \left(k_p^{u_{dc}} + \frac{k_i^{u_{dc}}}{s} + k_d^{u_{dc}} \frac{N_d}{1+N_d/s}\right)(V_{dc} - u_{dc}) \\
& - 2\left(R_{br}\frac{i_{dc}}{3} + L_{br}\frac{d}{dt}\frac{i_{dc}}{3}\right),
\end{aligned}
\tag{4.31}
$$

where $N_d = 1000$ is the filter coefficient to realise the derivative control. Figure 4.13 shows the control diagram of DC voltage stabilisation control. Note that reference signals for all three phases a, b, c are controlled by the same reference Δu_{dc}^{ref} to avoid unnecessary circulating current between phases.

4.3.4 Inner control of MMC

Inner control of MMC involves circulating current control in each phase and capacitor voltage balancing in each branch.

Circulating current suppression

According to Fig. 4.6, $i_{acom} + i_{bcom} + i_{ccom} = -i_{dc}$. Also in balanced and steady state i_{dc} does not contain alternating component, $-i_{dc}/3$ is used as common mode current reference for circulating current control. The circulating current control diagram is shown in Fig. 4.14 and the control reference u_{jcir}^{ref} is generated for phase j of the grid side converter.

Capacitor voltage balancing

Figure 4.15 illustrates the control scheme of capacitor voltage balancing in each branch where individual submodule capacitor voltage is compared with the average value. The voltage deviation will be compensated by adjusting each switching duration according to common current direction by control reference Δu_{Cju}^i and Δu_{Cjl}^i for the ith submodule in phase j.

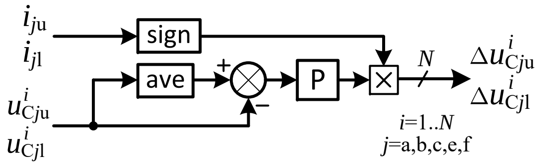

Fig. 4.15 Capacitor balance control diagram

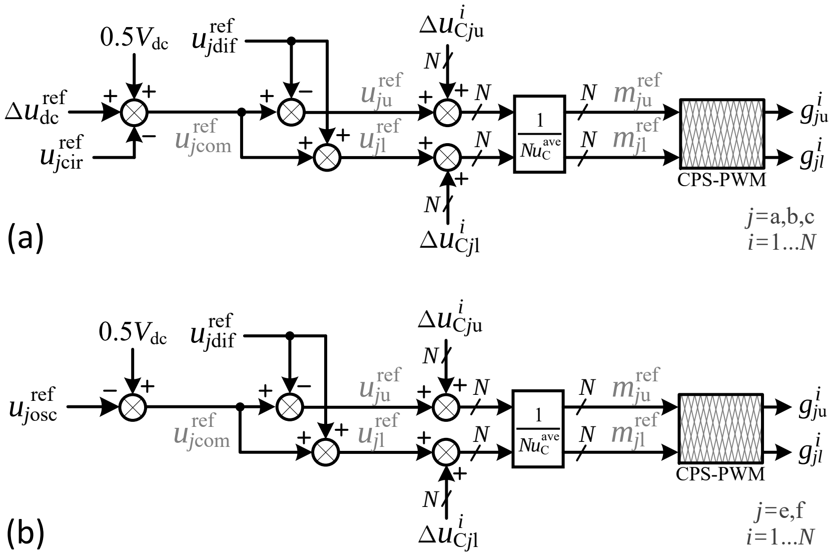

Fig. 4.16 MMC control reference calculation and modulation

4.3.5 MMC modulation

Modulation indices for each phase can be calculated from the voltage control references:

$$m_{j\mathrm{u}} = \frac{u_{j\mathrm{com}}^{\mathrm{ref}} - u_{j\mathrm{dif}}^{\mathrm{ref}}}{N u_{\mathrm{C}}^{\mathrm{ave}}}, \quad m_{j\mathrm{l}} = \frac{u_{j\mathrm{com}}^{\mathrm{ref}} + u_{j\mathrm{dif}}^{\mathrm{ref}}}{N u_{\mathrm{C}}^{\mathrm{ave}}}. \tag{4.32}$$

where $j = \mathrm{a,b,c,e,f}$, and $u_{j\mathrm{dif}}^{\mathrm{ref}}$ is the corresponding value in Fig. 4.9. In the grid side converter, $u_{j\mathrm{com}}^{\mathrm{ref}}$ is composed of the feedforward value $0.5V_{\mathrm{dc}}$, DC voltage stabilising term $\Delta u_{\mathrm{dc}}^{\mathrm{ref}}$ and circulating current control term $u_{j\mathrm{cir}}^{\mathrm{ref}}$. While in the traction side converter, $u_{j\mathrm{com}}^{\mathrm{ref}}$ is composed of the feedforward value $0.5V_{\mathrm{dc}}$, and oscillation suppression control term $u_{j\mathrm{osc}}^{\mathrm{ref}}$. Finally, the capacitor voltage balancing terms $\Delta u_{\mathrm{C}j\mathrm{u}}^{i}$ and $\Delta u_{\mathrm{C}j\mathrm{l}}^{i}$ are added in each submodule. Fig. 4.16a and Fig. 4.16b illustrate the control reference calculation and the modulation diagram for grid side MMC and traction side MMC respectively.

4.4 Simulation results and discussion

The control parameters for the MMC back to back converter are listed in Table 4.3. The measurements in the control system are converted into per-unit system using grid side MMC's power rating as the base value. Three sets of simulation tasks are designed to test the proposed control scheme. The

Table 4.3 Simulation and control parameters setting

MMC control parameters		
Grid side current controller	$[k_{\mathrm{p}}^{i_{dq}}, k_{\mathrm{i}}^{i_{dq}}]$	[1.5,30]
Traction side voltage controller	$[k_{\mathrm{p}}^{u_{\mathrm{o}}}, k_{\mathrm{r}}^{u_{\mathrm{o}}}]$	[1.09,84.6]
Double frequency oscillation controller	$[k_{\mathrm{p}}^{u_{\mathrm{osc}}}, k_{\mathrm{r}}^{u_{\mathrm{osc}}}]$	[1.92,170]
Capacitor average voltage controller	$[k_{\mathrm{p}}^{u_{\mathrm{C}}}, k_{\mathrm{i}}^{u_{\mathrm{C}}}]$	[1.2,20]
DC voltage stabilisation controller	$[k_{\mathrm{p}}^{u_{\mathrm{dc}}}, k_{\mathrm{i}}^{u_{\mathrm{dc}}}, k_{\mathrm{d}}^{u_{\mathrm{dc}}}]$	[4,40,0.004]
Simulation model time step	T_{s}	5 ms
Controller sampling time	T_{sc}	0.1 ms

effectiveness of voltage stabilisation control and voltage oscillation suppression are examined in both steady and transient states. In the conventional MMC rectifier control the DC-link voltage is maintained by controlling the submodule capacitors' average voltage which is equivalent to setting $\Delta u_{\mathrm{dc}}^{\mathrm{ref}}$ to 0 in the proposed scheme. So in this section, we use $\Delta u_{\mathrm{dc}}^{\mathrm{ref}} = 0$ to represent the conventional control method.

4.4.1 Train load profile and wind power profile

Case A is used to analyse the steady state performance of power delivery on each terminal and the DC voltage quality. *Case* $B_{1,2}$ consider one side step change and test the negative consequences on the other side. *Case* C_{1-4} investigates several worst scenarios that both sides are subject to rated power magnitude step change simultaneously, imposing the severest control challenges on $\mathrm{MMC_G}$. These simulation tasks are summarised as follows:

- *Case A* P_{W} is set to 10 MW; P_{L} is set to 0, 5 MW, 10 MW, 20 MW respectively.
- *Case* B_1 P_{W} is set to 10 MW; P_{L} changes from 10 MW to 20 MW then returns to 10 MW.
- *Case* B_2 P_{W} changes from 0 MW to 10 MW then to 0 MW; P_{L} is set to 10 MW.
- *Case* C_1 P_{W} changes from 10 MW to 0 MW; P_{L} changes from 0 MW to 20 MW at the same time.
- *Case* C_2 P_{W} changes from 0 to 10 MW; P_{L} changes from 20 to 0 MW at the same time.
- *Case* C_3 P_{W} changes from 0 MW to 10 MW; P_{L} changes from 10 MW to -10 MW at the same time.
- *Case* C_4 P_{W} changes from 10 MW to 0 MW; P_{L} changes from -10 MW to $+10$ MW at the same time.

4.4.2 Steady state performance analysis

The power flows across four coupling nodes are measured: three phase ac grid power p_{grid}, grid connection MMC DC side power p_{mmc}, PMSG converter DC side power p_{pmsg} and power consumed by traction load p_{train}. These four power flow data are plotted in Fig. 4.17. In steady states, both AC side power p_{grid} and p_{train} have very stable values. However, p_{pmsg} has noisy instantaneous power with ripples at the level of 3.91%–5.38%. As the load power increases, both generation power and MMC power present larger power fluctuations. Because in higher power operation, the MMC has heavier burden to suppress circulating current and maintain DC voltage, and also has larger voltage oscillations in each module.

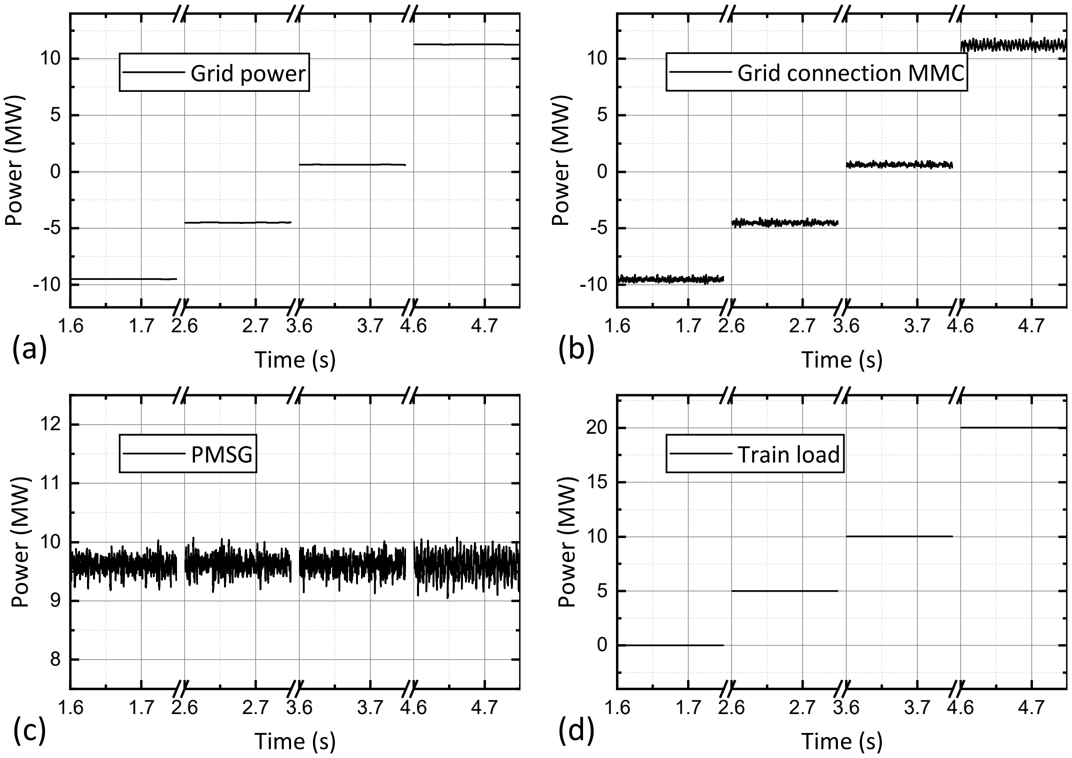

Fig. 4.17 Steady state power flow (*Case A*)

Figure 4.18 compares the DC-link voltage profiles using the proposed method and the conventional method by setting $\Delta u_{\mathrm{dc}}^{\mathrm{ref}} = 0$ (Fig. 4.16). Considering the simulation time during 4.6 s to 4.7 s in the largest traction load condition, the proposed method shows fewer fluctuations (0.068%) than the conventional approach (0.176%). Moreover, when ignoring the DC voltage stabilisation control action, there exists steady state error due to branch inductor voltage drop. The steady state error is reduced from 0.216% to 0.0037% with the proposed control method.

The effects of the proposed control on DC-link voltage oscillation suppression is shown in Fig. 4.19 where the Fig. 4.19a shows the result of ignoring the oscillation control term $u_{\mathrm{osc}}^{\mathrm{ref}}$ and Fig. 4.19b shows the profile without both proposed control terms. It is evident that Fig. 4.19b has the greatest voltage ripple caused by single phase traction load. During 4.6 s to 4.7 s, there is large magnitude of steady low frequency oscillation component which contributes to 6.26% voltage ripple. With the help of voltage stabilisation control, the ripple is reduced to 1.23% even we do not control the oscillating current in the traction side MMC. Nevertheless, none of these two cases is acceptable because the existence of 100 Hz oscillation voltage on the DC-link is detrimental to stable energy exchange through DC interface. This confirms the necessity of adding the two proposed control loops shown in Fig. 4.12 and Fig. 4.13.

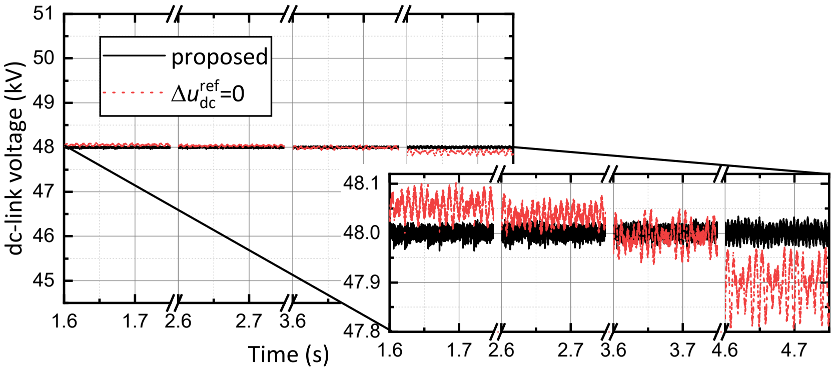

Fig. 4.18 Steady state DC-link voltage comparison 1 (*Case A*)

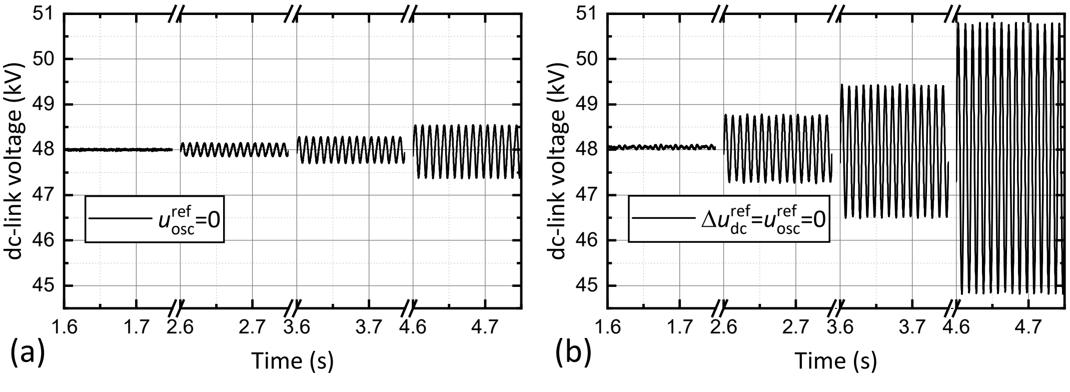

Fig. 4.19 Steady state DC-link voltage comparison 2 (*Case A*)

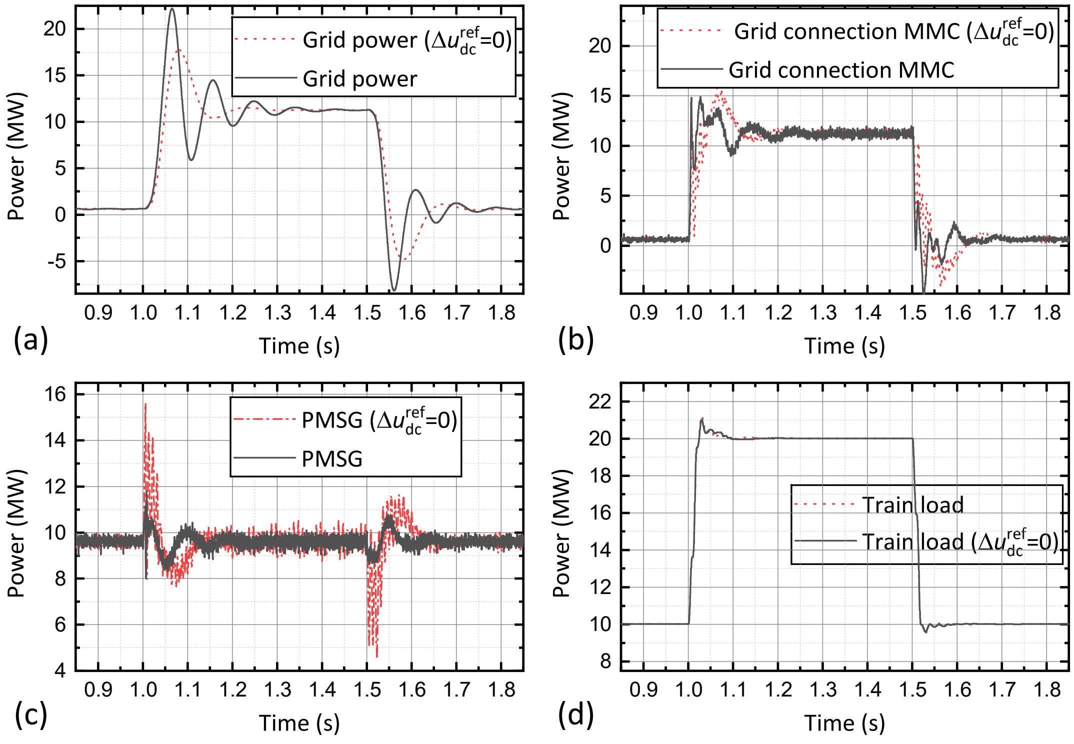

Fig. 4.20 Instantaneous power flow in *Case* B_1 simulation

4.4.3 Transient performance analysis

Case B

Case B_1 examines the traction side influence on the PMSG power delivery due to the load change which is first stepped up and then stepped down at 1.0 s and 1.5 s respectively. The improvement brought by the proposed DC voltage controller is plotted in Fig. 4.20. In both control approaches, these instantaneous power plots all have short time oscillation after load change. Both p_{pmsg} and p_{mmc} experienced fewer fluctuations and less settling time under the extra voltage stabilisation control. The renewable generation will be less affected by the traction load change. The price paid is a greater power overshoot on the grid side.

The greater power oscillations in the wind generation side was caused by deviations in the DC-link voltage. As shown in Fig. 4.21, if $\Delta u_{\mathrm{dc}}^{\mathrm{ref}}$ is ignored, the voltage deviation can be as big as 12% in this case study. This problem is greatly alleviated using the proposed control method that only 2.93% voltage dip remains, and the similar results were also observed at 1.5 s. The deviation reduction is above 75%.

Case B_2 tests the influence of wind generation fluctuation on the traction side. Similar to the previous results, the proposed control approach reduces power oscillation in all converters except the grid power as shown in Fig. 4.22. The proposed control again limits the voltage variation within 2.1% of the nominal value which is more than 76% reduction than the conventional approach. It can be seen that, although

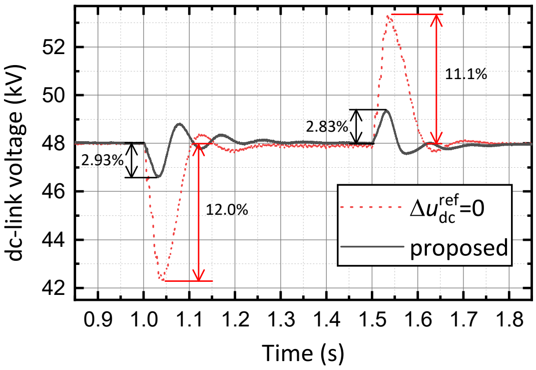

Fig. 4.21 DC link voltage comparison (*Case* B_1)

power change is equal to 10 MW in both case B_1 and B_2, the negative effect brought by wind generation unit is less than traction change, because the generator is a balanced three phase source.

Case C

The last four scenarios are deliberately designed to test the limit of the system capacity. In these worst cases, although adding $\Delta u_{\mathrm{dc}}^{\mathrm{ref}}$ improves DC voltage stability for more than 50%, the largest voltage deviation is still above 14.2%. Fortunately, these situations however rarely occur in real applications, and we can improve the system capacity by increasing the size of submodule capacitor or the converter current rating to withstand these cases if necessary.

Modulation

Figure 4.25 shows the voltage control references for upper branch of phase a in *Case* B_1. The voltage reference signals for DC voltage stabilisation, circulating current suppression and AC voltage control are plotted. As explained in Section 4.3.1, the differential mode modulation signal varies within $[-0.5, 0.5]$. And with the voltage stabilisation control, more submodules are switched on to support DC-link. As indicated by $\Delta u_{\mathrm{dc}}^{\mathrm{ref}}$ line, at 1.18 s, about 9% more modules are inserted in each branch.

The reference $u_{\mathrm{cir}}^{\mathrm{ref}}$ also controls the number of inserted modules, but the signals for each phase are symmetric. However, the $\Delta u_{\mathrm{dc}}^{\mathrm{ref}}$ term allows all three phase to shift uniformly to reject voltage fluctuations.

By synthesising all control references based on the method shown in Fig. 4.16, the final modulation signal is shown in Fig. 4.26. The result in Fig. 4.26b is consistent with previous analysis that the composite modulation has an extra degree of freedom brought by the proposed method. This extra degree of freedom improves the transient response and steady state performance of DC voltage control.

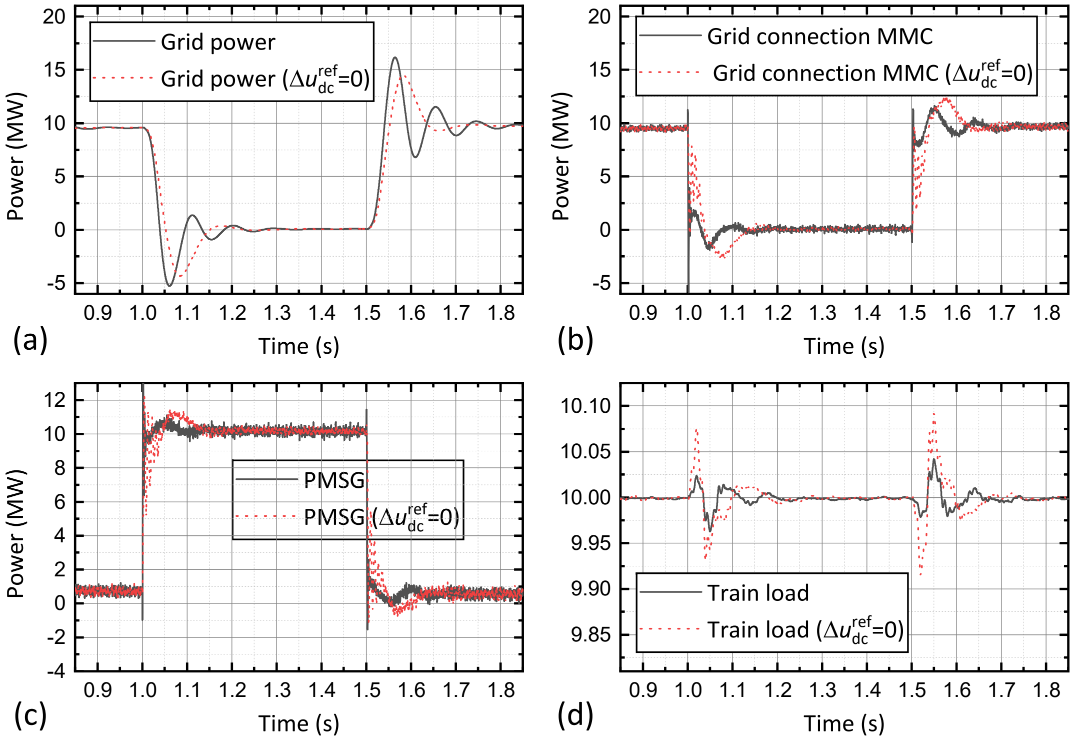

Fig. 4.22 Instantaneous power flow in *Case* B_2 simulation

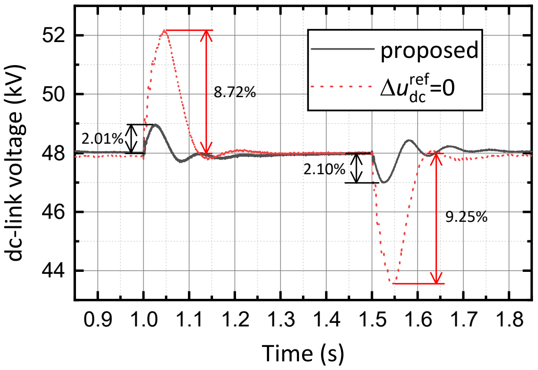

Fig. 4.23 DC link voltage comparison (*Case* B_2)

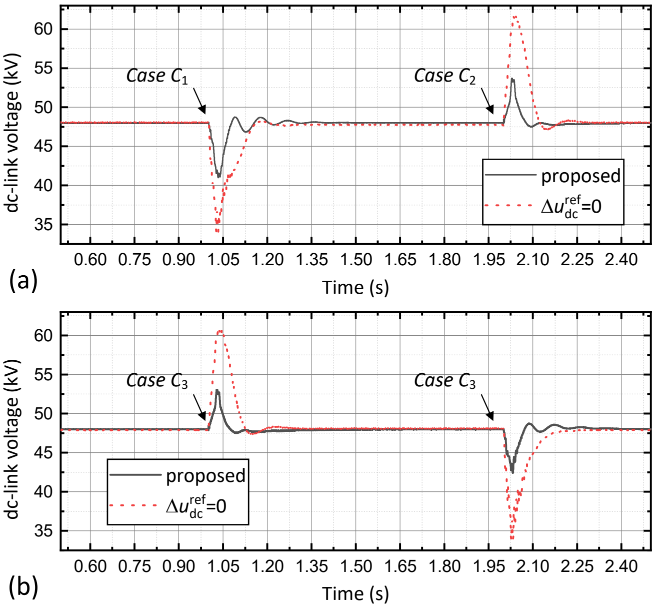

Fig. 4.24 DC link voltage (*Case* C_{1-4})

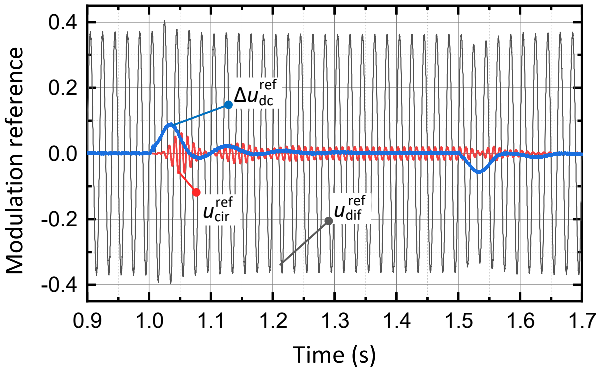

Fig. 4.25 Voltage references for upper branch of phase A (*Case* B_1)

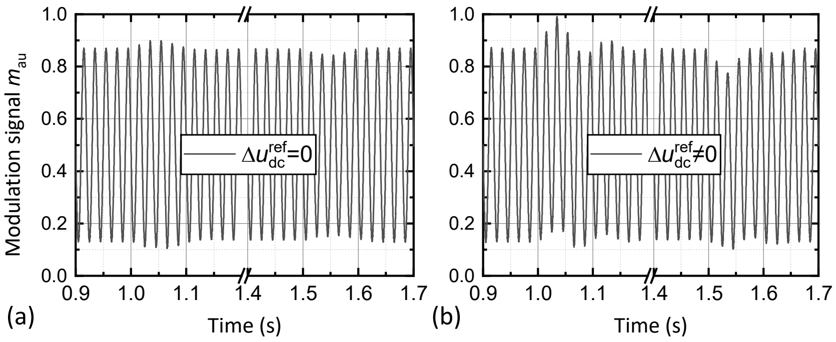

Fig. 4.26 Comparison of the composite modulation references of phase A upper branch m_{au}^{ref} (*Case* B_1)

4.5 Summary

This chapter has investigated a feasible connection topology for integrating renewable energy into a railway feeder station. A full converter station is realised by the MMC back to back conversion system, the renewable generation is connected to the DC-link inside the MMC. The wind generator is used to supply the traction load or supply to the grid. Other types of RESs can also be integrated in the same way.

The intermittent nature of renewable energy and fast changing characteristic of traction load challenge the stable power delivery. Single phase traction load further aggravates the situation by introducing low frequency oscillating power on the DC link. A systematic approach has been proposed to eliminate the oscillation power issue and reduce voltage deviations in transient response. By controlling common mode reference signal from the current perspective, the traction power supply converter can exchange power through DC-link without oscillation. Further by adding extra DC voltage stabilisation control loop, DC voltage is strictly controlled to the rated value in steady state and more than 75% deviation on 10 MW step change can be reduced.

Modelling and design considerations for the MMC back to back conversion system are explained under this control approach. The advantage of the proposed scheme is that the internal control freedom of MMC system is further utilised to actively solve these issues without resorting to large passive devices.

In conclusion, the proposed system is shown to provide a stable DC-link interface for renewable integration in the railway traction supply system, and has the potential to save the investment cost for grid connection converter in RES. Energy storage system can also be interfaced with the DC bus to mitigate the intermittent renewable energy while still benefits from the stable DC voltage performance.

Chapter 5

Modular multilevel converter with energy storage integration

5.1 Review of energy storage system integration in railway power supply

5.1.1 Energy storage research and application in railway

Two types of train braking methods are used in traction system [107]: the electric braking (regenerative brake) and traditional friction braking (air brake). During the regenerative braking, the traction motor is operating in generator mode where kinetic energy is converted back to electrical energy. If the regenerative energy is not consumed by nearby trains, stored by ESS or converted back to the grid, this might lead to 'inadmissible increase' in the catenary voltage [108]. A considerable part of the braking energy may still be dissipated via resistors [108]. To reduce the energy waste, ESS can be used to store the surplus energy and release it whenever needed. Energy storage devices can be applied to railway power supply stations or to running trains.

Onboard energy storage in railway trains

ESS can be mounted on vehicles and the vehicle can run without overhead line. This onboard ESS solution reduces transmission loss and wayside facilities but increases the train weight and space occupation. Because the onboard ESS solution is off the scope of this chapter, this chapter focuses on the Wayside Energy Storage (WES) applications.

Stationary energy storage in railway network

The advantage of stationary ESS over onboard solution is that there are fewer constraints in space and weight than onboard ESS. Additionally, one energy storage station can absorb and support energy for multiple trains. An ES railway station not only improves energy efficiency by storing braking energy, but also supports other trains' acceleration and reduces peak power demand especially in grid capacity limit condition. It can stabilise voltage between distant substations and can provide load-shifting capability.

The real world application of implementing wayside ESS has shown to achieve energy saving up to 30% [109]. There are four main regenerative energy storage devices, including battery storage, superconducting magnetic energy storage (SMES), ultracapacitor storage, and flywheel energy storage [107].

Demonstrable projects and commercial products

Bombardier adopted the supercapacitor into its 'Energstor' prototype wayside energy storage system for up to 5 kWh capacity [110]. This system has not only shown the braking energy recovery and power flow levelling functions but also the ability to improve system voltage quality at required locations without the need for additional traction power substations [111].

Hitachi developed stationary energy storage (SESS) technologies between 2007 and 2014 [112].The lithium-ion batteries are used in seven sites. Two main functions of these SESS are energy saving and provision of emergency power supply in power outage period. The system has power up to 3 MW, 160 kWh capacity.

Woojin Industrial System company (Korean) developed energy storage stations for 750 V, 1.5 kV, 55 kV railway system and claimed to save energy from 20 to 30% [113].

Siemens manufactured 'Sitras SES' static energy storage system with double layer capacitor bank which can provide 1 MW peak power and 1400 A DC current for DC traction service [114]. [115] It could help the power supply system to avoid short periods of electrical failure and could also reduce the effect on the voltage drop of many trains or trams consuming power simultaneously"

In 2012, Southeastern Pennsylvania Transit Authority built the 'Letterly' substation equipped with lithium-ion battery storage controlled by ABB converters. The result demonstrated that the substation achieved $28,000 in energy savings in 2015 plus an additional $143,000 in frequency regulation (FR) revenue [116]. Later supercapacitor is added into the original design at Griscom substation and the result is a hybrid system and higher FR performance and higher revenue.

In 2019, ABB manufactured the 'Enviline ERS' [117], an energy recuperation system for DC rail transportation. It uses supercapacitors for short term storage and recovery of the braking energy. Batteries are used for additional benefits and revenue generating services [117].

The existing ES substation examples prove that 10% to 30% energy cost can be saved through energy recovery. It reduces the peak demand charges and penalties and reduces the expenditures to sustain network voltage. It can be predicted that substation with energy storage is indispensable in the future smart railway network.

5.1.2 MMC integration with energy storage system

The application of integrating the energy storage device into MMC architecture has gradually emerged over the last decade. Conventional ESS station requires large numbers of battery connected in series, should any single battery module in battery string fails, the system will be adversely affected, and the power rating is degraded. The system having the high number of series connected battery is susceptible to reliability issues.

The MMC-ESS topology however provides a simpler way to integrate battery or superapacitor to each submodule, so that each individual battery module's voltage rating is lower. Then a shorter string of batteries is acceptable. Because fewer batteries are connected in series the system may become more reliable. Furthermore, the SOC balancing can be integrated within the MMC control system without the need of external balancing device. [118] proved that an MMC-ESS system has better efficiency at light loads than two level inverter solution which is favourable for electric vehicle.

Applications and system configuration

The MMC-ESS design is recognised with the advantage of modularity, expandability, high reliability. Typical topology and its application is briefly introduced as follows.

Application in transportation In 2012, Coppola [119] proposed to use ESS in every single submodule in the MMC for a traction drive in the 750 V DC line. In 2015, Vasiladiotis [120] proposed direct integration of AC/AC MMC converter with batteries to achieve distributed energy storage on 16.7 Hz railway system. In 2016, Qurran et al. [121] used the MMC-ESS system to reduce the overall weight of inductors used in the original boost converters. In 2019, Gan et al. [122] used MMC-ESS to support a variable DC bus with flexible charging functions and to realise fault tolerance for machine drive on an electric vehicle. 2020, Guo [123] applied MMC-ESS in railway power conditioner, so additional ESS station is avoided.

Application in grid service [124] used MMC-ESS to compensate active and reactive power for grid power quality enhancement. In [125], Ota presented ESS based single star MMC configuration to improve the reliability, availability and flexibility with LVRT and ZVRT. [126, 127] supported the grid with load levelling and frequency control by quickly delivering active power from the MMC-ESS system with fault-tolerant design. [128] designed an MMC-ESS with reactive power compensation function for grid voltage regulation. [129] integrated supercapacitors in submodules to gain independent control ability for AC and DC power, then the system can provide low power grid ancillary service such as fast frequency response.

Interface with MMC submodule According to the published materials, MMC modules can be connected with ESS in three ways [130]: direct connection without any interface converter [125, 121], connection through non-isolated buck boost converter [131] or connection through isolated dual active bridge [132]. In [133], Puranik pointed out that although the direct connection without DC-DC interface has the highest efficiency and lowest cost, the battery lifespan will be affected by low frequency components. These oscillating components have negative effect on the performance and lifespan. To deal with this issue, Wersland designed an alternative solution to DC-DC converters by using a passive filter to mitigate harmful AC currents [134]. Most researchers choose the buck-boost converter due to its simplicity.

Flexible connection topology Most of the proposed MMC-ESS system in the literature adopt the symmetric design where all submodules are integrated with the same type of ESS device. However, there is no restriction to force every one of the MMC submodule be employed with same type of ESS.

[131] discussed the power transfer between phase legs and phase arms when DERs are flexibly integrated into submodules. Soong and Lehn concluded that when a DERs is only connected to a subset of phase arms, a steady state fundamental frequency difference current is required, and they designed the controller to eliminate both 2nd and 3rd harmonic current to maximise efficiency [131].

Schroeder et al. [130] investigated MMC with unevenly equipped lithium-ion batteries. Different configurations of modular converters are evaluated in [130], and the author outlooked that diverse sources and loads with DC voltage terminals can be connected into the modular converter system.

[132] Bayat and Yadani proposed a PV and BES connected MMC system. Both PV and BES are interfaced with submodule DC side with DAB converters. So the embeded BES can smooth the output power of the PV generation and can also limit the rate of change of power delivered to the host grid. In [132], BES power references are designed to achieve power exchange capability to eliminate small power mismatches without creating differential currents and to keep the injected grid current balanced despite unequal PV generation in different legs.

In [128], a hybrid energy storage is designed by introducing supercapacitors for short-term power fluctuation compensation and by using batteries for long-term power compensation. Batteries and supercapacitors are distributed into the upper and lower arm of the MMC.

MMC-ESS control scheme

In early research applications, the discrepancy in different ESS modules are not considered, and all submodules are connected with the same type of battery. These batteries are treated as identical, so the battery energy balancing is not specifically designed. For instance in [119], the inherent energy balance in the MMC control and modulation is able to achieve the self-balancing of each ESS integrated submodule. Recently, due to the increase complexity of the topology and realistic demand for reliability, advanced active balancing control are introduced which is only realised in the hierarchical control scheme.

Hierarchical control Due to the system complexity, hierarchical control [120] is commonly used in the MMC-ESS system not only for balancing the internal ESS energy but also for different possible operation modes. The normal operation modes can be classified by the power flow direction, by load demand to grid capacity, or by charging state of the ESS.

Submodule SOC balancing control Due to the battery characteristics, the SOC and SOH of submodule ESS cannot be identical. Additional to the original MMC terminal current control, the SOC of the batteries in each arm have to be specially controlled.

In a simple DC bus support application, SOC balancing can be easily achieved by selecting the battery according to SOC level [122]. However, in the system for AC conversion, specially balancing scheme is required.

[135] proposed a balancing scheme for SOC balancing among phases, in single phase and in single arm. The SOC balancing is usually achieved through DC current and circulating current reference design. During the SOC balancing process, DC current and excessive circulating current still need to be attenuated at the same time. [129] pointed out that the controller for power exchange shall not affect the control philosophy of an MMC.

Typically, the inter phase balance is achieved by generating common mode current or voltage reference [120]. And the inter arm balance is achieved through imposing harmonic current associated with reactive injection in other phases to keep AC current unaffected [120]. Finally, the intra-arm submodule balance is achieved either by independent adding voltage references in PWM modulation or by sorting algorithm [121] in NLM modulation.

Most of the published works have used the above mentioned method. The result is a nested multiple current control loops. This control scheme usually contains power calculation, current reference design, current tracking and current suppression control [123].

The complex controller setup is difficult to tune and brings coupling effect. [136] Wand et al. proposed an improved voltage balancing control by adjusting AC and DC modulation indexes simultaneously. They analysed the transfer function from modulation index to the capacitor voltage and then optimise the coefficient between AC and DC modulation index to prevent over-modulation.

Fault tolerant control One of the advantage of MMC-ESS is that the ESS decoupled the MMC instantaneous power at DC and AC sides, so the grid fault can be overcome by the internal ESS directly.

[126] examined the valid operating regions in the battery failure mode, and concluded that the MMC integrated with ESS banks is capable of exchanging power normally even 33% of the ESS banks are shutdown.

[127] investigated operation in the short circuit fault condition, a novel SOC balancing control and voltage allocation method is designed to keep continuous power exchange with the grid. The design is a mixed of half-bridge module and full-bridge module for DC fault.

SOH control In recent years, researchers further investigated the SOH unbalance issue in this system. Because of the SOC balancing control schemes, batteries will inevitably demonstrate SOH deviation in the long time operation due to the different battery characteristics and uneven stresses. SOH balance is crucial to the optimise system capacity and lifespan. Li at al. [137] proposed a relative SOH evaluation method from average SOC variation rates and analysed the relation among SOH, DOD as well as

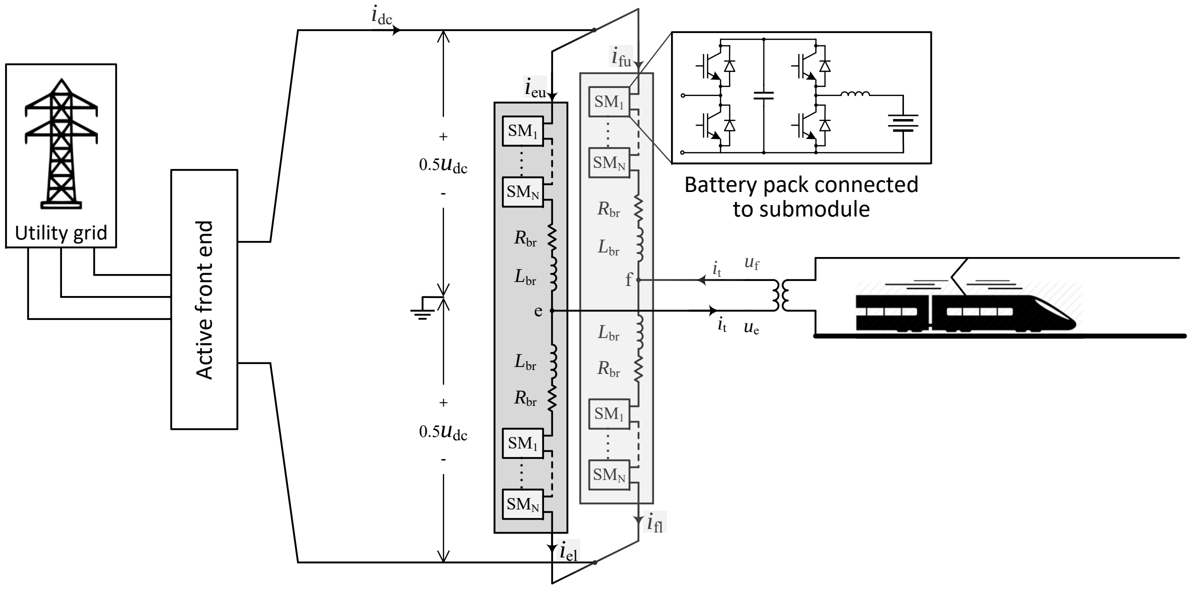

Fig. 5.1 System structure of the ESS integrated SFC station

life-cycles. Recycled batteries can be then be used as a cost-effective solution for grid service ESS application.

5.2 Model predictive controller for ESS integrated MMC substation

5.2.1 MMC-ESS topology

The topology of MMC-ESS substation is shown in Figure 5.1. A bi-directional buck boost converter is used to connect the battery pack unit to each submodule in MMC arms. Grid connection active front provides DC-link, and the MMC-ESS station inverts the voltage into single phase AC for the traction load. The focus is on MMC-ESS control, so the grid side converter is simplified by DC voltage source and the traction load is represented by single phase current reference.

Battery units can be bypassed or connected depending on the system operation mode. Other isolated DC/DC converters are also suitable for ESS integration. Assume all battery units are identical in each arm, four different types of connection topology are given in Figure 5.2.

Firstly all four arms can be connected with one type of battery unit as shown in 5.2(a). In this homogeneous type of ESS integration, the system operates like a conventional MMC and the batteries in MMC arms are charged and discharged evenly. Figure 5.2(b) shows a type of connection where only one phase is equipped with ESS or different phases have different types of storage device. In the second connection, energy management between phases is crucial. The MMC phase with ESS actively provides or absorbs energy to maintain the stable operation of all phase legs. In the last two types of ESS connection configurations, ESS is only connected to one arm in each phase. This type of unbalance configuration requires power exchange between upper and lower arms.

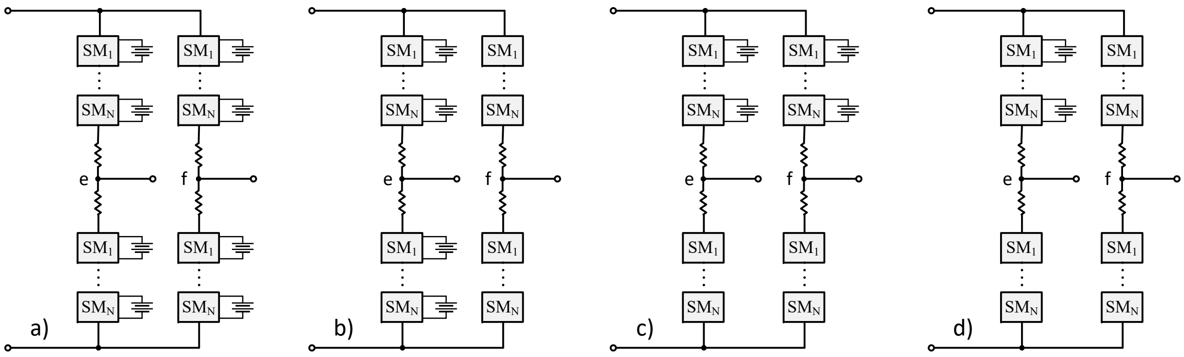

Fig. 5.2 Topology of ESS integration into MMC substation

5.2.2 Analysis of MMC arm energy dynamics

In the previous Chapter 3, the general form of ideal steady state arm energy variation reference is derived. That designed reference (3.49) describes the steady state condition when AC terminal current is a fundamental sine wave and the DC-link current is constant. When the MMC arms are connected with ESS, specific amount of power has to be delivered between each phase/arm, so that the ESS are successfully charged or discharged.

In this section, the general power exchange result in a single MMC phase arms is analysed. The instantaneous power exchanged at MMC arms are determined by DC and AC side voltage and current. Assume the general expression of AC side current and a general expression of DC side current are formulated as (5.1):

$$\begin{aligned} i_{\mathrm{ac}}(t,\alpha) &= I_{\mathrm{ac,m},\alpha}\cos\left(\alpha\omega_{\mathrm{g}}t-\varphi_{\alpha}\right), && \alpha = 1,2,3,4,5\ldots \\ i_{\mathrm{dc}}(t,\beta) &= I_{\mathrm{com},0}+I_{\mathrm{com},\beta}\cos\left(\beta\omega_{\mathrm{g}}t-\varphi_{\beta}\right), && \beta = 1,2,3,4,5\ldots \end{aligned} \tag{5.1}$$

where both AC terminal current and DC-link current contain arbitrary harmonics content having the frequency α and β times of the grid frequency; φ_α and φ_β are the phase lag for each harmonics respectively.

Because the DC-link impedance is small, we assume the AC voltage and DC voltage are approximately controlled as $V_{\mathrm{ac,m}}\cos(\omega_g t)$ and V_{dc}, then instantaneous voltage and current in upper and lower arms are expressed in (5.2) and (5.3):

$$\begin{aligned} u_{\mathrm{u}}(t,\alpha,\beta) = {} & 0.5V_{\mathrm{dc}} - I^{*}_{\mathrm{com},0}R_{\mathrm{br}} - I_{\mathrm{com},\beta}R_{\mathrm{br}}\cos\left(\beta\omega_{\mathrm{g}}t-\varphi_{\beta}\right) \\ & - V_{\mathrm{ac,m}}\cos\left(\omega_{\mathrm{g}}t\right) + I_{\mathrm{ac,m},\alpha}\left|Z_{\alpha}\right|\cos\left(\alpha\omega_{\mathrm{g}}t-\varphi_{\alpha}-\arg\left(Z_{\alpha}\right)\right) \\ u_{\mathrm{l}}(t,\alpha,\beta) = {} & 0.5V_{\mathrm{dc}} - I^{*}_{\mathrm{com},0}R_{\mathrm{br}} - I_{\mathrm{com},\beta}R_{\mathrm{br}}\cos\left(\beta\omega_{\mathrm{g}}t-\varphi_{\beta}\right) \\ & + V_{\mathrm{ac,m}}\cos\left(\omega_{\mathrm{g}}t\right) - I_{\mathrm{ac,m},\alpha}\left|Z_{\alpha}\right|\cos\left(\alpha\omega_{\mathrm{g}}t-\varphi_{\alpha}-\arg\left(Z_{\alpha}\right)\right) \end{aligned} \tag{5.2}$$

$$\begin{aligned} i_{\mathrm{u}}(t,\alpha,\beta) &= I^{*}_{\mathrm{com0}} + I_{\mathrm{com},\beta}\cos\left(\beta\omega_{\mathrm{g}}t-\varphi_{\beta}\right) - \frac{1}{2}I_{\mathrm{ac,m},\alpha}\cos\left(\alpha\omega_{\mathrm{g}}t-\varphi_{\alpha}\right) \\ i_{\mathrm{l}}(t,\alpha,\beta) &= I^{*}_{\mathrm{com0}} + I_{\mathrm{com},\beta}\cos\left(\beta\omega_{\mathrm{g}}t-\varphi_{\beta}\right) + \frac{1}{2}I_{\mathrm{ac,m},\alpha}\cos\left(\alpha\omega_{\mathrm{g}}t-\varphi_{\alpha}\right) \end{aligned} \tag{5.3}$$

Then the instantaneous power exchanged at upper and lower arm of one MMC phase can be calculated by $p_{\text{au}} = u_{\text{au}} i_{\text{au}}$, $p_{\text{al}} = u_{\text{al}} i_{\text{al}}$. The results of power expressions in upper and lower arms are classified into 8 groups, and the following list summarises the power exchange characteristics in each arm.

① and ② are external power terms which steadily charge or discharge each arm. ③ and ④ describe the mechanism of energy transfer between upper and lower arms. ⑤ represents the energy loss in the system. ⑥ – ⑧ represent the pure power oscillation terms which do not contribute to the averaged arm energy change.

① All arms are charged by a DC steady power from DC-link.
② If $\alpha = 1$ (AC terminal current has 50 Hz component), each arm is charged by single phase AC power. And the result is 100 Hz AC component and a steady DC component.
   If $\alpha > 1$, oscillated power exists having $(\alpha + 1)\,\omega_g$ and $(\alpha - 1)\,\omega_g$ frequency components.
③ If $\beta = 1$ (DC-link current has 50 Hz component), the upper arm energy is transferred to lower arm and 100 Hz oscillation component is introduced.
   If $\beta > 1$, oscillated power exists in each arm with opposite sign having $(\beta + 1)\,\omega_g$ and $(\beta - 1)\,\omega_g$.
④ If $\alpha = \beta$ (e.g. introducing 50 Hz in common mode current) lower arm energy will be transferred to the upper arm.
   If $\alpha \neq \beta$, then only oscillating power exists and has the frequency of $(\alpha + \beta)\omega_g$ and $(\alpha + \beta)\omega_g$.
⑤ Energy loss in both arms due to the impedance having steady DC component and oscillation components of $2\alpha\omega_g$, $2\beta\omega_g$.
⑥ The result power is a 50 Hz oscillation due to the coupling between AC voltage and DC current.
⑦ Power oscillation having $\alpha\omega_g$ frequency components.
⑧ Power oscillation having $\beta\omega_g$ frequency components.

5.2.3 MMC-ESS control scheme

Based on the aforementioned discussions, it is evident that 50 Hz common mode current or same frequency currents on AC/DC sides introduces energy exchange between upper and lower arms. However, one of the objective of optimal operation status in MMC is that I_{com} contains no AC components. Therefore, ESS configurations like Figure 5.2(a) and 5.2(b) are favoured than the other two.

Hierarchical control scheme

Figure 5.3 shows the hierarchical control approach applied to this MMC-ESS substation system. In this approach, the top level controller decides the current operation mode. An operation mode controller defines the ESS connection status, the amount of power reference delivered between ESS, grid, and traction network. Then depending on the power command, current references for each MMC phase are calculated. The MMC controller realises the current tracking and energy balance by adjusting the MMC arm voltage. In conventional cascaded linear control scheme, these objectives are realised by

Table 5.1 The instantaneous power exchange in MMC upper and lower arm

No.	Arm	Power expression
①	u	$0.5V_{\mathrm{dc}}I^*_{\mathrm{com0}}-\left(I^*_{\mathrm{com0}}\right)^2R_{\mathrm{br}}$
	l	$0.5V_{\mathrm{dc}}I^*_{\mathrm{com0}}-\left(I^*_{\mathrm{com0}}\right)^2R_{\mathrm{br}}$
②	u	$\frac{1}{4}V_{\mathrm{ac,m}}I_{\mathrm{ac,m},\alpha}\left(\cos\left(\left(\alpha+1\right)\omega_gt-\varphi_\alpha\right)+\cos\left(\left(\alpha-1\right)\omega_gt-\varphi_\alpha\right)\right)$
	l	$\frac{1}{4}V_{\mathrm{ac,m}}I_{\mathrm{ac,m},\alpha}\left(\cos\left(\left(\alpha+1\right)\omega_gt-\varphi_\alpha\right)+\cos\left(\left(\alpha-1\right)\omega_gt-\varphi_\alpha\right)\right)$
③	u	$-V_{\mathrm{ac,m}}I_{\mathrm{com},\beta}\left(\cos\left(\left(\beta+1\right)\omega_gt-\varphi_\beta\right)+\cos\left(\left(\beta-1\right)\omega_gt-\varphi_\beta\right)\right)$
	l	$+V_{\mathrm{ac,m}}I_{\mathrm{com},\beta}\left(\cos\left(\left(\beta+1\right)\omega_gt-\varphi_\beta\right)+\cos\left(\left(\beta-1\right)\omega_gt-\varphi_\beta\right)\right)$
④	u	$+\frac{1}{2}I_{\mathrm{com},\beta}I_{\mathrm{ac,m},\alpha}\left\lvert Z_\alpha\right\rvert\Big(\cos\left(\left(\alpha+\beta\right)\omega_{\mathrm{g}}t-\left(\varphi_\alpha+\varphi_\beta\right)-\arg\left(Z_\alpha\right)\right)$ $+\cos\left(\left(\alpha-\beta\right)\omega_{\mathrm{g}}t-\left(\varphi_\alpha-\varphi_\beta\right)-\arg\left(Z_\alpha\right)\right)\Big)$ $+\frac{1}{4}I_{\mathrm{ac,m},\alpha}I_{\mathrm{com},\beta}R_{\mathrm{br}}\Big(\cos\left(\left(\alpha+\beta\right)\omega_{\mathrm{g}}t-\left(\varphi_\alpha+\varphi_\beta\right)\right)$ $+\cos\left(\left(\alpha-\beta\right)\omega_{\mathrm{g}}t-\left(\varphi_\alpha-\varphi_\beta\right)\right)\Big)$
	l	$-\frac{1}{2}I_{\mathrm{com},\beta}I_{\mathrm{ac,m},\alpha}\left\lvert Z_\alpha\right\rvert\Big(\cos\left(\left(\alpha+\beta\right)\omega_{\mathrm{g}}t-\left(\varphi_\alpha+\varphi_\beta\right)-\arg\left(Z_\alpha\right)\right)$ $+\cos\left(\left(\alpha-\beta\right)\omega_{\mathrm{g}}t-\left(\varphi_\alpha-\varphi_\beta\right)-\arg\left(Z_\alpha\right)\right)\Big)$ $-\frac{1}{4}I_{\mathrm{ac,m},\alpha}I_{\mathrm{com},\beta}R_{\mathrm{br}}\Big(\cos\left(\left(\alpha+\beta\right)\omega_{\mathrm{g}}t-\left(\varphi_\alpha+\varphi_\beta\right)\right)$ $+\cos\left(\left(\alpha-\beta\right)\omega_{\mathrm{g}}t-\left(\varphi_\alpha-\varphi_\beta\right)\right)\Big)$
⑤	u	$-\frac{1}{4}\left(I_{\mathrm{ac,m},\alpha}\right)^2\left\lvert Z_\alpha\right\rvert\left(\cos\left(2\alpha\omega_{\mathrm{g}}t-2\varphi_\alpha-\arg\left(Z_\alpha\right)\right)+\cos\left(\arg\left(Z_\alpha\right)\right)\right)$ $-\frac{1}{2}\left(I_{\mathrm{com},\beta}\right)^2R_{\mathrm{br}}\left(\cos\left(2\beta\omega_{\mathrm{g}}t-2\varphi_\beta\right)+1\right)$
	l	$-\frac{1}{4}\left(I_{\mathrm{ac,m},\alpha}\right)^2\left\lvert Z_\alpha\right\rvert\left(\cos\left(2\alpha\omega_{\mathrm{g}}t-2\varphi_\alpha-\arg\left(Z_\alpha\right)\right)+\cos\left(\arg\left(Z_\alpha\right)\right)\right)$ $-\frac{1}{2}\left(I_{\mathrm{com},\beta}\right)^2R_{\mathrm{br}}\left(\cos\left(2\beta\omega_{\mathrm{g}}t-2\varphi_\beta\right)+1\right)$
⑥	u	$-I^*_{\mathrm{com0}}V_{\mathrm{ac,m}}\cos\left(\omega_gt\right)$
	l	$+I^*_{\mathrm{com0}}V_{\mathrm{ac,m}}\cos\left(\omega_gt\right)$
⑦	u	$-\frac{1}{4}V_{\mathrm{dc}}I_{\mathrm{ac,m},\alpha}\cos\left(\alpha\omega_{\mathrm{g}}t-\varphi_\alpha\right)+\frac{1}{2}I_{\mathrm{ac,m},\alpha}I^*_{\mathrm{com,0}}R_{\mathrm{br}}\cos\left(\alpha\omega_{\mathrm{g}}t-\varphi_\alpha\right)$ $+I^*_{\mathrm{com0}}I_{\mathrm{ac,m},\alpha}\left\lvert Z_\alpha\right\rvert\cos\left(\alpha\omega_{\mathrm{g}}t-\varphi_\alpha-\arg\left(Z_\alpha\right)\right)$
	l	$+\frac{1}{4}V_{\mathrm{dc}}I_{\mathrm{ac,m},\alpha}\cos\left(\alpha\omega_{\mathrm{g}}t-\varphi_\alpha\right)-\frac{1}{2}I_{\mathrm{ac,m},\alpha}I^*_{\mathrm{com,0}}R_{\mathrm{br}}\cos\left(\alpha\omega_{\mathrm{g}}t-\varphi_\alpha\right)$ $+I^*_{\mathrm{com0}}I_{\mathrm{ac,m},\alpha}\left\lvert Z_\alpha\right\rvert\cos\left(\alpha\omega_{\mathrm{g}}t-\varphi_\alpha-\arg\left(Z_\alpha\right)\right)$
⑧	u	$+\frac{1}{2}V_{\mathrm{dc}}I_{\mathrm{com},\beta}\cos\left(\beta\omega_{\mathrm{g}}t-\varphi_\beta\right)-I^*_{\mathrm{com,0}}I_{\mathrm{com},\beta}R_{\mathrm{br}}\cos\left(\beta\omega_{\mathrm{g}}t-\varphi_\beta\right)$ $-I^*_{\mathrm{com0}}I_{\mathrm{com},\beta}R_{\mathrm{br}}\cos\left(\beta\omega_{\mathrm{g}}t-\varphi_\beta\right)$
	l	$+\frac{1}{2}V_{\mathrm{dc}}I_{\mathrm{com},\beta}\cos\left(\beta\omega_{\mathrm{g}}t-\varphi_\beta\right)-I^*_{\mathrm{com,0}}I_{\mathrm{com},\beta}R_{\mathrm{br}}\cos\left(\beta\omega_{\mathrm{g}}t-\varphi_\beta\right)$ $-I^*_{\mathrm{com0}}I_{\mathrm{com},\beta}R_{\mathrm{br}}\cos\left(\beta\omega_{\mathrm{g}}t-\varphi_\beta\right)$

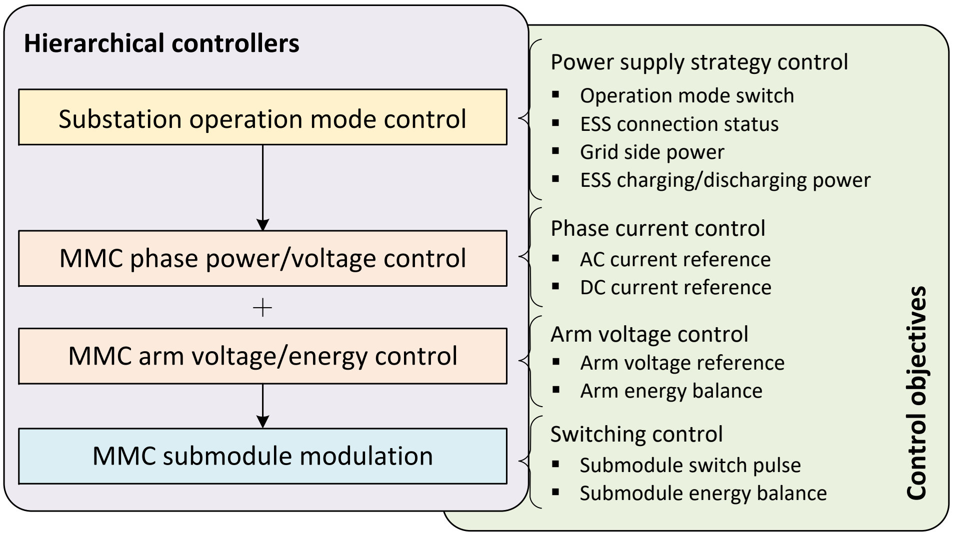

Fig. 5.3 Hierarchical approach for MMC-ESS substation operation control

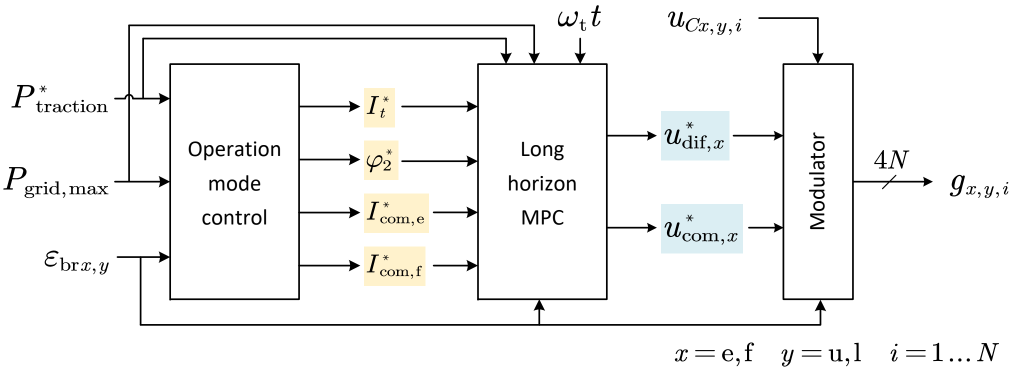

Fig. 5.4 Measurement and control scheme

separate control loops. In this chapter, the MPC explained in section 3 is modified for this task. Finally, the bottom layer is a typical MMC modulator which converts the continuous voltage reference signals into binary switch pulses.

Figure 5.4 illustatrates the measurement inputs and control reference outputs of each controller. Note that the required power at traction load side P^*_{traction}, the grid power limit $P_{\text{grid,max}}$ and MMC arm branch energy ε_{br} are sent into the 'Operation mode controller', and then depending on the operation mode decision, the current reference is updated to the MPC. The rest part of this scheme is similar to conventional MMC control shown in Section 3

Operation mode selection

Figure 5.5 shows the proposed strategy for operation mode decision making. It is realised by multiple switch cases. Each mode is explained in the following list.

Mode 1 In ‘Mode 1’, the traction network is fully supplied by the grid side power. This is the normal power supply mode like substation without ESS.

Mode 2 In ‘Model 2’ the traction network is fully supplied by the grid, and the ESS is also charged through the grid side power flow.

Mode 3 ‘Mode 3’ is a compromised operation status when the traction load is greater than the grid capacity and the stored energy in ESS is lower than minimum SOC limit. In this case, the traction load has to be reduced to maintain the network voltage.

Mode 4 In ‘Mode 4’ the grid and ESS jointly supply the traction load. Because the traction load exceeds the current grid capacity, the extra power is supplied by ESS.

Mode 5 ‘Mode 5’ is similar to ‘Mode 3’ where the required traction power cannot be fulfilled even the grid and the ESS are supplying at the same time.

Mode 6 ‘Mode 6’ is selected when the train is in decelerating and the power is flowing back to the substation. ESS can absorb the regenerative energy.

Mode 7 ‘Mode 7’ is selected when ESS cannot be charged any further and the regenerative power cannot flow back to the grid due to the front end topology or regulation. Then the excessive energy will be dissipated through the resistor to maintain the network voltage.

Mode 8 ‘Mode 8’ is selected when ESS SOC reaches its upper limit and the reverse power flow can be accepted by the grid. So the regenerative power is fed back to the grid.

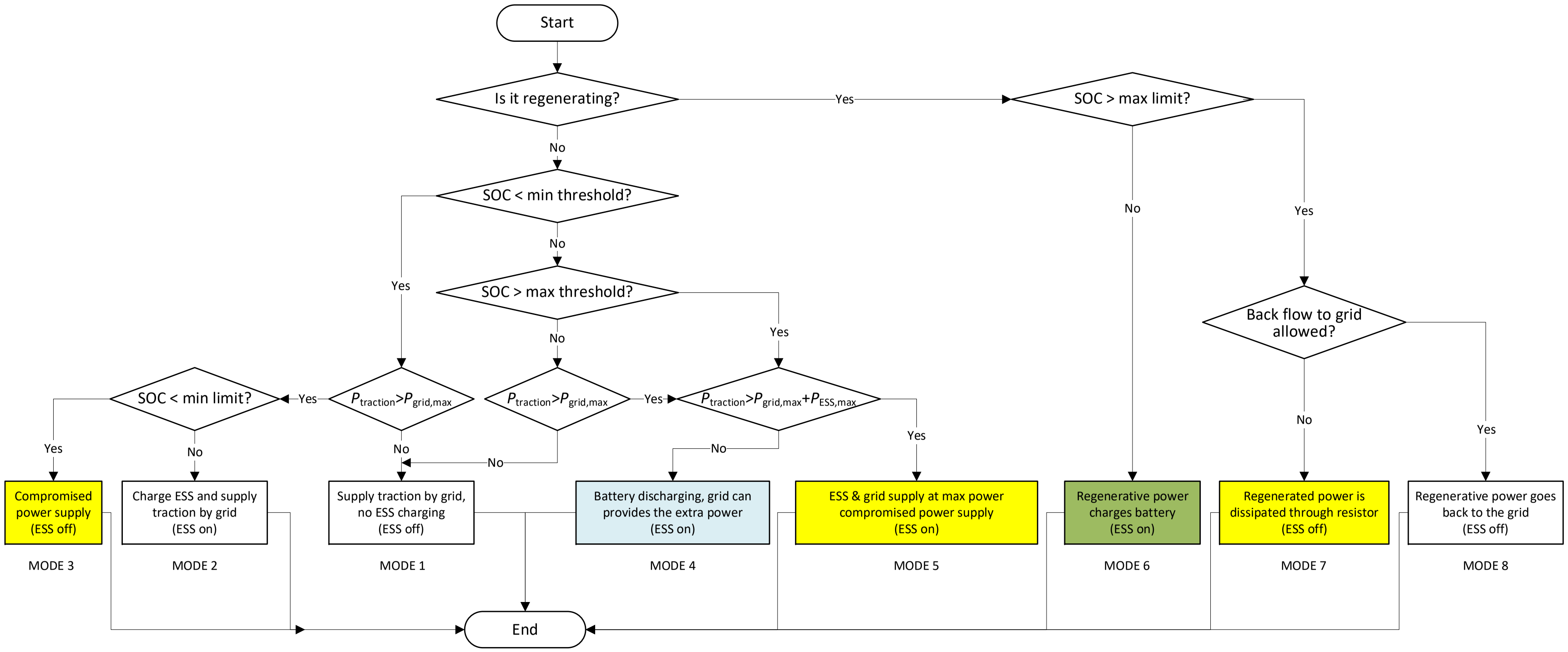

Fig. 5.5 MMC-ESS substation power supply mode decision flowchart

Model predictive controller

System model The model predictive controller implemented in this MMC-ESS system is similar to the previous Chapter 3.2. The system equation is shown as below which is the same to (3.22).

$$
\begin{aligned}
\frac{\mathrm{d}}{\mathrm{d}t}\boldsymbol{x}_{(8\times1)} &= \boldsymbol{A}_{t(8\times8)}\boldsymbol{x}_{(8\times1)} + \boldsymbol{B}_{t(8\times4)}\boldsymbol{u}_{(4\times1)} \\
\boldsymbol{x} &= \begin{bmatrix} i_{\mathrm{te}}, & i_{\mathrm{tf}}, & i_{\mathrm{com,e}}, & i_{\mathrm{com,f}}, & \varepsilon_{\mathrm{eu}}, & \varepsilon_{\mathrm{fu}}, & \varepsilon_{\mathrm{el}}, & \varepsilon_{\mathrm{fl}} \end{bmatrix}^{\top} \\
\boldsymbol{u} &= \begin{bmatrix} u_{\mathrm{dif,e}} - \frac{u_{\mathrm{t}}}{2}, & u_{\mathrm{dif,f}} + \frac{u_{\mathrm{t}}}{2}, & u_{\mathrm{com,e}} - \frac{V_{\mathrm{dc}}}{2}, & u_{\mathrm{com,f}} - \frac{V_{\mathrm{dc}}}{2} \end{bmatrix}^{\top}
\end{aligned}
$$

Constraints Similarly, the design of state variable and control input constraint for the MMC-ESS MPC has all the inequalities derived in Section 3.3.2. Additionally, another constraint (5.4) is added.

$$
I_{\mathrm{DC,min}} \leq \left(i_{\mathrm{com,e}} + i_{\mathrm{com,f}}\right) \leq I_{\mathrm{DC,max}} \tag{5.4}
$$

The DC current limit value $I_{\mathrm{DC,min}}$ and $I_{\mathrm{DC,max}}$ represent the grid condition. Should any contingency happens at the grid side, $I_{\mathrm{DC,max}}$ is updated to represent the maximum grid side available power. If the grid side rectifier does not allow back flow power (e.g. thyristor based front end), the $I_{\mathrm{DC,min}}$ can be set to zero so that all regenerative energy are stored inside the ESS.

Control reference design The key difference lies in the arm energy control that in the ESS integration case, MMC arms with ESS are deliberately charged or discharged. Common mode current reference for each phase and energy reference for each arm are modified in this chapter and the other formulation procedures remains the same. As shown in Figure 5.4 the common mode current reference is given by outer controller as $I_{\mathrm{com,e}}$ and $I_{\mathrm{com,f}}$. The DC component of the arm exchanged power at each arm is expressed by (5.5)

$$
p_{x,y,\mathrm{dc}} = \frac{1}{2}V_{\mathrm{dc}}I^{*}_{\mathrm{com},x} - R_{\mathrm{dc}}\left(I^{*}_{\mathrm{com},x}\right)^{2} + \frac{\sqrt{2}}{8}U_{\mathrm{t}}I^{*}_{\mathrm{t}}\cos\left(\varphi_{\mathrm{t}}\right) - \frac{1}{2}\left(I^{*}_{\mathrm{t}}\right)^{2}\left|Z_{\mathrm{t}}\right|\cos\left(\arg\left(Z_{\mathrm{t}}\right)\right), \tag{5.5}
$$

where x represents the MMC phase leg $x = \mathrm{e,f}$ and y represents the exact arm $y = \mathrm{u,l}$. Note that DC component current charges both arm equally. Integrate this result (5.5) and combine it with the oscillating component given in (3.49). The energy reference for MPC controller is shown as follows:

$$
\begin{aligned}
\varepsilon^{*}_{\mathrm{eu}}\left(t, I^{*}_{\mathrm{com,e}}, I^{*}_{\mathrm{t}}, \varphi_{\mathrm{t}}\right) = {} & \left(\frac{1}{2}V_{\mathrm{dc}}I^{*}_{\mathrm{com,e}} - R_{x}\left(I^{*}_{\mathrm{com,e}}\right)^{2} + \frac{\sqrt{2}}{8}U_{\mathrm{t}}I^{*}_{\mathrm{t}}\cos\left(\varphi_{\mathrm{t}}\right) - \frac{1}{2}\left(I^{*}_{\mathrm{t}}\right)^{2}\left|Z_{\mathrm{t}}\right|\cos\left(\arg\left(Z_{\mathrm{t}}\right)\right)\right)t \\
& - \frac{\sqrt{2}}{\omega_{\mathrm{t}}}V_{\mathrm{t}}I^{*}_{\mathrm{com,e}}\sin\left(\omega_{\mathrm{t}}t\right) + \frac{\sqrt{2}}{\omega_{\mathrm{t}}}I^{*}_{\mathrm{t}}I^{*}_{\mathrm{com,e}}\left|Z_{\mathrm{t}}\right|\sin\left(\omega_{\mathrm{t}}t - \varphi t - \arg\left(Z_{\mathrm{t}}\right)\right) \\
& - \frac{\sqrt{2}}{4\omega_{\mathrm{t}}}V_{\mathrm{dc}}I^{*}_{\mathrm{t}}\sin\left(\omega_{\mathrm{t}}t - \varphi_{\mathrm{t}}\right) + \frac{\sqrt{2}}{2\omega_{\mathrm{t}}}R_{\mathrm{br}}I^{*}_{\mathrm{com,e}}I^{*}_{\mathrm{t}}\sin\left(\omega_{\mathrm{t}}t - \varphi_{\mathrm{t}}\right) \\
& + \frac{1}{4\omega_{\mathrm{t}}}V_{\mathrm{t}}I^{*}_{\mathrm{t}}\sin\left(2\omega_{\mathrm{t}}t - \varphi_{\mathrm{t}}\right) - \frac{1}{4\omega_{\mathrm{t}}}\left(I^{*}_{\mathrm{t}}\right)^{2}\left|Z_{\mathrm{t}}\right|\sin\left(2\omega_{\mathrm{t}}t - 2\varphi_{\mathrm{t}} - \arg\left(Z_{\mathrm{t}}\right)\right)
\end{aligned} \tag{5.6}
$$

$$
\begin{aligned}
\varepsilon_{\mathrm{el}}^{*}\left(t, I_{\mathrm{com,e}}^{*}, I_{\mathrm{t}}^{*}, \varphi_{\mathrm{t}}\right) = & \left(\frac{1}{2} V_{\mathrm{dc}} I_{\mathrm{com,e}}^{*} - R_{x}\left(I_{\mathrm{com,e}}^{*}\right)^{2} + \frac{\sqrt{2}}{8} U_{\mathrm{t}} I_{\mathrm{t}}^{*} \cos\left(\varphi_{\mathrm{t}}\right) - \frac{1}{2}\left(I_{\mathrm{t}}^{*}\right)^{2}\left|Z_{\mathrm{t}}\right| \cos\left(\arg\left(Z_{\mathrm{t}}\right)\right)\right) t \\
& + \frac{\sqrt{2}}{\omega_{\mathrm{t}}} V_{\mathrm{t}} I_{\mathrm{com,e}}^{*} \sin\left(\omega_{\mathrm{t}} t\right) - \frac{\sqrt{2}}{\omega_{\mathrm{t}}} I_{\mathrm{t}}^{*} I_{\mathrm{com,e}}^{*}\left|Z_{\mathrm{t}}\right| \sin\left(\omega_{\mathrm{t}} t - \varphi t - \arg\left(Z_{\mathrm{t}}\right)\right) \\
& + \frac{\sqrt{2}}{4\omega_{\mathrm{t}}} V_{\mathrm{dc}} I_{\mathrm{t}}^{*} \sin\left(\omega_{\mathrm{t}} t - \varphi_{\mathrm{t}}\right) - \frac{\sqrt{2}}{2\omega_{\mathrm{t}}} R_{\mathrm{br}} I_{\mathrm{com,e}}^{*} I_{\mathrm{t}}^{*} \sin\left(\omega_{\mathrm{t}} t - \varphi_{\mathrm{t}}\right) \\
& + \frac{1}{4\omega_{\mathrm{t}}} V_{\mathrm{t}} I_{\mathrm{t}}^{*} \sin\left(2\omega_{\mathrm{t}} t - \varphi_{\mathrm{t}}\right) - \frac{1}{4\omega_{\mathrm{t}}}\left(I_{\mathrm{t}}^{*}\right)^{2}\left|Z_{\mathrm{t}}\right| \sin\left(2\omega_{\mathrm{t}} t - 2\varphi_{\mathrm{t}} - \arg\left(Z_{\mathrm{t}}\right)\right)
\end{aligned}
\tag{5.7}
$$

Cost function J_i is the cost calculated from output AC current and internal common mode current tracking error. J_ε is the cost of internal arm energy tracking error. These costs are evaluated over the prediction horizon length N_{h} and then are added up to the final cost J as shown in (5.8).

$$
\begin{aligned}
J_i &= \lambda_{i\mathrm{dif}}\left(i_t - I_t^{*}\right)^2 + \lambda_{i\mathrm{com,e}}\left(i_{\mathrm{com,e}} - I_{\mathrm{com,e}}^{*}\right)^2 + \lambda_{i\mathrm{com,e}}\left(i_{\mathrm{com,e}} - I_{\mathrm{com,e}}^{*}\right)^2 \\
J_\varepsilon &= \lambda_{\varepsilon\mathrm{e}}\left(\left(\varepsilon_{\mathrm{eu}} - \varepsilon_{\mathrm{eu}}^{*}\right)^2 + \left(\varepsilon_{\mathrm{el}} - \varepsilon_{\mathrm{el}}^{*}\right)^2\right) + \lambda_{\varepsilon\mathrm{f}}\left(\left(\varepsilon_{\mathrm{fu}} - \varepsilon_{\mathrm{fu}}^{*}\right)^2 + \left(\varepsilon_{\mathrm{fl}} - \varepsilon_{\mathrm{fl}}^{*}\right)^2\right) \\
J &= \sum_{l=0}^{N_{\mathrm{h}}} J_i\left(k+l+1\right) + J_\varepsilon\left(k+l+1\right)
\end{aligned}
\tag{5.8}
$$

Note that when ESS is not symmetrically connected, the weight factor λ_ε has to be adjusted according to the capacity value. For instance, if only phase e is connected to the ESS, the ratio $\frac{\lambda_{\varepsilon\mathrm{e}}}{\lambda_{\varepsilon\mathrm{f}}}$ shall equal to $\frac{\sum \varepsilon_{\mathrm{f}}}{\sum \varepsilon_{\mathrm{e}}}$.

5.3 Simulation and discussion

To fully use the operation mode proposed in Figure 5.5, real data is required. To simplify the simulation validation of the proposed method, the ESS is controlled to its nominal value whenever possible and the charging and discharging performance are tested using the following profile.

5.3.1 Simulation settings

The proposed control scheme is tested for network support (discharging) and regenerative energy charging purposes. Figure 5.6 shows the designed test profile[1] in 4 stages. A grid power limit is set to trigger ESS operation. This limit value can represent the capacity of the front end converter or the grid capacity in a fault condition. Four operation status are explained as follows:

S1 From 0 s to 1 s, the traction load is light, and the power grid can support the traction 100% without any additional support from ESS.

---

[1] The profile is for function test only which does not represent any real cases.

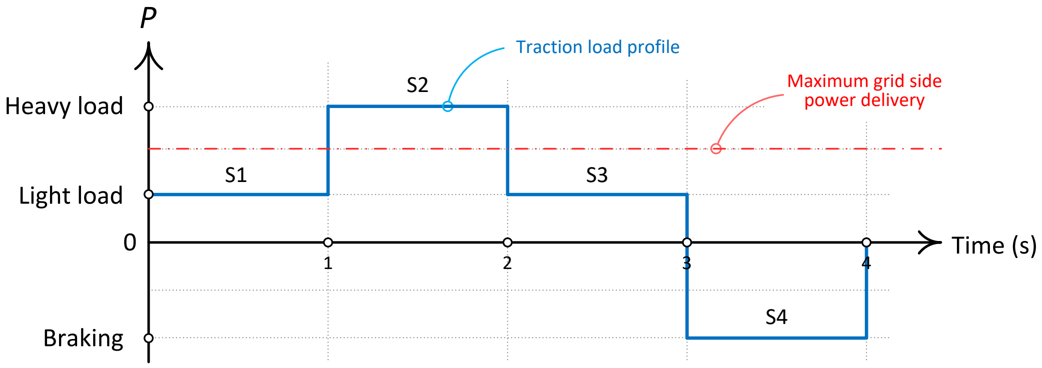

Fig. 5.6 Power profile for MMC-ESS simulation test

- S2 From 1 s to 2 s, the traction load increases to heavy load condition and the power demand exceeds the maximum grid limit. In this case, ESS in the MMC substation supplies the extra power to securely support the network.
- S3 From 2 s to 3 s, the traction load reduces to S1 state; the grid power can fully support the traction load and if necessary ESS can be charged.
- S4 From 3 s to 4 s, the traction power becomes negative meaning the train is decelerating; the regenerative energy flows through the substation will be stored into the ESS system.

5.3.2 Simulation result

Two set of simulation is evaluated based on MMC-ESS topology shown in Figure 5.2.

Type-I: Two MMC phase legs integrated with ESS

In the Type I connection, all MMC phases (e,f) are integrated with the same type of ESS. Figure 5.7 shows the DC and AC side power results.

It is evident that at S1, each the traction power matches DC-link power. But during S2 stage, the DC-link power is limited at 10 MW which is the grid power limit settings, the extra 5 MW is provided by ESS in all four arms. Then at S3 where the traction load is reduced back to 5 MW, the DC-link power not only supplies the traction load but also provide extra power to charge ESS to nominal SOC. Finally, at S4 stage, all regenerative power flows into the MMC phases, no power flows back to the grid as shown in Figure 5.7a. Although different power assignments switch between different operation modes, the traction side current is not affected (Figure 5.7b).

Common mode current of each phase shown in Figure 5.8 has the identical shape as the DC-link power because all four arms are equally connected with the same ESS.

In S2 stage, I_{com} increase to support heavier load, and the current is contributed from both the ESS and the grid.

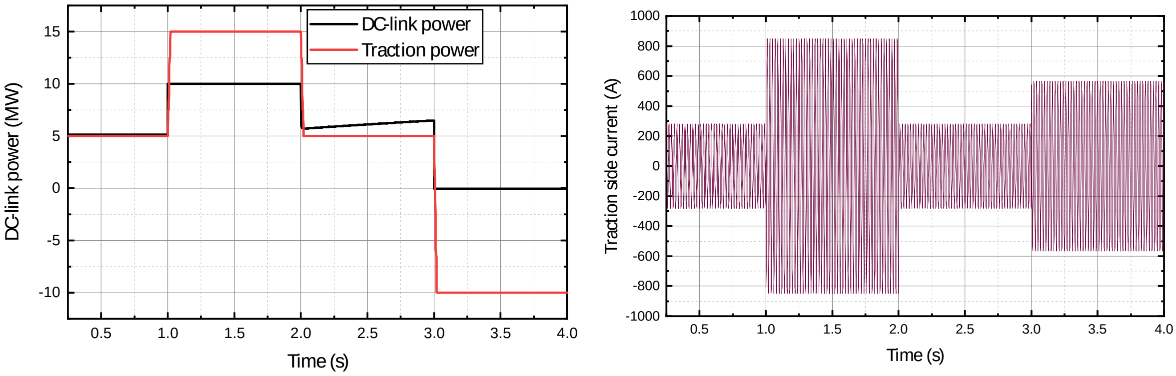

(a) DC and AC terminal power

(b) Traction side current

Fig. 5.7 Power and AC current result of the Type-I station

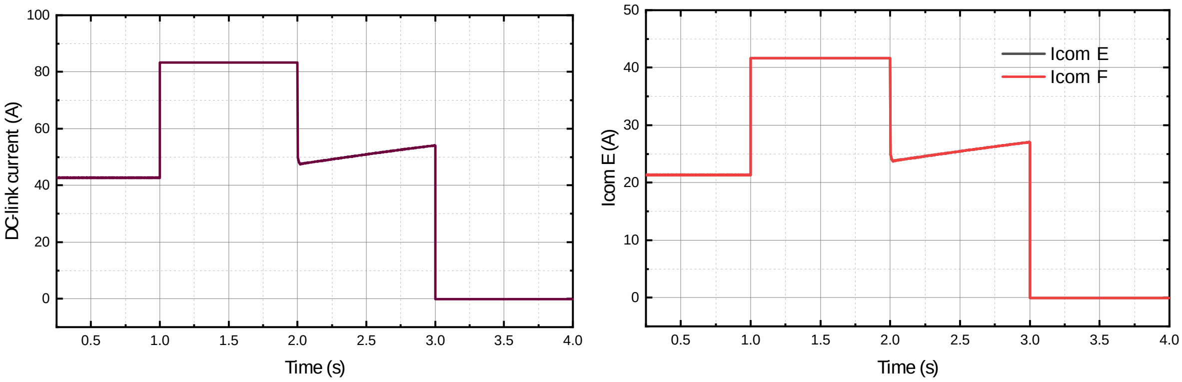

(a) DC-link current

(b) Common mode current of each phase

Fig. 5.8 DC current of the Type-I MMC-ESS station

In the S3 stage, I_{com} increase gradually though the traction load keeps the same. This is the result of battery charging reference generated by PI controller. The existence of the integrator accumulated the energy error so that the charging reference increased overtime.

In the S4 stage, I_{com} is controlled to zero, so that no power was flowing back to the grid. The ESS took whatever energy fed from the traction side.

In Figure 5.9, all four subfigures are also almost identical. It can be seen that at S1 the SOC of each arm stays the same and reduces at S2 for extra 5 MW power supply and then gradually gets charged by the grid at S3. Finally, at S4 stage, the regenerative power is equally absorbed into each arm.

Type-II: One MMC phase leg integrated with ESS

The second type of connection is that only phase e has ESS. Through Figure 5.10, we can observe that the system has almost the same performance as the previous Type I connection. The DC-link power is limited within 0 10 MW and the traction current is not adversely unaffected. ESS supports the extra power at S2 and slowly charge at S3. During S4 stage ESS in phase e took in all the back flow power.

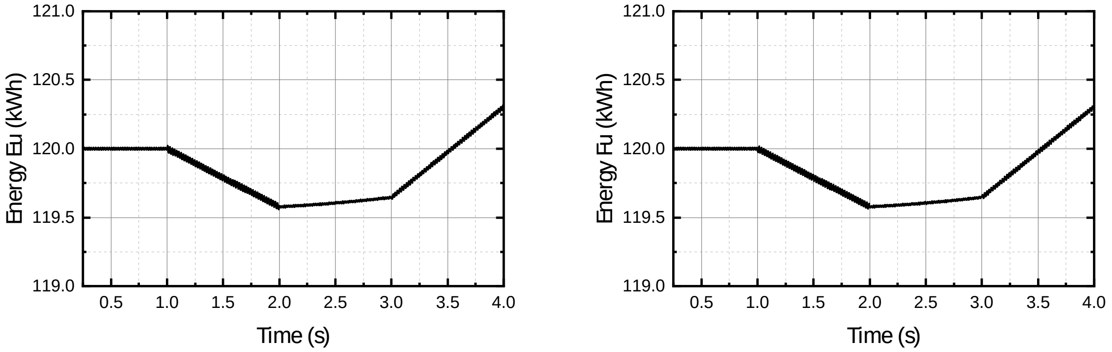

(a) Upper arm of phase E

(b) Upper arm of phase F

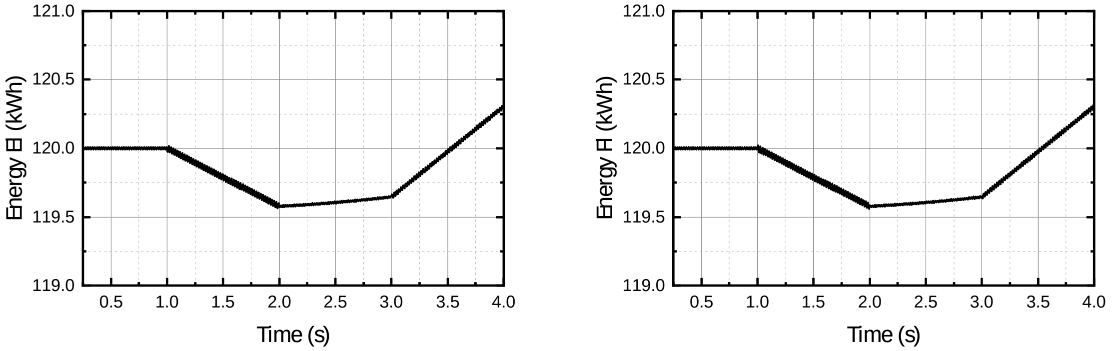

(c) Lower arm of phase E

(d) Lower arm of phase F

Fig. 5.9 Arm energy (filtered) of the Type-I MMC-ESS station

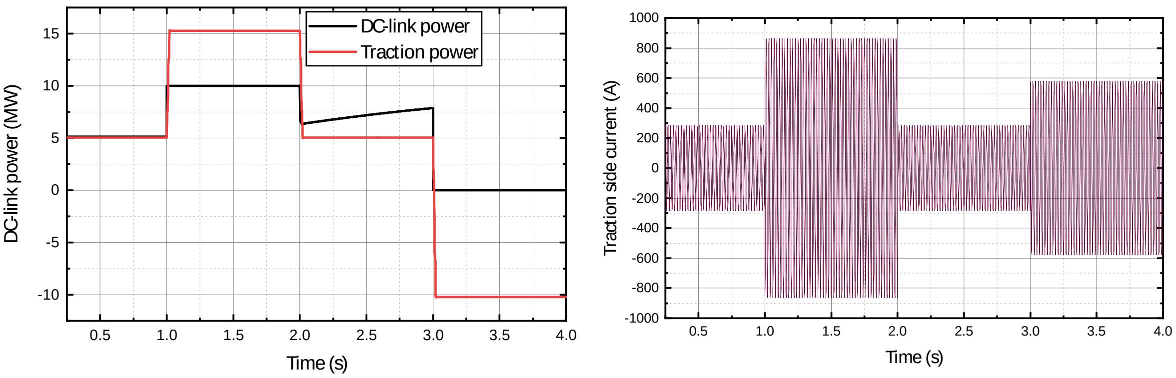

(a) DC and AC terminal power

(b) Traction side current

Fig. 5.10 Power and AC current result of the Type-II station

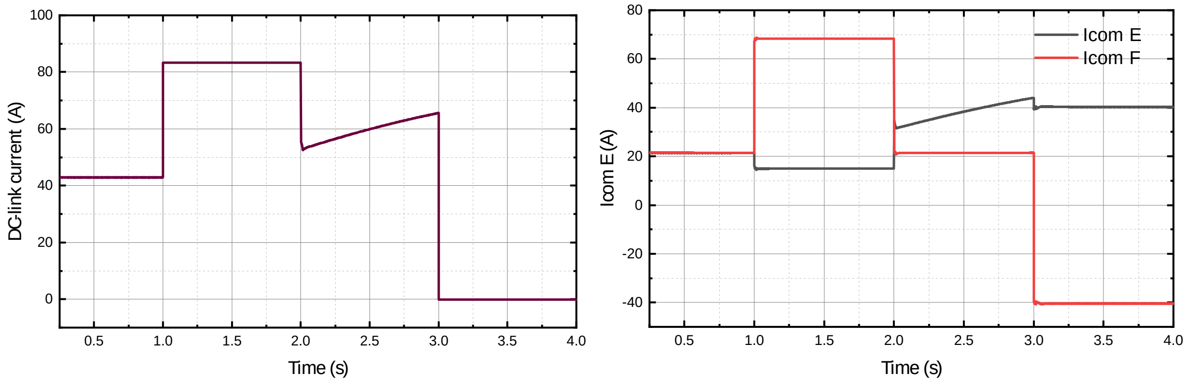

(a) DC-link current

(b) Common mode current of each phase

Fig. 5.11 DC current of the Type-II MMC-ESS station

Although in Figure 5.11, the DC-link is unchanged compared to Type I, the common mode is different. During S2 stage, current $I_{\text{com,e}}$ is much smaller than the Type I case and $I_{\text{com,f}}$ became higher meaning phase f was being charged by phase e. During S3, the ESS charging energy went into phase e which is shown in $I_{\text{com,e}}$ from 2 s to 3 s. At last, from 3 s to 4 s, $I_{\text{com,e}}$ equals to 40 A while $I_{\text{com,f}}$ is minus 40 A. This means, although the regenerative power symmetrically flows into both phase legs, the instantaneous power is redistributed inside the MMC with special controlled common mode current. The energy delivered to phase f is simultaneously transferred to phase e to keep DC-link current at zero.

Figure 5.12 plots the energy stored in each MMC arm where arm branches in phase e has similar pattern as Type I test. The energy stored in phase f has the normal dynamic like conventional MMC. This shows that the asymmetrical ESS connection to one phase can successfully operate by the proposed control method.

5.4 Summary

In this chapter, the long horizon MPC is modified to support MMC-ESS based substation operation. A hierarchical control approach is designed to switch among different operation modes.

The proposed system can support the traction network as an uninterruptible power supply when the grid capacity is limited due to various reasons. If braking power is sent back through the network to the MMC-ESS station, ESS can recycle the energy if the grid/rectifier does not require back flow power. When the station switches its operation mode, the traction network supply will not be affected. The MPC guarantees the fast dynamics and ideal internal arm energy control performance. Even in the asymmetric ESS connection, the phase with no ESS integration can still operate normally without any noticeable impact from the other phase. This provides possibility to equip different types of ESS such as supercapacitor and chemical batteries (e.g. cascade battery utilisation) to different phases.

This chapter presents a primary study of MPC controlled MMC-ESS railway substation application. In the future, constraints such as grid current rate of change limit, grid fault ride through, renewable

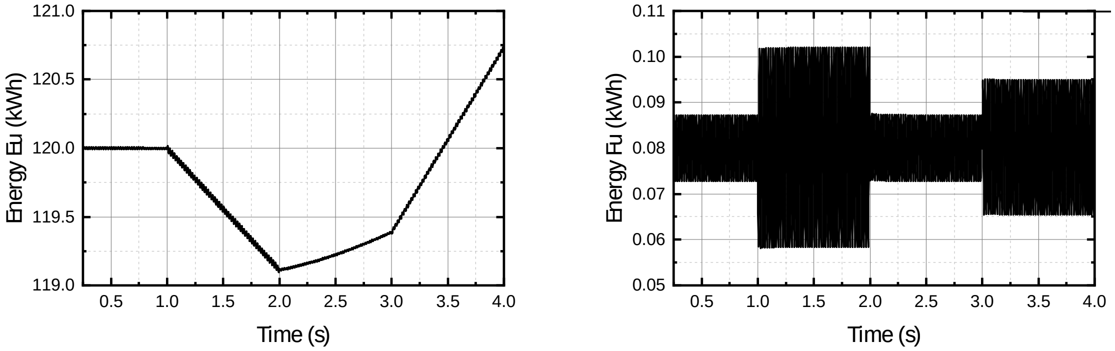

(a) Upper arm of phase E (b) Upper arm of phase F

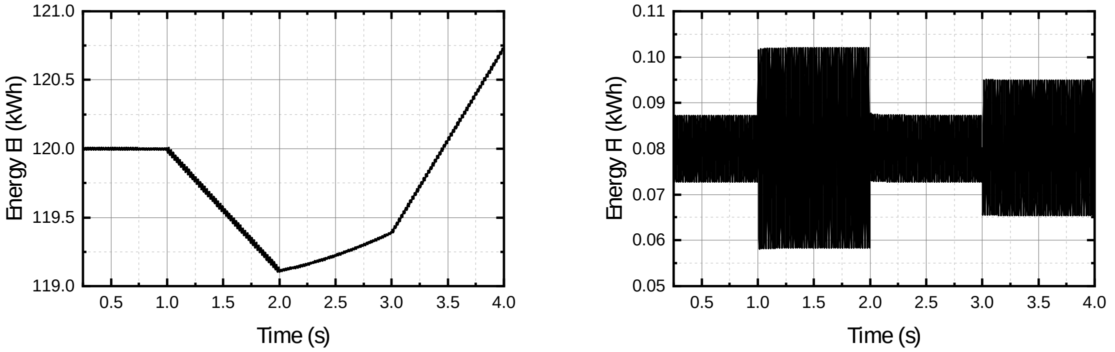

(c) Lower arm of phase E (d) Lower arm of phase F

Fig. 5.12 Arm energy (filtered) of the Type-II MMC-ESS station generation can be introduced to this scheme. There is also plenty of future work on system optimisation in the whole system design phase.

Chapter 6

Control of parallel SFC substations for continuous traction AC power supply

In the previous chapters, different applications of static converters are discussed in a single railway substation. A back to back MMC substation is able to connect three phase grid and single phase traction network in a decoupled manner, so that the traction side output AC voltage magnitude, frequency and phase can be freely controlled. Therefore, the neutral section can be eliminated between two substations and traction load can be supplied from multiple substations.

This chapter envisages the feasible future of using multiple substations to support railway traction network, viz. use parallel connected SFCs for continuous power supply to the trains without the need of neutral sections between two substations. Figure 6.1 illustrates the single-end substation TPSS and dual-end SFC based TPSS. It is obvious that the dual-end supply scheme can reduce the current load and can be used to gain a higher overall capacity than the single substation solution with the same power rating.

6.1 Overview of SFC applications for continuous railway power supply

The current trend of TPSS is to evolve towards a smarter railway grid using converter-based system [13]. Due to different phases in transformer substation supplied arms, the neutral sections are required which

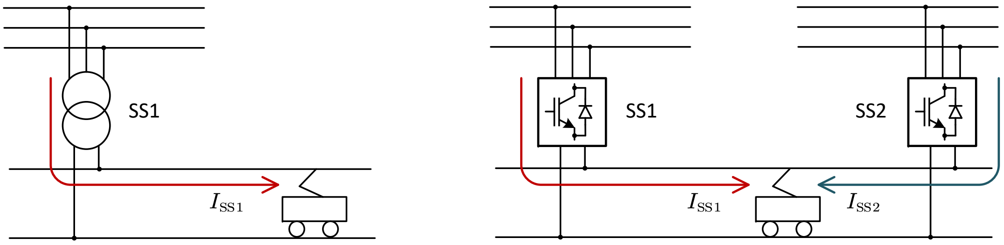

Fig. 6.1 Single-end power supply (left) and dual-end power supply (right)

precludes the possibility of continuous feeding between substations without the help of additional power conditioners.

Parallel feeding via additional power conditioner

The cophase power supply system is one way to directly cancel the neutral section at the exit of one substation [138]. Continuous current is achievable for locomotives between two supply arms from one substation. But the cophase connection cannot flexibly control the traction side voltage phase for arbitrary power sharing control when two or more cophase feeder substations are connected in parallel. The original objective of cophase is to reduce half of the neutral section and the discontinuity still exists between two substations.

Perin et al. realised load sharing between two stations by connecting power conditioner in between two supplied arms [139] and authors concluded that active power sharing between stations are necessary to help normalise the voltage. This power conditioning approach reduces capacity requirement of the converter and eliminate the overloading of transformers [139].

Parallel feeding in DC railway network

It is easier to use parallel feeding in DC railway network where distributed energy sources can be directly connected to the DC line [140], even the uni-directional diode rectifier substations can be connected in parallel to share traction loads [141]. To coordinate the distributed power supply, [142] developed a droop control method to ensure the proper power sharing between parallel sources, eliminate the voltage deviations and improve catenary network voltage profile.

Parallel feeding in AC railway network with SFC substations

SFCs have already been deployed in Germany, Switzerland, Sweden, Austria, Norway, Australia and UK's railway systems. However, the single phase output voltages are controlled to the same phase angle, i.e. SFCs on the same line are strictly synchronised [143]. This means the feeder stations' power is determined by the load condition without active control and each substation must have the capacity to supply the peak power of the train load. In the two SFCs in parallel scenario, traction power delivered from each side is approximately inversely proportional to the line distance between the train and SFCs [143, 144].

Droop control in AC supply has two degrees of freedom: the voltage magnitude and phase angle [100]. Chen et al. designed a droop controller based load sharing control for low voltage urban rail train [145]. A resistive droop method is used in this work where the output voltage decreases with active power. To improve the power share accuracy, the authors use large droop coefficient and designed an additional voltage compensation strategy to recover voltage drop [145].

The idea of continuous feeding scheme for AC railway network has also been reported. In [100], a train is placed at 17.5 km to the substation in a three feeder station network. These three feeder stations are controlled by one droop control profile and shares active power almost equally. [4] explained that in a train between two SFC continuous feedin condition, the train draws “a percentage of power substantially inversely proportional to the distance from each substation”. Sharifi et al. proposed a control system that enable each train to draw 50% of the traction power from each station in all positions along the network. This equal share principle will help to reduce the rating of each SFC station in future system or improving the capacity in the SFC installed system. In 2018, they proposed the ‘mesh feeding’ scheme and used a central smart controller to provide equal shared active power and limiting the reactive power [143]. Researchers also investigated the droop control for equal load sharing between two cascaded 3-level converters in parallel [146]. Chen et al. discussed a flexible traction power supply system where various types of renewable sources are integrated with converter based substations and these interconnected stations are coordinated by a centre controller [147]. The energy management strategy is optimised through day-ahead dispatch by MLP compensated with intra-day dispatch in rolling optimisation [147].

Summary

The literature review shows that droop controller are often designed to coordinate multiple substations’ traction load sharing. In these reports, the traction network is simplified into single node resistance and inductor between trains and stations [146, 4]. And the traction loads are always analysed in fixed position rather than continuously moving on the rail track [139, 100]. To better represent the railway network and the dynamic nature of the traction load, a simulation platform to model the SFC parallel feeding is built and reported in this chapter. And a special adaptive droop controller is designed to achieve a balanced power sharing between two SFC substations.

6.2 Modelling of a single track railway power supply network

This section presents the details of modelling the AC traction work system and the implementation in MATLAB/Simulink environment. The system model developed in this chapter provides an environment for designing and testing the proposed parallel feeding method. Each of the constituent parts are modelled by equivalent circuits in Simulink time domain simulation environment. Some assumptions in modelling are listed as follows:

- Nonlinear properties such as magnetic saturation, thermal effect in transformers and reactors are ignored.
- Harmonic components are not considered in modelling power converters and all AC component are controlled to produce sinusoidal signals.
- The high speed train is assumed to have unity power factor in steady state. Ideally no reactive power are to be produced by traction load [1].

---

[1] Due to the phase locked loop delay and sampling errors, tiny amount of reactive power exists.

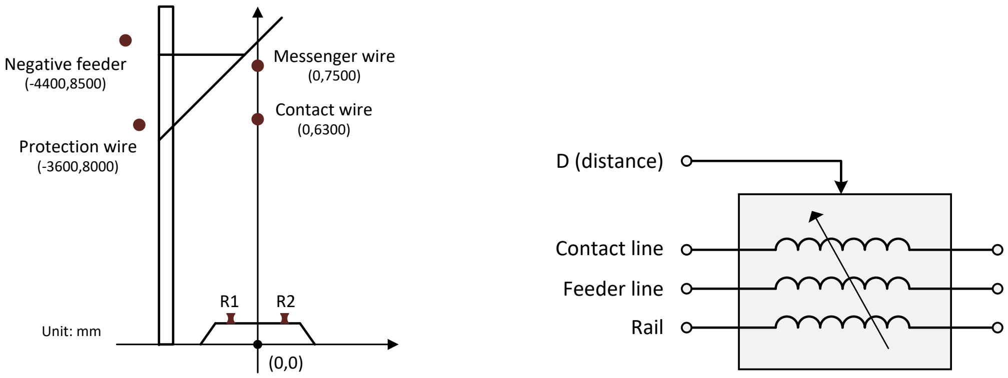

(a) Traction conductor spatial position

(b) Variable multi-conductor model

Fig. 6.2 Conductor line model

6.2.1 Substation and transformer model

Static frequency converter As elaborated in the previous chapters, SFC power supply station can be realised in different topology with different types of power electronics components. The similarity is the control principle that all the SFCs are operated as controlled voltage sources. Therefore, in the network simulation, the detailed power electronics dynamics can be simplified and SFCs are modelled as controlled voltage source where the supply terminal voltage is precisely controlled to reference signals.

Output transformer Output transformers or output reactors may or may not be needed based on the SFC design in a specific system. In this work, a three winding transformer is used to connect the SFC with the AT double voltage system and are treated as linear transformer.

Autotransformer The autotransformer stations can be described by two winding transformers with 1:1 turn ratio, and a two-winding linear transformer model is used to represent a AT station.

6.2.2 Conductor line model

The network comprises multiple conductor lines such as contact ware, messenger wire, feeder wire, protection wire, etc. A set of model parameter of a heavy-duty electrified railway line [148] is selected as the network model and its conductive line spatial position is demonstrated in Fig. 6.2a. This complex network can be simplified as parallel multi-conductor system and represented by mutual impedance model. The parameter of mutual impedance model needs to be updated at each sampling time according to different distance between two adjacent trains. Therefore, a constant valued impedance circuit model is not applicable.

Impedance values are derived using Carson theory. A detailed model of double track system has up to 8 to 10 conductors. To simplify the problem and still preserve the AT connection feature, a single-track

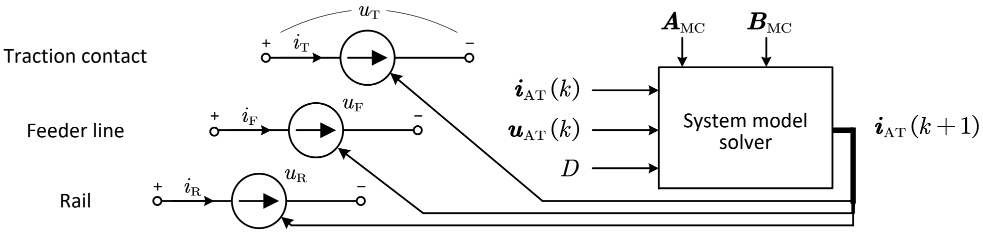

Fig. 6.3 Variable impedance multi-conductor component simulation model

line having 3 conductor model is used in this study. The circuit model is described in (6.1)

$$\boldsymbol{u}_N = \frac{\mathrm{d}}{\mathrm{d}t}\boldsymbol{\psi}_N + \boldsymbol{R}_N\boldsymbol{i}_N \approx \boldsymbol{L}_N\frac{\mathrm{d}}{\mathrm{d}t}\boldsymbol{i}_N + \boldsymbol{R}_N\boldsymbol{i}_N, \tag{6.1}$$

where $\boldsymbol{u}_N = [u_T \quad u_F \quad u_R]^T$ and $\boldsymbol{i}_N = [i_T \quad i_F \quad i_R]^T$ represent the voltage and current in each node and the subscript '$_T$' represents traction contact line, '$_F$' is for feeder line, and '$_R$' is for rail. The inductance and resistance matrices having self and mutual impedance respect to different distance value (D) are defined in (6.2)

$$\boldsymbol{L}_N = D\begin{bmatrix} L_T & L_{TF} & L_{TR} \\ L_{TF} & L_F & L_{FR} \\ L_{TR} & L_{FR} & L_F \end{bmatrix}, \quad \boldsymbol{R}_N = D\begin{bmatrix} R_T & R_{TF} & R_{TR} \\ R_{TF} & R_F & R_{FR} \\ R_{TR} & R_{FR} & R_F \end{bmatrix} \tag{6.2}$$

The multi-conductor can be modelled by a set of controlled current sources as expressed in (6.4). According to the dimensional analysis, current state matrix is constant which does not change with the conductor length, however the multi-conductor input matrix $\boldsymbol{A}_N$ is inverse proportional to the distance and has the dimension of 1/(m·H).

$$\frac{\mathrm{d}}{\mathrm{d}t}\boldsymbol{i}_N = \boldsymbol{A}_{MC}\boldsymbol{i}_N + \boldsymbol{B}_{MC}\boldsymbol{u}_N, \tag{6.3}$$

$$\boldsymbol{A}_{MC} = -\begin{bmatrix} L_T & L_{TF} & L_{TR} \\ L_{TF} & L_F & L_{FR} \\ L_{TR} & L_{FR} & L_F \end{bmatrix}^{-1}\begin{bmatrix} R_T & R_{TF} & R_{TR} \\ R_{TF} & R_F & R_{FR} \\ R_{TR} & R_{FR} & R_F \end{bmatrix}, \quad \boldsymbol{B}_{MC} = \frac{1}{D}\begin{bmatrix} L_T & L_{TF} & L_{TR} \\ L_{TF} & L_F & L_{FR} \\ L_{TR} & L_{FR} & L_F \end{bmatrix}^{-1} \tag{6.4}$$

Figure 6.4 illustrates the modelling principle in Simulink. To realise the variable multiconductor model, voltage of each line section is measured, then new matrices are updated according to line data and distance data. A discrete ODE solver is implemented using the trapezoidal method. The updated current state is then fed into each controlled current source. Note that in the real model shunt resistors with large resistance[2] are necessary to each line section to resolve the computational issue.

---

[2] The resistance is chosen as $10^8\,\Omega$.

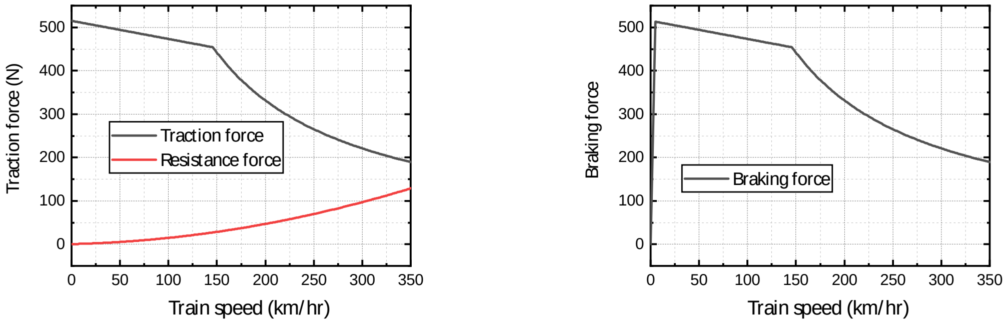

(a) Traction force and resistive force profile

(b) Braking force profile

Fig. 6.4 Traction load force profile

6.2.3 Traction load model

The CRH380BL is selected as the high-speed train model to generate power load according to the traction profile. One CRH380BL train has 16 carriages. It is a newly developed high-speed EMU which has high power and high-speed characteristics. The maximum operation speed is 310 km/hr with nominal total mass 972.8 t and maximum power for traction 18.4 MW

Traction force (F_{tr}) curve at full power is described by (6.5) which has constant power region and constant torque region. Braking force (F_{br}) curve at full power is expressed in (6.6). The resistive force (F_{re}) curve is approximated by "Davis" equation and the straight horizontal track scenario is formulated in (6.7).

$$F_{\mathrm{tr}} = \begin{cases} 515 & [\mathrm{kN}] \quad v \leq 146\,\mathrm{km/hr} \\ 454/v & [\mathrm{kN}] \quad v > 146\,\mathrm{km/hr} \end{cases} \tag{6.5}$$

$$F_{\mathrm{br}} = \begin{cases} 102.6v & [\mathrm{kN}] \quad v \leq 5\,\mathrm{km/hr} \\ 513 & [\mathrm{kN}] \quad 5\,\mathrm{km/hr} < v \leqslant 145\,\mathrm{km/hr} \\ 454/v & [\mathrm{kN}] \quad v > 146\,\mathrm{km/hr} \end{cases} \tag{6.6}$$

$$F_{\mathrm{re}} = 0.000755Mg + 192.55v' + 11.6\left(v'\right)^2 \; [\mathrm{N}], \quad v' = v + v_{\mathrm{wind}}, \tag{6.7}$$

where M is the train mass (set to 900 t), g is the gravitational acceleration, and v' is the sum of train speed and wind speed.

A special speed profile [3] with a typical duty cycle containing "accelerating", "cruising", "coasting" and "braking" is designed in the simulation. Each train will accelerate with the highest traction force, then drives with constant speed after reaching 300 km/hr, then starts coasting with zero traction force and finally starts to decelerate before arrival. This speed profile is specifically designed to 60 km travel distance in the simulation. Note that because of energy conversion efficiency the maximum power absorbed from the line is set to be 25% greater than the maximum regenerated power fed back to the contact line.

---

[3] The profile is designed to validate the proposed simulation environment and power sharing algorithm which is not representing any real scenario but a virtual design.

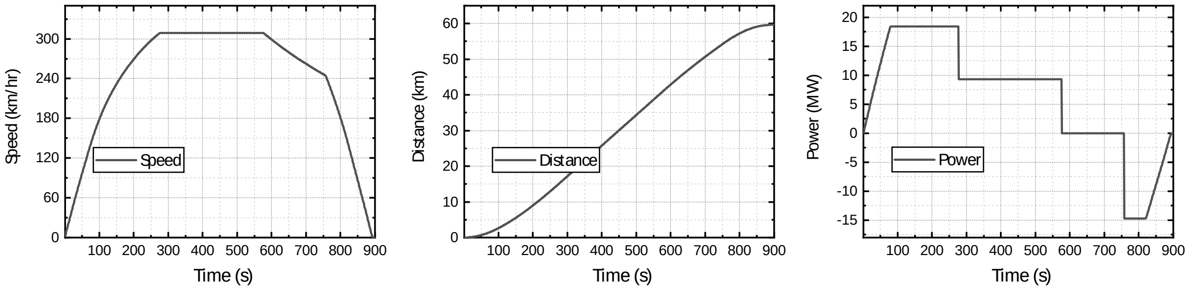

(a) Speed profile (b) Distance profile (c) Power profile

Fig. 6.5 Single traction load profile

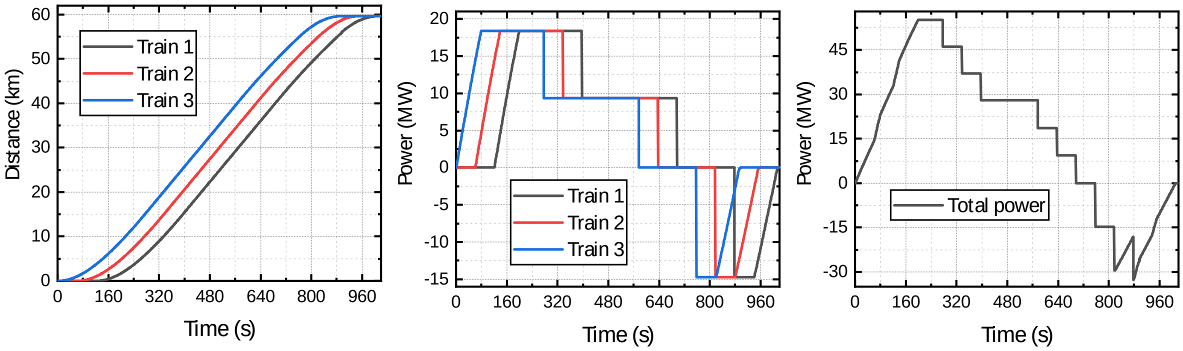

(a) Distance profile (b) Power profile (c) Total power profile

Fig. 6.6 Three trains' load profile

To test the power supply performance in the maximum power demand, a three train test is designed with the same speed profile. Each train will depart from one substation to another but has 1 minute departure interval for simulation test purpose. Figure 6.6 shows the designed load condition versus time. The figure shows that this load profile design generates different types of loading profile from a maximum active power about 55MW and a maximum regenerative power about 30MW.

High-speed trains use single phase active front converters to interface with the network. The power factor is guaranteed to be greater than 0.97. If the harmonics are ignored, the train load dynamics can be simplified as a controlled current source shown in Figure 6.7. The load current is calculated at each control time step and is injected into the network with the same phase angle as the supply voltage in steady state.

6.2.4 Simulation setup

The main model parameters of the traction network are listed in Table 6.1, 6.2 and 6.3

To explain the dynamic traction load simulation, a model of 2 trains and 1 AT station is presented in Figure 6.8 for simplicity. Both trains depart from left substation to the right. Each AT stations is in shunt connection to the network which splits the network into two sections. For this reason, the train model in

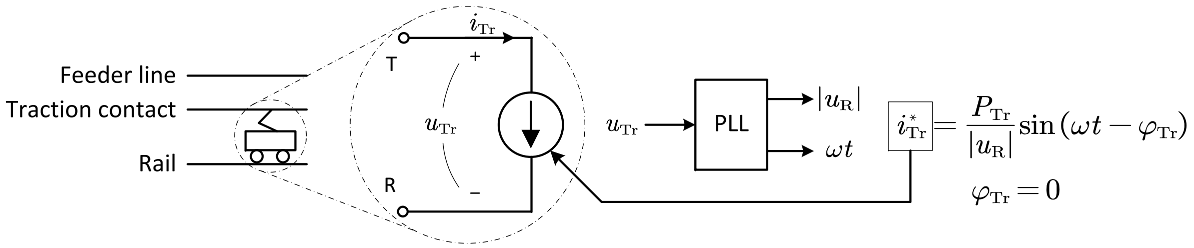

Fig. 6.7 Highspeed train simulation model

Table 6.1 Substation output transformer parameter

Nominal power rating	35 MW	Terminal voltage	27.5 kV
Short-circuit ratio	8%	Impedance ratio	1:4

Table 6.2 Autotransformer parameter

Nominal power rating	16 MW	Terminal voltage	27.5 kV
Short-circuit ratio	1.6%	Impedance ratio	1:4

Table 6.3 Multiconductor model parameter

Reactance data (50Hz)			
X_{T}	0.6019 Ω/km	X_{TF}	0.3272 Ω/km
X_{F}	0.7020 Ω/km	X_{TR}	0.3276 Ω/km
X_{R}	0.4617 Ω/km	X_{FR}	0.3402 Ω/km
Resistance data			
R_{T}	0.1445 Ω/km	R_{TF}	0.0515 Ω/km
R_{F}	0.2234 Ω/km	R_{TR}	0.0481 Ω/km
R_{R}	0.1098 Ω/km	R_{FR}	0.0414 Ω/km

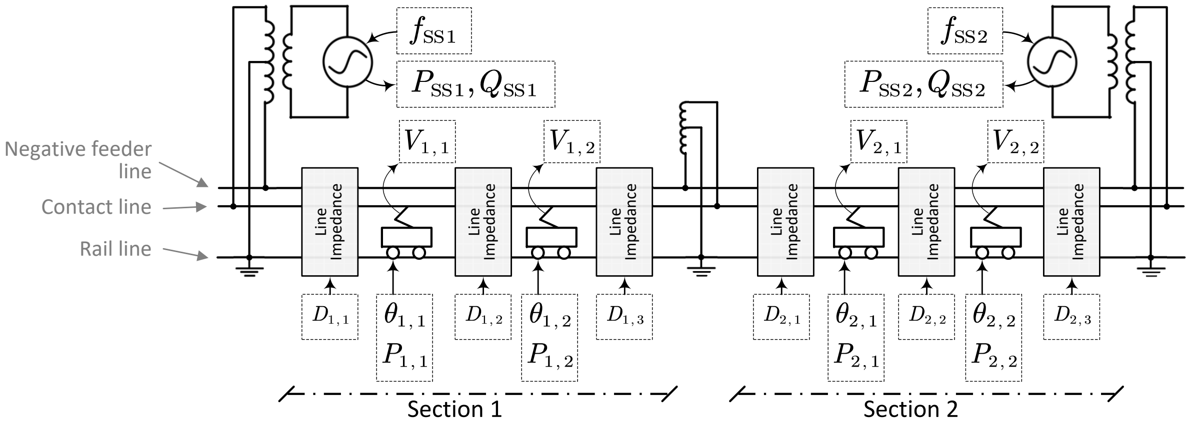

Fig. 6.8 Illustration of the dual-end parallel feeding simulation model

the simulation cannot pass through it. To solve this issue, two trains are assigned in each section and one multi-conductor model is connected between each model.

$D_{x,y}$ represents the conductor length of the yth multi-conductor component in the xth section ($\sum_y D_{x,y} = 60\,\text{km}$); $\theta_{x,y}$ is the yth train's distance to the left side substation in section x. At each simulation sampling time, the distance (contact line length) information is updated based on train location.

For example, if both trains are running in section 1, then real power value are assigned to both trains in section one. In this case, $D_{1,1...3}$ are calculated according to trains' position and $D_{2,1}, D_{2,2}$ are set to zero [4] for smooth transition when the train goes through the AT station into section 2.

If the one train is in section one and another one is in section two, only $P_{1,1}$ and $P_{2,2}$ are assigned with actual traction power values, while $P_{1,2}$ and $P_{2,1}$ are set to zero [5]. Then, $D_{1,3}, D_{2,1}$ are set to zero to ensure the smooth transition when the next train pass the AT station.

All of these settings are calculated and updated at each model sampling time. Two substations operating continuously and controlled by the droop controller which is presented in the next section. Voltage at the trains' pantograph and substation power data are logged. The model solver time step is set to 5 us and controller sampling time is 1 ms.

6.3 Adaptive droop controller for optimal power sharing of dual-end SFCs

Three key aspects are mainly considered in the power sharing control design: Joule effect losses on the conductor lines, voltage drop measured at traction load side and substation rating limit.

The proposed power sharing is realised through frequency droop control. As shown in Figure 6.9, each substation has a frequency droop line with different slope values. In the steady state, the voltage

---

[4] In the simulation, zero length implies zero impedance which is not feasible, so 0.1 m is used to approximate zero length.

[5] In the simulation 10^{-7} W is used instead of 0, to increase the numerical stability.

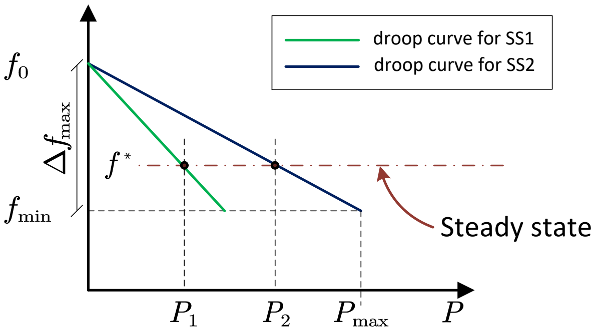

Fig. 6.9 Frequency droop line for two substations

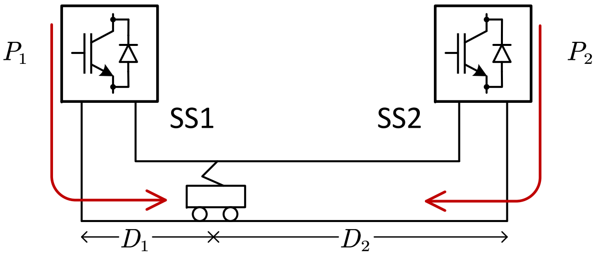

Fig. 6.10 Two SFC substation in dual-end feeding for single train load

frequency is converged to f^* then via the droop curve pattern. In this figure, we can find that SS1 is supporting the network with P_1 active power and SS2 is providing P_2.

In the modern traction network, high-speed EMUs are controlled to achieve near unity power factor, the reactive power is consumed by the conductive line rather than traction load. And the medium voltage network is more inductive than resistive. So only active power can be shared and the reactive power provided by each station will be different depending on the equivalent distance to the load [100]. Furthermore, the voltage level needs to be maintained near to the nominal value 25 kV. So the voltage droop control with reactive power is not applied in the proposed scheme, so only active power versus frequency droop characteristic is used.

6.3.1 Power sharing strategy for single train

When two substations are supplying in parallel and having synchronised phase angle, the substation that has traction loads nearby will provide most of the power and the substation that is distant from the train will provide less power. If we assume the system is symmetric, each side will naturally provides 50% of the total load power when the train is exactly in the middle between them.

In the AT connected multi-conductor model, it is difficult to derive close-form expression for optimal power sharing results (the least power losses). Numerical calculation is used to assess the performance of different power sharing ratios. The following optimisation procedure (6.8) is conducted using sequential quadratic programming (SQP) to search for the optimal active power ratio between two substations for the least power losses. Only 0 to 30 km are calculated because the system is symmetric.

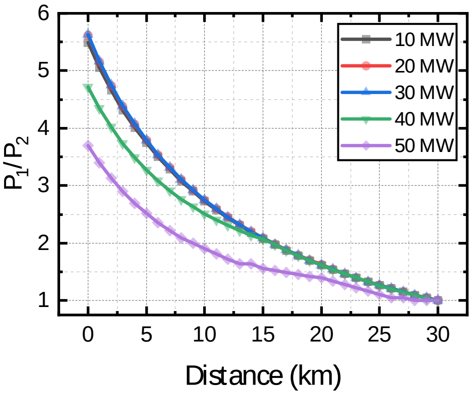

Fig. 6.11 Optimal power ratio for single traction load

$$\begin{aligned} \underset{P_1,P_2}{\text{minimise}} \quad & (P_1 + P_2 - P_{\text{Tr}}) \\ \text{subject to} \quad & V_{\text{Tr}} \geqslant 22\,\text{kV} \\ & P_{\text{Tr}} = 10, 20, \ldots 50.\,\text{MW} \\ & D_1 = 0, 1, 2, \ldots 30.\,\text{km} \end{aligned} \tag{6.8}$$

The result is shown in Figure 6.11. Similar to the previous discussions, the substation which is nearer to the train load supplies more. And two SFCs share an equal amount of the power when the train is in the middle. However, the ratio is not strictly inverse to the distance, in the heavier load condition, the ratio of power supply differences decreases because the network voltage has to be maintained above 22kV as set in the constraints.

In reality, a single high-speed train will not exceed 20 MW. The averaged ratio curve of 10, 20, 30 MW load is used and fitted by an exponential function (6.9), where D_1 is the train distance to the left SS1 substation and k is the power ratio of P_1/P_2.

$$k(D_1) = a \times e^{bD_1} + c \times e^{dD_1}, \quad a = 1.554, b = -0.1955, c = 4.026, d = -0.04656 \tag{6.9}$$

When the train is in 30 to 60 km away from SS1, the optimal ratio curve is centrosymmetric to the point (30,1) in Figure 6.11. Thus, we can formulate the optimal power share ratio curve for a single train load given arbitrary train location in this section in (6.10) .

$$\frac{P_1}{P_2} = \begin{cases} k(D_1) & D_1 <= 30; \\ k(60 - D_1) & D_1 > 30. \end{cases} \tag{6.10}$$

6.3.2 Power sharing strategy for three trains

it is quite common that more than one trains may run between two substations. Three trains scenario is considered in the test and 1000 random combinations of different locations and power loads are generated. In each instance, the optimal power sharing ratio P1/P2 is searched using the same approach (6.11) in the previous "single train case".

$$\begin{aligned}
\underset{P_1,P_2}{\text{minimise}} \quad & (P_1+P_2-\sum_{i=1}^{3}P_{\mathrm{Tr},i}) & & \\
\text{subject to} \quad & V_{x,y} \geq 22\,kV, & & x=1,2.\ y=1,2,3. \\
& 0 \leqslant P_{x,y} \leqslant 15\,\mathrm{MW}, & & x=1,2.\ y=1,2,3. \\
& 0 \leqslant D_y \leqslant 30\,\mathrm{km}, & & y=1,2,3. \\
& D_1 < D_2 < D_3 & &
\end{aligned} \tag{6.11}$$

The optimisation results provide a series optimal power ratios for different multiple load conditions. If this multiple train condition can be converted into the single train condition, we can adopt the previous answer. Using (6.12), an equivalent distance can be calculated. A virtual single train distance can be derived to represent the multiple trains' condition. Based on this approximation, the optimal power sharing ratio can be calculated by (6.13) where the function $k(D')$ is given in (6.9).

$$D' \approx \begin{cases} \frac{\Sigma_i P_i D_i}{\Sigma_i P_i} & \Sigma_i P_i \neq 0\,; \\ 30 & \Sigma_i P_i = 0\,. \end{cases} \tag{6.12}$$

$$\left(\frac{P_1}{P_2}\right)_{\mathrm{opt}} = \begin{cases} k\,(0) & D' < 0\,; \\ k\,(D') & 0 \leq D' \leq 60\,; \\ k\,(60) & D' > 60\,. \end{cases} \tag{6.13}$$

The power ratio generated by this approximated approach which transforms three train case into single train case has less than 1% difference with the original optimisation result. So the three train scenario is converted to the single train case with small errors.

6.3.3 Droop control design

The simple droop curve in Figure 6.9 shows that the frequency reference follows $f^* = f_0 - k_\mathrm{d}P$, $f_0 = 50\,\mathrm{Hz}$ where P_1, P_2 are the measured active power and $k_{\mathrm{d}1}, k_{\mathrm{d}2}$ is the droop coefficient. In the steady state, two substations have the same output voltage frequency, namely $f_1^* = f_2^*$, so the active power ratio is strictly inverse proportional to the droop coefficient ratio. The active power sharing ratio defined in (6.13) can be achieved by changing droop coefficient value.

$$k_{\mathrm{d}1}P_1 = k_{\mathrm{d}2}P_2 \quad \Rightarrow \quad \frac{k_{\mathrm{d}1}}{k_{\mathrm{d}2}} = \frac{P_2}{P_1} \tag{6.14}$$

However, with a simple linear droop characteristic, overloading situations may arise in excessive power demand situations. A modified droop curve to limit the maximum output power is designed and explained in Figure 6.12. In the light to medium load condition $P_1 + P_2 < P_\mathrm{sat}$, droop coefficients

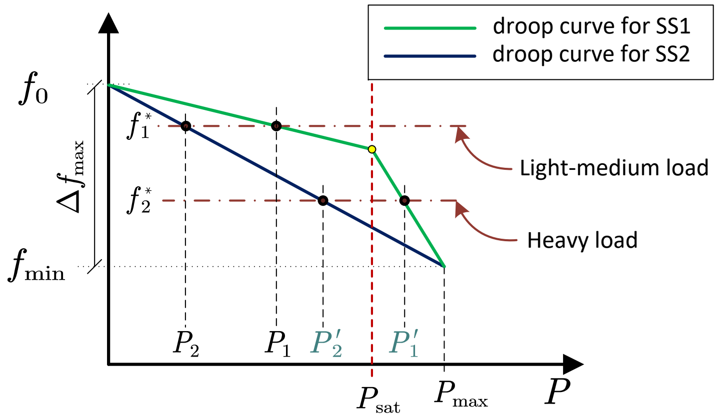

Fig. 6.12 Modified droop curve with power saturation protection

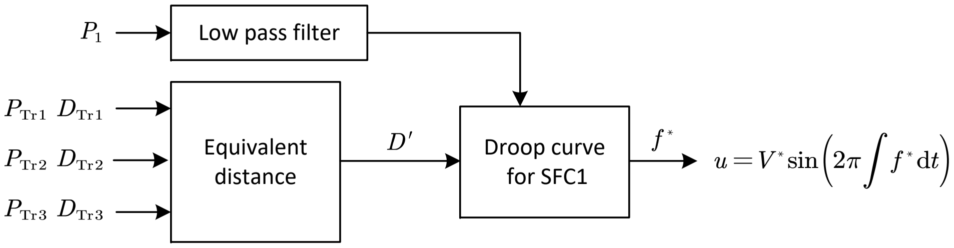

Fig. 6.13 Droop control scheme for SS1 substation

are designed according to the least resistance loss result in (6.9). Whenever the traction load becomes greater than a certain limit $P_1' + P_2' > P_{\text{sat}}$, a new droop coefficient is used to prevent overload. In this way two substations share the heavy load more evenly to prevent overload in one substation. Obviously, the least resistance loss is not obtainable in the heavy load condition.

6.3.4 Droop controller parameter design

The proposed droop control scheme is shown in Figure 6.13. Firstly, the equivalent load distance is calculated then based on the measured active power and distance information, the frequency reference is interpolated from the designed droop curve. Then each substation is controlled to track the voltage reference.

It is clear that in the droop controller, two tunable parameters affect system dynamics: 1) the power saturation point which defines droop coefficient in different load conditions, 2) the low pass filter (LPF) time constant. Assume the LPF is a first order filter that smooth the active power change. We can approximately analyse the system dynamics using following procedures.

In the frequency domain the measurement of active power is expressed in (6.15). Equation (6.16) is a first order low pass filter and T_f is the time constant.

$$P_m = \frac{\omega_f}{\omega_f + s} P(s) \tag{6.15}$$

$$G(s) = \frac{1}{Ts+1} = \frac{\omega_f}{s+\omega_f}, \omega_f = 1/T_f \tag{6.16}$$

Using the proposed droop strategy where only active power affects the frequency and the magnitude (denoted as E) remains constant, the system equation is given in (6.17).

$$\begin{cases} \omega = \omega_0 - k_{\mathrm{d}} P_m \\ E = E_0 \end{cases} \tag{6.17}$$

Assume there is a change in the active power denoted as $\Delta P(s)$, the resultant change in angular speed and voltage is given in (6.18):

$$\begin{cases} \Delta\omega(s) = -\frac{k_{\mathrm{d}}\omega_f}{\omega_f + s}\Delta P(s) \\ \Delta E = 0 \end{cases} \Rightarrow \begin{cases} \Delta\dot{\omega} = -\omega_f \Delta\omega - k_{\mathrm{d}}\omega_f \Delta P \\ \Delta\dot{E} = 0 \end{cases} \tag{6.18}$$

To evaluate the influence of the measurement value change to the system dynamics, voltage is mapped to d-q coordination shown in (6.19) for active power and reactive power update.

$$E = e_d + je_{\mathrm{q}}, \quad e_d = E\cos(\delta), e_q = \sin(\delta), \delta = \arctan\left(\frac{e_q}{e_d}\right) \tag{6.19}$$

Linearize the angle δ by first order approximation we can get (6.21):

$$\Delta\delta = \frac{\partial\delta}{\partial e_d}\Delta e_d + \frac{\partial\delta}{\partial e_q}\Delta e_q \tag{6.20}$$

$$\Rightarrow \Delta\delta = m_d \Delta e_d + m_q \Delta e_q,\ m_d = -\frac{e_q}{e_d^2 + e_q^2}, m_q = \frac{e_d}{e_d^2 + e_q^2} \tag{6.21}$$

Then the small signal model of the angular speed can be derived from (6.21) as (6.22):

$$\Delta\omega = \Delta\dot{\delta} = m_d \Delta\dot{e}_{\mathrm{d}} + m_q \Delta\dot{e}_{\mathrm{q}} = -\frac{e_q}{e_d^2 + e_q^2}\dot{e}_d + \frac{e_d}{e_d^2 + e_q^2}\dot{e}_q. \tag{6.22}$$

Note that because the voltage magnitude is kept as constant, so equation (6.23) holds:

$$\Delta\dot{E} = n_d \Delta\dot{e}_d + n_q \Delta\dot{e}_q = 0, \quad n_{\mathrm{d}} = \frac{e_d}{\sqrt{e_d^2 + e_q^2}}, n_{\mathrm{q}} = \frac{e_q}{\sqrt{e_d^2 + e_q^2}} \tag{6.23}$$

Combine (6.21), (6.23) and (6.22) we can build a state space model (6.24) about voltage of the i-th substation using this small signal analysis:

$$\begin{bmatrix} \Delta\dot{\omega}_i \\ \Delta\dot{e}_{d,i} \\ \Delta\dot{e}_{q,i} \end{bmatrix} = \begin{bmatrix} -\omega_f & 0 & 0 \\ \frac{n_{\mathrm{q}}}{m_d n_{\mathrm{q}} - m_q n_{\mathrm{d}}} & 0 & 0 \\ \frac{n_{\mathrm{d}}}{m_q n_{\mathrm{d}} - m_d n_{\mathrm{q}}} & 0 & 0 \end{bmatrix} \begin{bmatrix} \Delta\omega_i \\ \Delta e_{d,i} \\ \Delta e_{q,i} \end{bmatrix} + \begin{bmatrix} -k_{\mathrm{d}}\omega_f & 0 \\ 0 & 0 \\ 0 & 0 \end{bmatrix} \begin{bmatrix} \Delta P_i \\ \Delta Q_i \end{bmatrix} \tag{6.24}$$

Using the model (6.24) to update voltage output, the updated power can be expressed by (6.25) for each station (subscript i represents value of the i-th station)

$$\begin{aligned} P_i &= e_{d,i} i_{d,i} + e_{q,i} i_{q,i} \\ Q_i &= e_{d,i} i_{q,i} - e_{q,i} i_{d,i} \end{aligned} \tag{6.25}$$

The required current information in each station can be updated through the admittance matrix (6.27) of the network and voltage information from both substations:

$$\begin{bmatrix} I_1 \\ I_2 \end{bmatrix} = \begin{bmatrix} Y_{11} & Y_{12} \\ Y_{21} & Y_{22} \end{bmatrix} \begin{bmatrix} E_1 \\ E_2 \end{bmatrix}, \tag{6.26}$$

$$\begin{bmatrix} i_{d1} \\ i_{q1} \\ i_{d2} \\ i_{q2} \end{bmatrix} = \begin{bmatrix} \mathrm{Re}(Y_{11}) & -\mathrm{Im}(Y_{11}) & \mathrm{Re}(Y_{12}) & -\mathrm{Im}(Y_{12}) \\ \mathrm{Im}(Y_{11}) & \mathrm{Re}(Y_{11}) & \mathrm{Im}(Y_{12}) & \mathrm{Re}(Y_{12}) \\ \mathrm{Re}(Y_{21}) & -\mathrm{Im}(Y_{21}) & \mathrm{Re}(Y_{22}) & -\mathrm{Im}(Y_{22}) \\ \mathrm{Im}(Y_{21}) & \mathrm{Re}(Y_{21}) & \mathrm{Im}(Y_{22}) & \mathrm{Re}(Y_{22}) \end{bmatrix} \begin{bmatrix} e_{d1} \\ e_{q1} \\ e_{d2} \\ e_{q2} \end{bmatrix}, \tag{6.27}$$

where $\mathrm{Re}(\cdot)$ is the real part of a complex value, $\mathrm{Im}(\cdot)$ is the imaginary part of a complex value, complex matrices $Y_{11}, Y_{2,2}$ are self admittance matrix and $Y_{1,2}, Y_{2,1}$ are the mutual admittance matrices.

Recall that the active power is the input value in the state space mode (6.25) and the active power can be updated by (6.25) and (6.27). So the droop control supply dynamics can be represented as an autonomous system shown in (6.28).

$$\dot{\boldsymbol{X}} = \boldsymbol{A}\boldsymbol{X} \tag{6.28}$$

$$\text{where } \boldsymbol{X} = \begin{bmatrix} \Delta\omega_1 \\ \Delta e_{d1} \\ \Delta e_{q1} \\ \Delta\omega_2 \\ \Delta e_{d2} \\ \Delta e_{q2} \end{bmatrix}, \boldsymbol{A} = \left(\begin{bmatrix} \boldsymbol{M}_1 & 0 \\ 0 & \boldsymbol{M}_2 \end{bmatrix} + \begin{bmatrix} \boldsymbol{C}_1 & 0 \\ 0 & \boldsymbol{C}_2 \end{bmatrix} (\boldsymbol{I_n} + \boldsymbol{E_n}\boldsymbol{Y_n}) \begin{bmatrix} 0 & 1 & 0 & 0 & 0 & 0 \\ 0 & 0 & 1 & 0 & 0 & 0 \\ 0 & 0 & 0 & 0 & 1 & 0 \\ 0 & 0 & 0 & 0 & 0 & 1 \end{bmatrix} \right),$$

$$\boldsymbol{M} = \begin{bmatrix} -\omega_f & 0 & 0 \\ \frac{n_q}{m_d n_q - m_q n_d} & 0 & 0 \\ \frac{n_d}{m_q n_d - m_d n_q} & 0 & 0 \end{bmatrix}, \boldsymbol{C} = \begin{bmatrix} -k_{\mathrm{d}}\omega_f & 0 \\ 0 & 0 \\ 0 & 0 \end{bmatrix}, \boldsymbol{I}_n = \begin{bmatrix} i_{d1} & i_{q1} & 0 & 0 \\ 0 & 0 & i_{d2} & i_{q2} \end{bmatrix}, \boldsymbol{E}_n = \begin{bmatrix} e_{d1} & e_{q1} & 0 & 0 \\ 0 & 0 & e_{d2} & e_{q2} \end{bmatrix},$$

$$\boldsymbol{Y}_n = \begin{bmatrix} \mathrm{Re}(Y_{11}) & -\mathrm{Im}(Y_{11}) & \mathrm{Re}(Y_{12}) & -\mathrm{Im}(Y_{12}) \\ \mathrm{Im}(Y_{11}) & \mathrm{Re}(Y_{11}) & \mathrm{Im}(Y_{12}) & \mathrm{Re}(Y_{12}) \\ \mathrm{Re}(Y_{21}) & -\mathrm{Im}(Y_{21}) & \mathrm{Re}(Y_{22}) & -\mathrm{Im}(Y_{22}) \\ \mathrm{Im}(Y_{21}) & \mathrm{Re}(Y_{21}) & \mathrm{Im}(Y_{22}) & \mathrm{Re}(Y_{22}) \end{bmatrix}.$$

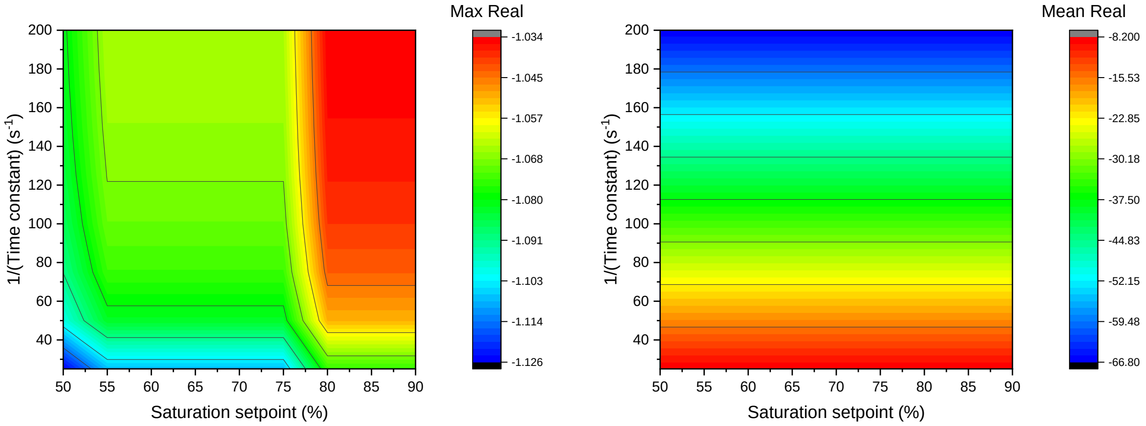

(a) Maximum value of real parts

(b) Mean value of real parts

Fig. 6.14 Eigenvalue analysis result (real parts)

Using the derived autonomous model, we can analyse the stability of two substations with the proposed droop control scheme. However, the admittance matrix $\boldsymbol{Y}_n$ is unknown. To estimate the admittance matrix, the whole network is viewed as a two-port network from both substation terminals. $\boldsymbol{Y}_n$ is then calculated as a complex matrix in respect to specific load condition [6].

By analysing the eigenvalue of matrix $\boldsymbol{A}$ in (6.28), we can evaluate the convergence performance of the dual-end supply system. It can be found that, the system is prone to be less stable when the load is in the vicinity of one substation. Also, in this condition, it is possible that the load change is too large and converter's droop curve enters the power saturation region.

A parameter sweep analysis is operated to evaluate the eigenvalue: 1) LPF time constant varying from 1/25 s to 1/200 s, 2) Droop curve saturation setpoint is set from 0.5 to 0.9, 3) Traction load power is set from 10 MW to 50 MW, 4) Load distance to left substation is varying from 0 to 30 km. In each combination instance, the eigenvalue of system matrix $\boldsymbol{A}$ in (6.28) is calculated. None of the result has positive real parts which shows the droop method controlled power supply system is stable.

The maximum and mean value of the eigenvalues' real parts in each parameter combination (different time constants and saturation setpoints) are extracted and plotted in Figure 6.14. The maximum value of real parts are insignificantly influenced by different T_f and $P_{\text{sat}}/P_{\text{max}}$ settings. The averaged value of real parts is only dependent on LPF effect, the smaller the time constant the faster the system restored to the equilibrium point.

The maximum absolute value of the imaginary parts is plotted in Figure 6.15 which shows that a large time constant LPF and a higher saturation setpoint leads to more severe oscillation.

The low-pass filter time constant defines the inertia of the system. A smaller time constant value results in faster frequency dynamics in respect to power change. A larger time constant slows down the frequency change. However, if the inertia is too large, and the frequency response is too slow, there will be more oscillating cycles in output frequency and also the overloading may happen. The saturation

---

[6] the matrix $\boldsymbol{Y}_n$ is dependent to train location and power supply frequency.

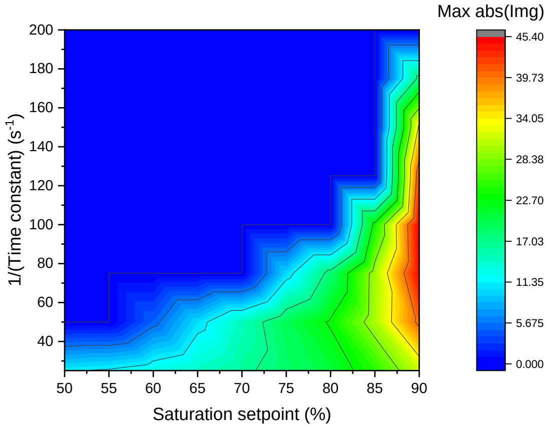

Fig. 6.15 Eigenvalue analysis result of maximum imaginary parts magnitude

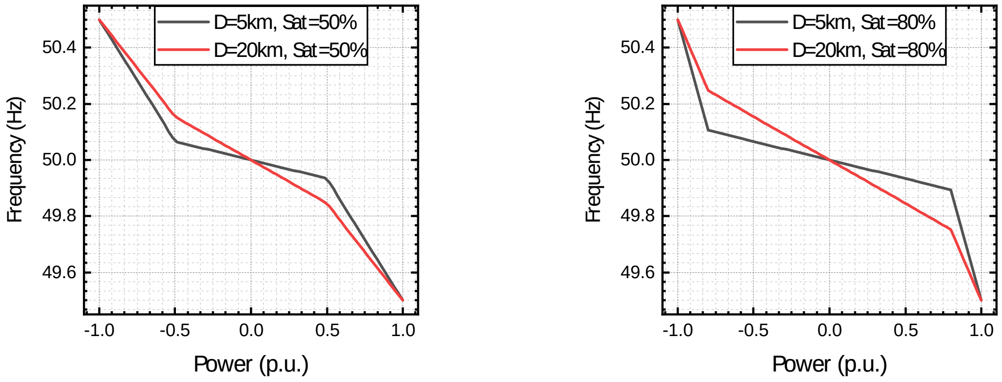

(a) Saturation setpoint at 50%

(b) Saturation setpoint at 80%

Fig. 6.16 Different droop curve with saturation point setting

setpoint determines the droop coefficient according to specific load conditions. A lower saturation setpoint (e.g. 50%) compromises the optimal resistance loss supply objective, but a higher setpoint (e.g. 90%) makes two substations having considerable difference in droop coefficient curve which retards the convergence speed.

To select the controller parameter, the rate of change of frequency (RoCoF) in the system is evaluated. Figure 6.17 and Figure 6.18 shows the frequency response of two substations when a step load is connected at 5 km away from one substation at 0.5 s. Figure 17 compares the influence of different time constant values when a 20 MW step load is connected at 0.5 s. Figure 18 tests the influence of different saturation setpoints when a 40 MW is connected at 0.5 s.

These results are consistent with the analytical eigenvalue results. A low inertia (small time constant) system suffers from greater RoCoF but can converge in shorter time, while a larger time constant reduce the RoCoF but results in more oscillation but takes longer time to converge. Note that small time constant may not be beneficial to the system dynamics as shown in Figure 6.17(c) that the convergence time is not significantly reduced but the RoCoF is exceeding 6 Hz/s. As previously discussed, if the saturation

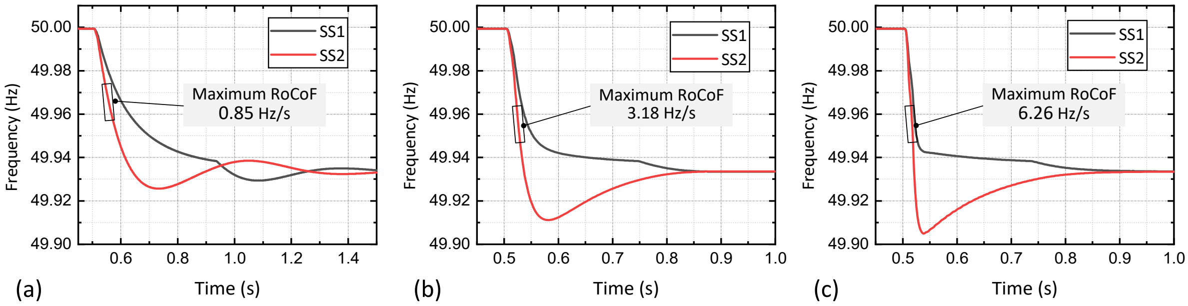

Fig. 6.17 Comparison of different droop controller inertia settings.
LPF T_f value: a) $1/10\,\mathrm{s}$, b) $1/50\,\mathrm{s}$, c) $1/200\,\mathrm{s}$.

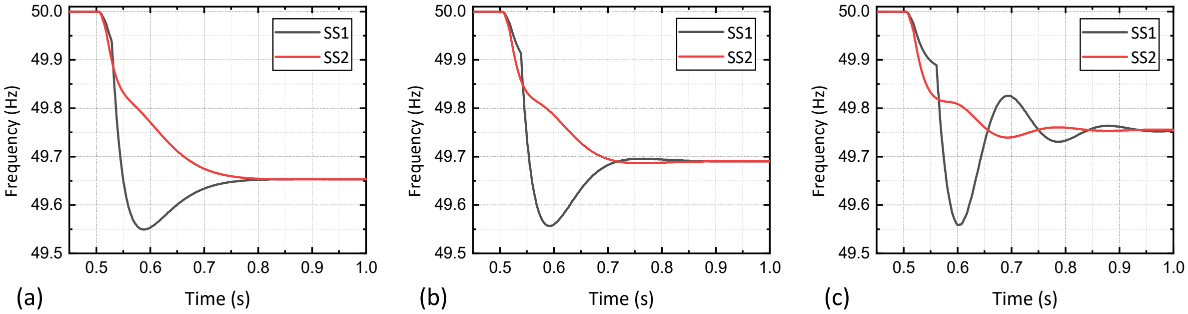

Fig. 6.18 Comparison of different saturation set points
$P_{\mathrm{sat}}/P_{\mathrm{max}}$ setting: a) 50%, b) 75%, c) 90%.

setpoint is set too high (e.g. 90% in Figure 6.18(c)), the system has more frequency oscillations in heavy load change condition because a sharper difference of droop coefficient exists due to the setpoint at 90%.

Finally, the time constant T_f is chosen as 1/20 s and the saturation setpoint is chosen at 70% this combination guarantees a less than 2 Hz/s RoCoF with 10 MW step load change.

6.4 Simulation results and discussion

Four types of power supply strategies are selected in the simulation comparison.

1. Single substation supply:
   Similar to the conventional power supply scheme, only one substation supplies the whole arm.
2. Two substations fixed frequency:
   Two substations are strictly synchronised with fixed 50 Hz voltage supply reference without any load sharing control.
3. Two substation equal sharing:
   Two substations use the same droop coefficient of 0.5 Hz/p.u.. So two substations share exactly the same amount of active power no matter the load condition.
4. The proposed adaptive droop curve:
   The proposed droop control power supply scheme in this chapter. The droop coefficient varies according to the equivalent load position and active power to each substation.

6.4.1 Simulation results

6.4.2 Comparison of power supply schemes - single traction load

Firstly, a 10 MW constant load is continuously moving from SS1 to SS2 in 1080 s (200 km/hr). The single train follows the load profile shown in Figure 6.5 is used to compare 4 different supply methods in terms of power consumption, train side voltage and supply side power factor.

Figure 6.19 compares the active power result. 6.19a shows that all the three dual-end supply schemes has lower the power loss than single substation supply because the current loading is reduced. Equal sharing supply exhibits the same power loss as other dual end supply methods when the traction load is located in the middle of two SFCs. But when the train is near to one substation, equal sharing scheme result in more losses because of its strict equal share principle.

In this light load (10 MW) scenario, the proposed droop control supply has almost the same energy loss as the fixed frequency approach. And both of these two methods get the least energy loss on conductor lines.

In Figure 6.19b, the active power consumption on SS1 substation is plotted. In the equal sharing method, active power provided by SS1 is maintained about 5 MW. The proposed method and fixed frequency method has similar load requirement.

The current measurement result reveals the capacity requirement for each substation. As shown in Figure 6.20, the equal sharing solution has the least capacity requirement even the traction is in the

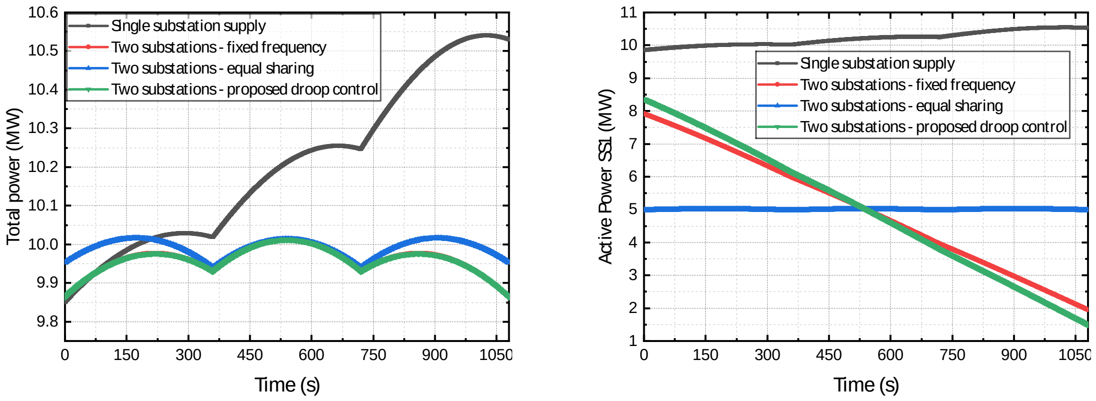

(a) Sum of active power ($P_{SS1} + P_{SS2}$)

(b) Active power of SS1 (P_{SS1})

Fig. 6.19 Comparison of active power consumption (single traction load)

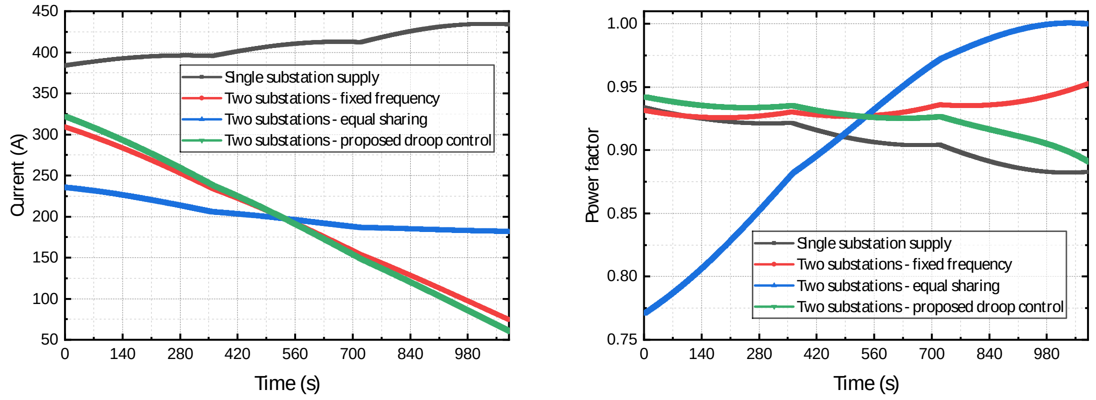

(a) Current RMS value measurement of SS1

(b) Power factor of SS1

Fig. 6.20 Comparison of capacity demand at SS1 substation (single traction load)

vicinity of SS1. However, as shown in 6.20b, when the train is near to SS1, the power factor is rather low compared to other methods. The low power factor is reflected in the power consumption where equal sharing methods suffer the highest resistive losses.

Figure 6.21 shows the voltage frequency. Because the load is constant, the frequency keeps nearly constant in equal sharing method. The proposed droop control method has variable frequency between equal sharing and the rest methods' results. Note that when the traction is in the middle location, the proposed method is identical to the equal sharing approach.

Figure 6.22 shows the voltage measured at the train side. All three dual-end supply schemes can achieve a minimum voltage drop for this light traction load. The measured voltage at the train is even higher than the nominal 25 kV[7], while in the single substation case, the voltage gets lower to 23.5 kV when the train is become distant to SS1. Figure 6.22b shows a magnified view of traction side voltage,

---

[7] The voltage reference for substation terminal is set to 27.5 kV.

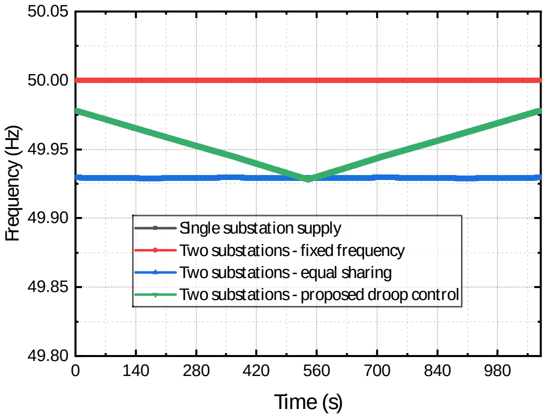

Fig. 6.21 Comparison of network voltage frequency

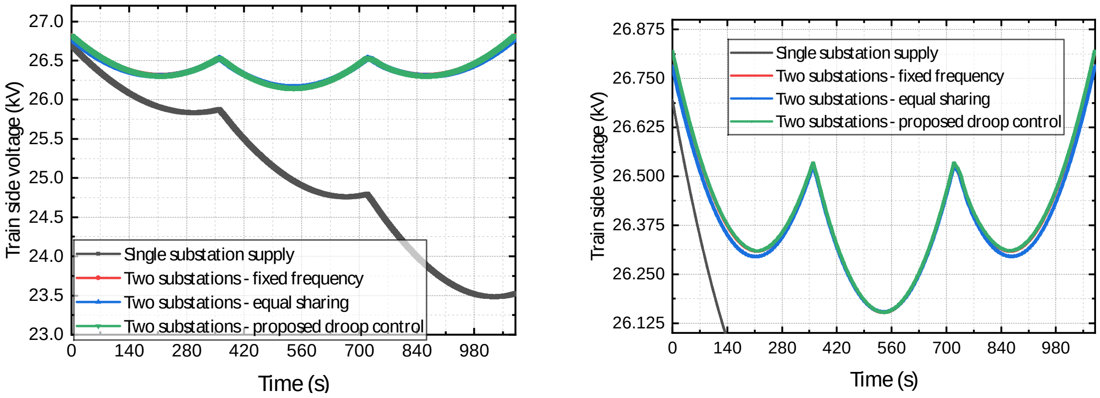

(a) Traction side voltage

(b) Magnified view

Fig. 6.22 Comparison of traction side voltage RMS value (single traction load)

although the three dual-end feeding has similar result, the equal sharing method has greater voltage droop because of the lower power factor.

6.4.3 Comparison of power supply schemes - three train scenario

To test the limit of the proposed droop control supply scheme in a more complex load condition, the three trains' profile shown in Figure 6.6 is simulated. In this profile, the load will have different types of rapid change from traction consumption to regenerative energy feedback. Only dual-end supply schemes are compared because the single end substation cannot support such a heavy load within permissible voltage range.

Figure 6.23 shows the total power consumption and the power loss plot of the three dual-end supply methods. During 0 to 120 s when the load is concentrating at the SS1, the proposed droop control method has the same energy loss as the fixed frequency one. Then during 180 to 240 s when the total traction load exceeds 50 MW, the proposed method has more similarity with equal sharing methods. And around 300 s the proposed method has medium power loss among the other two. Both fixed frequency

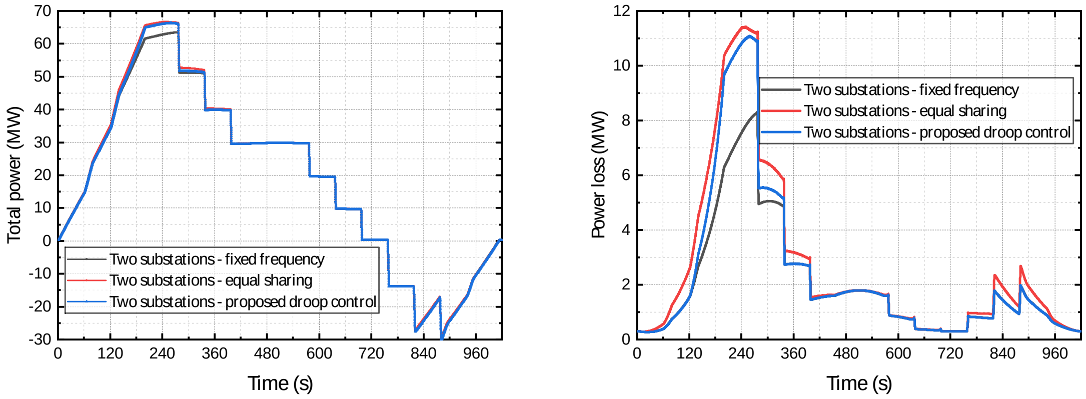

(a) Total power consumption

(b) Power loss comparison

Fig. 6.23 Comparison of active power consumption (three traction load)

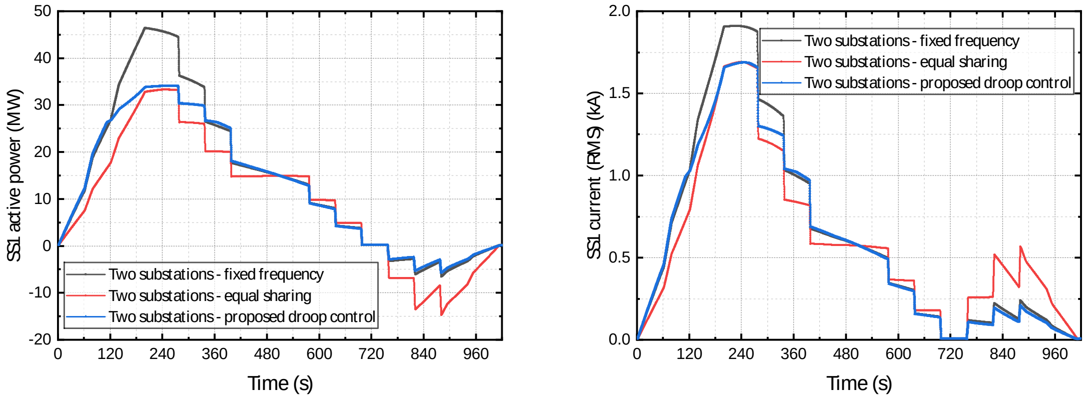

(a) SS1 substation active power

(b) SS1 substation current measurement

Fig. 6.24 Power demand on SS1 substation

method and the proposed one has better efficiency when the load is near to one substation no matter in traction supply or regeneration mode. The difference of these methods become indistinguishable when the equivalent load is in the middle.

Similar results can be drawn from the power profile on SS1 in Figure 6.24. In the proposed droop control simulation, the active power of SS1 is almost the same as the fixed frequency method in the light load condition. Only when the load exceeds the 30 MW large difference appears because the active power is limited by the designed droop curve. In heavy load condition, the proposed droop control behaves like the equal sharing method, and the output active power is limited below 35 MW. The measured current is also lower in equal sharing and the proposed approach in the maximum load condition. So that the proposed method reduce the rating in a single substation.

Figure 6.25 shows the voltage frequency results, frequency can be kept within the designed range. In traction supply status, the frequency is below 50 while in the regeneration mode, the frequency is raised above 50 Hz so that the power sharing ratio is still valid in reverse power flow condition. Again, when

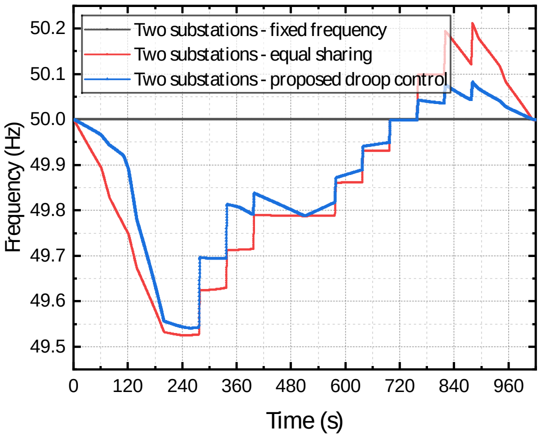

Fig. 6.25 Network frequency (three trains)

the equivalent load located at the middle place, the proposed method has the same frequency result with the equal sharing.

The voltage measured at all three trains are plotted in Figure 6.26. In order to clearly compare the results, Figure 6.27 compares the maximum and minimum voltage values measured at trains' interface to the network. In the light load condition, all three methods have almost the same voltage drop, but in the heavy load condition the proposed and the equal sharing schemes have greater voltage changes because of more even current sharing. In the medium load the proposed method has less voltage deviations than equal sharing. All three schemes can guarantee that train side voltage is above 19 kV which is the lowest permissible voltage.

It can be concluded that in the proposed droop control approach is a trade-off between the other two dual-end supply methods. In the lighter condition, the least resistive load character is preserved by the adaptive droop controller based on traction load profiles, time tables or communicated information. When the traction load increases to a certain level (the saturation setpoint), the droop controller gradually relaxes the least power loss objective, and gradually transforms to more evenly load sharing among the two substations.

6.5 Summary

With the development of power converter technology, the AC railway power supply is no longer an isolated system. In this chapter, a preliminary dynamic network simulation platform is built and a special dual-end optimal power sharing droop control is proposed.

This simulation platform enables a single track AT traction network simulation. It supports multiple trains' continuous moving along the track and dynamic load profiles. The voltage measured at train's pantograph can be tested continuously, and the transient dynamics can be approximately simulated.

The proposed power sharing droop control realises the least power losses supply in the light and medium load conditions. And this approach reduces the rating of each substation for peak/heavy load

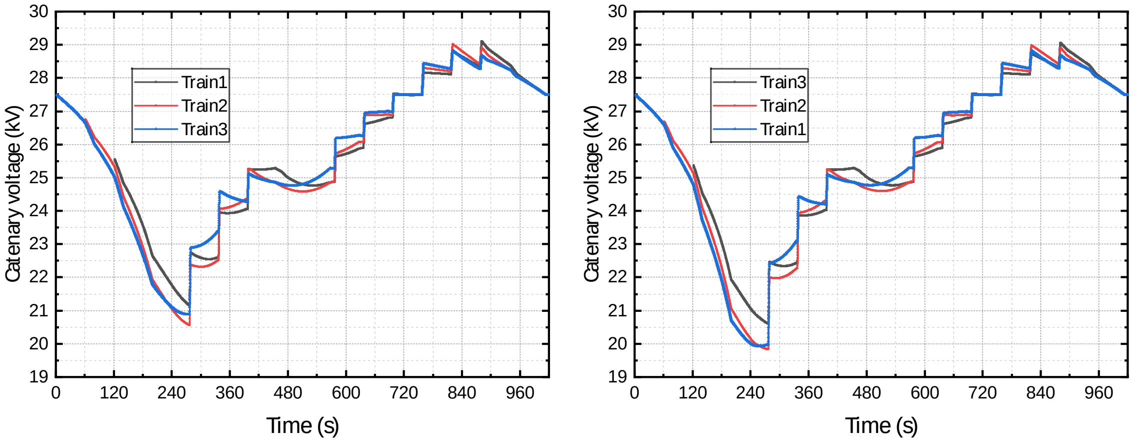

(a) Fixed frequency method

(b) Equal sharing method

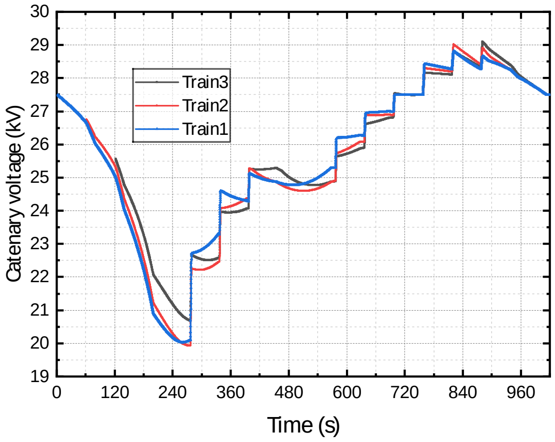

(c) The proposed method

Fig. 6.26 Train side voltage RMS measurement (three trains)

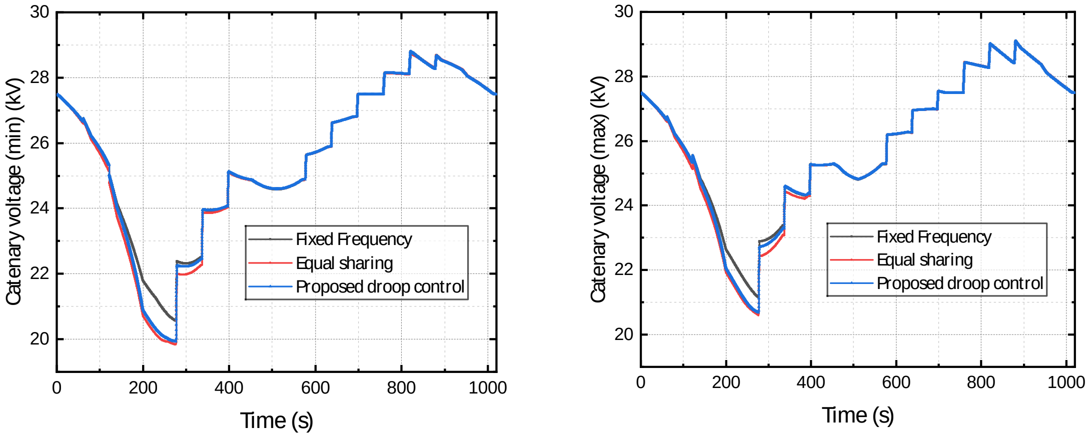

(a) Minimum voltage

(b) Maximum voltage

Fig. 6.27 Comparison of traction side voltage (three trains) supply. The proposed droop controller is analysed and designed to guarantee the frequency change rate and convergence speed.

A number of simplifications are applied in this preliminary study of the network modelling and power sharing control strategy design. The cross bond impedance is neglected to simplify the modelling procedure when a train continuously move along the line. The saturation effect in each component is not modelled and only linear models are used. The traction load can be improved to incorporate real driving control rather than following the designed power profiles. The model can also incorporate the harmonic issues and the harmonics control research in the parallel SFCs AC supply network.

The future work may include the update of the network model to reflect more detailed dynamics. New control strategy will be needed when the number of substations is more than two. Finally, the work should be validated in the real industrial case studies.

Chapter 7

Conclusion and future work

7.1 Summary of the research work

It is a foreseeable future that the TPSS will have significantly reduced green house gas emissions, greater power supply capacity and reduced negative impact on utility grid. This aligns with the smart grid development road map. This thesis presents a comprehensive investigation of MMC based substation technology for high speed railway power supply. Different topics are investigated to facilitate the future TPSS transformation.

The highlights of the thesis are listed as follows:

- Proposed a new compensation strategy for transformer feeder station power quality improvement. The proposed approach reduces the power rating of the expensive power electronic converter station.
- Designed a long horizon energy based MMC internal state predictive controller for MMC back to back feeder system. The new approach achieves the superior transient performance than conventional control scheme.
- Discussed the renewable generation connection through DC link of the SFC station and the control system improvement for stable voltage regulation and faster power conversion response.
- Analysed the detailed energy transfer mechanism in the MMC arms of the MMC-ESS hybrid system. Developed a model predictive control approach which is applicable for UPS support and energy recovery.
- Investigated the power sharing between two parallel connected feeder stations. Realised by the droop control principle, the proposed network system simulation results show a versatile performance of supply capacity and transmission line power loss.

In Chapter 2, MMC based cophase power conditioner for V/v type transformer TPSS is investigated. The three phase side unbalance mechanism is analysed by vector diagram. Based on power condition operation principle, the compensation current reference for MMC outer loop control is explicitly derived. A novel partial compensation strategy is optimised for the least converter capacity rating while complying with grid code under different load scenarios. The downsized MMC converter is capable of unbalance load compensation as well as harmonic suppression. The proposed method reduces the SFC capacity compared with previous full compensation strategy, the outer loop control rule is realised by look up table optimised for the minimal resistive loss.

In Chapter 3, a long horizon MPC is designed for three phase AC to single phase AC back to back (B2B) MMC systems. Unlike most researches using horizon one MPC for MMC, a longer horizon is adopted for multiple internal state control. In conventional MPC design, the energy balance is regulated by external control loop which is an indirect way. The MPC used in this work approximately predicts the internal MMC energy dynamics, so the energy balance and current tracking can be solved in a single constrained QP problem. For the best result, the ideal accurate reference (current & energy) for MMC average model is derived without simplification. Constraints are designed to avoid over-current and over-modulation which is commonly observed in conventional cascaded controller scheme. This approach fully utilises the MIMO nature of MPC to reduce the number of control loops. This eases the controller tuning and drives the MMC to achieve faster dynamics than the PI and deadbeat control methods.

In Chapter 4, the wind generation transmitted through MVDC line is coupled into the DC-link existing in the B2B MMC based SFC. Both renewable generation and traction load are variable and sometimes vary in large amount of power within short period of time. Should the power flow from intermittent RES generation and uncertain traction load be coupled at DC-link, large voltage deviation or serious oscillation may occur which destabilises the whole system. An additional DC voltage stabilising loop is added to the grid side MMC rectifier. The added control loop relaxes the total submodule insert index. So in the transient state when the capacitor voltage is deviated from nominal value, the DC-link voltage profile can be quickly maintained to the reference setting. The result shows that by adding the proposed control loop, both steady state error and transient undershot/overshot is reduced compared with conventional approaches.

In Chapter 5, energy storage integration with MMC is investigated. Once the MMC submodules are equipped with ESS, the AC side power and DC side power are decoupled, therefore various operation mode can be achievable. An operation mode controller is introduced to decide power flow assignment on the lop level which formulates a hierarchical scheme. The internal controller is an MPC which is similar to the one introduced in Chapter 4. The original MPC developed in Chapter 4 for traction side single phase power inversion is modified with the ability to freely control arm energy. For the sake of steady state DC-link performance, only two types of ESS connection topology are chosen, namely symmetrical ESS connection and a phase asymmetrical connection. The modified MPC successfully provides uninterrupted power supply to the traction load when the grid capacity is limited. Then regenerative power can also be stored inside MMC station for future use. The same performance is achieved regardless ESS connection type, and continuous feeding without neutral section phase split becomes feasible in the SFC supplied TPSS.

In Chapter 6, the control freedom of SFC is used for dual end power sharing supply which has several advantages over single end supply transformer substation. The dual end supply reduces current rating and increases the system capacity. An adaptive droop control is proposed to realise the least transmission losses for light to medium load conditions. The proposed method also supports heavy load which is greater than one single SFC substation rating. Extensive simulation studies are conducted based on a variable distance AT traction network where multiple trains can move continuously along the overhead line. A virtual train profile is used to test the proposed power sharing control method with other continuous feeding schemes. The results confirm that the proposed method can achieve higher efficiency as synchronised supply method in light load condition, and it can adaptive support heavy load like the equal sharing strategy.

In Appendix A, the fundamental MMC modelling and control logic is derived via transforming the MMC system into decoupled common mode and differential mode. The overview of control scheme which is applicable to different type of controllers has been summarised, and an open loop MMC operation prediction approach is proposed based on the accurate MMC internal dynamics analysis given in Chapter 3. This chapter provides a basic yet complete development tool for modelling and control of the single phase MMC converter.

7.2 Discussion and prospect

This thesis has presented a comprehensive study of modelling and control of MMC based TPSSs, yet a number of issues have yet to be researched.

In summary, all the research results presented in this thesis are based on simplified traction load and generic system parameters, some important components in the system may be ignored. Nevertheless, the modelling and controller design method shall be applicable to real systems. In the future, real-time data can be incorporated into the proposed framework for validation and to identify potential deficiencies from the industrial perspective.

Experimental validation

The proposed algorithms require experiment validation to justify their practicability. Especially the model predictive control which requires very short update interval for power electronics control. The experiment also provides natural uncertainty and noise into the control system.

Modelling uncertainty

The analysis in Chapter 2 ignores the complex impedance in both the grid and the transformer where they are considered as ideal component in the analytical equations. This brings modelling error to reflect actual systems. In the simulation, considering grid impedance and ideal transformers, there is 0.1% error in voltage unbalance result. If the actual transformer impedance is included, the error may further increase. But the close form result cannot be derived after these simplifications are lifted. Therefore, the data driven based approach such as reinforcement learning can be used to solve this issue hence worth investigation in the future.

In Chapter 3 should any other modelling error exists such as model mismatch caused by faults or component parameter drifting (due to temperature and ageing effect), the proposed MPC may not maintain the optimal results. Observer is required to cope with the potential model mismatch issue. Also, the robustness of this type of MMC requires further discussion.

Real case scenario

Both Chapter 4 and Chapter 5 use an extremely simplified model where wind farm dynamics, DC transmission line, and battery characteristics are not considered. Furthermore, a combination of these two chapters would be an interesting project where RES and ESS are both integrated in the SFC system.

In Chapter 6, the TPSS simulation model supports up to three trains and the conductor system is reduced into single track. It is necessary to upgrade modelling process in an automated process with real data set. Further, the proposed power strategy is for two substation dual end feeding. What if there are more than two multiple substations in continuous supply? What if one side is a transformer station? Can this system provide additional functionality such as harmonic suppression? These questions are also worth investigation in the future.

References

[1] T. Bagnall, F. Siliezar, *et al.*, “Power electronics based traction power supply for 50hz railways,” *CORE 2014: Rail Transport For A Vital Economy*, p. 413, 2014.

[2] C. Lucy, “Rail infrastructure and assets 2019-20,” 2020. Office of rail and road.

[3] R. Hill, “Electric railway traction. part 3. traction power supplies,” *Power Engineering Journal*, vol. 8, no. 6, pp. 275–286, 1994.

[4] D. Sharifi, P. Tricoli, and S. Hillmansen, “A new control technique enabling dual-feeding of 50 hz ac railways with static converter feeder stations,” in *8th IET International Conference on Power Electronics, Machines and Drives (PEMD 2016)*, pp. 1–7, IET, 2016.

[5] C. Stark, M. Thompson, C. C. Committee, *et al.*, “Net zero the uk’s contribution to stopping global warming,” 2019.

[6] K. G. Logan, J. D. Nelson, B. C. McLellan, and A. Hastings, “Electric and hydrogen rail: Potential contribution to net zero in the uk,” *Transportation Research Part D: Transport and Environment*, vol. 87, p. 102523, 2020.

[7] J. Loughran, “30-year programme of rail electrification needs to start now, MPs say,” 2021. https://eandt.theiet.org/content/articles/2021/03/30-year-programme-of-rail-electrification-needs-to-start-now-mps-say/.

[8] Railway-News, “British rail industry: Rail decarbonisation not possible without electrification,” 2021. https://railway-news.com/british-rail-industry-rail-decarbonisation-not-possible-without-electrification/.

[9] D. Shirres, G. Keenor, N. Dolphin, and P. Hooper, “Why rail electrification?,” 2021. Railway Industry Association.

[10] T. Committee, “Trains fit for the future?,” p. 42, 2021. House of Commons, Transport Committee.

[11] W. Alexander, “Government must get on track for UK rail electrification to hit emissions target,” 2021. https://theloadstar.com/government-must-get-on-track-for-uk-rail-electrification-to-hit-emissions-target/.

[12] R. E. issue 187, “The changing face of electrification | rail engineer,” 2020. https://www.railengineer.co.uk/the-changing-face-of-electrification/.

[13] D. Serrano-Jiménez, L. Abrahamsson, S. Castaño-Solís, and J. Sanz-Feito, “Electrical railway power supply systems: Current situation and future trends,” *International Journal of Electrical Power & Energy Systems*, vol. 92, pp. 181–192, 2017.

[14] A. Steimel, “Power-electronic grid supply of ac railway systems,” in *2012 13th International Conference on Optimization of Electrical and Electronic Equipment (OPTIM)*, pp. 16–25, IEEE, 2012.

[15] X. He, Z. Shu, X. Peng, Q. Zhou, Y. Zhou, Q. Zhou, and S. Gao, “Advanced cophase traction power supply system based on three-phase to single-phase converter,” *IEEE Transactions on Power Electronics*, vol. 29, no. 10, pp. 5323–5333, 2013.

[16] T. Shimizu, K. Kunomura, M. Kai, M. Onishi, H. Masuzawa, H. Miyajima, M. Otsuki, and Y. Tsuruma, “The application of electronic frequency converter to the shinkansen railyard power supply,” in *2014 International Power Electronics Conference (IPEC-Hiroshima 2014-ECCE ASIA)*, pp. 1054–1061, IEEE, 2014.

[17] B. Mitra, B. Chowdhury, and M. Manjrekar, “Hvdc transmission for access to off-shore renewable energy: a review of technology and fault detection techniques,” *IET Renewable Power Generation*, vol. 12, no. 13, pp. 1563–1571, 2018.

[18] Y. Jing, R. Li, L. Xu, and Y. Wang, “Enhanced ac voltage and frequency control of offshore mmc station for wind farm connection,” *IET Renewable Power Generation*, vol. 12, no. 15, pp. 1771–1777, 2018.

[19] X. Zeng, T. Liu, S. Wang, Y. Dong, B. Li, and Z. Chen, “Coordinated control of mmc-hvdc system with offshore wind farm for providing emulated inertia support,” *IET Renewable Power Generation*, vol. 14, no. 5, pp. 673–683, 2019.

[20] A. A. Taffese, A. G. Endegnanew, S. D’Arco, and E. Tedeschi, “Power oscillation damping with virtual capacitance support from modular multilevel converters,” *IET Renewable Power Generation*, vol. 14, no. 5, pp. 897–905, 2020.

[21] SIEMENS, “Sitras SFC plus: Static frequency converter for AC traction power supply,” 2018.

[22] T. A. Kneschke, “Static frequency converter for septa’s wayne junction traction substation,” *IEEE transactions on industry applications*, no. 2, pp. 295–300, 1985.

[23] H. Hayashiya and K. Kondo, “Recent trends in power electronics applications as solutions in electric railways,” *IEEJ Transactions on Electrical and Electronic Engineering*, vol. 15, no. 5, pp. 632–645, 2020.

[24] S. Aubert, C. Zhao, C. Banceanu, T. Schaad, and P. Maibach, “Static frequency converters: a flexible and cost efficient method to supply single phase railway grids in australia,” in *AusRAIL PLUS 2015, Doing it Smarter. People, Power, Performance, 24-26 November 2015, Melbourne, Victoria, Australia*, 2015.

[25] I. Perin, P. F. Nussey, U. M. Cella, T. V. Tran, and G. R. Walker, “Application of power electronics in improving power quality and supply efficiency of ac traction networks,” in *2015 IEEE 11th International Conference on Power Electronics and Drive Systems*, pp. 1086–1094, IEEE, 2015.

[26] J. Ranneberg, “Transformerless topologies for future stationary ac-railway power supply,” in *2007 European Conference on Power Electronics and Applications*, pp. 1–11, IEEE, 2007.

[27] RIA, “RIA electrification cost challenge,” 2019. Railway Industry Association.

[28] L. Abrahamsson, T. Schütte, and S. Östlund, “Use of converters for feeding of ac railways for all frequencies,” *Energy for Sustainable Development*, vol. 16, no. 3, pp. 368–378, 2012.

[29] H. Hu, Y. Shao, L. Tang, J. Ma, Z. He, and S. Gao, “Overview of harmonic and resonance in railway electrification systems,” *IEEE Transactions on Industry Applications*, vol. 54, no. 5, pp. 5227–5245, 2018.

[30] A. Ogunsola and A. Mariscotti, *Electromagnetic compatibility in railways: Analysis and management*, vol. 168. Springer Science & Business Media, 2012.

[31] A. Luo, C. Wu, J. Shen, Z. Shuai, and F. Ma, “Railway static power conditioners for high-speed train traction power supply systems using three-phase V/V transformers,” *IEEE Transactions on Power Electronics*, vol. 26, no. 10, pp. 2844–2856, 2011.

[32] A. Luo, F. Ma, C. Wu, S. Q. Ding, Q.-C. Zhong, and Z. K. Shuai, “A dual-loop control strategy of railway static power regulator under V/V electric traction system,” *IEEE Transactions on Power Electronics*, vol. 26, no. 7, pp. 2079–2091, 2011.

[33] K.-W. Lao, N. Dai, W.-G. Liu, and M.-C. Wong, “Hybrid power quality compensator with minimum dc operation voltage design for high-speed traction power systems,” *IEEE transactions on power electronics*, vol. 28, no. 4, pp. 2024–2036, 2012.

[34] K.-W. Lao, M.-C. Wong, N. Dai, C.-K. Wong, and C.-S. Lam, “A systematic approach to hybrid railway power conditioner design with harmonic compensation for high-speed railway,” *IEEE Transactions on industrial electronics*, vol. 62, no. 2, pp. 930–942, 2014.

[35] B. Chen, C. Zhang, W. Zeng, G. Xue, C. Tian, and J. Yuan, “Electrical magnetic hybrid power quality compensation system for V/V traction power supply system,” *IET Power Electronics*, vol. 9, no. 1, pp. 62–70, 2016.

[36] M. Chen, Q. Li, C. Roberts, S. Hillmansen, P. Tricoli, N. Zhao, and I. Krastev, “Modelling and performance analysis of advanced combined co-phase traction power supply system in electrified railway,” *IET Generation, Transmission & Distribution*, vol. 10, no. 4, pp. 906–916, 2016.

[37] B. Chen, C. Zhang, C. Tian, J. Wang, and J. Yuan, “A hybrid electrical magnetic power quality compensation system with minimum active compensation capacity for V/V cophase railway power supply system,” *IEEE Transactions on Power Electronics*, vol. 31, no. 6, pp. 4159–4170, 2015.

[38] K.-W. Lao, M.-C. Wong, N. Y. Dai, C.-K. Wong, and C.-S. Lam, “Analysis of dc-link operation voltage of a hybrid railway power quality conditioner and its pq compensation capability in high-speed cophase traction power supply,” *IEEE Transactions on Power Electronics*, vol. 31, no. 2, pp. 1643–1656, 2015.

[39] Q.-C. Zhong and T. Hornik, *Control of power inverters in renewable energy and smart grid integration*, vol. 97. John Wiley & Sons, 2012.

[40] W. Song, S. Jiao, Y. W. Li, J. Wang, and J. Huang, “High-frequency harmonic resonance suppression in high-speed railway through single-phase traction converter with lcl filter,” *IEEE Transactions on Transportation Electrification*, vol. 2, no. 3, pp. 347–356, 2016.

[41] C. R. Cutler and B. L. Ramaker, “Dynamic matrix control??a computer control algorithm,” *Joint Automatic Control Conference*, vol. 17, p. 72, 1980.

[42] C. E. Garcia, D. M. Prett, and M. Morari, “Model predictive control: Theory and practice—a survey,” *Automatica*, vol. 25, no. 3, pp. 335–348, 1989.

[43] D. Q. Mayne, “Control of constrained dynamic systems,” *European Journal of Control*, vol. 7, no. 2-3, pp. 87–99, 2001.

[44] A. Linder and R. Kennel, “Model predictive control for electrical drives,” in *2005 IEEE 36th Power Electronics Specialists Conference*, pp. 1793–1799, IEEE, 2005.

[45] P. Cortés, M. P. Kazmierkowski, R. M. Kennel, D. E. Quevedo, and J. Rodríguez, "Predictive control in power electronics and drives," *IEEE Transactions on industrial electronics*, vol. 55, no. 12, pp. 4312–4324, 2008.

[46] R. E. Pérez-Guzmán, M. Rivera, and P. W. Wheeler, "Recent advances of predictive control in power converters," in *2020 IEEE International Conference on Industrial Technology (ICIT)*, pp. 1100–1105, IEEE, 2020.

[47] T. Geyer and D. E. Quevedo, "Multistep finite control set model predictive control for power electronics," *IEEE Transactions on power electronics*, vol. 29, no. 12, pp. 6836–6846, 2014.

[48] T. Geyer and D. E. Quevedo, "Multistep direct model predictive control for power electronics—part 2: Analysis," in *2013 IEEE Energy Conversion Congress and Exposition*, pp. 1162–1169, IEEE, 2013.

[49] T. Geyer, "Computationally efficient model predictive direct torque control," *IEEE Transactions on Power Electronics*, vol. 26, no. 10, pp. 2804–2816, 2011.

[50] M. Novak, *Model Predictive Control of Multilevel Power Electronic Converters: design, optimization and performance evaluation*. phdthesis, Aalborg Universitetsforlag, 2019.

[51] M. Novak and T. Dragicevic, "Supervised imitation learning of finite-set model predictive control systems for power electronics," *IEEE Transactions on Industrial Electronics*, vol. 68, no. 2, pp. 1717–1723, 2020.

[52] P. Karamanakos, T. Geyer, N. Oikonomou, F. D. Kieferndorf, and S. Manias, "Direct model predictive control: A review of strategies that achieve long prediction intervals for power electronics," *IEEE Industrial Electronics Magazine*, vol. 8, no. 1, pp. 32–43, 2014.

[53] R. Cagienard, P. Grieder, E. C. Kerrigan, and M. Morari, "Move blocking strategies in receding horizon control," *Journal of Process Control*, vol. 17, no. 6, pp. 563–570, 2007.

[54] F. Kieferndorf, P. Karamanakos, P. Bader, N. Oikonomou, and T. Geyer, "Model predictive control of the internal voltages of a five-level active neutral point clamped converter," in *2012 IEEE Energy Conversion Congress and Exposition (ECCE)*, pp. 1676–1683, IEEE, 2012.

[55] T. Geyer, N. Oikonomou, G. Papafotiou, and F. D. Kieferndorf, "Model predictive pulse pattern control," *IEEE Transactions on Industry Applications*, vol. 48, no. 2, pp. 663–676, 2011.

[56] F. Herrera, R. Cárdenas, M. Rivera, J. A. Riveros, and P. Wheeler, "Predictive voltage control operating at fixed switching frequency of a neutral-point clamped converter," in *2019 IEEE 15th Brazilian Power Electronics Conference and 5th IEEE Southern Power Electronics Conference (COBEP/SPEC)*, pp. 1–6, IEEE, 2019.

[57] L. Tarisciotti, P. Zanchetta, A. Watson, J. C. Clare, M. Degano, and S. Bifaretti, "Modulated model predictive control for a three-phase active rectifier," *IEEE Transactions on Industry Applications*, vol. 51, no. 2, pp. 1610–1620, 2014.

[58] F. Donoso, A. Mora, R. Cardenas, A. Angulo, D. Saez, and M. Rivera, "Finite-set model-predictive control strategies for a 3l-npc inverter operating with fixed switching frequency," *IEEE Transactions on Industrial Electronics*, vol. 65, no. 5, pp. 3954–3965, 2017.

[59] Y. Yang, H. Wen, M. Fan, L. He, M. Xie, R. Chen, M. Norambuena, and J. Rodriguez, "Multiple-voltage-vector model predictive control with reduced complexity for multilevel inverters," *IEEE Transactions on Transportation Electrification*, vol. 6, no. 1, pp. 105–117, 2020.

[60] L. Tarisciotti, P. Zanchetta, A. Watson, J. Clare, S. Bifaretti, and M. Rivera, “A new predictive control method for cascaded multilevel converters with intrinsic modulation scheme,” in *IECON 2013-39th Annual Conference of the IEEE Industrial Electronics Society*, pp. 5764–5769, IEEE, 2013.

[61] A. Bemporad, M. Morari, V. Dua, and E. N. Pistikopoulos, “The explicit linear quadratic regulator for constrained systems,” *Automatica*, vol. 38, no. 1, pp. 3–20, 2002.

[62] M. Jeong, S. Fuchs, and J. Biela, “When fpgas meet regionless explicit mpc: An implementation of long-horizon linear mpc for power electronic systems,” in *IECON 2020 The 46th Annual Conference of the IEEE Industrial Electronics Society*, pp. 3085–3092, IEEE, 2020.

[63] M. Kvasnica, B. Takács, J. Holaza, and S. Di Cairano, “On region-free explicit model predictive control,” in *2015 54th IEEE conference on decision and control (CDC)*, pp. 3669–3674, IEEE, 2015.

[64] G. Darivianakis, T. Geyer, and W. van der Merwe, “Model predictive current control of modular multilevel converters,” in *2014 IEEE Energy Conversion Congress and Exposition (ECCE)*, pp. 5016–5023, IEEE, 2014.

[65] X. Chen, J. Liu, S. Song, S. Ouyang, H. Wu, and Y. Yang, “Modified increased-level model predictive control methods with reduced computation load for modular multilevel converter,” *IEEE Transactions on Power Electronics*, vol. 34, no. 8, pp. 7310–7325, 2018.

[66] S. Fuchs and J. Biela, “Impact of the prediction error on the performance of model predictive controllers with long prediction horizons for modular multilevel converters-linear vs. nonlinear system models,” in *2018 20th European Conference on Power Electronics and Applications (EPE’18 ECCE Europe)*, pp. P–1, IEEE, 2018.

[67] W. Tian, X. Gao, Y. Pang, and R. Kennel, “Comparative study of model predictive control for modular multilevel converters with separate and decoupled circulating current,” in *2020 IEEE 9th International Power Electronics and Motion Control Conference (IPEMC2020-ECCE Asia)*, pp. 1017–1022, IEEE, 2020.

[68] F. Zhang, W. Li, and G. Joós, “A voltage-level-based model predictive control of modular multilevel converter,” *IEEE Transactions on Industrial Electronics*, vol. 63, no. 8, pp. 5301–5312, 2016.

[69] X. Gao, W. Tian, Q. Yang, and R. Kennel, “Model predictive control for modular multilevel converters based on a box-constrained quadratic problem solver,” in *2020 IEEE 9th International Power Electronics and Motion Control Conference (IPEMC2020-ECCE Asia)*, pp. 3068–3072, IEEE, 2020.

[70] Z. Wang, X. Yin, and Y. Chen, “Model predictive arm current control for modular multilevel converter,” *IEEE Access*, vol. 9, pp. 54700–54709, 2021.

[71] X. Chen, J. Liu, S. Song, and S. Ouyang, “Circulating harmonic currents suppression of level-increased nlm based modular multilevel converter with deadbeat control,” *IEEE Transactions on Power Electronics*, vol. 35, no. 11, pp. 11418–11429, 2020.

[72] J. Wang, X. Liu, Q. Xiao, D. Zhou, H. Qiu, and Y. Tang, “Modulated model predictive control for modular multilevel converters with easy implementation and enhanced steady-state performance,” *IEEE Transactions on Power Electronics*, vol. 35, no. 9, pp. 9107–9118, 2020.

[73] H. Mei, C. Jia, J. Fu, and X. Luan, “Low voltage ride through control strategy for MMC photovoltaic system based on model predictive control,” *International Journal of Electrical Power & Energy Systems*, vol. 125, p. 106530, 2021.

[74] J. Yin, J. I. Leon, M. A. Perez, A. Marquez, L. G. Franquelo, and S. Vazquez, “Fs-mpc method for mmcs with large number of submodules with reduced computational cost,” in *2020 IEEE International Conference on Industrial Technology (ICIT)*, pp. 1083–1088, IEEE, 2020.

[75] Z. Gong, X. Wu, P. Dai, and R. Zhu, “Modulated model predictive control for mmc-based active front-end rectifiers under unbalanced grid conditions,” *IEEE Transactions on Industrial Electronics*, vol. 66, no. 3, pp. 2398–2409, 2018.

[76] P. Poblete, S. Neira, R. P. Aguilera, J. Pereda, and J. Pou, “Sequential phase-shifted model predictive control for modular multilevel converters,” *IEEE Transactions on Energy Conversion*, 2021.

[77] X. Gao, W. Tian, Y. Pang, and R. Kennel, “Model predictive control for modular multilevel converters operating at wide frequency range with a novel cost function,” *IEEE Transactions on Industrial Electronics*, 2021.

[78] J. Pou, S. Ceballos, G. Konstantinou, V. G. Agelidis, R. Picas, and J. Zaragoza, “Circulating current injection methods based on instantaneous information for the modular multilevel converter,” *IEEE Transactions on Industrial Electronics*, vol. 62, no. 2, pp. 777–788, 2014.

[79] S. Fuchs, M. Jeong, and J. Biela, “Long horizon, quadratic programming based model predictive control (MPC) for grid connected modular multilevel converters (MMC),” in *IECON 2019-45th Annual Conference of the IEEE Industrial Electronics Society*, vol. 1, pp. 1805–1812, IEEE, 2019.

[80] A. Rodríguez-Cabero, F. H. Sánchez, and M. Prodanovic, “A unified control of back-to-back converter,” in *2016 IEEE Energy Conversion Congress and Exposition (ECCE)*, pp. 1–8, IEEE, 2016.

[81] J.-Z. Zhang, T. Sun, F. Wang, J. Rodriguez, and R. Kennel, “A computationally efficient quasi-centralized dmpc for back-to-back converter pmsg wind turbine systems without dc-link tracking errors,” *IEEE Transactions on Industrial Electronics*, vol. 63, no. 10, pp. 6160–6171, 2016.

[82] Z. Zhang, *On control of grid-tied back-to-back power converters and permanent magnet synchronous generator wind turbine systems*. PhD thesis, Technische Universität München, 2016.

[83] Z. Zhang, F. Wang, T. Sun, J. Rodriguez, and R. Kennel, “Fpga-based experimental investigation of a quasi-centralized model predictive control for back-to-back converters,” *IEEE Transactions on Power Electronics*, vol. 31, no. 1, pp. 662–674, 2015.

[84] F. Grimm and M. Baghdadi, “Variable switching point model predictive control for dc-link capacitance minimization of back-to-back converters,” in *2020 27th International Workshop on Electric Drives: MPEI Department of Electric Drives 90th Anniversary (IWED)*, pp. 1–6, IEEE, 2020.

[85] F. Grimm and Z. Zhang, “Multistep sequential model predictive control of 3-level npc pmsg wind turbines,” in *2019 IEEE International Conference on Sustainable Energy Technologies and Systems (ICSETS)*, pp. 224–229, IEEE, 2019.

[86] F. Grimm and M. Baghdadi, “Sequential model predictive control of electric drives using a k-best sphere decoding algorithm,” in *2020 27th International Workshop on Electric Drives: MPEI Department of Electric Drives 90th Anniversary (IWED)*, pp. 1–6, IEEE, 2020.

[87] E. P. de la Fuente, S. K. Mazumder, and I. G. Franco, “Railway electrical smart grids: An introduction to next-generation railway power systems and their operation.,” *IEEE Electrification Magazine*, vol. 2, no. 3, pp. 49–55, 2014.

[88] H. Hayashiya, H. Itagaki, Y. Morita, Y. Mitoma, T. Furukawa, T. Kuraoka, Y. Fukasawa, and T. Oikawa, “Potentials, peculiarities and prospects of solar power generation on the railway premises,” in *2012 International Conference on Renewable Energy Research and Applications (ICRERA)*, pp. 1–6, IEEE, 2012.

[89] H. Hayashiya, S. Kikuchi, K. Matsuura, M. Hino, M. Tojo, T. Kato, M. Ando, T. Oikawa, M. Kamata, and H. Munakata, “Possibility of energy saving by introducing energy conversion and energy storage technologies in traction power supply system,” in *2013 15th European Conference on Power Electronics and Applications (EPE)*, pp. 1–8, IEEE, 2013.

[90] H. Hayashiya, T. Suzuki, K. Kawahara, and T. Yamanoi, “Comparative study of investment and efficiency to reduce energy consumption in traction power supply: A present situation of regenerative energy utilization by energy storage system,” in *2014 16th International Power Electronics and Motion Control Conference and Exposition*, pp. 685–690, IEEE, 2014.

[91] Y. Liu, M. Chen, Y. Chen, and L. Chen, “Energy management of connected co-phase traction power system considering hess and pv,” in *2019 14th IEEE Conference on Industrial Electronics and Applications (ICIEA)*, pp. 1408–1412, IEEE, 2019.

[92] İ. Şengör, H. C. Kılıçkıran, H. Akdemir, B. Kekezoğlu, O. Erdinc, and J. P. Catalao, “Energy management of a smart railway station considering regenerative braking and stochastic behaviour of ess and pv generation,” *IEEE Transactions on Sustainable Energy*, vol. 9, no. 3, pp. 1041–1050, 2017.

[93] X. Zhu, H. Hu, H. Tao, and Z. He, “Stability analysis of PV plant-tied MVdc railway electrification system,” *IEEE Transactions on Transportation Electrification*, vol. 5, no. 1, pp. 311–323, 2019.

[94] J. A. Aguado, A. J. S. Racero, and S. de la Torre, “Optimal operation of electric railways with renewable energy and electric storage systems,” *IEEE Transactions on Smart Grid*, vol. 9, no. 2, pp. 993–1001, 2016.

[95] H. Novak, V. Lešić, and M. Vašak, “Hierarchical model predictive control for coordinated electric railway traction system energy management,” *IEEE Transactions on Intelligent Transportation Systems*, vol. 20, no. 7, pp. 2715–2727, 2018.

[96] Y. Sun, Z. Li, M. Shahidehpour, and B. Ai, “Battery-based energy storage transportation for enhancing power system economics and security,” *IEEE Transactions on Smart Grid*, vol. 6, no. 5, pp. 2395–2402, 2015.

[97] M. A. Vitorino, L. F. S. Alves, R. Wang, and M. B. de Rossiter Corrêa, “Low-frequency power decoupling in single-phase applications: A comprehensive overview,” *IEEE Transactions on Power Electronics*, vol. 32, no. 4, pp. 2892–2912, 2016.

[98] T. Egan, H. A. Gabbar, A. M. Othman, and R. Milman, “Design and control of resilient interconnected microgrid for sustained railway,” in *2017 IEEE International Conference on Smart Energy Grid Engineering (SEGE)*, pp. 131–136, IEEE, 2017.

[99] F. Ma, X. Wang, L. Deng, Z. Zhu, Q. Xu, and N. Xie, “Multi-port railway power conditioner and its management control strategy with renewable energy access,” *IEEE Journal of Emerging and Selected Topics in Power Electronics*, 2019.

[100] I. Krastev, P. Tricoli, S. Hillmansen, and M. Chen, "Future of electric railways: advanced electrification systems with static converters for ac railways," *IEEE Electrification Magazine*, vol. 4, no. 3, pp. 6–14, 2016.

[101] Y. Wang, B. Li, Z. Zhou, Z. Chen, W. Wen, X. Li, and C. Wang, "Dc voltage deviation-dependent voltage droop control method for vsc-mtdc systems under large disturbances," *IET Renewable Power Generation*, vol. 14, no. 5, pp. 891–896, 2019.

[102] L. Yu, R. Li, and L. Xu, "Hierarchical control of offshore wind farm connected by parallel diode-rectifier-based hvdc and hvac links," *IET Renewable Power Generation*, vol. 13, no. 9, pp. 1493–1502, 2019.

[103] Y. LI, Y. Li, and Q. Wang, "Robust predictive current control with parallel compensation terms against multi-parameter mismatches for pmsms," *IEEE Transactions on Energy Conversion*, pp. 1–1, 2020.

[104] Z. Xu, H. Xiao, and Z. Zhang, "Selection methods of main circuit parameters for modular multilevel converters," *IET Renewable Power Generation*, vol. 10, no. 6, pp. 788–797, 2016.

[105] K. Sharifabadi, L. Harnefors, H.-P. Nee, S. Norrga, and R. Teodorescu, *Design, control, and application of modular multilevel converters for HVDC transmission systems*. John Wiley & Sons, 2016.

[106] J. Huang, Y. Lu, B. Zhang, N. Wang, and W. Song, "Harmonic current elimination for single-phase rectifiers based on pr controller with notch filter," in *2012 15th International Conference on Electrical Machines and Systems (ICEMS)*, pp. 1–5, IEEE, 2012.

[107] Y. Jiang, J. Liu, W. Tian, M. Shahidehpour, and M. Krishnamurthy, "Energy harvesting for the electrification of railway stations: Getting a charge from the regenerative braking of trains.," *IEEE Electrification Magazine*, vol. 2, no. 3, pp. 39–48, 2014.

[108] F. Meishner and D. U. Sauer, "Wayside energy recovery systems in dc urban railway grids," *eTransportation*, vol. 1, p. 100001, 2019.

[109] M. Khodaparastan, A. A. Mohamed, and W. Brandauer, "Recuperation of regenerative braking energy in electric rail transit systems," *IEEE Transactions on Intelligent Transportation Systems*, vol. 20, no. 8, pp. 2831–2847, 2019.

[110] Bombardier, "Bombardier selects maxwell technologies ultracapacitors for EnerGstor rail transit braking energy recuperation system," 2021. https://www.greencarcongress.com/2012/01/energstor-20120119.html.

[111] S. Fouda and T. Hollett, "Energstor–a new wayside energy storage system," in *2011 American Public Transportation Association (APTA) Rail ConferenceAmerican Public Transportation Association*, 2011.

[112] A. Maoka, H. Ikarashi, and F. Kurino, "Demonstration testing and evaluation of a train running under its own power using a stationary energy storage system," *Hitachi Review*, vol. 63, no. 10, p. 679, 2014.

[113] Woojin, "Energy storage system for railway systems," 2015. www.wjis.co.kr/data/bbsData/15673999411.pdf.

[114] Siemens, "Increasing energy efficiency optimized traction power supply in mass transit systems," 2016.

[115] T. Ratniyomchai, S. Hillmansen, and P. Tricoli, “Recent developments and applications of energy storage devices in electrified railways,” *IET Electrical Systems in Transportation*, vol. 4, no. 1, pp. 9–20, 2014.

[116] ABB, “SEPTA rolls on with wayside energy storage systems (WESS),” 2016. https://search.abb.com/library/Download.aspx?DocumentID=9AKK106930A9058&LanguageCode=en&DocumentPartId=&Action=Launch.

[117] ABB, “EnvilineTM ERS energy recuperation system for DC rail transportation,” 2019. https://library.e.abb.com/public/348174e8288f4093a3eca60b7d05d4a2/Enviline%20ERS%20EN.pdf.

[118] M. Quraan, P. Tricoli, S. D’Arco, and L. Piegari, “Efficiency assessment of modular multilevel converters for battery electric vehicles,” *IEEE Transactions on Power Electronics*, vol. 32, no. 3, pp. 2041–2051, 2016.

[119] M. Coppola, A. Del Pizzo, and D. Iannuzzi, “A power traction converter based on modular multilevel architecture integrated with energy storage devices,” in *2012 Electrical Systems for Aircraft, Railway and Ship Propulsion*, pp. 1–7, IEEE, 2012.

[120] M. Vasiladiotis, N. Cherix, and A. Rufer, “Single-to-three-phase direct ac/ac modular multilevel converters with integrated split battery energy storage for railway interties,” in *2015 17th European Conference on Power Electronics and Applications (EPE’15 ECCE-Europe)*, pp. 1–7, IEEE, 2015.

[121] M. Quraan, T. Yeo, and P. Tricoli, “Design and control of modular multilevel converters for battery electric vehicles,” *IEEE Transactions on Power Electronics*, vol. 31, no. 1, pp. 507–517, 2015.

[122] C. Gan, Q. Sun, J. Wu, W. Kong, C. Shi, and Y. Hu, “Mmc-based srm drives with decentralized battery energy storage system for hybrid electric vehicles,” *IEEE Transactions on Power Electronics*, vol. 34, no. 3, pp. 2608–2621, 2018.

[123] P. Guo, Q. Xu, Y. Yue, F. Ma, Z. He, A. Luo, and J. M. Guerrero, “Analysis and control of modular multilevel converter with split energy storage for railway traction power conditioner,” *IEEE Transactions on Power Electronics*, vol. 35, no. 2, pp. 1239–1255, 2019.

[124] R. Bin, X. Yonghai, and L. Qiaoqian, “A control method for battery energy storage system based on mmc,” in *2015 IEEE 2nd International Future Energy Electronics Conference (IFEEC)*, pp. 1–6, IEEE, 2015.

[125] J. I. Y. Ota, T. Sato, and H. Akagi, “Enhancement of performance, availability, and flexibility of a battery energy storage system based on a modular multilevel cascaded converter (mmcc-ssbc),” *IEEE Transactions on Power Electronics*, vol. 31, no. 4, pp. 2791–2799, 2015.

[126] T. Soong and P. W. Lehn, “Assessment of fault tolerance in modular multilevel converters with integrated energy storage,” *IEEE Transactions on Power Electronics*, vol. 31, no. 6, pp. 4085–4095, 2015.

[127] Q. Chen, R. Li, and X. Cai, “Analysis and fault control of hybrid modular multilevel converter with integrated battery energy storage system,” *IEEE Journal of Emerging and Selected Topics in Power Electronics*, vol. 5, no. 1, pp. 64–78, 2016.

[128] L. Zhang, Y. Tang, S. Yang, and F. Gao, “Decoupled power control for a modular-multilevel-converter-based hybrid ac–dc grid integrated with hybrid energy storage,” *IEEE Transactions on Industrial Electronics*, vol. 66, no. 4, pp. 2926–2934, 2018.

[129] F. Errigo, F. Morel, C. M. de Vienne, L. Chedot, A. Sari, and P. Venet, “A submodule with integrated supercapacitors for hvdc-mmc providing fast frequency response,” *IEEE Transactions on Power Delivery*, 2021.

[130] M. Schroeder, S. Schmitt, S. Henninger, J. Jaeger, H. Rubenbauer, and O. Reimann, “Measurement results of a modular energy storage system unevenly equipped with lithium-ion batteries,” in *2015 17th European Conference on Power Electronics and Applications (EPE’15 ECCE-Europe)*, pp. 1–11, IEEE, 2015.

[131] T. Soong and P. W. Lehn, “Internal power flow of a modular multilevel converter with distributed energy resources,” *IEEE Journal of Emerging and Selected Topics in Power Electronics*, vol. 2, no. 4, pp. 1127–1138, 2014.

[132] H. Bayat and A. Yazdani, “A hybrid mmc-based photovoltaic and battery energy storage system,” *IEEE Power and Energy Technology Systems Journal*, vol. 6, no. 1, pp. 32–40, 2019.

[133] I. Puranik, L. Zhang, and J. Qin, “Impact of low-frequency ripple on lifetime of battery in mmc-based battery storage systems,” in *2018 IEEE Energy Conversion Congress and Exposition (ECCE)*, pp. 2748–2752, IEEE, 2018.

[134] S. B. Wersland, A. B. Acharya, and L. E. Norum, “Integrating battery into mmc submodule using passive technique,” in *2017 IEEE 18th Workshop on Control and Modeling for Power Electronics (COMPEL)*, pp. 1–7, IEEE, 2017.

[135] F. Gao, L. Zhang, Q. Zhou, M. Chen, T. Xu, and S. Hu, “State-of-charge balancing control strategy of battery energy storage system based on modular multilevel converter,” in *2014 IEEE Energy Conversion Congress and Exposition (ECCE)*, pp. 2567–2574, IEEE, 2014.

[136] Z. Wang, H. Lin, and Y. Ma, “Improved capacitor voltage balancing control for multimode operation of modular multilevel converter with integrated battery energy storage system,” *IET Power Electronics*, vol. 12, no. 11, pp. 2751–2760, 2019.

[137] N. Li, F. Gao, T. Hao, Z. Ma, and C. Zhang, “Soh balancing control method for the MMC battery energy storage system,” *IEEE Transactions on Industrial Electronics*, vol. 65, no. 8, pp. 6581–6591, 2017.

[138] M. Chen, R. Liu, S. Xie, X. Zhang, and Y. Zhou, “Modeling and simulation of novel railway power supply system based on power conversion technology,” in *2018 International Power Electronics Conference (IPEC-Niigata 2018-ECCE Asia)*, pp. 2547–2551, IEEE, 2018.

[139] I. Perin, G. R. Walker, and G. Ledwich, “Load sharing and wayside battery storage for improving ac railway network performance, with generic model for capacity estimation, part 1,” *IEEE Transactions on Industrial Electronics*, vol. 66, no. 3, pp. 1791–1798, 2018.

[140] A. Gómez-Expósito, J. M. Mauricio, and J. M. Maza-Ortega, “Vsc-based mvdc railway electrification system,” *IEEE Transactions on power Delivery*, vol. 29, no. 1, pp. 422–431, 2013.

[141] F. Hao, G. Zhang, J. Chen, Z. Liu, D. Xu, and Y. Wang, “Optimal voltage regulation and power sharing in traction power systems with reversible converters,” *IEEE Transactions on Power Systems*, vol. 35, no. 4, pp. 2726–2735, 2020.

[142] X. Yang, H. Hu, Y. Ge, S. Aatif, Z. He, and S. Gao, “An improved droop control strategy for VSC-based MVDC traction power supply system,” *IEEE Transactions on Industry Applications*, vol. 54, no. 5, pp. 5173–5186, 2018.

[143] D. Sharifi, “STATIC FREQUENCY CONVERTERS THE FUTURE FOR RAILWAY TRACTION,” 2018. SFC mesh feeding PPT.

[144] A. J. Buttery, T. M. Bagnall, *et al.*, “Protection and control concepts for sfc fed railways,” *CORE 2016: Maintaining the Momentum*, p. 81, 2016.

[145] J. Chen, L. Wang, L. Diao, H. Du, and Z. Liu, “Distributed auxiliary inverter of urban rail train—load sharing control strategy under complicated operation condition,” *IEEE Transactions on Power Electronics*, vol. 31, no. 3, pp. 2518–2529, 2015.

[146] P. Han, Y. Wang, X. Peng, X. He, Z. Shu, and S. Gao, “Current-sharing performance of an advanced co-phase traction power substation system based on cascade-parallel converter,” in *2017 IEEE 3rd International Future Energy Electronics Conference and ECCE Asia (IFEEC 2017-ECCE Asia)*, pp. 1932–1937, IEEE, 2017.

[147] M. Chen, Z. Cheng, Y. Liu, Y. Cheng, and Z. Tian, “Multitime-scale optimal dispatch of railway ftpss based on model predictive control,” *IEEE Transactions on Transportation Electrification*, vol. 6, no. 2, pp. 808–820, 2020.

[148] H. Junwen, L. Qunzhan, Z. Xiaohui, *et al.*, “General mathematical model for simulation of ac traction power supply system and its application,” *Power System Technology*, vol. 34, no. 7, pp. 18–23, 2010.

[149] A. Nami, J. Liang, F. Dijkhuizen, and G. D. Demetriades, “Modular multilevel converters for hvdc applications: Review on converter cells and functionalities,” *IEEE Transactions on Power Electronics*, vol. 30, no. 1, pp. 18–36, 2014.

[150] M. Winkelnkemper, A. Korn, and P. Steimer, “A modular direct converter for transformerless rail interties,” in *2010 IEEE International Symposium on Industrial Electronics*, pp. 562–567, IEEE, 2010.

[151] Y. Zhao, N. Dai, *et al.*, “Application of three-phase modular multilevel converter (MMC) in co-phase traction power supply system,” in *2014 IEEE Conference and Expo Transportation Electrification Asia-Pacific (ITEC Asia-Pacific)*, pp. 1–6, IEEE, 2014.

[152] L. Liu and N. Dai, “Hybrid railway power conditioner based on half-bridge modular multilevel converter,” in *2016 IEEE Energy Conversion Congress and Exposition (ECCE)*, pp. 1–7, IEEE, 2016.

[153] J. Peralta, H. Saad, S. Dennetière, J. Mahseredjian, and S. Nguefeu, “Detailed and averaged models for a 401-level mmc–hvdc system,” *IEEE Transactions on Power Delivery*, vol. 27, no. 3, pp. 1501–1508, 2012.

[154] K. Ilves, S. Norrga, L. Harnefors, and H.-P. Nee, “On energy storage requirements in modular multilevel converters,” *IEEE transactions on power electronics*, vol. 29, no. 1, pp. 77–88, 2013.

[155] G. A. Reddy and A. Shukla, “Circulating current optimization control of mmc,” *IEEE Transactions on Industrial Electronics*, vol. 68, no. 4, pp. 2798–2811, 2020.

[156] E. Sanchez-Sanchez, E. Prieto-Araujo, and O. Gomis-Bellmunt, “The role of the internal energy in mmcs operating in grid-forming mode,” *IEEE Journal of Emerging and Selected Topics in Power Electronics*, vol. 8, no. 2, pp. 949–962, 2019.

[157] S. Fuchs, M. Jeong, and J. Biela, “Reducing the energy storage requirements of modular multilevel converters with optimal capacitor voltage trajectory shaping,” in *2020 22nd European Conference on Power Electronics and Applications (EPE’20 ECCE Europe)*, pp. P–1, IEEE, 2020.

[158] R. Darus, J. Pou, G. Konstantinou, S. Ceballos, R. Picas, and V. G. Agelidis, “A modified voltage balancing algorithm for the modular multilevel converter: Evaluation for staircase and phase-disposition pwm,” *IEEE transactions on power electronics*, vol. 30, no. 8, pp. 4119–4127, 2014.

[159] A. Poorfakhraei, M. Narimani, and A. Emadi, “A review of modulation and control techniques for multilevel inverters in traction applications,” *IEEE Access*, vol. 9, pp. 24187–24204, 2021.

[160] S. Du, J. Liu, and T. Liu, “Modulation and closed-loop-based dc capacitor voltage control for mmc with fundamental switching frequency,” *IEEE Transactions on Power Electronics*, vol. 30, no. 1, pp. 327–338, 2014.

[161] J. Yin, J. I. Leon, M. A. Perez, L. G. Franquelo, A. Marquez, B. Li, and S. Vazquez, “Variable rounding level control method for modular multilevel converters,” *IEEE Transactions on Power Electronics*, vol. 36, no. 4, pp. 4791–4801, 2020.

[162] Z. Li, P. Wang, H. Zhu, Z. Chu, and Y. Li, “An improved pulse width modulation method for chopper-cell-based modular multilevel converters,” *IEEE Transactions on Power Electronics*, vol. 27, no. 8, pp. 3472–3481, 2012.

[163] S. Kouro, M. Malinowski, K. Gopakumar, J. Pou, L. G. Franquelo, B. Wu, J. Rodriguez, M. A. Pérez, and J. I. Leon, “Recent advances and industrial applications of multilevel converters,” *IEEE Transactions on industrial electronics*, vol. 57, no. 8, pp. 2553–2580, 2010.

[164] B. Li, R. Yang, D. Xu, G. Wang, W. Wang, and D. Xu, “Analysis of the phase-shifted carrier modulation for modular multilevel converters,” *IEEE Transactions on Power Electronics*, vol. 30, no. 1, pp. 297–310, 2014.

[165] R. Naderi and A. Rahmati, “Phase-shifted carrier pwm technique for general cascaded inverters,” *IEEE Transactions on power electronics*, vol. 23, no. 3, pp. 1257–1269, 2008.

Appendix A

Modelling and control of modular multilevel converters

This section explains the commonly used MMC modelling approach: the common mode and differential model decomposition for a single phase MMC leg analysis. The typical control system design is explained for external reference tracking and internal energy control. The converter modelling and control scheme basics are used as in Chapter 2 to Chapter 5.

MMC has been recognised as a popular topology for medium to high voltage power conversion applications such as HVDC, high voltage DC/DC transformers, static grid connection compensator and medium voltage machine drive etc. There are different types of modular multilevel converter typology built by modular switch blocks [149], this thesis only focuses on the traditional half-bridge commutation module structure while the focus is on the modelling and control to improve the system performance.

Early application of MMC for railway interties can be found in [150] where MMC convert 50 Hz to 16.7 Hz (or 25 Hz). Several MMC based active power conditioner can be found in recent literature [151, 152] for power quality compensation in the traction power supply system. The MMC can be connected to the catenary system without coupling transformers which reduces system cost.

A.1 MMC modelling

Modular multilevel converter for AC/DC conversion consists of a series connected submodules and inductors in each phase [153]. As shown in Figure A.1, a single phase AC/DC conversion is constructed by two arms which connect the DC-link terminals and the AC terminal. In each arm, N half-bridge modules ($\mathrm{SM}_1, \dots, \mathrm{SM}_N$) are connected in series as one branch. A branch inductor L_{br} exists in each arm for filtering the current and the equivalent resistance of the arm branch is represented by R_{br}.

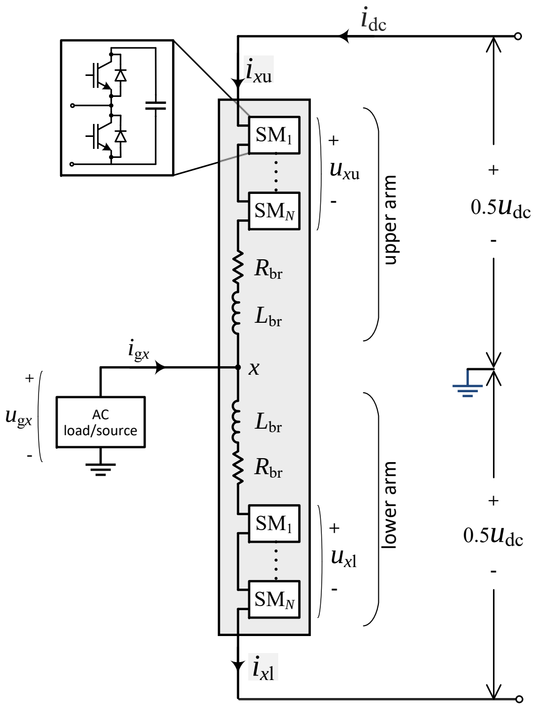

Fig. A.1 Single phase MMC circuit diagram

A.1.1 MMC basic topology

Figure A.1 shows a single phase MMC labeled as phase 'x' with one side connecting to grid phase x and another side connecting to a DC-link. The current flowing into the converter is denoted as positive. In this system, $i_{\mathrm{g}x}$ denotes the current flowing into the AC terminal x; i_{dc} is the DC-link current flowing through the whole phase. $i_{x\mathrm{u}}$, $i_{x\mathrm{l}}$ represent the current in the upper and lower arm respectively. $u_{\mathrm{g}x}$ is the measured voltage at the AC load or source to ground. The DC-link voltage is u_{dc}.

Each submodule in the MMC is a half-bridge unit having two switches and a capacitor [1]. If the upper switch is 'ON' and the lower switch is 'OFF', the capacitor is inserted into the MMC branch and external current determines the charging condition. If the upper switch is 'OFF' and the lower switch is 'ON', then the capacitor is bypassed in the MMC branch.

In Figure A.2, the sub-figures a) to d) show the 4 different modes under normal operation. Figure A.2 e) and f) show the 'blocked' mode of submodule which is used in fault ride through or initial charging conditions. The combination of both switches' 'ON' state is not allowed which can be prevented by dead-time mechanism in the PWM design.

Define the number of modules switched on in each arm as $N_{x,\mathrm{u}}$ and $N_{x,\mathrm{l}}$ and assume the capacitors have a balanced voltage $u_{C,\mathrm{ave}}$. So the $u_{x,\mathrm{u}}$ and $u_{x,\mathrm{l}}$ are expressed as (A.1). By using various modulation methods, we can freely adjust the averaged capacitor branch voltage from 0 to $Nu_{C,\mathrm{ave}}$. So we can approximate one MMC arm branch into a variable controlled voltage source.

---

[1] It is common to use multiple capacitors in one submodule. All capacitors can be viewed as an equivalent capacitor C_{sub}.

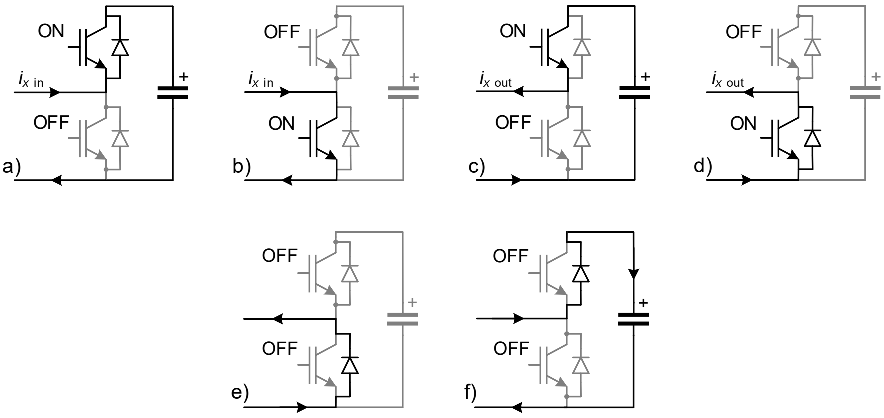

Fig. A.2 MMC submodule operating mode

$$\begin{array}{l} u_{x,\mathrm{u}} = N_{x,\mathrm{u}} u_{C,\mathrm{ave}} \\ u_{x,\mathrm{l}} = N_{x,\mathrm{l}} u_{C,\mathrm{ave}} \end{array}, \quad u_{C,\mathrm{ave}} = \frac{1}{2N} \sum_{i}^{N} \left(u_{C\mathrm{u},i} + u_{C\mathrm{l},i} \right). \tag{A.1}$$

A.1.2 Single phase MMC analysis

An averaged MMC model [153] is illustrated in Figure A.3(a) where submodules in each arm are represented by a controlled voltage source. The circuit equations can be written as:

$$\begin{array}{l} u_{\mathrm{ac}} = +0.5u_{\mathrm{dc}} - R_{\mathrm{br}} i_{\mathrm{u}} - L_{\mathrm{br}} \dfrac{\mathrm{d}i_{\mathrm{u}}}{\mathrm{d}t} - u_{\mathrm{u}} \\ u_{\mathrm{ac}} = -0.5u_{\mathrm{dc}} + R_{\mathrm{br}} i_{\mathrm{l}} + L_{\mathrm{br}} \dfrac{\mathrm{d}i_{\mathrm{l}}}{\mathrm{d}t} + u_{\mathrm{l}} \end{array}, \tag{A.2}$$

where u_{ac} is measured AC terminal to ground voltage. By adding and subtracting these two circuit equations in (A.2).

$$\begin{array}{l} u_{\mathrm{dc}} = 2\dfrac{u_{\mathrm{u}} + u_{\mathrm{l}}}{2} + 2R_{\mathrm{br}} \dfrac{i_{\mathrm{u}} + i_{\mathrm{l}}}{2} + 2L_{\mathrm{br}} \dfrac{\mathrm{d}}{\mathrm{d}t} \dfrac{i_{\mathrm{u}} + i_{\mathrm{l}}}{2} \\ u_{\mathrm{ac}} = \dfrac{-u_{\mathrm{u}} + u_{\mathrm{l}}}{2} + R_{\mathrm{br}} \dfrac{-i_{\mathrm{u}} + i_{\mathrm{l}}}{2} + L_{\mathrm{br}} \dfrac{\mathrm{d}}{\mathrm{d}t} \dfrac{-i_{\mathrm{u}} + i_{\mathrm{l}}}{2} \end{array} \tag{A.3}$$

We can have (A.3) which shows that the system can be decoupled into two subsystems. Figure A.3(b) and Figure A.3(c) show the two equivalent sub-models in differential mode and common mode. It is clear to see that the AC side is controlled by the difference of u_{u}, u_{l} while the DC side is controlled by the sum of u_{u}, u_{l}. Define the differential mode variables as x_{dif} and common mode variables as x_{com} in

$$x_{\mathrm{diff}} = (-x_{\mathrm{u}} + x_{\mathrm{l}})/2, \quad x_{\mathrm{com}} = (x_{\mathrm{u}} + x_{\mathrm{l}})/2, \tag{A.4}$$

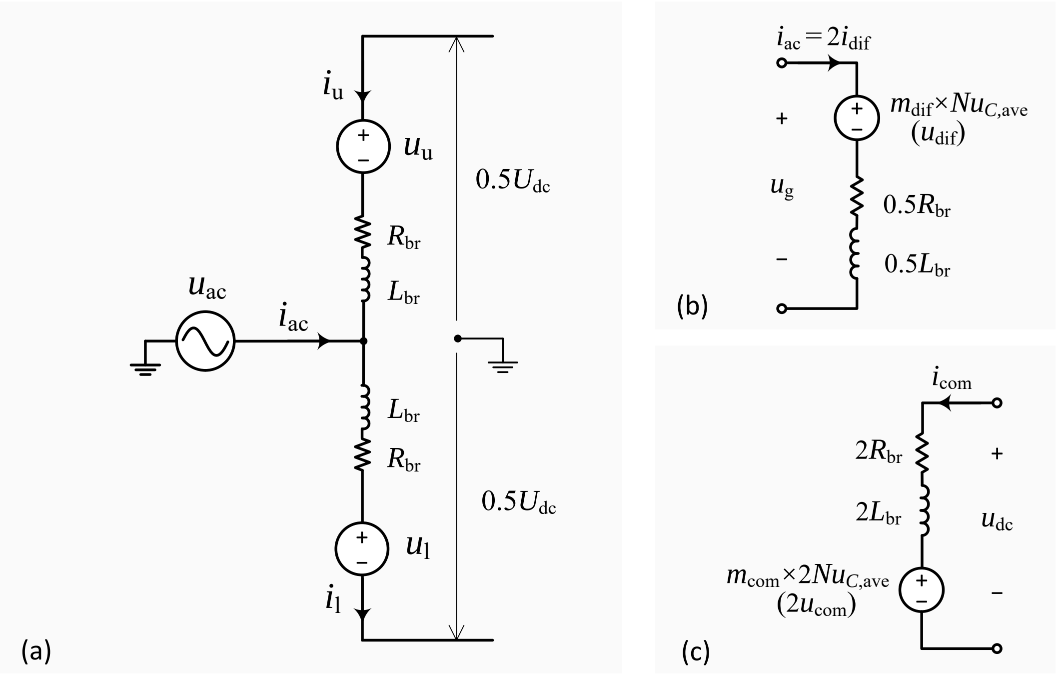

Fig. A.3 MMC single phase model: (a) averaged model, (b) differential mode model, (c) common mode model

so that the current and voltage measurements in upper and lower arms can be rewritten u_dif, u_com, i_dif and i_com[2].

Define the modulation index m in the differential and common mode in (A.5).

$$\begin{aligned} m_\mathrm{dif} &= \frac{u_\mathrm{dif}}{Nu_{C,\mathrm{ave}}} = \frac{1}{2}\frac{-u_\mathrm{u}+\mathrm{u}_\mathrm{l}}{Nu_{C,\mathrm{ave}}} \\ m_\mathrm{com} &= \frac{u_\mathrm{com}}{Nu_{C,\mathrm{ave}}} = \frac{1}{2}\frac{u_\mathrm{u}+\mathrm{u}_\mathrm{l}}{Nu_{C,\mathrm{ave}}} \end{aligned} \tag{A.5}$$

Then (A.3) can be written as (A.6). It is easy to see that common mode current and differential mode current can be controlled by adjusting two modulation variables m_com, m_dif. The typical control structure of a single phase MMC leg is explained in the next section.

$$\begin{aligned} u_\mathrm{dc} &= 2m_\mathrm{com}Nu_{C,\mathrm{ave}} + 2R_\mathrm{br}i_\mathrm{com} + 2L_\mathrm{br}\frac{\mathrm{d}}{\mathrm{d}t}i_\mathrm{com} \\ u_\mathrm{ac} &= m_\mathrm{dif}Nu_{C,\mathrm{ave}} + R_\mathrm{br}i_\mathrm{dif} + L_\mathrm{br}\frac{\mathrm{d}}{\mathrm{d}t}i_\mathrm{dif} \end{aligned} \tag{A.6}$$

---

[2] Note that in some materials, researchers name the common and differential value reversely, due to different current direction definition.

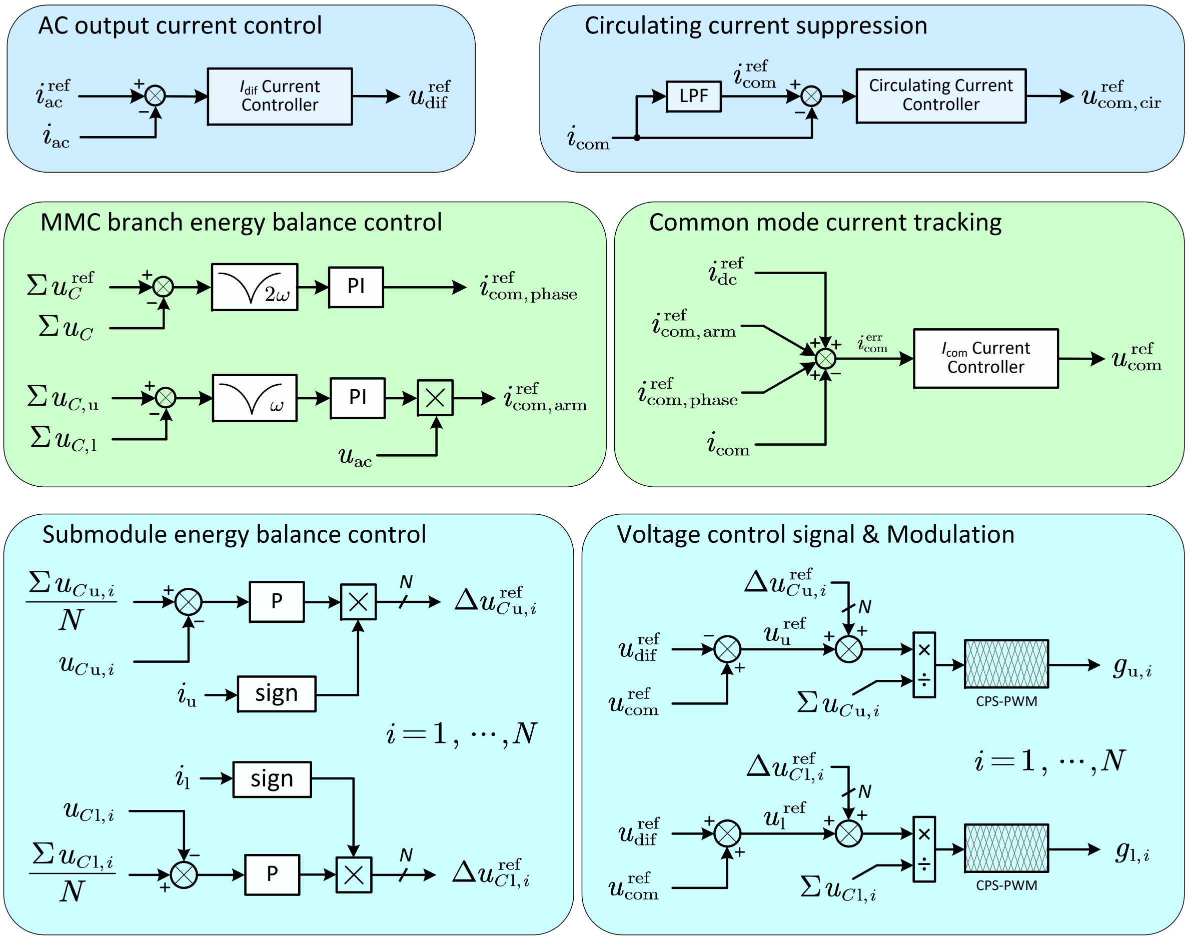

Fig. A.4 MMC internal dynamics control principle

A.2 MMC control and operation

As discussed above, if each MMC submodule branch can be viewed as a controlled voltage sources having $[0, Nu_{C,\mathrm{ave}}]$ output range. Then the AC side current (i_{dif}) and DC side current (i_{com}) can be controlled by adjusting the modulation index m_{dif}, m_{com} in a decoupled manner. However, in reality, capacitors in each submodule are charged/discharged not only by i_{com} but also i_{dif} where the latter one is a single phase AC current. Therefore, the capacitor voltage will always be oscillating rather than staying at a near constant value like the conventional two level converters.

The complex dynamic of the submodule capacitor [154] brings two challenges: 1) the oscillation of the capacitor voltages might get itself coupled into the AC and DC side currents; 2) the averaged capacitors' voltage in different modules will diverge away from the nominal value. These potential issues threaten the stable operation and degrade the system performance. So in a conventional control scheme, the output current, circulating current and the capacitor energy are controlled in designated controllers which are explained as follows.

Figure A.4 shows the principle of MMC internal control logic. Some controller design details such as feedforward terms, scaling factors are ignored.

A.2.1 Current control

AC side current control

A typical AC current control loop is illustrated in Figure A.4. Controller based on proportional-resonant (PR), hysteresis or model based approach are commonly used. This AC current control loop generates voltage control reference $u_{\text{dif}}^{\text{ref}}$ from the instantaneous measurement of i_{ac} and $i_{\text{ac}}^{\text{ref}}$. If PI controllers are adopted in the AC current control, rotational frame to dq frame transformation is necessary. This control principle is identical to the traditional 2-level DC/AC converter.

Circulating current control

If the explicit common mode current reference control is not included in the MMC control system, and a traditional normalisation method[3] is used before modulation. A circulating current having a doubled AC side frequency might be coupled into i_{com} in steady state. This issue is caused by the double frequency oscillation in the energy difference between upper and lower arms.

This oscillating current [155] does not contribute to the efficient energy conversion inside MMC. Should this issue exist, a circulating current controller is required. The reference signal is extracted by filtering the measured i_{com} by a low pass filter (LFP)[4] Then a resonant controller can be used in the circulating current suppression control and the control output $u_{\text{com,cir}}^{\text{ref}}$ will be added into the common mode voltage reference.

DC side current control

If an explicit DC current reference is used in the MMC internal control, a specific common model current controller is needed. By controlling the $u_{\text{com}}^{\text{ref}}$ in each phase, i_{com} can track the designed reference $i_{\text{com}}^{\text{ref}}$ accurately in steady states. This current controller can be parallel connected proportional, integral, resonant controller (PIR) or model based ones such as deadbeat and model predictive controller.

A.2.2 Internal energy control

MMC internal energy control [156, 157] task is managed into three different scopes: 1) phase energy, 2) arm energy and 3) submodule energy. For simplicity, energy control is achieved by averaged capacitor voltage control. The detailed explanation of energy transfer analysis is explained in Chapter 3. The control principle is explained as follows:

---

[3] This means the control voltage signal is normalised by the measured DC-link voltage value.

[4] The LPF can be a mean filter or notch filter.

Phase energy control Phase energy is indicated by the averaged value of all submodule capacitor voltages. The nominal value of sum of voltage is given by $\Sigma u_C^{\mathrm{ref}} = 2Nu_C^{\mathrm{nom}}$, where u_C^{nom} is the nominal capacitor voltage of each submodule. In steady state, if the circulating current is eliminated, the sum of all submodules in one phase Σu_C comprise a DC component and double frequency AC component. Therefore, a double frequency notch filter is used to extract the DC voltage error, then PI controller is capable of compensating the phase energy error.

Arm energy control Similarly, arm energy is indicated by the difference of upper and lower arm capacitor voltage $\Sigma u_{C,\mathbf{u}} - \Sigma u_{C,\mathbf{l}}$. In the ideal steady state, this subtraction result contains a DC component and a fundamental frequency AC component. So a fundamental frequency notch filter is used to extract the DC voltage error and PI controller is used afterwards. However, to balance the upper and lower arm energy, the common mode current would better be a fundamental frequency signal with the same phase angle as terminal voltage u_{ac}. So a reference AC signal with the same phase angle as AC terminal voltage is used to modulate the common mode current reference for arm energy balance.

Submodule energy control Despite the previously introduced phase and arm controller designs, submodules in each arm still diverge from each other if they are not properly controlled. To balance out the energy difference, (take upper arm as the example), averaged capacitor voltage $\Sigma u_{C,\mathrm{u},i}/N$ is used as voltage reference. Voltage error in respect to each individual submodule is denoted as $u_{\mathrm{Cu},i}^{\mathrm{err}}$. These submodule voltage error values are calculated and then magnified by a proportional gain. The resultant $\Delta u_{C,\mathrm{u},i}^{\mathrm{ref}}$ is applied to each submodules' modulation index. The sign of this control input is determined by the direction of common mode current. For instance, if the current i_{com} is positive meaning the capacitors are charging, then submodules having less voltage will increase the switch 'ON' period to charge more.

Another way to balance submodule capacitor energy is the sorting method [158] where the selection of modules to be or not to be inserted depends on the sorting result of the measured instantaneous voltage and arm current direction.

A.2.3 Modulation

The differential mode voltage reference controls AC output current tracking. The common mode voltage reference controls the DC side current for circulating current suppression, energy balancing and fast power delivery on DC-link side. By adding and subtracting these two terms, the desired arm voltage references $u_{\mathrm{u}}^{\mathrm{ref}}$, $u_{\mathrm{l}}^{\mathrm{ref}}$ are obtained. Then each voltage reference is modified by a N dimension submodule voltage control input. Finally, these voltage control references are normalised for modulation.

Two types of normalisation can be used: direct or indirect normalisation. The direct method uses the sum of available voltage in one arm, so that the most accurate voltage control result is guaranteed. The indirect method uses the measured DC-link voltage. The latter one makes the dynamics of upper

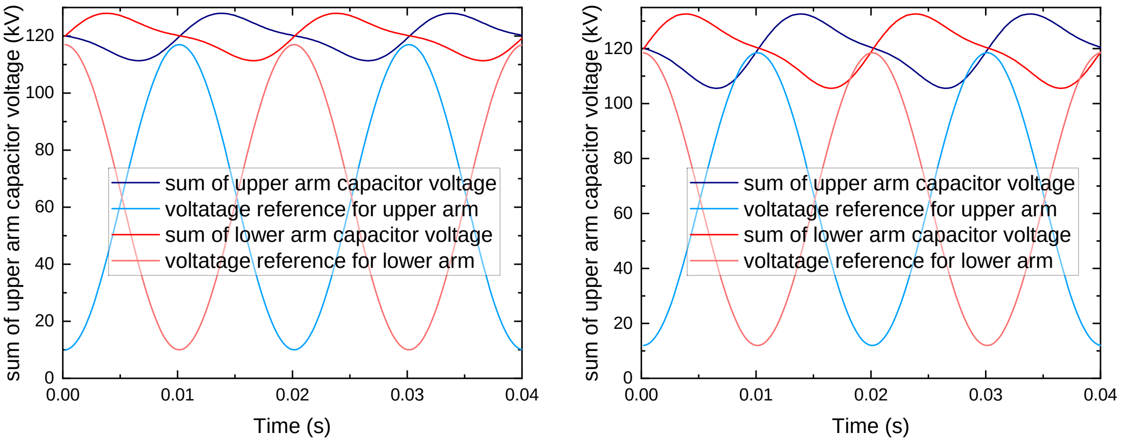

(a) Acceptable voltage reference (20 MW)

(b) Over-modulation condition (30 MW)

Fig. A.5 Arm voltage control reference versus available voltage

and lower arm voltage coupled into AC and DC current. So dedicated circulating current suppression control is indispensable in the indirect approach.

Modulation index

Unlike the conventional two level three phase converter where all phase legs share a common DC-link capacitor, the MMC capacitors are distributed into each arm. This means even in the ideal steady state, the available voltage in each arm might be varying significantly rather than stays near a constant DC value. During the design and control period, feasible operation range should be evaluated to avoid over-modulation especially for the small capacitor value design. An open loop prediction method is presented using the result derived in Chapter 3.3.1.

Figure A.5 presents phase A of a three phase MMC rectifying power from AC to DC side. Figure A.5a shows the predicted steady state of voltage signals for 20 MW active power deliver condition. The sum of arm branch capacitor voltage is the upper limit of available voltage to be modulated. It can be seen that in Figure A.5b, the control reference is greater than the available voltage supported by all submodules. This shows that this system cannot not operate in 30 MW operation.

Modulation methods

Three different types of modulation are commonly used in the MMC modulation [159].

Staircase modulation / The Nearest level modulation The nearest level modulation is based on round method which is suitable for MMC with large number of submodules. Some variant of the nearest level modulation can be found in [160, 161] This can be combined with PWM method for reduced harmonic content [162].

Phase-disposition / Level-shift PWM The PD-PWM is realised by shifting carrier wave level to output multilevel signal which is used in NPC [163]. This method is also applicable to MMC system, but it brings unbalanced stress to each module in MMC [164].

Phase-shift PWM The PS-PWM (or CPS-PWM) is widely adopted in the cascaded H-bridge multilevel converters [165]. Each carrier wave has frequency $f_{\mathrm{c}} = f_{\mathrm{eq}}/N$, where f_{eq} is the equivalent switching frequency for the whole MMC phase. Each carrier wave has $2\pi/N$ phase shift angle for each submodule. This method is widely used because of several merits: even power stress distribution, low THD and easy implementation.

Appendix B

Deadbeat controller implementation for MMC

This section explains the derivation of deadbeat controlled for MMC single phase converter. Using the notation and circuit equation given in Appendix A, the dc terminal voltage u_{dc} and ac terminal voltage u_{ac} are expressed in (B.1):

$$\begin{aligned} u_{\mathrm{dc}} &= 2u_{\mathrm{com}} + 2R_{\mathrm{br}} i_{\mathrm{com}} + 2L_{\mathrm{br}} \frac{\mathrm{d}}{\mathrm{d}t} i_{\mathrm{com}} \\ u_{\mathrm{ac}} &= u_{\mathrm{dif}} + \frac{1}{2} R_{\mathrm{br}} i_{\mathrm{g}} + \frac{1}{2} L_{\mathrm{br}} \frac{\mathrm{d}}{\mathrm{d}t} i_{\mathrm{g}} \end{aligned} . \tag{B.1}$$

The voltage and current values in the above equations are time variables. At k-th sampling instance and T_{sc} sampling interval, assume the controlled current can reach the given reference at the next sampling time $(k+1)$ which means $i_{\mathrm{com}}(k+1) = i^*_{\mathrm{com}}(k+1), i_{\mathrm{g}}(k+1) = i^*_{\mathrm{g}}(k+1)$. We can estimate the differential mode voltage and common mode voltage that can fulfil this assumption. For example $u_{\mathrm{dc}}(t)$ can be discretized as $u_{\mathrm{dc}}(k)$, and the first order derivative $\frac{\mathrm{d}}{\mathrm{d}t} i_{\mathrm{com}}(t)$ can be discretized into $\frac{i^*_{\mathrm{com}}(k+1) - i_{\mathrm{com}}(k)}{T_{\mathrm{sc}}}$. Therefore, we can convert (B.1) into discrete form as shown in (B.2).

$$\begin{aligned} u^*_{\mathrm{com}} &= 0.5u_{\mathrm{dc}}(k) - R_{\mathrm{br}} i_{\mathrm{com}}(k) - L_{\mathrm{br}} \frac{i^*_{\mathrm{com}}(k+1) - i_{\mathrm{com}}(k)}{T_{\mathrm{sc}}} \\ u^*_{\mathrm{dif}} &= u_{\mathrm{ac}}(k) - \left(\frac{1}{2} R_{\mathrm{br}} + R_{\mathrm{g}}\right) i_{\mathrm{g}}(k) - \left(\frac{1}{2} L_{\mathrm{br}} + L_{\mathrm{g}}\right) \frac{i^*_{\mathrm{g}}(k+1) - i_{\mathrm{g}}(k)}{T_{\mathrm{sc}}} \end{aligned} \tag{B.2}$$

Finally, the upper and lower arm voltage expression can be given as (B.3) which is the deadbeat controller expression used in the controller design.

$$\begin{aligned}
u_{\mathrm{u}}^{*} &= -u_{\mathrm{ac}}(k) + 0.5u_{\mathrm{dc}}(k) - R_{\mathrm{br}}i_{\mathrm{com}}(k) - L_{\mathrm{br}}\frac{i_{\mathrm{com}}^{*}(k+1) - i_{\mathrm{com}}(k)}{T_{\mathrm{sc}}} + \left(\frac{1}{2}R_{\mathrm{br}} + R_{\mathrm{g}}\right)i_{\mathrm{g}}(k) \\
&\quad + \left(\frac{1}{2}L_{\mathrm{br}} + L_{\mathrm{g}}\right)\frac{i_{\mathrm{g}}^{*}(k+1) - i_{\mathrm{g}}(k)}{T_{\mathrm{sc}}} \\
u_{\mathrm{l}}^{*} &= u_{\mathrm{ac}}(k) + 0.5u_{\mathrm{dc}}(k) - R_{\mathrm{br}}i_{\mathrm{com}}(k) - L_{\mathrm{br}}\frac{i_{\mathrm{com}}^{*}(k+1) - i_{\mathrm{com}}(k)}{T_{\mathrm{sc}}} - \left(\frac{1}{2}R_{\mathrm{br}} + R_{\mathrm{g}}\right)i_{\mathrm{g}}(k) \\
&\quad - \left(\frac{1}{2}L_{\mathrm{br}} + L_{\mathrm{g}}\right)\frac{i_{\mathrm{g}}^{*}(k+1) - i_{\mathrm{g}}(k)}{T_{\mathrm{sc}}}
\end{aligned}, \tag{B.3}$$

where i_{com}^{*} and i_{g}^{*} are the current control references calculated from the outer control loop.